2011

ATOMIC FORCE MICROSCOPY METHOD DEVELOPMENT FOR SURFACE ENERGY ANALYSIS

Clare Aubrey Medendorp
University of Kentucky, ceamedendorp@gmail.com

ABSTRACT OF DISSERTATION

Clare Aubrey Medendorp

The Graduate School

University of Kentucky

2011

ATOMIC FORCE MICROSCOPY METHOD DEVELOPMENT FOR SURFACE ENERGY ANALYSIS

ABSTRACT OF DISSERTATION

A dissertation submitted in partial fulfillment of the requirements for the degree of Doctor of Philosophy in the College of Pharmacy at the University of Kentucky

By

Clare Aubrey Medendorp

Lexington, Kentucky

Director: Dr. Tonglei Li, Professor of Pharmaceutical Sciences

Lexington, Kentucky

2011

ABSTRACT OF DISSERTATION

ATOMIC FORCE MICROSCOPY METHOD DEVELOPMENT FOR SURFACE ENERGY ANALYSIS

The vast majority of pharmaceutical drug products are developed, manufactured, and delivered in the solid-state where the active pharmaceutical ingredient (API) is crystalline. With the potential to exist as polymorphs, salts, hydrates, solvates, and co-crystals, each with their own unique associated physicochemical properties, crystals and their forms directly influence bioavailability and manufacturability of the final drug product. Understanding and controlling the crystalline form of the API throughout the drug development process is absolutely critical. Interfacial properties, such as surface energy, define the interactions between two materials in contact. For crystal growth, surface energy between crystal surfaces and liquid environments not only determines the growth kinetics and morphology, but also plays a substantial role in controlling the development of the internal structure. Surface energy also influences the macroscopic particle interactions and mechanical behaviors that govern particle flow, blending, compression, and compaction. While conventional methods for surface energy measurements, such as contact angle and inverse gas chromatography, are increasingly employed, their limitations have necessitated the exploration of alternative tools. For that reason, the first goal of this research was to serve as an analytical method development report for atomic force microscopy and determine its viability as an alternative approach to standard methods of analysis. The second goal of this research was to assess whether the physical and the mathematical models developed on the reference surfaces such as mica or graphite could be extended to organic crystal surfaces. This dissertation, while dependent upon the requisite number of mathematical assumptions, tightly controlled experiments, and environmental conditions, will nonetheless help to bridge the division between lab-bench theory and successful industrial implementation. In current practice, much of pharmaceutical formulation development relies on trial and error and/or duplication of historical methods. With a firm fundamental understanding of surface energetics, pharmaceutical scientists will be armed with the knowledge required to more effectively estimate, predict, and control the physical behaviors of their final drug products.

KEYWORDS: contact angle, atomic force microscopy, polymorphs, crystal habit, surface energy

Multimedia Elements Used: JPEG (.jpg); Bitmap (.bmp); TIF (.tif); GIF (.gif).

Clare Aubrey Medendorp

_____

Student's Signature

August 2011

_____

Date

ATOMIC FORCE MICROSCOPY METHOD DEVELOPMENT FOR SURFACE ENERGY ANALYSIS

By

Clare Aubrey Medendorp

Tonglei Li

_____

Co-Director of Dissertation

Paul Bummer

_____

Co-Director of Dissertation

Jim Pauly

_____

Director of Graduate Studies

August 2011

_____

Date

RULES FOR THE USE OF DISSERTATIONS

Unpublished dissertations submitted for the Doctor's degree and deposited in the University of Kentucky Library are as a rule open for inspection, but are to be used only with due regard to the rights of the authors. Bibliographical references may be noted, but quotations or summaries of parts may be published only with the permission of the author, and with the usual scholarly acknowledgments.

Extensive copying or publication of the dissertation in whole or in part also requires the consent of the Dean of the Graduate School of the University of Kentucky.

A library that borrows this dissertation for use by its patrons is expected to secure the signature of each user.

Name	Date

DISSERTATION

Clare Aubrey Medendorp

The Graduate School

University of Kentucky

2011

ATOMIC FORCE MICROSCOPY METHOD DEVELOPMENT FOR SURFACE ENERGY ANALYSIS

DISSERTATION

A dissertation submitted in partial fulfillment of the requirements for the degree of Doctor of Philosophy in the College of Pharmacy and Economics at the University of Kentucky

By

Clare Aubrey Medendorp

Lexington, Kentucky

Director: Dr. Tonglei Li, Professor of Pharmaceutical Sciences

Lexington, Kentucky

2011

for Joseph, Jopatrice, and Frank

ACKNOWLEDEGEMENTS

This dissertation would not have been possible without the support of numerous individuals. First, I would like to thank my advisor Dr. Tonglei Li for the opportunity to study under his leadership. His guidance, support, and patience contributed towards my scientific education and professional development. I would also like to thank my co-advisor Dr. Paul Bummer for his support. His enthusiasm and passion for developing scientist creates a rewarding environment to work in. I would also like to thank my dissertation committee: Dr. Brad Anderson and Dr. Carolyn Brock for their time, support, and contributions to my development and the advancement of this project. I would like to thank Dr. Constance Wood for her training and guidance in statistics.

Many thanks to the PhRMA Foundation and Computational and Computer Sciences program at the University of Kentucky for their financial support to complete my dissertation.

On a personal note, I would like to thank all of the members of the Li lab, Matt Swadley, Sihui Long, Alessandra Mattei, Shaoxin Feng, and Hua Zhang. I would especially like to thank Christin Hollis for her support and friendship. I would like to thank several colleagues at Merck for their support. I would like to thank my family and friends for their love and support. They continued to believe in me and push me towards professional and personal development. I would like to thank my loving husband, Joseph, without him, this dissertation would not have been possible. Thank you for being extremely supportive and caring. Thank you!

TABLE OF CONTENTS

ACKNOWLEDEGEMENTS x

List of Tables xiv

List of Figures xviii

List of Abbreviations xxi

Chapter 1 - Introduction 1

1.1 Dissertation Purpose 1

1.2 Review of Surface Energetics 1

1.3 Current State-of-the-Art 2

1.4 Objectives 9

1.4.1 Specific Aim 1 9
1.4.2 Specific Aim 2 11

Chapter 2 – Contact Angle 13

2.1 Contact Angle and Young's Equation 13

2.2 Review of the Geometric Mean and Indirect Models 16

2.2.1 Fowkes 20
2.2.2 Van Oss, Chaudhury, Good 20
2.2.3 Owens-Wendt-Rabel-Kaelble 23
2.2.4 Neumann 24
2.2.5 Model Summary 26
2.3.1 Contact Angle Hysteresis 28
2.3.2 Contact angle measurements with hygroscopic solvents and additive solutions 29
2.3.3 Temperature effect on contact angle measurements 31
2.3.4 Contact angles on deformable surfaces 32
2.4 Methodology for the Evaluation of Indirect Models on Inert Surfaces 34

2.4.1 Inert surfaces 34
2.4.2 Contact angle measurements 34
2.5 Contact Angle Results and Evaluation of Indirect Models on Inert Surfaces 39

2.5.1 Static contact angle measurements 39
2.5.2 Advancing contact angle measurements 48
2.5.3 Static contact angle measurements with hygroscopic liquids 53
2.6 Contact Angle Summary 58

Chapter 3 – Atomic Force Microscopy 60

3.1 Atomic Force Microscopy Introduction 60

3.2 Imaging Modes and Techniques 65

3.3 AFM Tip Characterization 69

3.3.1 Calibration of spring constants 69
3.3.2 Tip radius measurements 74
3.4 AFM Scanning Parameters 77

3.4.1 Scan size 77
3.4.2 Scan rate 81
3.4.3 Force applied and contact area 81
3.5 Statistical Analysis of AFM Measurements 84

3.5.1 Identification of variables 85
3.6 AFM Methodology 93

3.6.1 Spring constant 93
3.6.2 Tip radius 105
3.6.3 AFM scanning parameters 109
3.6.4 AFM measurements 112
3.7 Summary 119

Chapter 4 – AFM Math Models 121

4.1 Contact Mechanics 121

4.2 Surface Energy Models 128

4.2.1 Surface energy model 1 128
4.2.2 Surface energy model 2 135
4.2.3 Surface energy model 3 138
4.2.4 Surface energy model 4 139
4.3 Summary 142

Chapter 5 – AFM Results 144

5.1 Introduction 144

5.1 AFM Measurements 144

5.1.1 Solid-vapor surface energy 145
5.1.2 Solid-liquid surface energy 166
5.2 Summary 229

Chapter 6 – Applying the AFM Methodology to Aspirin 234

6.1 Aspirin Crystal Growth and Indexing Review 234

6.1.1 Introduction 234
6.1.2 Background on aspirin 236
6.1.3 Crystal growth 238
6.1.4 Aspirin crystal structure 238
6.2 Contact Angle Method 242

6.2.1 Contact angles 242
6.2.2 Surface energy calculations from contact angle indirect models 244
6.3 AFM Application 255

6.3.1 Solid-vapor surface energy 255
6.3.2 Solid-liquid surface energy 266
6.4 Summary 314

Chapter 7 – Conclusion and Future Directions 320

Appendix 1 - Report Generation for Calculation of Spring Constant 324

Appendix 2 - Matlab code for Calculation of Spring Constant 328

References 331

Vita 343

List of Tables

Table #	Table Title	Page
2.1	Surface tensions of various solvents used to measure contact angles	36
2.2	Average sessile drop contact angles on mica and graphite	41
2.3	Average solid-vapor surface energy for mica and graphite	42
2.4	Average solid-liquid surface energies for mica and graphite	46
2.5	Average advancing and receding contact angles on mica and graphite	50
2.6	Advancing average solid-vapor surface energies for mica and graphite	51
2.7	Average solid-liquid surface energies calculated from advancing contact angle data	52
2.8	Water content of liquids used in contact angle measurements after being dried	55
2.9	Contact angles measured on mica and graphite with dried and rehydrated ethylene glycol and formamide	56
3.1	Statistics table showing the combined sample, tips, location, and surface energy	89
3.2	Statistics results from a repeated measures mixed model	92
3.3	Results for spring constant from the added mass method	97
3.4	AFM tip radii measured from blind reconstruction and SEM images	108
4.1	Contact mechanics equations for Hertzian, JKR, and DMT models	125
4.2	Comparison of the four mathematical used to determine surface energy with AFM force measurements	143
5.1	Tip radius and ambient and controlled humidity average tip-vapor surface energy used to determine graphite solid-vapor surface energy.	150
5.2	Average solid-vapor surface energy of graphite determined using the AFM and contact angle methods.	151
5.3	Mixed model statistics for graphite AFM measurements in ambient environmental conditions.	152
5.4	Mixed model statistics for graphite AFM measurements with controlled humidity environment.	153
5.5	Tip radius and ambient and controlled humidity average tip-vapor surface energy used to determine mica solid-vapor surface energy.	161
5.6	Mixed model statistics for mica AFM measurements in ambient environmental conditions.	162
5.7	Mixed model statistics for mica AFM measurements in controlled humidity environmental conditions.	163
5.8	Average solid-vapor surface energy of mica determined using the AFM and contact angle methods.	165
5.9	Spring constant, tip radius, and average tip-liquid surface energy are listed for the AFM tips used to measure the solid-liquid surface energy of graphite and mica in water.	170
5.10	Mixed model statistics for graphite AFM measurements in water.	171

5.11	Average solid-liquid surface energy of graphite with water determined using the AFM and contact angle methods.	173
5.12	Mixed model statistics for mica AFM measurements in water.	177
5.13	Average solid-liquid surface energy of mica with water determined using the AFM and contact angle methods.	179
5.14	Spring constant, tip radius, and average tip-liquid surface energy are listed for the AFM tips used to measure the solid-liquid surface energy of graphite and mica in diiodomethane.	183
5.15	Mixed model statistics for graphite AFM measurements in diiodomethane.	184
5.16	Average solid-liquid surface energy of graphite with diiodomethane determined using the AFM and contact angle methods.	186
5.17	Mixed model statistics for mica AFM measurements in water.	190
5.18	Average solid-liquid surface energy of mica with diiodomethane determined using the AFM and contact angle methods.	192
5.19	Tip radius and average tip-liquid surface energy are listed for the AFM tips used to measure the solid-liquid surface energy of graphite in formamide.	194
5.20	Mixed model statistics for graphite AFM measurements with dry formamide.	200
5.21	Mixed model statistics for graphite AFM measurements with 0.5% w/w water/formamide.	201
5.22	Mixed model statistics for graphite AFM measurements with 1% w/w water/formamide.	202
5.23	Mixed model statistics for graphite AFM measurements with 5% w/w water/formamide.	203
5.24	Average solid-liquid surface energy of graphite with dry formamide determined using the AFM and contact angle methods.	208
5.25	Average solid-liquid surface energy of graphite with 0.5% w/w water/formamide determined using the AFM and contact angle methods.	209
5.26	Average solid-liquid surface energy of graphite with 1% w/w water/formamide determined using the AFM and contact angle methods.	210
5.27	Average solid-liquid surface energy of graphite with 5% w/w water/formamide determined using the AFM and contact angle methods.	211
5.28	Tip radius and average tip-liquid surface energy are listed for the AFM tips used to measure the solid-liquid surface energy of mica in ethylene glycol.	213
5.29	Mixed model statistics for mica AFM measurements with dry ethylene glycol.	217
5.30	Mixed model statistics for mica AFM measurements with 0.5% w/w ethylene glycol.	218
5.31	Mixed model statistics for mica AFM measurements with 1% w/w ethylene glycol.	219

5.32	Mixed model statistics for mica AFM measurements with 5% w/w ethylene glycol.	220
5.33	Average solid-liquid surface energy of mica and dry ethylene glycol determined using the AFM and contact angle methods.	225
5.34	Average solid-liquid surface energy of mica with 0.5% w/w water/ethylene glycol determined using the AFM and contact angle methods.	226
5.35	Average solid-liquid surface energy of mica with 1% w/w water/ethylene glycol determined using the AFM and contact angle methods.	227
5.36	Average solid-liquid surface energy of mica with 5% w/w water/ethylene glycol determined using the AFM and contact angle methods.	228
6.1	Contact angles on the (100) and (001) faces of aspirin measure in selected solvents.	243
6.2	Average solid-vapor surface energy calculated from the three indirect contact angle models.	245
6.3	Average solid-liquid surface energy on the (001) and (100) faces determined from contact angle measurements.	249
6.4	Tip radius and average tip-vapor surface energy for the tips used to calculate the solid-vapor surface energy of the (001) and (100) faces of aspirin.	259
6.5	Mixed model statistics for AFM Measurements on the (100) face of aspirin in a controlled humidity environment.	260
6.6	Average solid-vapor surface energy of the (100) face of aspirin determined using the AFM and contact angle methods.	261
6.7	Mixed model statistics for AFM Measurements on the (001) face of aspirin in a controlled humidity environment.	262
6.8	Average solid-vapor surface energy of the (001) face of aspirin determined using the AFM and contact angle methods.	263
6.9	Tip radius and average tip-vapor surface energy for the tips used to calculate the solid-liquid surface energy of the (001) and (100) faces of aspirin with diiodomethane	269
6.10	Mixed model statistics for AFM Measurements on the (100) face of aspirin in diiodomethane.	270
6.11	Average solid-liquid surface energy of the (100) face of aspirin with diiodomethane determined using the AFM and contact angle methods.	271
6.12	Mixed model statistics for AFM Measurements on the (001) face of aspirin in diiodomethane.	272
6.13	Average solid-liquid surface energy of the (001) face of aspirin with diiodomethane determined using the AFM and contact angle methods.	273
6.14	Tip radius and average tip-vapor surface energy (standard deviation) for the tips used to calculate the solid-liquid surface energy of the (001) and (100) faces of aspirin with 12, 14, 16, 18,	279

and 20mM ASA solutions.
6.15 Mixed model statistics for AFM Measurements on the (001) face of aspirin in 12mM ASA Solution. 280
6.16 Mixed model statistics for AFM Measurements on the (100) face of aspirin in 12mM ASA solution. 281
6.17 Mixed model statistics for AFM Measurements on the (001) face of aspirin in 14mM ASA Solution. 288
6.18 Mixed model statistics for AFM Measurements on the (100) face of aspirin in 14mM ASA solution. 289
6.19 Mixed model statistics for AFM Measurements on the (001) face of aspirin in 16mM ASA Solution. 296
6.20 Mixed model statistics for AFM Measurements on the (100) face of aspirin in 16mM ASA solution. 297
6.21 Average solid-liquid surface energy of the (001) and (100) faces of aspirin with 16mM ASA solution determined using the AFM and contact angle methods. 300
6.22 Mixed model statistics for AFM Measurements on the (001) face of aspirin in 18mM ASA Solution. 304
6.23 Mixed model statistics for AFM Measurements on the (100) face of aspirin in 18mM ASA solution. 305
6.24 Average solid-liquid surface energy of the (001) and (100) faces of aspirin with 18mM ASA solution determined using the AFM and contact angle methods. 308
6.25 Mixed model statistics for AFM Measurements on the (001) face of aspirin in 20mM ASA Solution. 309
6.26 Mixed model statistics for AFM Measurements on the (100) face of aspirin in 20mM ASA solution. 310
6.27 Average solid-liquid surface energy of the (001) and (100) faces of aspirin with 20mM ASA solution determined using the AFM and contact angle methods. 313

List of Figures

Figure #	Figure Title	Page
1.1	Determining surface energy using IGC	6
2.1	Sessile drop of a liquid on a solid	14
2.2	Cohesion and adhesion process	19
2.3	Deformation effect on the geometry of a liquid drop on a solid	33
2.4	Contact angle system and environmental chamber	37
2.5	Sessile drop software fitting	38
2.6	Range of solid-liquid surface energies for mica and graphite	47
2.7	Effect of water on contact angle measurements for hygroscopic liquids	52
3.1	Schematic of atomic force microscope with key features	62
3.2	The AFM piezo scanner	64
3.3	Typical AFM force curve	67
3.4	A typical power spectral density that is generated from thermal vibrations of the tip	73
3.5	SEM image of a silicon nitride tip	76
3.6	AFM advance force mode controls	79
3.7	AFM force curve hysteresis	80
3.8	An example of relative and absolute trigger mode curves.	83
3.9	Diagram of the sample collection for AFM force curves of mica or graphite.	88
3.10	Resonance frequencies of silicon nitride cantilevers before and after a tungsten sphere is added	95
3.11	Example of the addition of a tungsten sphere	96
3.12	SEM image of a tungsten sphere added to an AFM cantilever	98
3.13	Electronics board under the AFM stage that is manipulated to bypass filters and measure raw thermal vibration	100
3.14	Diagram illustrating the technique for measuring the Z sensitivity for the thermal analysis	103
3.15	SEM and blind reconstruction images for an AFM tip.	107
3.16	The force curve and parameters used to determine the force applied	111
3.17	AFM tip holder for vapor measurements	114
3.18	MultiMode AFM with an environmental chamber	115
3.19	Fluid cell used to measure forces with solvents and solutions	117
3.20	MultiMode AFM with the fluid cell and syringe to inject liquids	118
4.1	Illustration of Hertzian, JKR, and DMT models.	126
4.2	Tip-tip AFM scan that is performed in both vapor and liquid environments to determine the tip-vapor and tip-liquid surface energies	130
4.3	Experimental flow chart in order to study solid-liquid surface energy using the AFM and mathematical model 1	134
4.4	Experimental flow chart in order to study solid-liquid surface energy using the AFM and mathematical models 2 and 3	137
4.5	Experimental flow chart in order to study solid-liquid surface	141

	energy using the AFM and mathematical model 4	
5.1	The force, work, and surface energy of a) graphite measured in ambient conditions and b) graphite measured in controlled humidity conditions.	154
5.2	Iterative calculation to determine the value of β and the surface-vapor term.	155
5.3	Iterative calculation to illustrate how the value of β and the surface-vapor term are determined.	156
5.4	The force, work, and surface energy of a) mica measured in ambient conditions and b) mica measured in controlled humidity conditions.	164
5.5	The force, work, and surface energy of graphite measured in water.	172
5.6	The force, work, and surface energy of mica measured in water.	178
5.7	The force, work, and surface energy of graphite-diiodomethane.	185
5.8	The force, work, and surface energy of mica-diiodomethane.	191
5.9	The force, work, and surface energy of graphite-dried formamide.	204
5.10	The force, work, and surface energy of graphite-0.5% w/w formamide.	205
5.11	The force, work, and surface energy of graphite-1% w/w formamide.	206
5.12	The force, work, and surface energy of graphite-5% w/w formamide.	207
5.13	The force, work, and surface energy of mica-dried ethylene glycol.	221
5.14	The force, work, and surface energy of mica-0.5% w/w ethylene glycol.	222
5.15	The force, work, and surface energy of mica-1% w/w ethylene glycol.	223
5.16	The force, work, and surface energy of mica-5% w/w ethylene glycol.	224
6.1	Aspirin crystals grown from a) ethanol, b) acetone, and c) water.	240
6.2	Growth morphology and crystal structure of aspirin.	241
6.3	The solid-liquid surface energies on the (001) face determined from three contact angles models.	250
6.4	The solid-liquid surface energies on the (100) face determined from three contact angles models.	251
6.5	The diiodomethane solid-liquid surface energy from three contact angle models calculated on the (001) and (100) faces of aspirin crystals.	252
6.6	The water solid-liquid surface energy from three contact angle models calculated on the (001) and (100) faces of aspirin crystals.	253
6.7	The glycerol solid-liquid surface energy from three contact angle models calculated on the (001) and (100) faces of aspirin crystals.	254
6.8	The solid-vapor surface energy from AFM force measurements in controlled humidity environment on the (001) face of aspirin crystals.	264
6.9	The solid-vapor surface energy from AFM force measurements in controlled humidity environment on the (100) face of aspirin	265

crystals.
6.10 The solid-liquid surface energy from AFM force measurements with diiodomethane on the (100) face of aspirin crystals. 274
6.11 The solid-liquid surface energy from AFM force measurements with diiodomethane on the (001) face of aspirin crystals. 275
6.12 Model 1 solid-liquid surface energy from AFM force measurements using a 12mM ASA solution on the (001) and (100) faces of aspirin crystals. 282
6.13 Model 2 and model 3 solid-liquid surface energy from AFM force measurements using a 12mM ASA solution on the (001) and (100) faces of aspirin crystals. 283
6.14 Model 4 solid-liquid surface energy from AFM force measurements using a 12mM ASA solution on the (001) and (100) faces of aspirin crystals. 284
6.15 Model 1 solid-liquid surface energy from AFM force measurements using a 14mM ASA solution on the (001) and (100) faces of aspirin crystals. 290
6.16 Model 2 and model 3 solid-liquid surface energy from AFM force measurements using a 14mM ASA solution on the (001) and (100) faces of aspirin crystals. 291
6.17 Model 4 solid-liquid surface energy from AFM force measurements using a 14mM ASA solution on the (001) and (100) faces of aspirin crystals. 292
6.18 The solid-liquid surface energy from AFM force measurements with 16mM ASA solution on the (001) face of aspirin crystals. 298
6.19 The solid-liquid surface energy from AFM force measurements with 16mM ASA solution on the (100) face of aspirin crystals. 299
6.20 The solid-liquid surface energy from AFM force measurements with 18mM ASA solution on the (001) face of aspirin crystals. 306
6.21 The solid-liquid surface energy from AFM force measurements with 18mM ASA solution on the (100) face of aspirin crystals 307
6.22 The solid-liquid surface energy from AFM force measurements with 20mM ASA solution on the (001) face of aspirin crystals. 311
6.23 The solid-liquid surface energy from AFM force measurements with 20mM ASA solution on the (100) face of aspirin crystals 312
6.24 The solid-liquid surface energy from the AFM force measurements with 12mM to 20mM ASA solution on the (001) face of aspirin crystals compared with contact angle solid-liquid surface energy from a) the Neuman method, b) the OWRK method, and c) the van Oss method. 318
6.25 The solid-liquid surface energy from the AFM force measurements with 12mM to 20mM ASA solution on the (100) face of aspirin crystals compared with contact angle solid-liquid surface energy from a) the Neuman method, b) the OWRK method, and c) the van Oss method. 319

List of Abbreviations

AB	Acid-Base
AFM	Atomic Force Microscopy
AN	Electron Acceptor
API	Active Pharmaceutical Ingredient
ASA	Aspirin
CA	Contact angle
DMT	Deryaguin-Muller-Toporov
DN	Electron Donor
F	Force
HOPG	Highly Ordered Pyrolytic Graphite
HPLC	High performance liquid chromatography
ICH	International Conference on Harmonisation
IGC	Inverse gas chromatography
JKR	Johnson-Kendall-Roberts
KF	Karl Fisher
LV	Liquid-vapor
PXRD	Powder X-ray diffraction
RH	Relative Humidity
SA	Salicylic acid
SE	Surface energy
SEM	Scanning electron microscopy
SL	Solid-liquid
ST	Surface-tip
STM	Scanning tunnel microscopy
SV	Solid-vapor
W	Work
XRD	X-ray diffraction

Chapter 1 - Introduction

1.1 Dissertation Purpose

The research conducted for the purposes of this dissertation was designed with two overarching goals in mind: 1) to serve as an analytical method development report for atomic force microscopy (AFM) measurement and determine its viability as an approach of surface energy analysis and 2) to assess whether models developed on reference surfaces such as mica or graphite could be extended to organic crystalline surfaces. Though quite comprehensive on the subjects of contact angle and AFM, the enormity of these topics precludes a single source solution to the questions at hand. As such, this dissertation will additionally provide a current state-of-the-art review of alternative approaches used in industrial and academic environments alike.

1.2 Review of Surface Energetics

For the bulk of a liquid in a beaker, each molecule is pulled equally in every direction by the neighboring molecules. These results are a net force of zero. However, molecules at the surface are not surrounded and as such are pulled inwards. The inward pull creates an internal pressure forcing the liquid surface to contract to a minimum surface area. Thus, the surface tension of a liquid is defined as a force per unit length.[1] Surface tension is an older term and mostly used when referring to liquids. Surface free energy or the energy per unit area, is typically just referred to as surface energy. Throughout this report, surface energy will be used to express the energy of liquids and solids.

Surface energy is relevant whenever a solid comes into contact with another solid or liquid. The surface energetics of the system largely dictates particle interactions. Therefore, surface energy is not just important in crystallization, but in any

pharmaceutical processes where particle associations and disassociations are required for the desired outcome of the process. Despite the importance, not much recognition is given to the characterization of surface energy and its role on product performance.[2] For example, dissolution of solids entails the creation of two units from the separation of one. Conversely, wet granulation, roller compaction, and crystallization are processes based on the combination of two units to form a single larger unit. Much of pharmaceutical formulation development is either based on trial and error or historical practice, without necessarily investing the requisite upfront effort to rigorously investigate the underlying scientific fundamentals of these processes. A proper understanding of surface energetics could help in several ways. First, to aid synthetic chemists on polymorph screening and selection, second, to help analytical chemists select the proper dissolution media, and third, to assist formulation scientists on particle size selection, excipient selection for enhanced compatibility and stability, or manufacturing unit operations and process trains. There is a need to address fundamental questions of how surface energy, measured both at the atomic and bulk scales, can be used to estimate and predict physical behaviors of pharmaceutical materials. Without this information, pharmaceutical development will likely continue to advance only as quickly as duplication of historical practice allows. Thus, the goal of this work is to develop a reliable and practical technique to evaluate surface energy.

1.3 Current State-of-the-Art

The total surface energy consists of a number of different forces. These forces can be split into dispersion (D) and polar (P) interactions.[3]

$$\gamma = \gamma^{D} + \gamma^{P} \quad \textbf{1.1}$$

The principal dispersion interactions result from induced dipole-induced dipole (London), dipole-induced dipole (Debye) and dipole-dipole (Keesom) interactions. The polar or Lewis acid-base interactions (as the second term has also been identified) involve electron acceptance and donation. All materials have dispersive forces, and most materials will have polar forces (e.g. hydrogen bonding or acid-base forces).[2] Historically, a number of techniques have been explored to measure the surface energy. The most common techniques are contact angle and inverse gas chromatography (IGC). More recently, the AFM has been used to evaluate surface energy. Subsequent chapters will be dedicated to an in-depth discussion of AFM and contact angle. However, it is important to provide an overall comparison of these three techniques and present the limitations that led to focusing more research towards developing the AFM.

To characterize materials with IGC, a liquid probe is injected into a column pack with the material of interest and the time required for the probe to pass through the column is measured. The time defines the magnitude of the interaction between the probe and the stationary phase. The dispersive surface energy is determined using a series of aploar probes, typically n-alkanes. The measured retention volume (V_N) is related to the dispersive component as long as the interaction surface area (a) and the dispersive surface tension of the probe are known (γ_L^D):

$$RT \ln V_N = a \cdot \left(\gamma_L^D\right)^{1/2} * 2N \left(\gamma_S^D\right)^{1/2} + C \quad \textbf{1.2}$$

where R is the gas constant, T is the temperature, N is Avogadro's Number, and γ_S^D is the dispersive solid-vapor surface energy to be determined.[3, 4] The dispersive surface energy is the slope determined by plotting RT ln V_N against $a \cdot \left(\gamma_L^D\right)^{1/2}$ as shown in **Figure 1-1**. When a liquid with both polar and dispersive free energy components is used in the IGC measurements, the vapors will interact differently and points will lie above the alkane line. The magnitude of this difference is equal to the specific component of the surface energy $\left(\Delta G_A^{SP}\right)$ of the powder material in the column. The electron donor (K_D) and electron acceptor (K_A) properties of the materials can then be related to specific surface energy by:

$$\Delta G_A^{SP} = K_A \cdot DN + K_D \cdot AN^* \qquad \textbf{1.3}$$

where DN and AN describes the electron donor or base and electron acceptor or acid properties of the liquids, respectively. Using several probes with dispersion and polar properties to measure $\left(\Delta G_A^{SP}\right)$, and plotting DN/AN* against $\Delta G_A^{SP} / AN^*$, the values of K_A and K_D can be calculated for the material of interest. [3, 5]

IGC has been used to evaluate the surface energy differences of different batches of excipients, crystalline polymorphs, and amorphous material. IGC is an effective method for investigating the surface energy of powder samples, but IGC is thought to preferentially probe only the highest energy sites. Also, with polar probes, the reproducibility of the measurements is questionable because retention times are inconsistent between sample runs.[4] The biggest reason IGC was not a focus for this work is because of the inability to measure the surface energy on individual crystalline

faces. In order to understand the contribution of surface energy during crystallization, another method will have to be used.

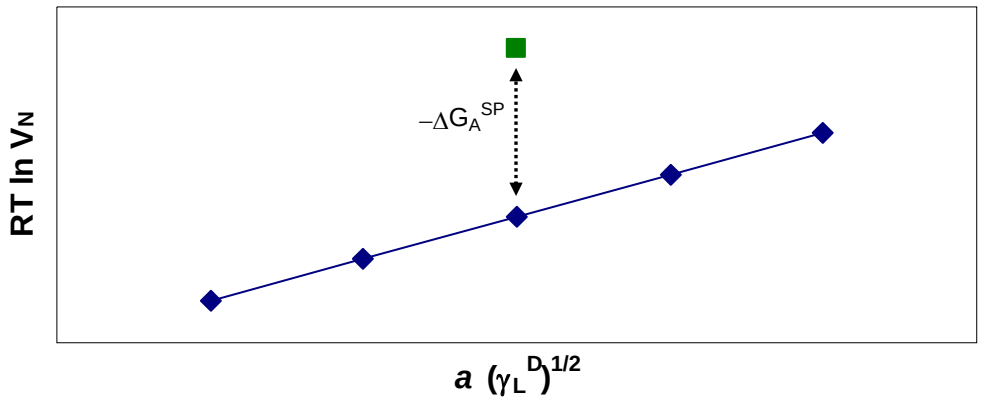

Figure 1-1: Schematic diagram showing how to determine the dispersion surface energy and the specific surface energy component.

The most common method for measuring contact angles is by sessile drop. A small drop of liquid is placed on the surface of a solid from a syringe and recorded with a video based goniometer. The static contact angle can be measured directly by measuring the angle between the tangent to the drop surface at the point of contact with the solid and the horizontal solid surface, **Figure 2-1**. The advancing and receding angles can be determined by repeatedly adding or removing the liquid to the forming drop. The process is recorded and the angles are analyzed by software that is integrated with the contact angle system. Once the angles are measured, several indirect models have been used to calculate the surface energy. Most of these models split the total surface energy into dispersion and polar (or acid-base) components, similar to the IGC model. These models are discussed extensively in Chapter 2.

The contact angle method has been used on powders compressed into tablet compacts and single crystalline faces. The experimental challenges for contact angle measurements will be discussed in detail in Chapter 2. The main limitations of this method are, one, the sessile drop is complicated by the stress at the edge of the contact circle causing additional surface changes[5, 6], which, in turn, affects the surface energy. Second, the sessile drop method may not be sensitive enough to detect the change in surface energy due to the subtle structure change, and large single crystals are needed in order to measure the contact angle on particular faces.[7, 8]

The major problem with IGC is the instrument's inability to distinguish the surface energy of each crystalline face. Sessile drop can measure surface energy on each face, but the limitations listed above drove the need for development of other methods that can provide comprehensive surface energy information.

Atomic force microscopy is a scanning probe measurement based upon the variable displacement of a cantilever tip as it scans across the topography of a solid surface. The forces between the solid surface and the tip result in a deformation of the cantilever, measurable by a spatially resolved photodetector. The instrument is typically operated in either contact mode, where the cantilever tip is dragged across the surface or in tapping mode, where the tip is oscillated at a known frequency. However, contact mode is the only mode that a positive deflection can be measured and adhesion can be studied. The measured AFM forces are then converted into work of adhesion using either the Johnson-Kendall-Roberts (JKR) or Deryaguin-Muller-Toporov (DMT) contact mechanics models. The work of adhesion (W) is then defined by surface energy (SE). Thus, the mathematical sequence for determining surface energy with the AFM is

$$F \rightarrow W \rightarrow SE$$

The contact mechanics models and surface energy models are discussed in Chapter 4, and Chapter 3 provides a review of the AFM and the methodology used to measure forces.

The AFM was an attractive tool to use for investigating surface energy because of its ability to resolve interactions sub-angstrom, on the molecular level, and because of the various disadvantages of using contact angle and IGC. IGC cannot evaluate single crystalline faces and the AFM can evaluate a range of materials because of the nanometer sized tips. While the contact angle can evaluate various surfaces, it is a macroscopic method, averaging over surface features that can be different within a specific area. For a surface which is not ideal and inert, it may be difficult to obtain a meaningful surface energy based on contact angle measurement. For these reasons the following objectives were investigated to evaluate the capabilities of the AFM.

1.4 Objectives

1.4.1 Specific Aim 1

The first purpose of this research was to develop the AFM as an analytical method and determine its viability as a potential technique for measuring surface energies of various crystal systems. Linearly, this goal was subdivided into five specific tasks: 1) determine the surface energy of inert materials using a contact angle method and demonstrate its limitations for determining solid-liquid surface energies, 2) evaluate tip properties of an AFM probe to calculate forces and evaluate tip sharpness, 3) establish repeatability and a model for statistical analysis, 4) assess adhesion mechanics models and develop surface energy models for the AFM, and 5) compare the AFM calculations to contact angle results. More concisely, these subdivisions were organized to develop and utilize a reference method for comparison (contact angle), to understand the hardware and physical considerations of the new method (AFM), to understand and select the most appropriate scientifically rigorous mathematical and theoretical models for the new method, and to compare the reference standard with the incumbent method. Much like any secondary method of analysis, the AFM required correlation to a primary reference method to establish its position.

1.4.1.1 Determine the surface energy of reference materials using a contact angle method and demonstrate the limitations for determining solid-liquid surface energies.

To address specific aim 1, contact angle was used to determine the surface energy of reference materials, and thereby, its limitations were evaluated for measuring solid-liquid

surface energies. Graphite and mica were selected as the reference-surface test systems, and the sessile drop method was used to measure static, advancing, and receding contact angles. Water, ethylene glycol, formamide, and diiodomethane were selected as the liquids to measure wettability and spreadability on the graphite and mica surfaces. These liquids were chosen to investigate how relative degrees of polarity (water > formamide > ethylene glycol > diiodomethane) affected their respective contact angles. Typical indirect models were used to determine the solid-vapor surface energy of the two surfaces and then the solid-liquid surface energies were calculated from Young's equation.

1.4.1.2 Evaluate tip properties of an AFM probe to calculate forces and evaluate tip sharpness.

To calculate the force of adhesion with an AFM measurement, the spring constant of the cantilever needed to be determined. One destructive method and one nondestructive method were tested, each of which will be described in detail in subsequent chapters. Tip radii were measured with SEM images from five probes and averaged. Then a novel nondestructive method was used relying on tip reconstruction by scanning a rough image and evaluating this image with calculations in SPIP software. Tip radii are continually evaluated with this technique to determine when the tip becomes blunt and unusable.

1.4.1.3 Establish reproducibility among AFM measurements and develop a statistical model for error analysis.

Parameters were tested to increase repeatability of the force measurements at different locations on a discrete sample and with the same tip. The parameters tested included scan size, scan rate, forces applied, and contact area. Once the forces were measured, a

repeated measure mixed model statistical analysis was performed to summarize the AFM data.

1.4.1.4 Assess adhesion mechanics models and develop surface energy models for the AFM.

First, the three adhesion mechanics models that have been developed were evaluated. These models are reviewed in Chapter 4 lending to an understanding of the most applicable model for samples in this study and determining applicability in future studies. Next, four surface energy models were developed. Since there is currently no method to directly measure surface energy, the advantages, assumptions, and limitations are presented.

1.4.1.5 Compare AFM calculations to contact angle results

All forces were measured using the same liquids from contact angle measurements. Environmental conditions were controlled to increase repeatability, including ambient, zero percent relative humidity achieved by purging the chamber with nitrogen gas, dried hygroscopic solvents (ethylene glycol and formamide), and controlled hydration of solvents. The repeated measures mixed model statistical analysis was used to identify any difference in the measurements and what the possible sources of deviation are.

1.4.2 Specific Aim 2

The second purpose of this research was to apply the methodology and mathematical models developed on references surfaces, such as mica or graphite, to organic crystalline surfaces.

1.4.2.1 Determine the surface energy of aspirin using the contact angle method.

Sessile drop was used to measure the contact angles on the two major faces of aspirin. Three liquids with different properties were used to explore wettability. The same indirect models were used to determine the solid-vapor surface energy of the two surfaces and then the solid-liquid surface energies were calculated from Young's equation.

1.4.2.2 Use the methods developed on inert surfaces with the AFM and apply them to the crystalline measurements.

Forces were measured in only controlled relative humidity to determine solid-vapor surface energy because solvent trapped in the crystals and water vapor that can adsorbed on the surface in ambient conditions prevented engagement of the microscope. Forces were pure aqueous solution, but dissolution on the surface of the crystalline was too rapid because of solubility. Hence, the forces were measured in varying solute concentrations on the major faces of aspirin until saturation was reached. Stability and repeatability in measurements were observed at saturation and above.

The goal in the following chapters is to present the theory and methods of contact angle and AFM. In these chapters, the results from each specific aim will be presented and discussed.

Chapter 2 – Contact Angle

In this chapter, the definition of contact angle and a literature review on the evaluation of indirect models developed to calculate surface energy is presented. Then, the sessile drop method is used to determine the contact angles of two reference samples, mica and graphite, so that the solid-vapor and solid-liquid surface energy of these samples can be calculated. The final sections of this chapter present the contact angle measurements on mica and graphite, the surface energy results determined from the indirect models, and the drawbacks of using the contact angle method.

2.1 Contact Angle and Young's Equation

Contact angle is defined as the angle, θ, formed between the liquid-vapor, solid-vapor, and liquid-solid interfaces at a three phase contact line (**Figure 2-1)**. In principle, on a smooth, homogeneous, rigid, isotropic solid surface, the equilibrium contact angle of a pure liquid is a unique quantity[9], and Young's equation is obeyed and can be defined by:

$$\gamma_{sv} = \gamma_{sl} + \gamma_{lv}\cos(\theta) \qquad \textbf{2.1}$$

where γ_{sv} is the solid-vapor interfacial free energy, γ_{sl} is the solid-liquid interfacial free energy, and γ_{lv} is the liquid-vapor interfacial tension (for liquids, often called surface tension).

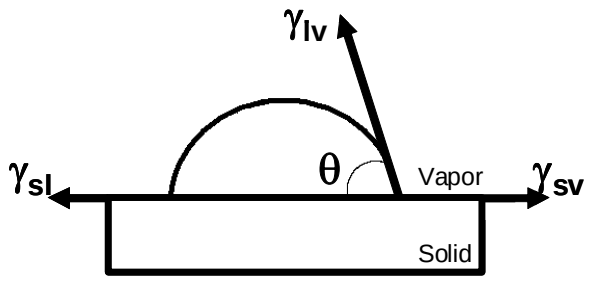

Figure 2-1: Sessile drop of a liquid on a solid demonstrating the three-phase boundary.

Young's equation is based on the assumption that the liquid and solid surfaces in contact are in equilibrium at a saturated vapor pressure. However, it is likely that the saturated vapor will adsorb onto the solid surface. The equilibrium spreading pressure, π_e is defined as an adsorption vapor layer that causes a decrease in the solid surface's free energy. [9]Thus,

$$\gamma_{sv} = \gamma_{sl} + \gamma_{lv}\cos(\theta) + \pi_e \qquad \textbf{2.2}$$

For low surface energy solids, such as polymers and most pharmaceuticals, the surface free energy of a solid in vacuum is presumed to be similar to the surface free energy of a solid with an adsorbed vapor film present. For liquids that exhibit finite $\theta > 10°$, it is assumed that the spreading pressure is negligible ($\pi_e \approx 0$). [2]

At the surface of liquids, the surface tension results from an imbalance of molecular forces. The liquid molecules are attracted to each other and exert a net attractive force. The stronger these molecules interact, the higher the surface tension. The hydrogen bonding of water causes this liquid to have a high surface tension. Organic molecules with polar groups (such as iodide and hydroxyl) have slightly lower surface energies than water.[1] Pure hydrocarbons have even lower surface energies as only dispersion or Lifshitz-Van der Waals forces exist. The literature reports surface tension values of common liquids.[10-12] Unlike the surface tension of liquids, the surface energy of solids cannot be measured directly because of elastic and viscous constraints of the bulk phase.[9] Therefore, in order to study surface energy of solids, indirect methods have been developed.

2.2 Review of the Geometric Mean and Indirect Models

In the past 40 years, a series of semi-empirical analytical models have been developed to relate contact angle data to solid surface free energy. Surface energy component approaches, such as Fowkes[13], Owens-Wendt-Rabel-Kaelble[14], Chen-Chang[15], and van Oss et al[16] have been used to evaluate the surface free energy components of many solid materials. All of the models are based on the assumption that the surface free energy of a solid and/or a liquid consists of independent or partially independent components. These independent components represent different types of intermolecular interactions. In this review, the most common indirect models will be discussed and evaluated.

Before the indirect models could be formulated, it was recognized that one of the unknowns in Young's equation needed to be eliminated. This was possible through the use of the geometric mean combining rule.[2, 9] It was hypothesized that the free energy of adhesion is equal to the geometric mean of the free energies of cohesion of the individual components. The free energy of cohesion, ΔG^c, is the change of the reversible process of bringing two identical bodies, Figure 2-2**a**, together so that:

$$\Delta G^c = -W^c = -2\gamma \qquad \textbf{2.3}$$

However, when two dissimilar bodies, Figure 2-2**b**, are brought together reversibly, the free energy change of adhesion, ΔG^a_{12} , is:

$$\Delta G^a_{12} = -W^a_{12} = \gamma_{12} - \gamma_1 - \gamma_2 \qquad \textbf{2.4}$$

where, phases 1 and 2 represent the separate phases, and 12 represents the interface between phase 1 and phase 2.

To eliminate one of the terms, consideration was given to van der Waals interactions. The principal interactions are induced-dipole-induced dipole (London), dipole-induced dipole (Debye) and dipole-dipole (Keesom) interactions. The intermolecular potential energy function for these interactions has the same form: [2]

$$U = \frac{-\beta_{12}}{r^6} \qquad \textbf{2.5}$$

London dispersion forces considered from equation **2.5** can be expressed as follows: [2]

$$\beta_{12}^d = \frac{2\sqrt{I_1 I_2}}{I_1 + I_2}\left(\beta_{11}^d \beta_{22}^d\right)^{1/2} = \frac{2\beta_{11}^d \beta_{22}^d}{\beta_{11}^d\left(\frac{\alpha_2}{\alpha_1}\right) + \beta_{22}^d\left(\frac{\alpha_1}{\alpha_2}\right)} \qquad \textbf{2.6}$$

where 11 and 22 refer to interactions between like molecules and 12 refers to the interactions between dissimilar molecules. β is a coefficient in Equation **2.5**, α is the polarizability, and I is the ionization potential. If $I_1 \approx I_2$ then [2]

$$\beta_{12}^d = \left(\beta_{11}^d \beta_{22}^d\right)^{1/2} \qquad \textbf{2.7}$$

The basis of the Berthelot principle is that the dispersion interaction between dissimilar molecules can be estimated as the geometric mean of the interactions of the like molecules, Equation **2.7**.

Thus, binary interactions for van der Waals components can be determined from the pure components by:

$$\Delta G_{12}^{d} = \left(\Delta G_{11}^{d} \Delta G_{22}^{d}\right)^{1/2} = -2\left(\Delta \gamma_{11}^{d} \Delta \gamma_{22}^{d}\right)^{1/2} \qquad \textbf{2.8}$$

The combining rule makes it possible to predict properties of the 12 interface from the separate properties of phase 1 and 2 phases. With this assumption it is possible to eliminate γ_{12} from Young's equation and develop indirect models.[1, 2, 9, 17]

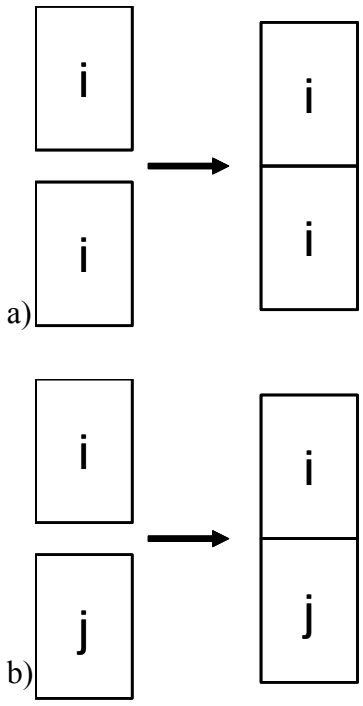

Figure 2-2: Illustration of thermodynamic processes: **a)** is a cohesion process and **b)** is an adhesion process

2.2.1 Fowkes

Initially, Fowkes proposed that a solid's surface free energy, γ_s, could be considered to be the sum of a dispersive, (London, γ^d), an apolar, (Keesom, γ^p), an induction, (Debye, γ^{ind}), and a hydrogen bonding (γ^h) component such that:[9]

$$\gamma = \gamma^d + \gamma^p + \gamma^{ind} + \gamma^h \qquad \textbf{2.9}$$

However, Fowkes finally settled on two dominant terms:

$$\gamma = \gamma^d + \gamma^{AB} \qquad \textbf{2.10}$$

where d is the dispersive and AB is the acid-base component. In Fowkes equation, the acid-base component is comprised of the polar, induction, and hydrogen bonding interactions.[2] Fowkes reason for the integration was supported by proving that the contributions of dipole-dipole attraction (γ^p) and dipole-induced dipole attraction (γ^{ind}) were significantly smaller than the dispersive surface energy component (γ^d).[2, 9]

2.2.2 Van Oss, Chaudhury, Good

Van Oss, Chaudhury, and Good explored Fowkes' model in more detail, and after evaluating Lifshitz calculations and theory, arrived at a different conclusion. Their investigation showed it is not possible to separate out a γ^p or γ^{ind} term. The only measurable interaction is the Lifshitz-van der Waals, γ^{LW}, which includes all electromagnetic interactions together, γ^d, γ^p, and γ^{ind}. Therefore the model equation becomes:[2, 9]

$$\gamma = \gamma^{LW} + \gamma^{AB} \qquad \textbf{2.11}$$

Using the geometric mean and parameters from Young's equation, the components in Equation **2.11** can be broken down further to evaluate the interaction between dissimilar bodies:

$$W_{sl}^{LW} = \sqrt{W_{sv}^{LW} W_{lv}^{LW}} = 2\sqrt{\gamma_{sv}^{LW} \gamma_{lv}^{LW}},$$
$$W_{sl}^{AB} = \sqrt{W_{sv}^{+} W_{lv}^{-}} + \sqrt{W_{sv}^{-} W_{lv}^{+}} = 2\sqrt{\gamma_{sv}^{+} \gamma_{lv}^{-}} + 2\sqrt{\gamma_{sv}^{-} \gamma_{lv}^{+}} \qquad \textbf{2.12}$$

In the development of the acid-base term it was recognized that a molecule can be bipolar, containing both a Lewis acid, γ^+, and a Lewis base, γ^-, as with water. If either the acidic or basic property is negligible, then the substance is termed monopolar.[2] When the substance does not exhibit either acidic or basic properties, it is considered apolar. Hydrogen bonding is another example of a Lewis acid and Lewis base interaction.[9] Therefore, this model provides more insight as to whether a substance can accept or donate electrons.

To determine γ_{sv}, Equations **2.12** are combined to produce:

$$\gamma_{sl} = \gamma_{sv} + \gamma_{lv} - 2\sqrt{\gamma_{sv}^{LW} \gamma_{lv}^{LW}} - 2\sqrt{\gamma_{sv}^{+} \gamma_{lv}^{-}} - 2\sqrt{\gamma_{sv}^{-} \gamma_{lv}^{+}} \qquad \textbf{2.13}$$

Then, combining Equations **2.1** and **2.13** the following equations are derived:

$$2\sqrt{\gamma_{sv}^{LW} \gamma_{lv}^{LW}} + 2\sqrt{\gamma_{sv}^{+} \gamma_{lv}^{-}} + 2\sqrt{\gamma_{sv}^{-} \gamma_{lv}^{+}} = \gamma_{lv}\left(1 + \cos(\theta)\right) \qquad \textbf{2.14}$$

In order to use the van Oss et. al. model, at least three liquids must be used to measure contact angles. First an apolar liquid is chosen and Equation **2.14** is reduced to: [2, 9, 12, 16]

$$2\sqrt{\gamma_{sv}^{LW}\gamma_{lv}^{LW}} = \gamma_{lv}\left(1+\cos(\theta)\right) \qquad \textbf{2.15}$$

The Lifshitz-van der Waals component can be calculated from a single contact angle measurement. Once the γ_{sv}^{LW} is known, the acid-base components can be calculated using the data from the other two liquids and Good's equations (a determinant method).[2, 9, 12, 16]

$$\sqrt{\gamma_s^-} = \frac{BC - AE}{CF - DE} \quad , \quad \sqrt{\gamma_s^+} = \frac{AF - BD}{CF - DE}$$

$$A = \gamma_2\left(1+\cos(\theta)\right) - 2\sqrt{\gamma_s^{LW}\gamma_2^{LW}}$$

$$B = \gamma_3\left(1+\cos(\theta)\right) - 2\sqrt{\gamma_s^{LW}\gamma_3^{LW}} \qquad \textbf{2.16}$$

$$C = 2\sqrt{\gamma_2^-} \ , \ D = 2\sqrt{\gamma_2^+}$$

$$E = 2\sqrt{\gamma_3^-} \ , \ F = 2\sqrt{\gamma_3^+}$$

Negative and small values of $\sqrt{\gamma_s^+}$ occur often. The small values usually can be taken as zero, but a definitive method for handling negative numbers has not yet been proposed.[2, 9] It is possible that the phenomenon is real and thus the equation to determine the acid base component is written:

$$\gamma_s^{AB} = 2\sqrt{\gamma_s^+}\sqrt{\gamma_s^-} \qquad \textbf{2.17}$$

One criticism made of this model is the numerical designation made for water, $\gamma^+ = \gamma^- = 25.5\,\mathrm{mJ/m^2}$. Most researchers also agree that when using this model, the calculated values of surface free energy components depend upon the choice of liquids.[2] There is less dependence when more liquids are used for the calculation.

2.2.3 Owens-Wendt-Rabel-Kaelble

After Fowkes's early reports, Owens-Wendt-Rabel-Kaelble (OWRK), described surface free energy in terms of two components (dispersive, γ^d,and polar, γ^p) such that:[14]

$$\gamma = \gamma^d + \gamma^p \qquad \textbf{2.18}$$

Assuming the dispersive and polar interactions are independent and additive at the interfaces, the OWRK model indicates:

$$\gamma_{sv} = \gamma_{sv}^d + \gamma_{sv}^p \;; \qquad \gamma_{lv} = \gamma_{lv}^d + \gamma_{lv}^p \qquad \textbf{2.19}$$

Based on Berthelot's principle, the dissimilar molecules can be estimated as the geometric mean of the interactions between the pure components:

$$W_{sl} = \sqrt{W_{sv}^d W_{lv}^d} = 2\sqrt{\gamma_{sv}^d \gamma_{lv}^d} \;; \quad W_{sl} = \sqrt{W_{sv}^p W_{lv}^p} = 2\sqrt{\gamma_{sv}^p \gamma_{lv}^p} \qquad \textbf{2.20}$$

combining Equations **2.4** and **2.20** for:

$$\gamma_{sl} = \gamma_{sv} + \gamma_{lv} - 2\left(\sqrt{\gamma_{sv}^d \cdot \gamma_{lv}^d} + \sqrt{\gamma_{sv}^p \cdot \gamma_{lv}^p}\right) \qquad \textbf{2.21}$$

Then joining Equations **2.1** and **2.21** the following equations are derived:

$$2\left(\sqrt{\gamma_{sv}^{d}\cdot\gamma_{lv}^{d}}+\sqrt{\gamma_{sv}^{p}\cdot\gamma_{lv}^{p}}\right)=\gamma_{lv}\left(1+\cos(\theta)\right) \qquad \textbf{2.22}$$

then:

$$\sqrt{\gamma_{sv}^{d}}+\sqrt{\frac{\gamma_{lv}^{p}}{\gamma_{lv}^{d}}}\cdot\sqrt{\gamma_{sv}^{p}}=\frac{\gamma_{lv}\left(1+\cos(\theta)\right)}{2\cdot\sqrt{\gamma_{lv}^{d}}} \qquad \textbf{2.23}$$

Therefore, contact angles must be measured using at least two or more liquids whose disperse and polar components of surface tension are known. By plotting $\sqrt{\frac{\gamma_{lv}^{p}}{\gamma_{lv}^{d}}}$ *vs.* $\frac{\gamma_{lv}\left(1+\cos(\theta)\right)}{2\cdot\sqrt{\gamma_{lv}^{d}}}$ the solid surface energy, γ^{d}_{sv} and γ^{p}_{sv}, can be calculated from the intercept and slope, respectively.[14] This model makes the assumption that for any combination of liquids, solid-vapor surface energy is the same. However, literature reports have shown that this is not always the case, especially when only two liquids are used.[18, 19] The other complication is the polar component. In the Fowkes model, γ^{p} refers to dipole-dipole interactions. The van Oss, Chaudhury, and Good model have incorporated γ^{p} into the γ^{LW} component.[2] Thus, many believe the polar component in the OWRK model is unable to cover interactions outside of what would be covered in the dispersive term.

2.2.4 Neumann

Many indirect models have explored various surface energy components to better define the intermolecular interactions. All of the models are in agreement with having a dispersion/Lifshitz-van der Waals component; however they disagree significantly with

the definition of the second component. Neumann et al. tried to improve this problem using the equation of state and not separate interactions.

The equation of state is simply:

$$\gamma_{sl} = f(\gamma_{sv}, \gamma_{lv}) \qquad \textbf{2.24}$$

Since both γ_{sv} and γ_{sl} in Young's equations are parameters to be determined, an additional equation providing a relation among the surface tensions was required. The approach taken by Neumann and his coworkers does not consider the molecular origins of surface energy like previous models. The method developed is an extension and modification of the Berthelot Rule, (Equation **2.8**): [19, 20]

$$W = 2\sqrt{\gamma_{sv}\gamma_{lv}}\, e^{-\beta(\gamma_{lv}-\gamma_{sv})^2} \qquad \textbf{2.25}$$

where β is an unknown constant added as part of the modification and now is an empirical constant that has been determined to be 1.247×10^{-4} m^4mJ^{-2}. The modification was made because the geometric mean overestimates the strength of the unlike-pair interactions. Thus, a modification factor is added to decrease the function of the difference ($\gamma_{lv} - \gamma_{sv}$) and is equal to unity when the difference is zero.

Then substituting Equation **2.25** into Equation **2.4** gives:

$$\gamma_{sl} = \gamma_{sv} + \gamma_{lv} - \sqrt{\gamma_{sv}\gamma_{lv}}\, e^{-\beta(\gamma_{lv}-\gamma_{sv})^2} \qquad \textbf{2.26}$$

Combining Equation **2.26** with Young's equation (Equation **2.1**) and simplifying yields:

$$\cos(\theta) = -1 + 2\sqrt{\frac{\gamma_{sv}}{\gamma_{lv}}} e^{-\beta(\gamma_{lv}-\gamma_{sv})^2} \qquad \textbf{2.27}$$

In Equation **2.27**, β and γ_{sv} are the unknowns and can be determined by finding the best fit from the measured data using nonlinear least-squares analysis. When simplified equation **2.27** becomes:

$$\ln\left[\sqrt{\gamma_{lv}}\left(\frac{\cos(\theta)+1}{2}\right)\right] = \frac{1}{2}\ln\gamma_{sv} - \beta(\gamma_{lv}-\gamma_{sv})^2 \qquad \textbf{2.28}$$

where:

$$Y = \ln\left[\sqrt{\gamma_{lv}}\left(\frac{\cos(\theta)+1}{2}\right)\right];\ X = \gamma_{lv} \qquad \textbf{2.29}$$

This model assumes that for a group of liquids γ_{sv} will be constant. This model is based on molecular interactions of like pairs and specifically long range dispersion forces. The dispersion energy coefficient for two dissimilar molecules can be expressed in terms of the similar molecules, which is the basis for the geometric mean. The main criticism of this model is the contrast with the statistical thermodynamic approach used by Fowkes, OWRK, and van Oss, Chaudhury, and Good. Since this model does not consider the molecular origins of surface tension, no statistical mechanical insight is gained.[2]

2.2.5 Model Summary

In summary, several indirect models have been developed and can be used to determine solid vapor surface energy. Once γ_{sv} is determined from an indirect model, its value along with the contact angle determined from various liquids can be substituted back into

Young's Equation to calculate γ_{sl}. So far there is no unified agreement on one universal indirect model. There are two unknowns in Young's equation and the use of the geometric mean helps eliminate one unknown. The geometric mean overestimates surface energy; therefore modifications have been made and surface energy components have been evaluated. Neumann found an empirical modification to correct for the overestimation. This has been an approach mainly used when mixing liquids. [21]Van Oss et al. and OWRK evaluated the total surface energy based on components. The total surface energy was defined by dispersive/van der Waals and polar/AB. To evaluate the binary interactions of each component, the geometric mean was used. The geometric mean was developed for van der Waals interactions and not the polar/AB interactions. In order to use the geometric mean with the polar and AB components, the assumption made is that the pure components' differences in electronic properties and molecular size are small. [21] Fowkes found that the geometric mean may not satisfactorily describe polar liquid/solid interactions and noted that a direct proportionality between γ_{sl}^{p} and γ_{l}^{p} maybe more accurate. However, until it is possible to directly measure surface energy, indirect models will have to be used. Hence, consideration should be given to the assumptions each model makes before applying that model to a particular surface of interest. In this chapter, the OWRK, van Oss-Chadhury-Good, and Neumann indirect models will be applied to contact angle data collected on mica and graphite to evaluate similarities and discrepancies between the models.

2.3 Experimental Challenges of Contact Angles Measurements

When using sessile drop and other methods to measure contact angles, there are various challenges that must not be ignored. The factors that can effect the contact angle

measurements are surface heterogeneity and roughness, solvent purity, temperature, and surface stability. This section reviews some limitations experienced with contact angle measurements.

2.3.1 Contact Angle Hysteresis

In section 2.1, the assumption was made that Young's equation holds and an equilibrium angle can be measured if the solid surface is smooth, homogeneous, rigid, and isotropic. However, this is not frequently seen. Typically there is appreciable hysteresis observed. Hysteresis is defined as the difference between the advancing angle, θ_a, and the receding angle, θ_r

$$H = \theta_a - \theta_r \qquad \textbf{2.30}$$

Hysteresis of one or two degrees has been regarded as negligible and within the uncertainty of the experimental measurement. However a hysteresis of 10º or larger has been observed in some cases that cannot be attributed to the measurement.[9] The theoretical basis for hysteresis is the failure of the system to meet the conditions of ideality. Examples of non-ideality are roughness and heterogeneity. When hysteresis occurs, the advancing contact angle is used to determine the surface energy.[9] Good stated that when an equilibrium angle is observed on a homogeneous, flat surface with lower free energy components, the maximum contact angle value is taken, which is the advancing contact angle.[9, 17] For example, on a patchy (heterogeneous) surface whose areas have different surface energies, and the advancing angle is greater than the receding angle, which is most commonly observed, the equilibrium angle will be the advancing

angle. When there are smaller surface energy components on the surface, the liquid's cohesive forces cannot be overcome. Through this phenomenon, a larger contact angle is observed. The large contact is the advancing angle. The receding angle is observed as the liquid is retracted from the surface. The contact angle software allows control over the amount of liquid and the rates of application onto a surface and retraction from the surface. The entire experiment is recorded with a video based goniometer and the contact angle software analyzes the angles. The advancing angle is observed when the liquid stops spreading and the receding angle is measured as the liquid is retracted.

2.3.2 Contact angle measurements with hygroscopic solvents and additive solutions

The uptake of moisture in the liquid can affect the interaction the hygroscopic liquid has with the surface which therefore, influences the resultant contact angle. In Section 2.5.3, the presence of water will be evaluated with two hygroscopic solvents, ethylene glycol and formamide.

With contact angle measurements, studies have shown that only the use of pure solvents will provide unambiguous results. In the literature, surface tensions are available for only pure solvents. While the additions of additives or surfactants can affect the surface tension of a liquid, it is thought that the adsorption is not equally distributed across the three interfaces when the solution is dropped on a surface.[17, 22] Studies done in the Zografi lab illustrated the nonequivalent adsorption in two ways: [22]

1. The liquid-vapor surface energy (γ_{lv}), also known as the surface tension of a liquid, is different for a pure liquid and that same liquid with an additive or surfactant, and

2. The liquid-vapor surface energy (γ_{lv}) is not different for a pure liquid and that same liquid with an additive or surfactant.

For the first case, if the surface tension of a liquid is different between a pure solvent and a solution, but the surfactant or additive in the solution does not wet or adsorb well at the solid-liquid surface, there won't be a change in γ_{sl}, as compared to the γ_{sl} measured by the pure solvent. This could mean that the particular additive or surfactant used has little interaction with the surface or is a poorer wetting agent. However, when other pure liquids with distinctive γ_{lv} are used, a difference is observed in the contact angles. Thus the solid-liquid interaction results in different γ_{sl}. It is difficult to say that no change in γ_{sl} is just because of poor wetting. It could also mean that the additive is not dispersed homogeneously across the three interfaces.

For the second case, the surface tension of the solution is the same as the pure liquid, but there is a change in the solid-liquid surface energy from an increase or decrease in the contact angle. In this instance, it is unclear if the adsorption of the surfactant or additive is affected by a strong interaction with the surface or a lack of interaction at the liquid-vapor interface.

All of these results show that the relative adsorption of an additive or surfactant to the liquid-vapor interface and the solid-liquid interfaces is critical to understanding the wetting characteristics. Therefore, the study of contact angles will not yield how additives can affect crystal growth.

2.3.3 Temperature effect on contact angle measurements

Studies have been conducted to evaluate how temperature affects surface tension of liquid and surface energy of solids. For solvents, as temperature increases, the surface tension of the liquid decreases.[1] Intuitively, if there is an increase in thermal motion of molecules, there would be a decrease in the surface tension. Since indirect surface energy models evaluate various surface energy components, the solvent's surface tension terms have to be reevaluated at varying temperatures. However, for solids, the temperature effect has been more difficult to study with the indirect models. The dispersive forces, which exist in all types of matter, depend on electrical properties of the elements involved and the distance between them, and therefore, are independent of temperature.[23] Thus, it was established that only the polar term (which was indicated in this study to include all non-dispersive forces, such as Lewis acid-base interactions) decreases with an increase in temperature.[23] Therefore, the polar/AB surface tension terms at certain temperatures must be found in the literature or measured if temperatures deviate from reported values. The decrease in solid-vapor surface energy should be less than what is observed for a liquid because of elastic and viscous restraints of the bulk phase. McGuire saw an insignificant change in the polar work of adhesion between 30 and 40 degrees centigrade on copper, stainless steel, high density polyethylene, and polytetrafluoroethylene.[23] Fowkes and Harkin stated that the angles between water and graphite and water and paraffin increase by 0.06 per degree centigrade with an increase in temperature. Results from this work will show that 2 to 5 degree contact angle differences do not significantly change the solid-vapor surface energy. So these studies

would indicate temperature control in ambient room conditions (15 – 30 ºC) is unnecessary.[24]

2.3.4 Contact angles on deformable surfaces

Some solids can be described as rigid and insoluble. For these solids, the vertical component (not shown in **Figure 2-1**) of surface tension is resisted by elastic distortions of the solid, which are generally regarded as negligible. However, for solids that cannot be described in this way, high experimental temperatures or high solubility in a particular solvent can lead to solution precipitation or some local diffusion. When this happens, a small ridge can develop at the triple junction (**Figure 2-3**).[6] When measuring contact angles, distinction is not made on surfaces containing ridges. If the ridge is present, the contact angle will be affected, and it is hard to get an accurate surface energy determination. The possible formation of a ridge can be a big risk when measuring contact angles with solvents that can dissolve pharmaceutical materials. As a result, this presents another experimental challenge with contact angle measurements.

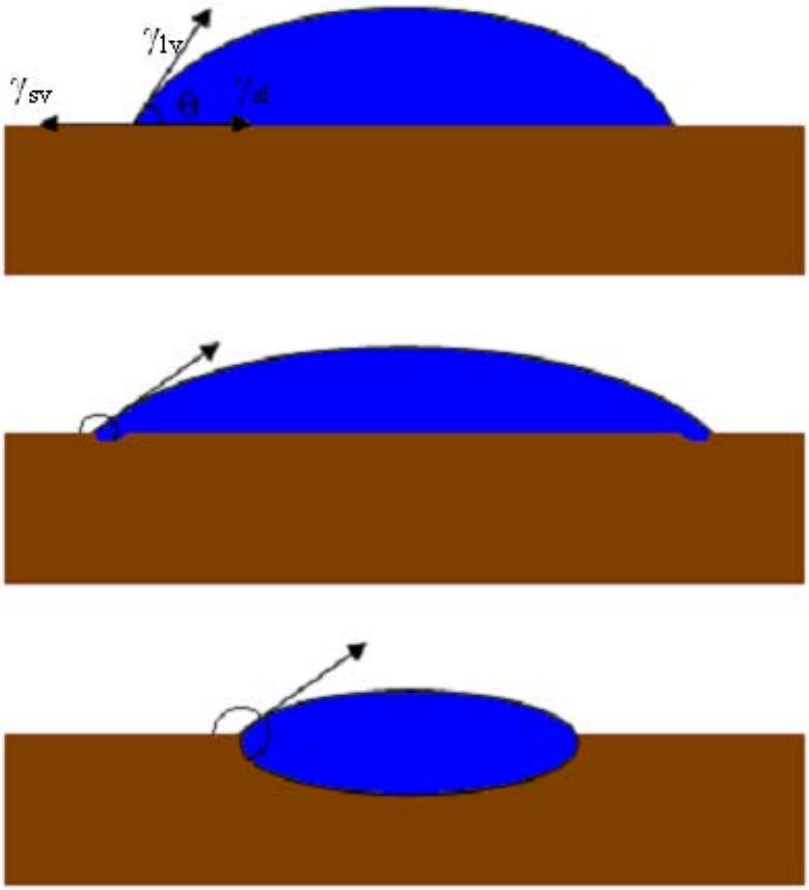

Figure 2-3: Geometry of a liquid drop on a large, isotropic solid depends on the contact line. Initially the solid is rigid (a). Subsequently, a small ridge will form (b) and growth of the perturbation will eventually reach equilibrium (c).[6]

2.4 Methodology for the Evaluation of Indirect Models on Inert Surfaces

The sessile drop method will be used since it has become the "gold standard" for surface energy determination, and it is capable of evaluating individual crystalline faces. [7, 25]This section will discuss the methodology used in to measure contact angles.

2.4.1 Inert surfaces

Mica (Ted Pella, Inc., Redding, CA) and highly-oriented pyrolytic graphite (HOPG) (Digital Instruments, Santa Barbara, CA) were chosen for model validation standards because the surfaces are free from major defects, relatively smooth, homogeneous, and inert. Also, the surface properties of these two samples are different so polar and/or nonpolar interactions can be tested to identify the AFM's limitation. Studying polar and nonpolar surfaces is an ongoing challenge with the contact angle method. The different surface interactions are what triggered the development of several indirect models mentioned in the previous sections.[9] Before taking a measurement, mica and graphite (HOPG) were cleaved to expose fresh faces and secured on a microscope slide using adhesive tape.

2.4.2 Contact angle measurements

The contact angles were obtained using a video-based contact angle system (OCA, Future Digital Scientific Co., Bethpage, NY). First, static contact angles were measured. Drops (5μL) of water, diiodomethane, and formamide or ethylene glycol were dispensed using a motor driven syringe. The surface tensions of these liquids are listed in **Table 2-1**.[2] The indirect model component values are included in the table. Water contact angles

were measured in a saturated water vapor environmental chamber to prevent evaporation during spreading. A picture of the contact angle system and the environmental chamber designed in this lab is shown in **Figure 2-4a** and **Figure 2-4b**, respectively. The other liquids did not evaporate as quickly; therefore, those studies were conducted in ambient conditions. Each droplet was recorded for 240 seconds and ten contact angle values were measured. The OCA software uses axisymmetric drop shape analysis [26] to analyze the measurements and a screen shot is shown in **Figure 2-5**. This figure shows how the software draws the tangents to the droplet based on where the user defines the baseline. This figure also shows the output of the right and left angle. All of these data are captured and an average is calculated from the right and left angle.

Advancing and receding contact angles were measured using the same liquids and drop size. The advancing angle was recorded for 45 seconds, and then, the liquid was retracted and recorded until the end. Ten contact angle values were measured using the axisymmetric drop shape analysis [26] incorporated with the software. The advancing angle is taken at the end of the spreading and the receding angle is seen when the liquid "jumps" in.

Lastly, the effect of hygroscopicity with formamide and ethylene glycol is evaluated using static contact angle measurements. Molecular sieves were used to dry ethylene glycol over a 24 hour period. Formamide was slowly distilled over three hours because of impurities and the likelihood of degradation in the molecular sieves. The water content of the solvents was then tested using Coulometric Karl Fisher (KF) titration (737, Metrohm USA Inc., Riverview, FL). Finally, the dried solvents were hydrated to 0.5, 1.0, and 5% w/w for comparison. These exact amounts were also confirmed using KF.

Table 2-1: Surface tensions of various solvents used to measure contact angles and the separate surface tension components for the indirect models

	Neumann	Van Oss – Chaudhury – Good			OWRK	
	γ_{lv}	γ_{lv}^{LW}	γ_{lv}^{+}	γ_{lv}^{-}	γ_{lv}^{d}	γ_{lv}^{p}
	(mJ/m^2)					
Diiodomethane	50.8	50.8	0.0	0.0	50.8	0.0
Ethylene Glycol	48.0	29.0	1.9	47.0	29.0	19.0
Formamide	58.0	39.0	2.3	39.6	39.0	19.0
Water	72.8	21.8	25.5	25.5	21.8	51.0

a)

b)

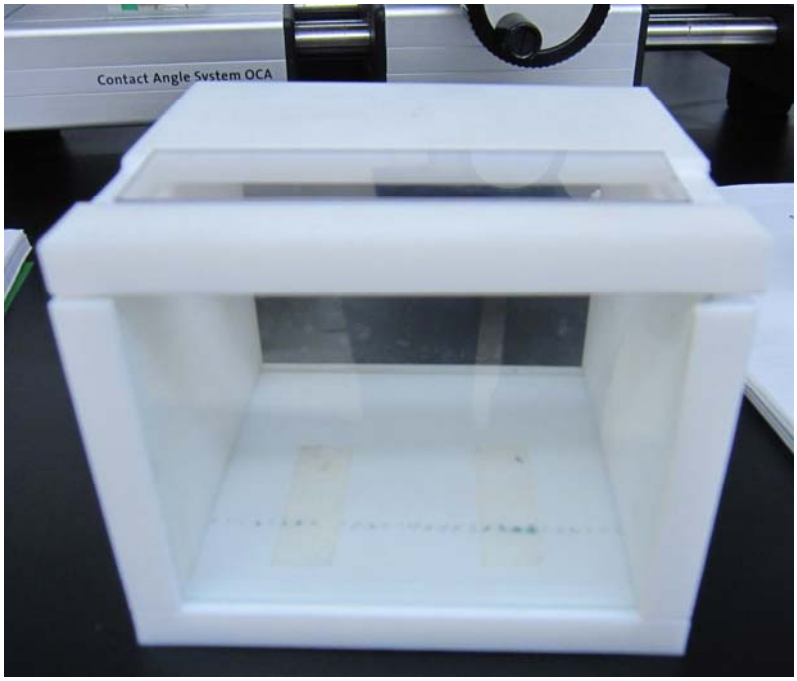

Figure 2-4: Contact angle measurements were made using: a) a Future Digital contact angle system with b) an environmental chamber.

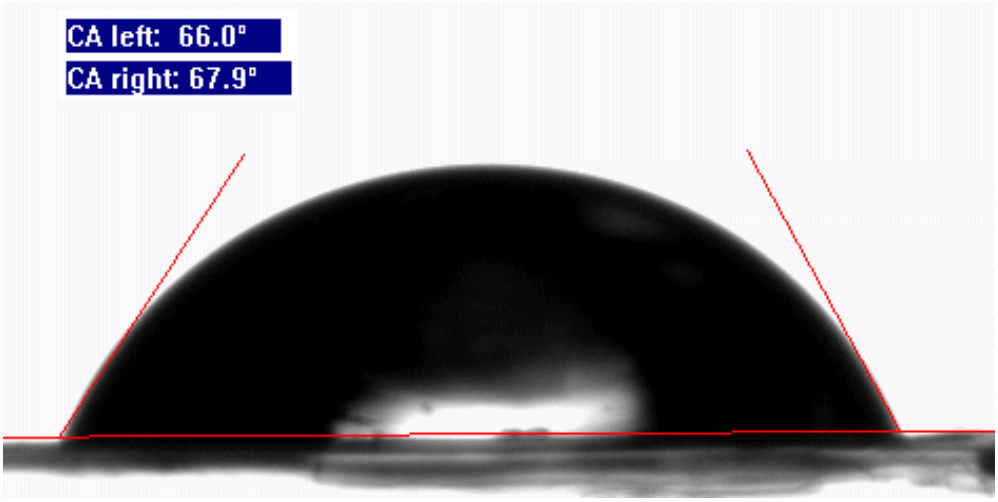

Figure 2-5: A screen shot of a **s**essile drop of a liquid on a solid. The fitting is done using the contact angle system software.

2.5 Contact Angle Results and Evaluation of Indirect Models on Inert Surfaces

The results in this section were necessary to establish a baseline of solid-vapor and solid-liquid surface energy for reference standards. The results obtained from AFM measurements presented in Chapter 5 will be compared to the results in this section. This will help evaluate the AFM's capabilities and/or limitations.

2.5.1 Static contact angle measurements

The average contact angles for mica and graphite are summarized in **Table 2-2**. Mica, a hydrophilic surface, was wetted most significantly with water and least significantly with diiodomethane,

$$\theta_{\text{diiodomethane}} > \theta_{\text{ethylene glycol}} > \theta_{\text{water}}$$

Water's polar or AB component was stronger than the other liquids used, illustrating mica's hydrophilicity. Ethylene glycol also has a polar/AB component, but the dispersive/LW component was stronger and thus, the spreading of the droplet is less compared to water. Diiodomethane only has a dispersive/LW component so the contact angle was expected to be largest. In summary, the spreadability order on mica was:

$$S_{\text{water}} > S_{\text{ethylene glycol}} > S_{\text{diiodomethane}}$$

where S is the spreading of a liquid across the surface. The term gives a different order than contact angle because spreadability was controlled by all the interfacial properties of the surface and liquid used in the study. Thus, with a hydrophilic surface, spreading of water was stronger and the contact angle was small.

Graphite, a nonpolar surface, has the strongest interaction with diiodomethane and the least interaction with water.

$$\theta_{water} > \theta_{formamide} > \theta_{diiodomethane}$$

The weak interaction with water confirms the surface hydrophobicity, and the strong interaction with diiodomethane confirms that the LW forces on the surface of graphite were strongest. The interaction with formamide was stronger than water because the dispersive/LW was larger and the polar/AB component was smaller. Therefore, the order of spreadability on graphite is

$$S_{diiodomethane} > S_{formamide} > S_{water}$$

The reason ethylene glycol was used on mica and not on graphite was because the contact angle of graphite-ethylene glycol was similar to the water-diiodomethane angle, which could have affected the surface energy determination. The reason formamide was not used on mica was because the spreading was similar to that of water, leading to an inaccurate fitting with the surface energy models. Many of the indirect models are criticized for dependence on the liquids used. Therefore, to have three independent and different interactions, formamide was used with graphite and ethylene glycol was used with mica.

The ten contact angle measurements from each liquid were used to determine ten solid-vapor surface energies. The average and standard deviation of these values for both mica and graphite were determined using the three indirect models previously discussed. The values are shown in **Table 2-3**.

Table 2-2: Average sessile drop contact angles on the surfaces of mica and graphite

	Mica (θ)	Graphite (θ)
Diiodomethane	41. 0 ± 2.9	37.8 ± 1.4
Ethylene Glycol	23.1 ± 1.2	NA
Formamide	NA	60.9 ± 2.4
Water	10.0 ± 2.4	80.6 ± 3.6
Standard deviations were determined from an n=10.		

Table 2-3: Average solid-vapor surface energy for mica and graphite calculated using various indirect models

	Van Oss – Chaudhury - Good				
	γ_{sv}	γ_{sv}^{LW}	γ_{sv}^{AB}	γ_{sv}^{-}	γ_{sv}^{+}
Mica	41.3 ± 2.7	39.8 ± 2.3	1.5 ± 0.7	72.6 ± 1.5	9.3E-03 ± 7.9E-03
Graphite	42.7 ± 2.6	41.5 ± 1.4	1.2 ± 1.3	7.2 ± 3.7	0.1 ± 0.1
	OWRK			Neumann	
	γ_{sv}	γ_{sv}^{d}	γ_{sv}^{p}	γ_{sv}	
Mica	65.2 ± 0.3	29.7 ± 1.2	35.5 ± 1.2	57.0 ± 0.4	
Graphite	40.3 ± 0.7	37.0 ± 1.7	3.3 ± 1.7	36.8 ± 1.1	
Standard deviations were determined from an n=10.					

The solid-vapor surface energy range for mica is 41.3 to 65.2 mJ/m^2. The lower value compares to the literature value 43 mJ/m^2 because the report from the literature used the van Oss-Chaudhury-Good model to determine the solid-vapor surface energy.[27] This model evaluates surface energy based on LW and AB components discussed in the previous section. Though the overall γ^{AB} is small compared to the γ^{LW} component, the γ^- is significant. This means that mica's surface was extremely electron donating. A similar observation was made with the OWRK model. The polar component in this model was 35.5 mJ/m^2 and was actually larger than the dispersive component. Etzler believes γ^p is covered in the γ^{LW} component, referring to dipole-dipole interactions. Thus, the strong mica-water interaction could be explained by the large polar surface energy component from the OWRK model and a large electron donating surface energy component by the van Oss model. Even though the two models are not in agreement with the total solid-vapor surface energy, it was clear mica will have a stronger interaction with liquids whose characteristics are similar to water and ethylene glycol. As mentioned previously, no statistical mechanical insight can be gained from the Neumann model, but the average γ_{sv} was found to be between the other models, making it difficult to determine a single true value for the solid-vapor surface energy of mica.

The solid vapor surface energy range for graphite was 36.8 to 42.7 mJ/m^2. The higher value was obtained using the van Oss-Chaudhury-Good. The value reported in the literature was 46 mJ/m^2, determined using the OWRK model. There was better agreement between indirect models when evaluating the average solid-vapor surface energy of graphite instead of mica. The OWRK and van Oss-Chaudhury-Good model show that the polar/acid-base components respectively were small for graphite. Small

values were calculated when the van Oss-Chaudhury-Good model was broken into the electron donating-accepting components. These results bring up a point of contention with this model. The total γ^{AB} component for both mica and graphite was small; however, the γ^- for mica was much larger in comparison, though not reflected in the overall term because of a small γ^+. At first glance, it would seem the dispersive/LW interactions were dominant on the surface of both mica and graphite. However, the strong mica-water and mica-ethylene glycol interaction indicated another force must be contributing to the surface energetics. Lastly, the Neumann model was used to calculate γ_{sv}. The Neumann value was comparable to the γ^d term in the OWRK model. Neumann's modification to the geometric mean was made in order to prevent overestimation of the surface energy. Calculation of the γ^{LW} of van Oss-Chaudhury-Good model was solely based on the geometric mean, and therefore, it is larger than Neumann's γ_{sv}.

The mica and graphite solid-vapor surface energy results illustrate how each model evaluated van der Waals and polar/AB forces differently. Since there was no agreement in the solid-vapor surface energies on mica, these models might be better suited for analyzing surfaces dominated by van der Waals forces. Each model relies on the foundation of the geometric mean which evaluates van der Waals interactions: London dispersion, Debye, and Keesom interactions. These models have incorporated the polar interaction, the acid-base interaction, or a corrections factor, but these components were not comparable with mica. For this reason, the AFM may be a more attractive tool for studying surface energy on a variety of surfaces.

Now that the solid-vapor surface energy has been calculated, the solid-liquid surface energy can be calculated from Young's Equation and contact angle data. Results are shown in **Table 2-4**.

As expected, the range of solid-liquid surface energies for mica was very large because of the large difference in the solid-vapor surface energies. As with solid-vapor surface energies, the solid-liquid surface energy values for all of the liquids makes it difficult to identify a so called "true" value. However, the graphite data was more comparable because of the similarities with the solid-vapor surface energy. **Figure 2-6** shows the range of mica and graphite solid-liquid surface energy using histograms. The Y axis was the frequency plotted against the solid-liquid surface energy. The range of solid-liquid surface energy for graphite-diiodomethane was -3 to 1 mJ/m^2 (shown in blue). The negative numbers for graphite have no physical meaning and were a result of limitations from the indirect models. Young's equation attempts to balance the forces among the three phases; therefore, the solid-liquid surface energy may result in negative numbers when γ_{sv} is less than $\gamma_{lv} \cos(\theta)$. The ranges of solid-liquid surface energy for graphite-formamide (9-14 mJ/m^2) and graphite-water (25-30 mJ/m^2) were consistent with the results of the contact angles. The lowest solid-liquid surface energy was graphite-diiodomethane because there was a stronger interaction (smaller contact angle). The largest solid-liquid surface energy was graphite-water because there was a weaker interaction (large contact angle).

Table 2-4: Average solid-liquid surface energies for mica and graphite calculated from solid-vapor surface energies of various indirect models.

	Mica			Graphite		
	OWRK	Van Oss-Chaudhury-Good	Neumann	OWRK	Van Oss-Chaudhury-Good	Neumann
	γ_{sl} (mJ/m^2)					
Diiodomethane	26.9 ± 1.5	0.8 ± 0.2	18.7 ± 1.7	0.7 ± 0.9	0.6 ± 0.1	-3.3 ± 1.6
Ethylene Glycol	21.1 ± 0.4	-3.6 ± 1.7	12.8 ± 0.3	NA		
Formamide	NA			12.6 ± 2.2	13.7 ± 2.8	8.7 ± 1.9
Water	-6.4 ± 0.5	-31.1 ± 2.3	-14.7 ± 0.6	29.0 ± 4.2	30.0 ± 3.9	25.0 ± 3.5
Standard deviations were determined from an n=10.						

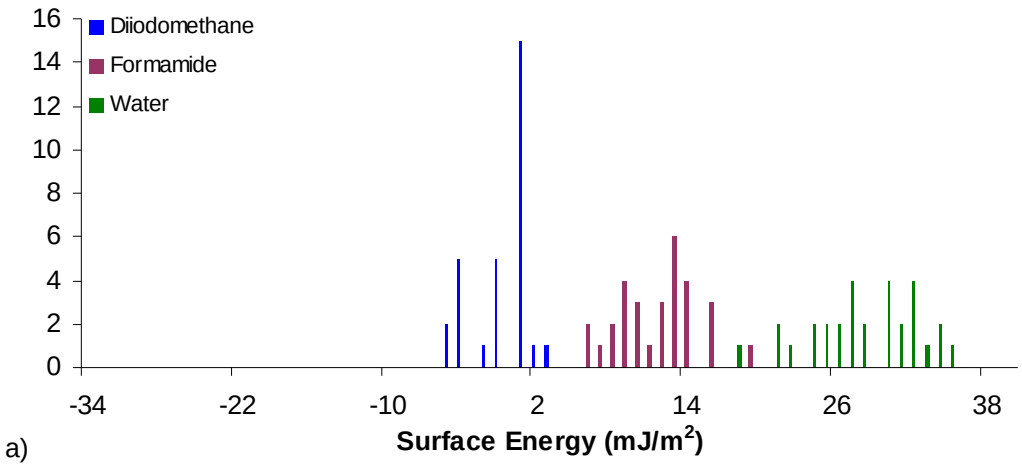

a)

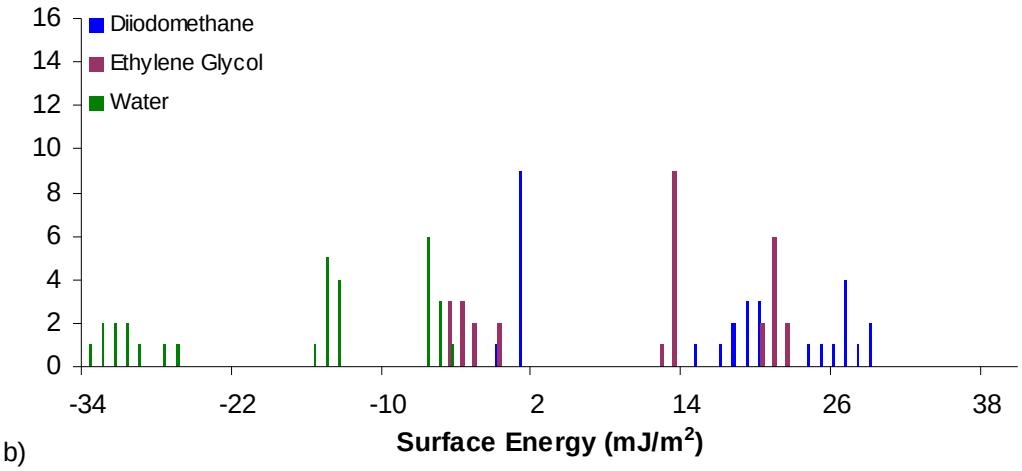

b)

Figure 2-6: Solid-liquid surface energies of a) graphite and b) mica for the liquids used to measure contact angles and determine solid-vapor surface energy.

2.5.2 Advancing contact angle measurements

Advancing and receding contact angle measurements, **Table 2-5**, were performed on mica and graphite to evaluate the difference between the static equilibrium angle and the advancing angle. These data also helped to reevaluate the indirect models and how change in contact angle measurements can affect the calculated solid-vapor and solid-liquid surface energies.

The trend for the advancing contact angle measurements and spreadability was the same as what was determined from static contact angles, on mica $\theta_{diiodomethane} > \theta_{ethylene\ glycol} > \theta_{water}$ and graphite $\theta_{water} > \theta_{formamide} > \theta_{diiodomethane}$. There was no substantial difference between the advancing contact angle and the receding contact angle on mica and the difference was within the standard 2 degree experimental error. However, there was a larger difference between graphite-formamide and graphite-water advancing and receding contact angles. The grade of graphite used in all of the experiments was a lower grade that affects the cleavage properties. There are three grades of graphite, and each grade differs in the mosaic spread angle. The smaller the angle the fewer steps observed on a cleaved face. The grade used in these experiments was ZYH. The mosaic angle for the ZYH grade is 3.5°± 1.5°. Thus, steps will be observed after cleavage causing the surface to be rougher than higher grades of graphite would be after cleavage.[28] Then, when measuring angles with more polar solvents, the roughness could cause a larger jump in when the drop recedes, lowering the contact angle. In comparing the static contact angles with the advancing contact angles, the only measurable differences were small and were between mica-diiodomethane and graphite-water. These interactions were less favorable

than mica-water and graphite-diiodomethane; therefore, a three or four degree difference was not uncommon. Since there were few differences between the static and advancing contact angles, the average solid-vapor and solid-liquid energies should also be comparable. The advancing solid-vapor and solid-liquid surface energies are shown in **Table 2-6** and **Table 2-7**. Reviewing **Table 2-3** and **Table 2-4**, the solid-vapor and solid-liquid surface energies calculated from static contact angles, prove the assumption of comparability to be true. The small difference in mica-diiodomethane and graphite-water did not change the overall solid-vapor surface energy and did not change the components. There were still major differences in the three indirect models when evaluating γ_{sv} for mica, but it remains easier to compare the solid-vapor surface energy of graphite among the three models.

Table 2-5: Average advancing and receding contact angles measured on the surfaces of mica and graphite

	Mica		Graphite	
	Advancing (θ)	Receding (θ)	Advancing (θ)	Receding (θ)
Diiodomethane	46.1 ± 0.8	44.2 ± 1.1	37.9 ± 2.3	36.4 ± 1.4
Ethylene Glycol	23.7 ± 3.7	23.2 ± 3.6	NA	
Formamide	NA		58.5 ± 3.2	54.7 ± 3.6
Water	11.1 ± 2.4	10.3 ± 2.1	83.0 ± 2.8	76.0 ± 3.7
Standard deviations were determined from an n=10.				

Table 2-6: Average solid-vapor surface energies for mica and graphite calculated from advancing contact angles and various indirect models

	Van Oss – Chaudhury - Good				
	γ_{sv}	γ_{sv}^{LW}	γ_{sv}^{AB}	γ_{sv}^{-}	γ_{sv}^{+}
Mica	42.8 ± 3.6	38.6 ± 2.4	4.2 ± 1.6	73.2 ± 1.7	6.9E-02 ± 5.6E-02
Graphite	42.7 ± 1.3	41.2 ± 1.3	1.5 ± 0.6	4.3 ± 2.6	0.3 ± 0.3
	OWRK			Neumann	
	γ_{sv}	γ_{sv}^{d}	γ_{sv}^{p}	γ_{sv}	
Mica	64.9 ± 1.2	29.7 ± 1.0	37.0 ± 0.6	57.0 ± 0.4	
Graphite	41.3 ± 1.1	38.8 ± 1.6	2.5 ± 0.9	36.5 ± 0.9	
Standard deviations were determined from an n=10.					

Table 2-7: Average solid-liquid surface energies calculated from advancing contact angle data and solid-vapor surface energy from various indirect models.

	Mica			Graphite		
	OWRK	Van Oss-Chaudhury-Good	Neumann	OWRK	Van Oss-Chaudhury-Good	Neumann
	γ_{sl} (mJ/m^2)					
Diiodomethane	29.7 ± 0.8	1.2 ± 0.1	21.7 ± 0.7	1.4 ± 1.1	0.6 ± 0.1	-3.5 ± 1.4
Ethylene Glycol	21.1 ± 1.0	-3.3 ± 0.9	13.1 ± 1.4	NA		
Formamide	NA			11.2 ± 2.4	11.9 ± 2.6	6.3 ± 2.6
Water	-6.5 ± 0.7	-30.8 ± 1.8	-14.4 ± 0.8	32.7 ± 3.9	33.3 ± 3.8	27.7 ± 2.8
Standard deviations were determined from an n=10.						

The purpose of these experiments was to evaluate the contact angle hysteresis. Since graphite and mica are relatively ideal surfaces, there was no substantial difference in advancing and receding contact angles. Also, the advancing angles were comparable to the static equilibrium angles. Therefore, the advancing and receding evaluation did not change the results of the calculated surface energies. The solid-vapor and solid-liquid surface energy range for mica was still large, and the results for graphite were comparable between the models. The negative numbers were still seen with mica-water and graphite-diiodomethane, illustrating the dependence of the indirect models.

2.5.3 Static contact angle measurements with hygroscopic liquids

Evaluation of the effect hygroscopic liquids have on contact angle measurements was the final study performed. The two hygroscopic solvents used in these studies were ethylene glycol and formamide.

Table 2-8 shows the water content of the liquids after drying. A typical plot for contact angle measurements is shown in **Figure 2-7a**. This plot differs from the plots obtained after the liquids were hydrated, **Figure 2-7b**. Instead of reaching an equilibrium which is obtained after the droplet has finished spreading, the contact angle continues to get larger. After waiting 240 seconds, the same droplet was recorded for 3 minutes, and a possible equilibrium angle was found **Figure 2-7c.** These angles were recorded and an average was determined for dry, 0.5, 1.0 and 5.0% w/w formamide-water on graphite and ethylene glycol-water on mica, **Table 2-9**. It was hypothesized that water in ethylene glycol would cause a decrease in contact angle from the dried angle because water has a strong interaction with mica; however, an increase was observed. The difference in the concentration of water present, between 0.5% and 5.0%, did not affect the angle

measured since the angles are very similar. For formamide on graphite, an increase in water should increase the contact angles because water interacts weakly with graphite. This was observed when measuring the contact angles with formamide containing water. The standard deviations between the different concentrations of formamide-water were larger than what is seen with pure liquids. Therefore, it is important to use pure liquids when measuring contact angles in order to find the "true" interaction between that liquid and the sample. The measured angles from the dried liquids were used in Section 2.5 to calculate the solid-vapor and solid liquid surface energies.

Since diiodomethane was the other solvent used in the contact angle experiments, the water content was evaluated using KF. The initial value was as low as the values for dried ethylene glycol and dried formamide. Hydration of diiodomethane was attempted. Excess water was added to a vial of diiodomethane and rotated continuously for three days. Each day the water content was tested. The water content did not increase from the initial value shown in **Table 2-8.**

Table 2-8: Water content of liquids used in contact angle measurements after being dried and the initial amount of water for diiodomethane measured directly from the bottle.

Solvent	Water Content % w/w
Dried Formamide	0.04
Dried Ethylene Glycol	0.03
Diiodomethane	0.01

Table 2-9: Contact angles measured on mica and graphite with dried and rehydrated ethylene glycol and formamide respectively

Mica		Graphite	
Ethylene Glycol	(θ)	Formamide	(θ)
Dried	23.1 ± 1.2	Dried	60.9 ± 2.4
0.5 % w/w water	30.9 ± 1.3	0.5 % w/w water	65.6 ± 4.5
1.0% w/w water	32.2 ± 2.3	1.0% w/w water	62.4 ± 3.8
5.0% w/w water	30.5 ± 1.3	5.0% w/w water	64.3 ± 4.1
Standard deviations were determined from an n=10.			

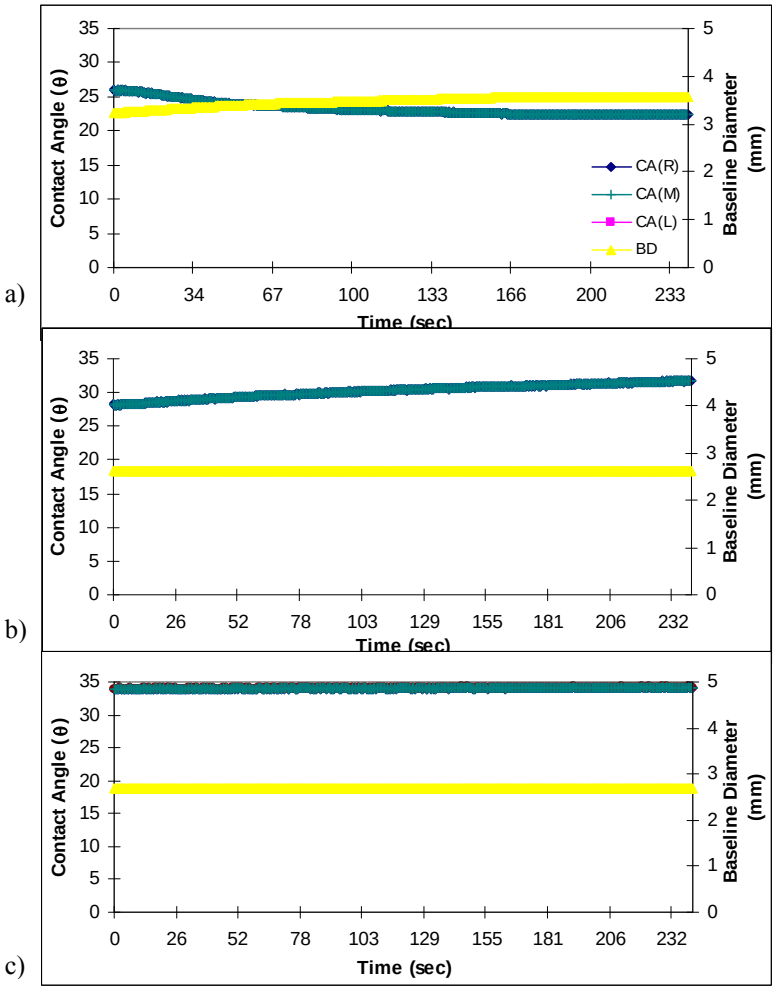

Figure 2-7: Contact angle measurements shown over time for a) a dried solvent, b) a hydrated solvent, and c) the possible equilibrium angle of the hydrated solvent 3 minutes after the initial recording

2.6 Contact Angle Summary

Young's equation defines the forces at the three-phase boundary of a liquid droplet on a surface. In order to determine the solid-vapor surface energy from Young's equation, indirect models were developed. These equations are part of the limitations of contact angle measurements. The indirect models did not agree in the process of defining independent interactions (van Oss et al and OWRK) or if the division of components is the best approach (Neumann). Since there were theoretical differences in the models, the overall surface energy values derived by these models could not be compared when measured for mica, a hydrophilic material. However, the surface energies determined for graphite using all three models were comparable. Graphite was dominated by dispersive energies, and since the models are mathematically based on the geometric mean, which defines the London dispersive, Debye, and Keesom forces, the surface energy values of graphite were expected to be comparable.

One limitation from the contact angle measurements was the difficulty or inability to draw conclusions from data without scientific meaning. Negative solid-liquid surface energies were calculated for both mica and graphite. These values do not have a physical meaning and will be difficult to compare with AFM results.

The other challenges with contact angle measurements were the experimental methodologies. Controlling the humidity is difficult because of a restricted number of useful solvents to attain an equilibrium contact angle. Water and other solvents that evaporate rapidly require a saturated environmental chamber to measure the angle. Only pure liquids can be used, and if the liquid interacts with the surface causing deformation, measuring the true contact angle is difficult.

All of these disadvantages made investigating the AFM a necessity. Although contact angle measurements are still used to investigate surface energetics, the shortcomings prompted the need to evaluate the performance of other techniques. Therefore, the results in this chapter will provide a baseline for surface energy values with mica and graphite. The AFM was then used to evaluate the surface energy on mica and graphite. To determine the AFM's capability, the surface energy results will be compared to the contact angle results in this chapter.

Chapter 3 – Atomic Force Microscopy

The focus of this chapter is to review the operations of atomic force microscopy (AFM) and how that instrument can be used to measure forces. The methodology of characterizing AFM tip properties, measuring forces, and using statistical analysis is presented. The overarching goal is to establish a robust experimental method to obtain repeatable measurements that can be used to evaluate surface energy.

3.1 Atomic Force Microscopy Introduction

Scanning probe microscopes are unique in that they can provide three-dimensional real space images and can allow spatially localized measurements of structure and properties.[29] The scanning probe microscopes create images with a very fine probe tip which scans over the sample instead of the typical visual observations. The atomic force microscope (AFM), depicted in **Figure 3-1**, was invented by Binning et al [30] in 1986 and belongs to the series of scanning probe microscopes. The AFM, since its discovery, has become an important tool for imaging topography and measuring forces of sample surfaces as it is not limited to conducting samples.[31] The AFM is comprised of three major components: the tip, the piezoelectric crystal, and the detection mechanism.

The stylus, or tip, is the key piece of the AFM that scans and interacts with the sample surface. The basic tip is micro-fabricated, extremely sharp, and mounted on the end of a cantilever. The cantilever is bonded to a glass chip that is easily mounted in the sample holders. The interaction of the tip with the sample is recorded through movement of the cantilever. The cantilever typically has a low force constant allowing for precise control of the force between the tip and sample.[31] The force constant of the cantilever will be

discussed further in **Section 3.3**. Different tips have developed as imaging techniques advance. Therefore, the silicon and silicon nitride tips are not the only tips commercially available. AFM tips can also be modified chemically or "naked" cantilevers can be purchased to tailor the tip to a specific interaction of interest.

The critical feature that allows the three dimensional scanning of the tip is the piezoelectric crystal. The AFM utilizes the reverse piezoelectric effect. When a potential difference is applied to opposite faces of the crystal, it changes shape. The piezoelectric tube is arranged with five electrodes: z is in the middle, –x and +x are across from each, and –y and +y are also opposite each other, **Figure 3-2**. When a bias voltage is applied between the inner and the outer electrodes, the tube expands or contracts and moves in the z direction. If voltage is applied to one of the outer electrodes, the tube will bend and then move in either the x or y directions. When the tip is in contact with the surface, the exact movement of the cantilever is known, because the exact movement of the piezocrystal is known.[31]

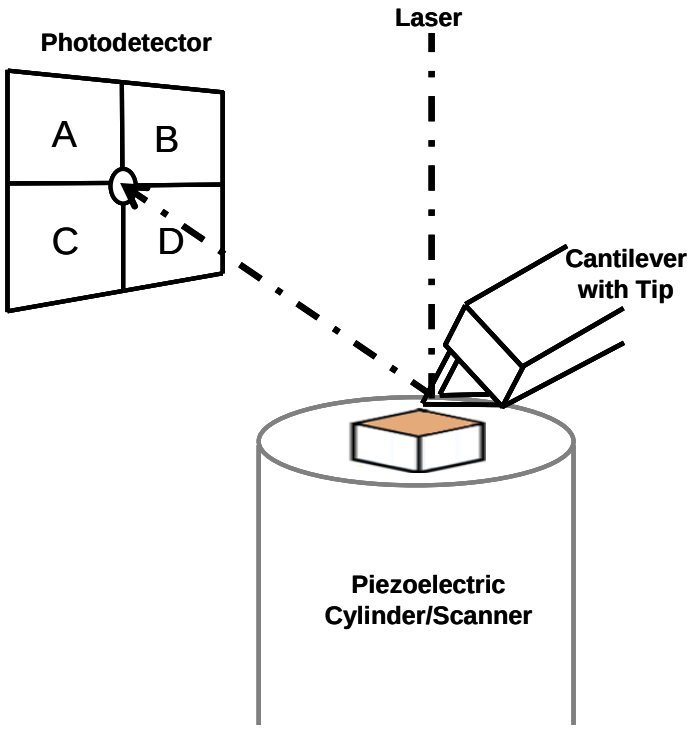

Figure 3-1: Schematic of atomic force microscope with key features.

The most common detection of the cantilever movement is the optical lever technique. A beam from a laser diode is focused onto the end of the cantilever and the beam is reflected into a photodetector. The sensitivity of the change in cantilever movement is derived from the large distance between the cantilever and the photodiiode. Most photodetectors are simple photodiodes. A photodiode is a semiconductor device which turns the laser into an electrical signal. The photodiode is split into four sections, as shown in **Figure 3-1**, allowing for lateral and torsional motion of the cantilever to be detected.[31] The cantilever's lateral deflection is measured by monitoring the laser's change in position on the photodetector. The vertical signal is (A + B) − (C + D), while the (A + C) − (B + D) signal responds to friction due to torsion of the cantilever, providing lateral force information, **Figure 3-1**.[32, 33]

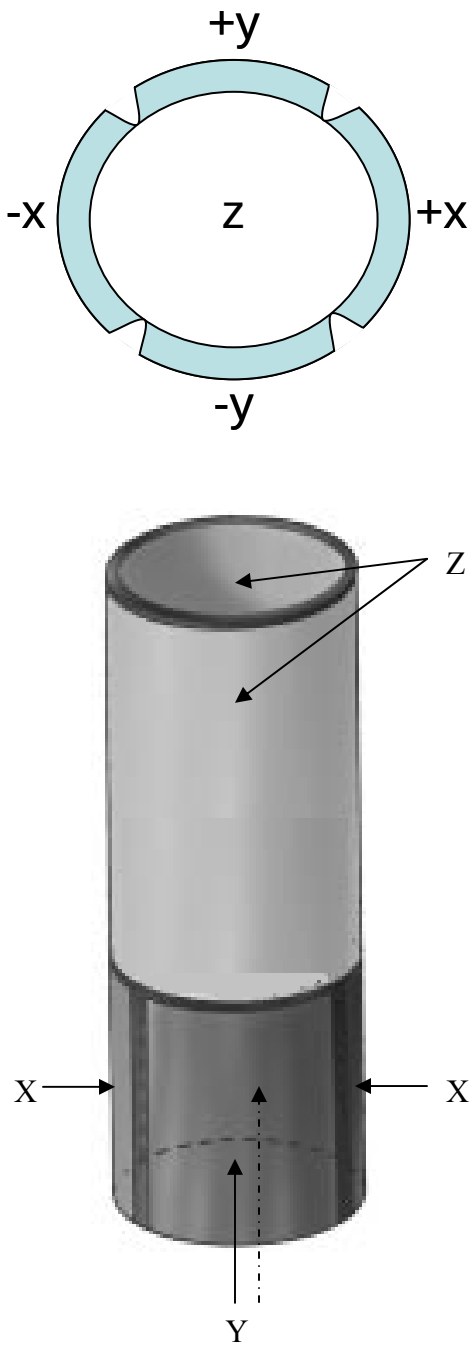

Figure 3-2: The piezo scanner moves the sample in three direction: x, y, and z movements. The top view schematic a) shows the five electrodes needed to achieve this, and b) is a 3D view to help visualize the z or vertical movement.

3.2 Imaging Modes and Techniques

The first scanning probe microscope was the scanning tunneling microscope (STM). The STM allowed for real-space determination of surface structure, including nonperiodic structures. The images of the surface are created by electrons tunneling between the surface and a small metal tip. The conducting tip is brought very near to the surface and a voltage difference is applied between the two producing an electrical field allowing electrons to tunnel between them. Electrons have wavelike properties that taper off quickly as opposed to ending abruptly. Therefore, the tunneling current can occur when the distance between the tip and the sample is extremely small.[34, 35] STM images represent the electronic structure (local density of states) of a surface. This structure closely correlates with the geometric surface topography, so that defects and surface roughness can be observed. The disadvantage of this method is that the sample must be electrically conductive. This is what made the AFM such an attractive tool because topographical images could be produced on samples that are non-conductive.

Since its beginning, the AFM has advanced and more imaging techniques have been developed. However, the initial use of the AFM was mapping a topographic image of the sample. The topographic picture is produced by plotting the deflection of the cantilever versus its position.[32] The images can be used to observe structural or dynamic features. The AFM has been employed to image semiconductors,[36] biologics,[37] etching patterns,[38, 39] and dissolution of crystalline faces.[40] Two modes are used to produce the topographical image, tapping and contact. In the tapping mode, a stiff rectangular cantilever oscillates, or taps, at or near the cantilever's resonance frequency as it traverses over the sample. The major advantage of using tapping mode is the

reduction in time on the surface. Less drag occurs, which enhances the resolution of a topographical image. Another benefit is delicate samples can be imaged without damage or severe image distortion. In addition, capillary and lateral (side to side) forces can be lessened or avoided with less time on the sample.[31] During tapping mode trapped electric charges on the surfaces are also eliminated. Tapping mode can be operated in air and in liquid. As previously stated, the goal of this work is to evaluate the AFM's ability in studying surface energy. Therefore, tapping mode cannot be used because this mode does not measure forces of adhesion.

The easiest and most widely used mode of the AFM is contact mode. In this mode, the AFM tip is in intimate repulsive contact with the surface of the sample. The scanner traces over the sample causing the cantilever to bend because of changes in topography or the probe-sample forces. There are two variations of the contact mode: constant-force and variable-deflection mode. In constant-force mode, the cantilever deflection is kept constant with a feedback loop that adjusts the height of the sample such that a constant deflection is maintained. The height is varied by extending or retracting the piezo along the z axis. The other mode is variable-deflection mode. In this mode the height is held constant and cantilever deflection is monitored. One disadvantage of contact mode is the effect capillary forces can have on the image and force measurements. However, controlling humidity and using liquids can reduce or eliminate the effect of capillary forces.[31]

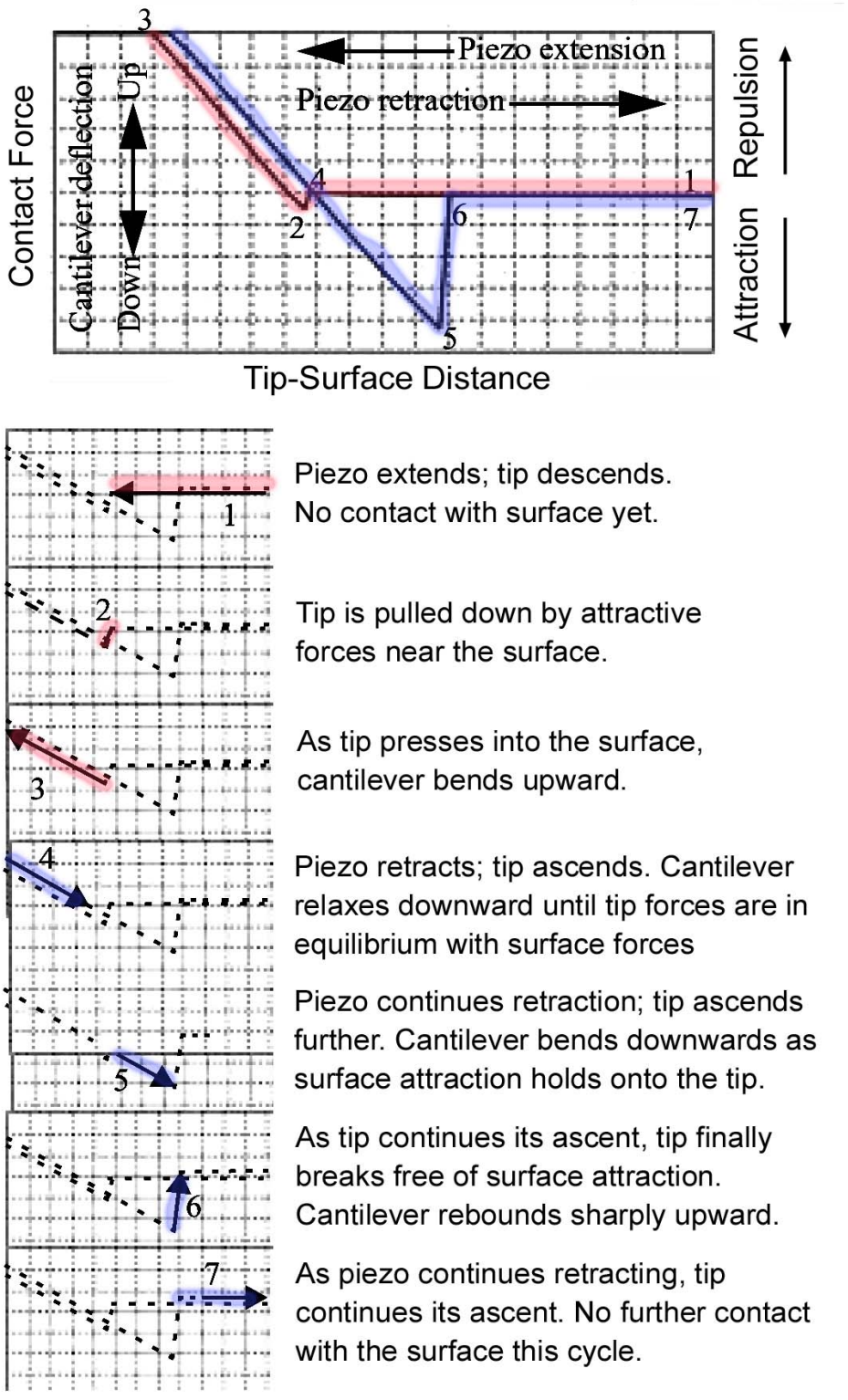

Figure 3-3: Typical AFM force curve.

The other prominent imaging technique of the AFM used for this study is force-imaging. During contact mode scanning, the force of adhesion between the tip and the sample is evaluated by measuring the deflection of the cantilever. The forces can be derived from the force curve output by AFM, as shown in **Figure 3-3**. In a typical force measurement, two plots are obtained as the piezocrystal is extended and retracted. At the start of extension, marked by point 1 in **Figure 3-3**, there is a large distance between the tip and the sample. As the voltage is applied, the piezocrystal starts to extend, the distance decreases, and the force acting on the tip exceeds the stiffness of the cantilever. This causes the tip to jump into contact with the sample surface, points 2-4. Deflections are dominated by mutual repulsions, causing the piezocrystal to begin retracting, separating the tip from the sample. However, separation does not occur until the bent cantilever overcomes the adhesion forces, pulling off sharply to a non-contact position, points 4-7 in **Figure 3-3**.[33] Initially, the output is expressed as cantilever deflection (in terms of volts on the photo diode) *vs.* piezocrystal displacement, since the only known is the movement of the piezo, Z distance. This plot can be translated into a force *vs*. distance plot based on Hooke's Law ($F=-k*\Delta x$) where Δx is the displacement measured by the AFM and k is the spring constant.[32] The methods for determining spring constant will be discussed in the next section. To determine the deflection (Δx) from the force curves, SPIP software was used. However, the theoretical determination of Δx is shown in Section 3.6.3. With proper calibration, these two parameters, and therefore, F, can be obtained with good accuracy.

3.3 AFM Tip Characterization

The cantilever is a key element of the AFM. Cantilevers can be either rectangular or triangular. The triangular cantilevers typically experience less torsional force, which is important when measuring vertical displacement. The mechanical properties of cantilevers are characterized by the spring constant and resonance frequency and are mainly responsible for the AFM's performance. Cantilevers are typically made from silicon or silicon nitride. The top side is coated with gold or aluminum to increase reflectivity of the laser into the photodiode. This section details the evaluation of the spring constant and the tip radius. In Chapter 4, the importance of the tip radius is in determining surface energy for AFM force measurements will be discussed.

3.3.1 Calibration of spring constants

A cantilever should have high sensitivity, and this is achieved with a low spring constant.[29] The spring constant describes the stiffness of the cantilever in force per unit length and must be determined to calculate the force.[31, 32] There have been several methods established to measure the spring constant of a cantilever. Added mass and thermal methods have been the most popular, but a geometric analysis was the initial technique using[41]

$$k = \frac{Ewt_c^3}{4L^3} \qquad \textbf{3.1}$$

where k is the spring constant, E is the Young's modulus, t_c is the thickness, w is the width, and L is the length. Using a scanning electron microscope (SEM), the cantilever's width and length can be measured. It is much more difficult to measure the thickness and the Young's modulus: therefore, manufacturers will report an average for these values.

Consequently, the geometric method is not preferred because the thickness and Young's modulus of the individual cantilevers vary. It has been shown that cantilevers are not perfectly homogeneous and since thickness in Equation **3.1** is to the third power, a small difference in thickness can lead to a significant change in spring constant. The Young's modulus of a thin layer can deviate from the bulk material and Khan has shown that a silicon nitride sample 800 nm thick had a Young's modulus of 280 GPa rather than the reported 146 GPa.[42] The thickness of the native oxide layer and the gold layer are both unknown. These unknowns add to the mass of the cantilever which influences the resonance frequency and the spring constant.[32]

3.3.1.1 Added mass method

A more prevalent method, regarded as the "gold standard" to measuring the spring constant, is the added mass method developed by Cleveland et al.[43] The technique for this method relies on measuring the resonance frequency of the cantilever before (ν_0) and after (ν_1), the addition of a tungsten sphere behind the tip. By adding a mass M to the cantilever the resonant frequency becomes:

$$\nu = \frac{1}{2\pi}\sqrt{\frac{k}{M+m}} \qquad \textbf{3.2}$$

where m is the mass of the cantilever. After the sphere is added, the equation for the spring constant becomes:

$$\mathrm{k} = (2\pi)^2 \frac{\mathrm{M}}{\left(\nu_1^{-2} - \nu_0^{-2}\right)} \qquad \textbf{3.3}$$

The diameter of the tungsten sphere (density 19.3 g/cm^3) that is added to the cantilever is then analyzed using the SEM. Using the diameter and known density, the mass of the sphere can be calculated, followed by the spring constant.

3.3.1.2 Thermal method

Since the added mass method is destructive from the epoxy needed to glue the tungsten sphere and the gold coating for the SEM measurement, it is not possible to measure the spring constant of each individual cantilever. Therefore the thermal method[44] was developed. This method models the cantilever as a simple harmonic oscillator relying on the thermal vibrations that occur at room temperature. The potential energy based on the equipartition theorem of this system is:

$$\frac{1}{2}m\omega_0^2\left\langle z^2\right\rangle = \frac{1}{2}k_B\left\langle z^2\right\rangle \qquad \textbf{3.4}$$

where m is the oscillating mass of the cantilever, ω_0 is the resonant frequency of the system, z is the displacement of the oscillating cantilever, and k_B is Boltzmann's constant. Since $\omega_2^0 = k/m$, Equation **3.4** becomes:

$$\mathrm{k} = \frac{k_B \mathrm{T}}{\left\langle \mathrm{z}^2\right\rangle} \qquad \textbf{3.5}$$

The thermal data is collected in the time domain. A Fourier transform is used to transform the data to the frequency domain, thereby generating the power spectrum, **Figure 3-4**. Since no other noise sources are likely to have a resonance at the resonant frequency of the cantilever, the area below the peak is measured to determine the power,

P. The integration under the power spectrum equals the mean-square in the time data; therefore, the estimation of the spring constant is:

$$k = \frac{k_B T}{P} \qquad \textbf{3.6}$$

This method can be used to measure the spring constant in air and in liquids without destroying the tip or cantilever. Therefore, this method has become the preferred method for spring constant determination.

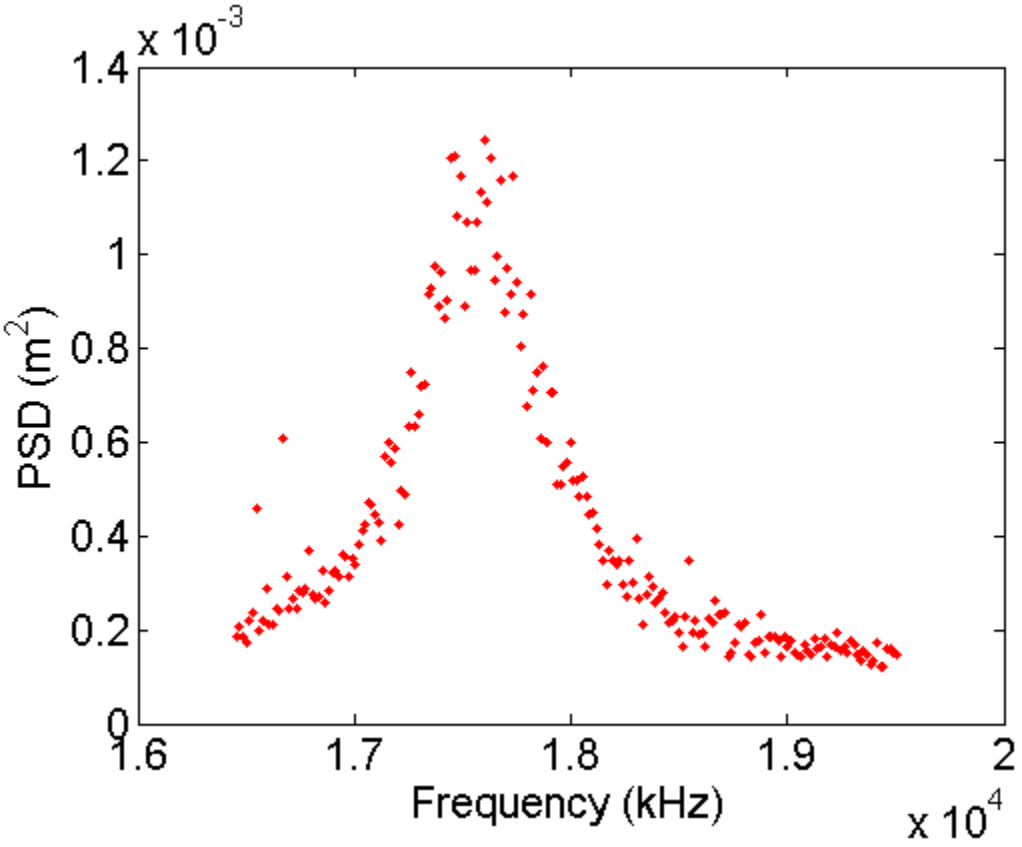

Figure 3-4: A typical power spectral density that is generated from thermal vibrations of the tip.

3.3.2 Tip radius measurements

Two methods have been used to measure tip radius. One direct way is capturing an image with scanning electron microscopy (SEM). The other method utilizes the information gained in a topography scan with the AFM. The quantity of the tip radius is not necessary for calculating forces, but in Chapter 4, the importance of tip radius will be presented.

3.3.2.1 SEM method

The SEM creates an image of the sample surface by scanning it with a high-energy beam of electrons. From this image the radius of the tip can be determined, **Figure 3-5**. The evaluation of the SEM image to determine the tip radius is limited at the nanometer scale. Due to the electron beam size, focus, charging effects, and beam-sample interaction, the tip's edge positions are uncertain at the nanometer level.[45] The tip must also be coated before imaging to prevent charging of the sample. Dongmo showed the coating can overestimate the tip radius by about 4 nm.[45] The limitation of the SEM image also makes it hard for comparison with the other methods of interest.

3.3.2.2 Blind reconstruction method

Blind reconstruction uses the AFM to scan a specific tip characterizer sample to determine the shape of the probe. The reconstruction method uses a so called "self-imaging" technique, meaning the image obtained from a tip scanning the topography of the sample is then used to estimate that tip's radius. Each pixel from the image contains information about the tip geometry and the sample surface. The topography image reveals the inverted geometry of the end of the tip. First, an upper limit on the size of the probe is determined from the image because the features of the image are always broader

than the probe used. The upper limits are based on point of inflection, or maxima on the topography image. These upper limits are created by the shape of the tip. The intersection of the two points gives an estimation of the tip. Dongmo illustrated this with an overlaid image of a trace of what an AFM probe would create on top of an image of the actual surface.[45] The algorithm developed by Villarrubia for blind reconstruction extracts the maxima, and by calculating the intersection, the tip radius can be determined.[46-48]

Since the SEM is a destructive method of measuring the tip radius and the radius is an important parameter in determining surface energy, a method was needed to constantly monitor the tip radius. The constant monitoring would also allow users to know when a tip becomes dull. Dull tips can skew force measurements because they can change the contact area. The contact area is one parameter that was determined to be crucial in controlling variability of force measurements.

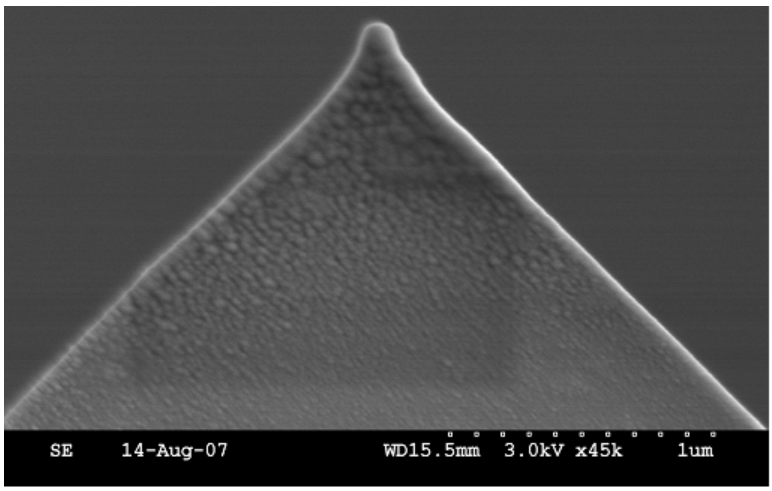

Figure 3-5: SEM image of a silicon nitride tip.

3.4 AFM Scanning Parameters

Thus far the operations of the AFM have been discussed. The objective of this work is to be able to use the AFM to determine surface energy. Therefore, the force imaging function of the AFM is going to be used. It was realized that in order to develop a technique, the probe's properties, such as tip radius and spring constant, will have to be evaluated, as will other parameters that can affect the precision and accuracy of the instrument. Key parameters were identified and evaluated to increase the repeatability of force measurements at different locations on a sample and with the same tip. The critical scan parameters that were identified are scan size, scan rate, force applied and contact area.

3.4.1 Scan size

Following the engagement of the tip with the sample, the next step is to view and optimize the scan in the *advance force mode*, shown in **Figure 3-6**. This mode allows the user to view the force plot output created by the tip-sample interaction. In this mode, the scan parameters can be changed to establish control over the tip-sample interaction. Scan size is affected by the type of AFM scanner that is used. Some common scanners are *E* and *J* with maximum scans size of 10 x 10 μm and 125 x 125 μm respectively. These various sizes are more important when evaluating topography. For a force curve it is best to take force measurements in a single spot and then move to other discrete spots on the sample to gather more force data. There were several reasons for choosing a proper scan size. First, in some liquids and on rough surfaces, a large scan size can cause drag and skew the actual tip-sample interaction. Drag typically causes hysteresis, an offset seen with force curves when the "snap off" or retracting line does not follow the

same path as the "snap in" or advancing line. When there is hysteresis, it is difficult to determine the "true" force between the tip and surface, as illustrated in **Figure 3-7**. Second, tip diameters range from 80 to 120 nm, so when using a scan area smaller than the tip, the information gleaned is similar to a moving average and not a discrete measurement. Lastly, when investigating the forces on rough or heterogeneous samples, the results over a larger area might be confounding because of the AFM's sensitivity. It will be hard to elucidate the range of force resulting from the various chemical moieties, roughness, or true tip-sample interaction. For these reasons, multiple discrete measurements were made instead of large area measurements.

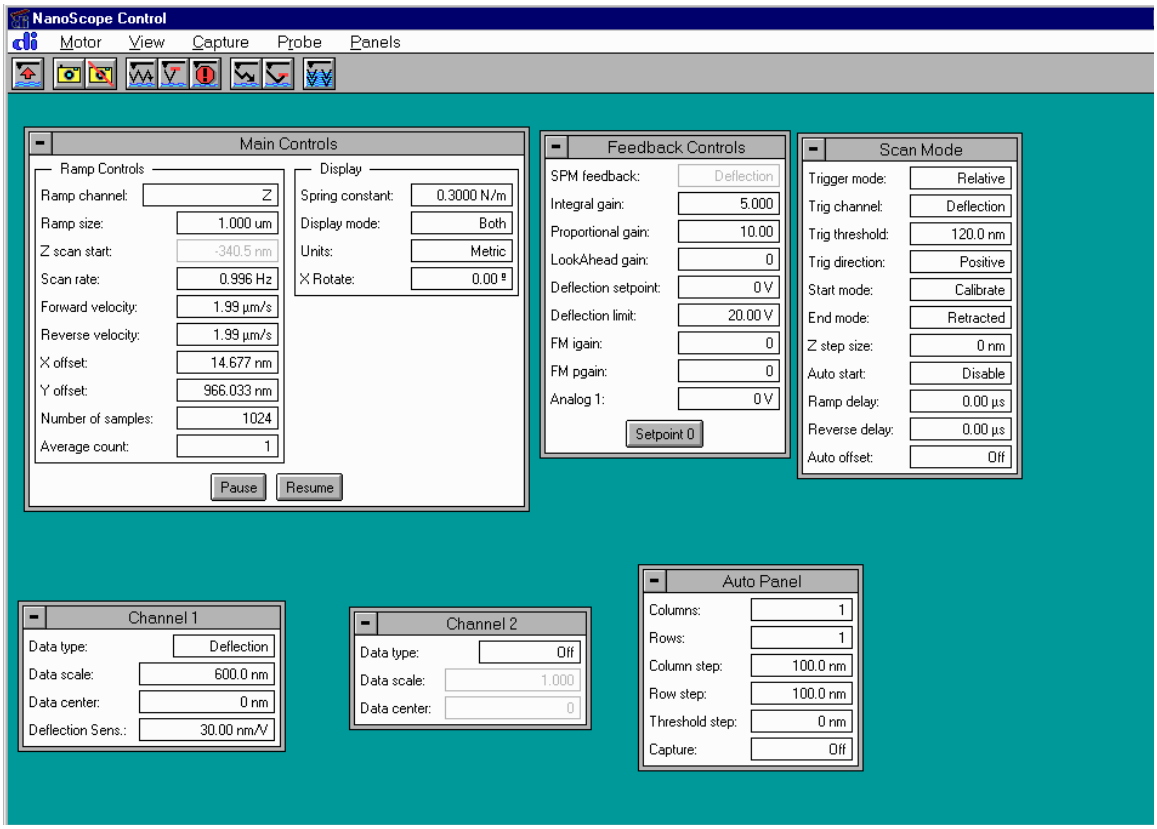

Figure 3-6: Advance force mode controls – At this screen, force calibration settings can be manipulated so that the best force curve may be obtained. This screen is the first step once the tip is engaged with the surface. From this screen, the start position, scan size, scan rate, and amplitude applied to the Z piezo can be controlled. The setpoint value of the deflection voltage used in the feedback loop can be adjusted, and the type of trigger threshold can be varied. This force mode is used to adjust the force applied so that the contact area is reached and maintained. Once the parameters are set and an optimal force curve is observed, this mode can be exited and data can be collected.[49]

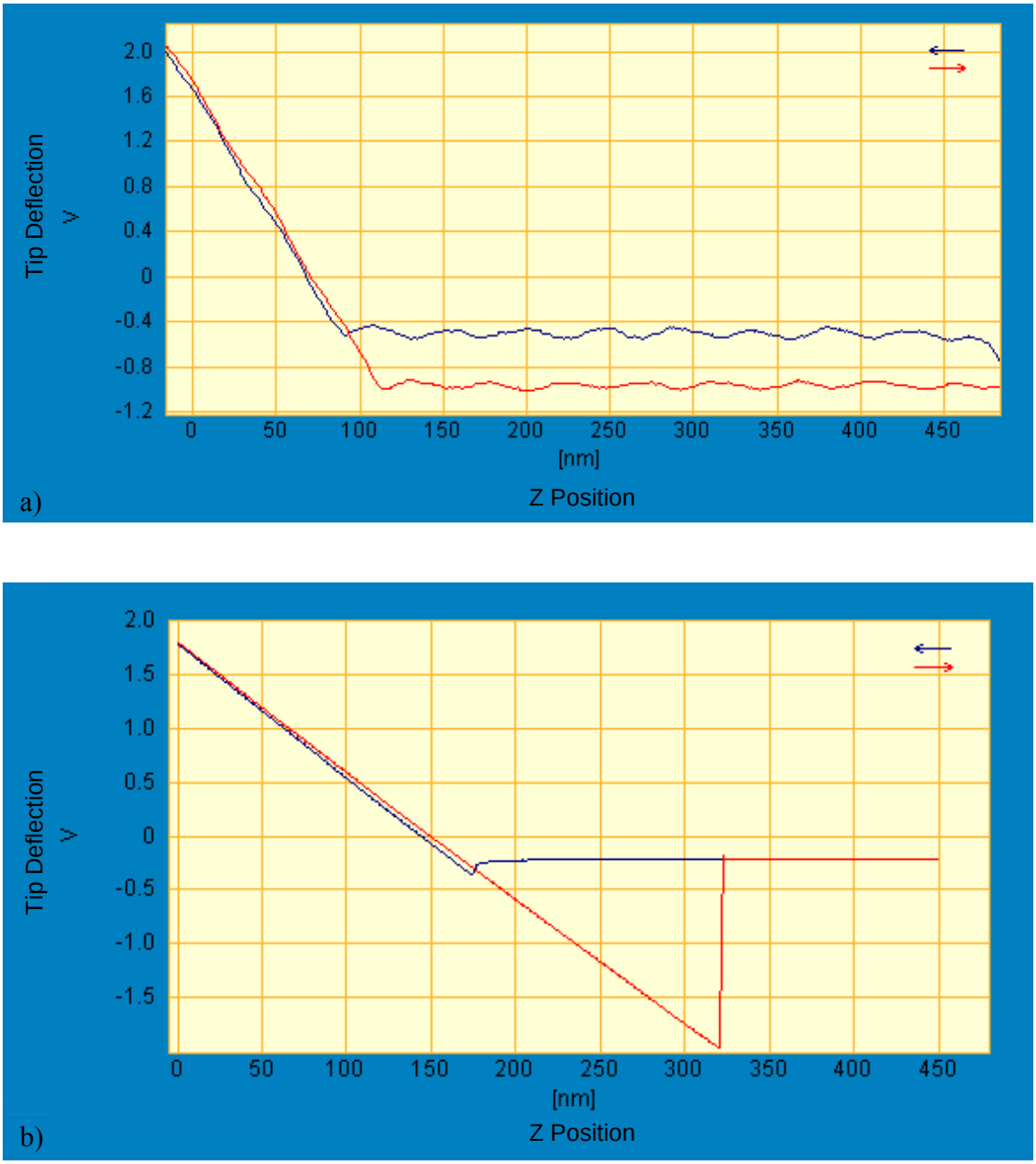

Figure 3-7: Force curve hysteresis (a) can be observed if the parameters used for AFM measurements are not optimized. A Force curve without hysteresis is shown in (b). The "snap off" line retraces the "snap in" line. NOTE: In these figures the blue line represents extension of the piezo crystal (the "snap in") and the red line represents the retraction of the piezo crystal (the "snap off").

3.4.2 Scan rate

The second parameter tested was scan rate. Scan rate and number of samples scanned per area affect the speed at which the tip moves vertically and horizontally. When the scan size is increased, the scan rate should be decreased to help prevent drift. However, when scanning the same spot, scan rate did not have an effect on repeatability except in viscous liquids, such as glycerol and ethylene glycol. **Figure 3-7**a shows hysteresis that occurs when the scan rate is too fast in certain liquids. **Figure 3-7**b shows what a force curve looks like without hysteresis. It has been shown that hysteresis can affect the "true" force between the tip and sample. A larger force is measured because the tip-sample distance is greater than what it would be if the retracting curve was able to trace the advancing line. Hysteresis can be minimized in most cases by slowing the scan rate. However, if a liquid is too viscous, it can be difficult to execute AFM measurements and observe true interactions between the sample and tip.

3.4.3 Force applied and contact area

Force applied and contact area, the next two parameters that were controlled, work together. In order to maintain reproducible tip-sample interaction, the contact area must be held constant throughout the experiments. Contact area impacts the depth the tip penetrates into a sample. At different depths the tip can make contact with other chemical moieties and this can cause variations in the forces. In Chapter 4, the elastic deformation observed in the JKR model demonstrates this effect. The amount of force applied to the tip will control the contact area. This relationship is seen in **Table** 4-1. The force applied can vary depending on the softness of a sample. Since mica and graphite were used in this study, a larger force could be applied. It is also important to be able to

maintain this constant force from initial measurement to the last measurement on a sample surface. Within the force imaging controls, a trigger mode can be set, either relative or absolute. Relative mode will maintain a constant force level defined by the trigger threshold parameter, even if there are shifts from the defined setpoint (**Figure 3-8**). The absolute mode does not allow for applied force to be held constant. This mode permits drift in the setpoint and the force applied (**Figure 3-8**). Relative mode was chosen for better control over the contact area, as it is dependent upon applied force. During setup, the force applied was kept constant between 10-12 nN. Section 3.6.3 will discuss how to calculate force applied during measurements.

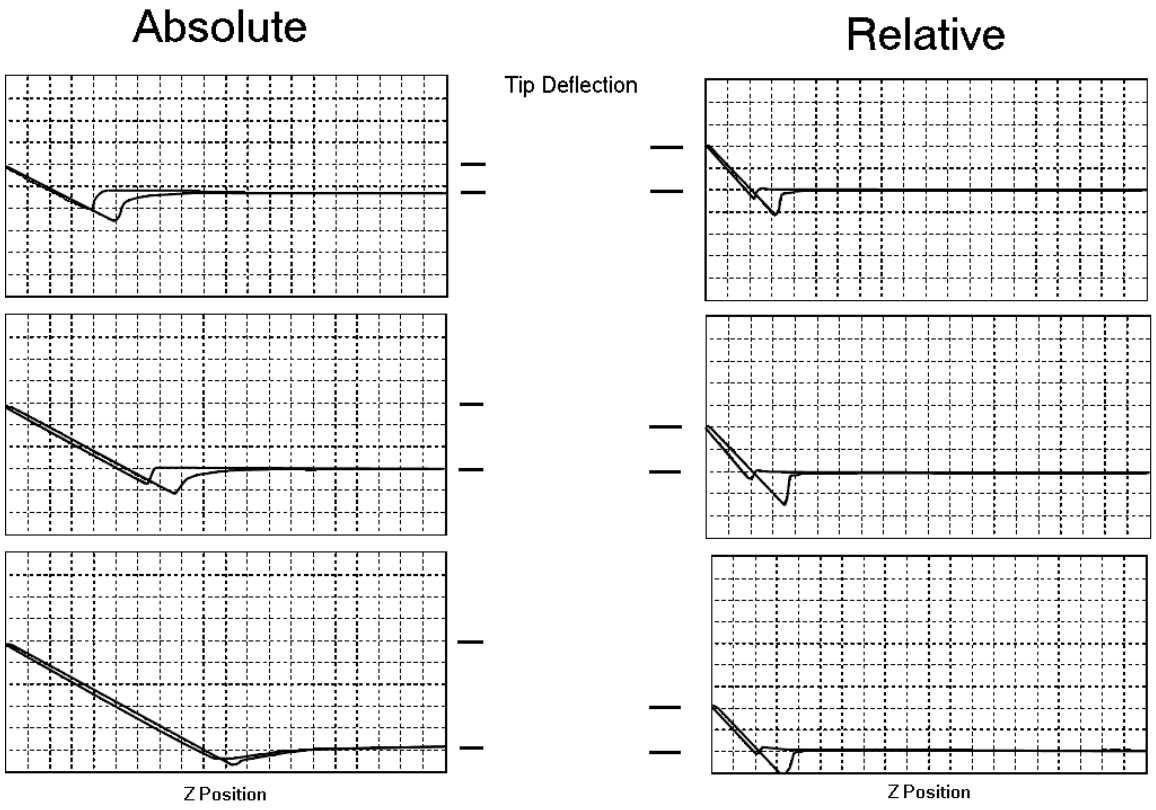

Figure 3-8: The two types of trigger mode used in AFM measurements are shown here. The plot shows the effect of drift on each of the trigger modes. Relative mode was chosen for the force measurements used in this study. This mode allows a constant force to be sustained, which helps to maintain the contact area, a critical parameter in achieving consistent AFM measurements.[49]

3.5 Statistical Analysis of AFM Measurements

The goal of this work is to measure the force of adhesion with the AFM and then calculate surface energy. However, before surface energy can be determined, the force data must be analyzed and understood. In all studies, multiple measurements on multiple samples must be made to get a reliable result. Because of the substantial amount of data generated, a statistical model was developed to help analyze the data and determine which parameters caused the most error. The following steps were taken in order to develop the statistical model:

1. Identify the variables that contribute to data collection. Determine a methodical approach to measure forces with selected surfaces and tips that will allow for a conclusion to be drawn.
2. Review data collection and decide on a statistical model that can incorporate the variables.
3. Test the model.

The overall goal of a statistical model is to compare the averages of forces between different samples and tips. In statistics, a way to look at this is with hypothesis testing. The hypotheses being considered are typically formulated in terms of the null (H_0) and alternative hypotheses (H_1). For this study there are three hypotheses being tested. These would be

Hypothesis 1:

H_0: The variance (s^2) between the locations, locations on each sample, locations between each tip are similar.

H_1: The variance (s^2) between the locations, locations on each sample, locations between each tip are not similar.

Hypothesis 2:

H_0: The variance (s^2) between each sample is similar.

H_1: The variance (s^2) between each sample is not similar.

Hypothesis 3:

H_0: The variance (s^2) between each tip is similar.

H_1: The variance (s^2) between each tip is not similar.

3.5.1 Identification of variables

The variables that may influence the force measurement are the samples (mica and graphite), the tips, and the locations on the samples, as further explained below.

- Tips – The tips are necessary for any AFM measurement. This is an important component for measuring forces, and therefore, can introduce large variability. Tips will have variable radii which affect the contact areas. Also, if the tip radius is not monitored, the user will not know when it becomes dull. A tip and cantilever can also pick up small particulates in the air or liquids or on the sample surface, which can change the tip characteristics and the resonance of the cantilever. Therefore, to find the influence of the tip variation on force measurements, it was thought that multiple tips should be tested. For statistical power with the model three tips per condition were used.

- Samples (mica and graphite) – Mica and graphite were chosen as the samples because they were inert to the solvents used in contact angle measurements, and the surfaces are homogeneous and relatively smooth. It was also important to evaluate the AFM's ability to measure multiple samples to find the variability among samples. For the statistical model to have power, two different sample surfaces were used with each tip.

- Locations – On a sample surface, many spots can be tested. It was already shown that the scan size should be 0 so that the data collected are meaningful. To have a trusted value at one spot, multiple measurements (256 force curves) can be obtained. Since these measurements are made in about a 5 to 15 nm^2 area, multiple areas on each sample should be measured to get an average surface energy for each sample. Thus, one force value will be obtained from the average of 256 force curves per spot. Sometimes these force curves will not have a normal distribution, but because of the large data set, the central limit theorem states that it can be assumed normal so that an average can be calculated. Therefore, to extract enough data on one sample surface and evaluate the effect location can have, ten locations were measured per sample.

The method for data collection described above is better illustrated in **Figure 3-9**. This figure shows for each condition, two samples, three tips, and ten locations per sample were measured. At the end of data collection, there should be 60 points of surface energy data that can be evaluated over three tips and two samples. **Table 3-1** helps to illustrate the final results and how they can be split up for a statistical analysis. The headings for each column are: sample (mica or graphite), tip, location, and SE (surface energy). In the

sample column there is either a 1 or 2, representing sample number 1 or sample number 2. In the tip column there is a 1, 2, or 3, representing tip 1, 2, or 3. In the location column there are 10 numbers illustrating the ten locations data was collected. And finally, in the last column, the average surface energy from 256 force curves at each of the locations. (To illustrate this, the data from mica in diiodomethane was used. The analysis of data will be discussed further in section 5.4.2.2. The presentation in this chapter is to help demonstrate the statistical model.)

Once the method to collect data was chosen and the variables were defined, a statistical model was selected. The repeated measures mixed model[50] was used because repeated measures are made on a sample surface and the model has fixed (locations) and random (sample, tip) variables. The model utilizes a repeated measures analysis of variance (ANOVA) to calculate the F-value, which allows the user to accept or reject the null hypothesis mentioned above that the variances between the tips, samples, and location is similar.

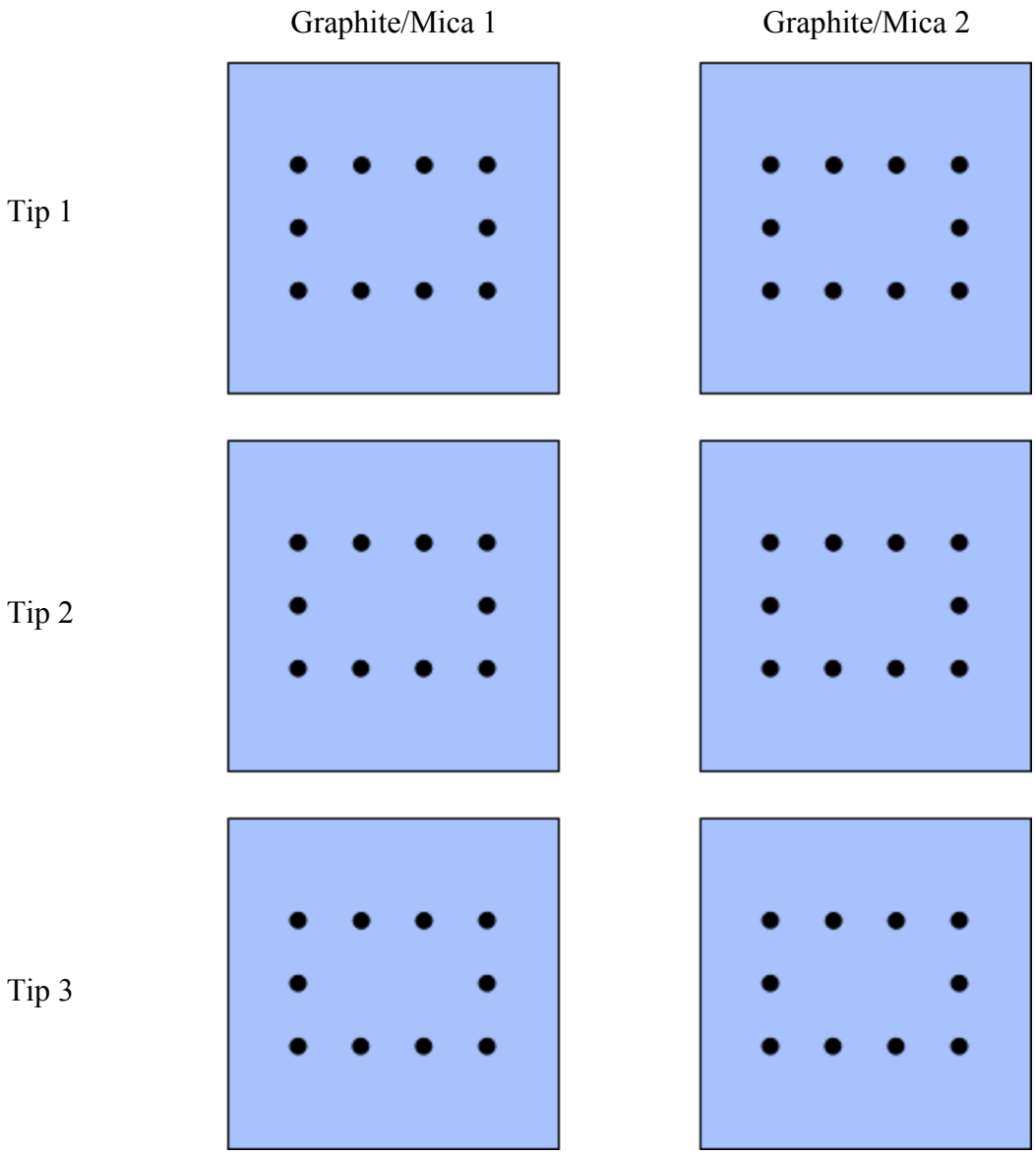

Figure 3-9: Diagram of the number of mica or graphite samples, tips, and locations evaluated using the AFM. This approach was used for all environmental conditions and solvents.

Table 3-1: Statistical table showing the combined sample, tips, location, and surface energy. This table is formed because of the data collection method shown in **Figure 3-9**.

Sample	Tip	Location	Force
1	1	1	2.1
1	1	2	2.0
1	1	3	2.1
1	1	4	2.0
1	1	5	2.1
1	1	6	2.1
1	1	7	2.3
1	1	8	2.1
1	1	9	2.2
1	1	10	2.1
2	1	1	2.1
2	1	2	2.3
2	1	3	2.1
2	1	4	2.0
2	1	5	2.2
2	1	6	2.2
2	1	7	2.1
2	1	8	2.1
2	1	9	1.9
2	1	10	1.9
1	2	1	2.0
1	2	2	2.2
1	2	3	2.0
1	2	4	2.0
1	2	5	2.1
1	2	6	2.0
1	2	7	2.2
1	2	8	2.3
1	2	9	2.3
1	2	10	2.2
2	2	1	2.3
2	2	2	2.2
2	2	3	2.0
2	2	4	2.0
2	2	5	2.4
2	2	6	2.4
2	2	7	2.3
2	2	8	2.3
2	2	9	2.3
2	2	10	2.3
1	3	1	2.18
1	3	2	2.05
1	3	3	2.04
1	3	4	1.95
1	3	5	1.84
1	3	6	2.06
1	3	7	1.89
1	3	8	1.95
1	3	9	2.02
1	3	10	1.93
2	3	1	2.1
2	3	2	2.1
2	3	3	2.1
2	3	4	2.1
2	3	5	2.1
2	3	6	2.1
2	3	7	2.1
2	3	8	2.1
2	3	9	2.0
2	3	10	2.1

For the statistical analysis, JMP (version 7, SAS Institute Inc., Cary, NC) and SAS (version 6.11, SAS Institute Inc., Cary, NC) were used to calculate the F-value and determine if there were differences among measurements. The output from SAS and JMP are shown in **Table 3-2a and b** and **Table 3-2c**, respectively. The SAS output is a typical ANOVA with the sum of squares, mean squared, F-values, and the corresponding p values from the F distribution tables. From the SAS tables a decision can be made whether to accept or reject the null hypothesis and if the surface energy data can be combined. The p values are the probability of obtaining an experimental result as different or more different than the expected result by chance alone. The p-value in hypothesis testing is the α level, or significance level, at which one could accept or reject the null hypothesis. The default α level is 0.05 and the null hypothesis is accepted when $p>0.05$ and rejected when $p<0.05$. The data presented **Table 3-2a and b** shows the null hypothesis could be accepted.

SAS **Table 3-2a** is the statistical analysis for within subjects, which is the variability of the locations. If there is variability within the locations between tips or samples, then the data set of one or all samples is statistically different. When the data is statistically different, taking an average of the combined results will lead to an erroneous conclusion. Instead, the experimental set up for measuring forces will have to be evaluated and retested. An example of this will be discussed in Chapter 6.

SAS **Table 3-2b** is the statistical analysis between subject effects. The table shows the comparison of all the samples and tips and evaluates the interaction between the samples and tips. If there are statistical differences between mica or tips, combining the data and calculating the average will result in an invalid conclusion. It would be better to present

the data separately. If the data is found to be statistically significant, then the repeated measures mixed model would have found limitations in the AFM. These limitations could be caused by the sample of interest or the conditions used to measure the forces.

If there are not statistical differences in location, mica, and tips, the JMP software is able to evaluate which component contributes to the most variation, **Table 3-2c**. These tables are used throughout Chapter 5 and 6 to show the AFM's capability in making consistent force of adhesion measurements and its challenges. The software is limited though because it yields negative numbers when a variable or interaction being tested has no contribution to the variability of the measurements. In these scenarios, the negative numbers were made zero and the percent contributions of the others were recalculated.

For the example in **Table 3-2**, the null hypothesis was accepted, the data set was combined and an average force, work, and surface energy value could be determined. The JMP data shows that the largest variation comes from the residual error of the measurements. Therefore, there are no apparent problems in evaluating mica-diiodomethane with the AFM.

Table 3-2: Mixed model statistics for mica AFM measurements with diiodomethane. a) Repeated measures ANOVA for within subject effects, b) repeated measures ANOVA for between subjects, and c) the variable that demonstrates the largest percentage of variance for mica – diiodomethane AFM measurements.

a)

	Degrees of Freedom	Sum of Square	Mean Square	F Value	P
Location	9	16.1	1.8	1.48	0.23
Location*Mica	9	12.7	1.4	1.17	0.37
Location*Tip	18	34.7	1.9	1.60	0.16
Error	18	21.7	1.2	-	-

b)

	Degrees of Freedom	Sum of Square	Mean Square	F Value	P
Mica	1	12.3	12.3	3.27	0.21
Tip	2	0.4	0.2	0.06	0.95
Error	2	7.5	3.8	-	-

c)

Variable	% of the Total	% Truncated
Mica	15.3	14.0
Tip	-9.5	0.0
Mica*Tip	12.0	10.9
Mica*Tip*Location (Error)	82.3	75.1
Total	15.3	14.0

3.6 AFM Methodology

To use the AFM to investigate surface energy, force measurements were made in ambient, controlled relative humidity (RH), and in the same liquids that were used in contact angle measurements. Before discussing how the AFM can be used to evaluate surface energy, this section will provide the details of the methods used to obtain forces.

3.6.1 Spring constant

Two methods were presented in Section 3.3. However, the goal was to have a nondestructive method that could be used on each tip. Therefore, to employ the thermal method as the main technique for measuring the spring constant of the AFM, studies were done using the added mass method and then compared to results obtained from the thermal method.

3.6.1.1 Added mass method

Resonance frequencies of ten silicon nitride cantilevers (Veeco, Camarillo, CA), specifically 200μm narrow, were measured with a Nanoscope MultiMode AFM (Veeco, Santa Barbara, CA) before and after a tungsten sphere was added, **Figure 3-10**.

The tungsten sphere was added using an Axiovert S100 (Zeiss, Thornwood, NY) microscope. To get the tungsten sphere to adhere to the cantilever, epoxy was first placed on the same side as the probe. Using a needle attached to a micromanipulator (Eppendorf, Westbury, NY), a tungsten sphere was then added behind the probe,

Figure 3-11.

Scanning electron microscopy (SEM) images were taken of each sample using a Hitachi S-4300 FE-SEM (Hitachi, Pleasanton, CA). The samples were coated with gold prior to

imaging to reduce charging and destruction of the sample. The electron beam was set to 5kV and the current supplied was maintained around 20mA. An SEM image of the tungsten sphere is shown in **Figure 3-12**.

The initial resonance frequency measured for the 200 μm cantilevers averaged around 16 kHz, shown in **Figure 3-10**. The nominal frequency reported by Veeco for these types of cantilevers is 18 kHz. The measured values of all ten tips are reported in **Table 3-3**. Once the sphere was added, the resonance frequencies decreased as expected (**Table 3-3)**. A typical before and after image of the resonance frequencies is shown in **Figure 3-10.**

Once the initial and final resonance frequencies were measured, the radii of the attached spheres were measured with the SEM, shown in **Table 3-3**. The average radius of the tungsten sphere was 9.2μm. **Figure 3-12** shows a standard tungsten sphere as seen using the SEM. Initially, the tips were not coated with gold, and the electron beam of the SEM was set at 20kV. These settings destroyed the samples and caused a significant amount of charging. Therefore, the rest of the samples were coated and lower beam strength was used.

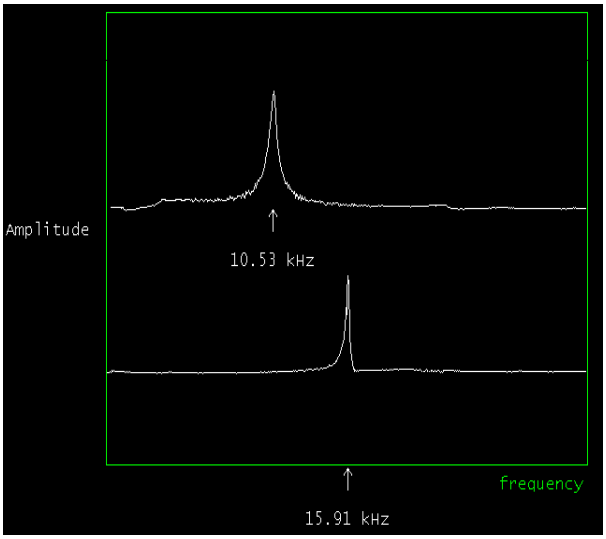

Figure 3-10: Resonance frequencies of silicon nitride cantilevers before (15.91 kHz) and after (10.53 kHz) a tungsten sphere is added.

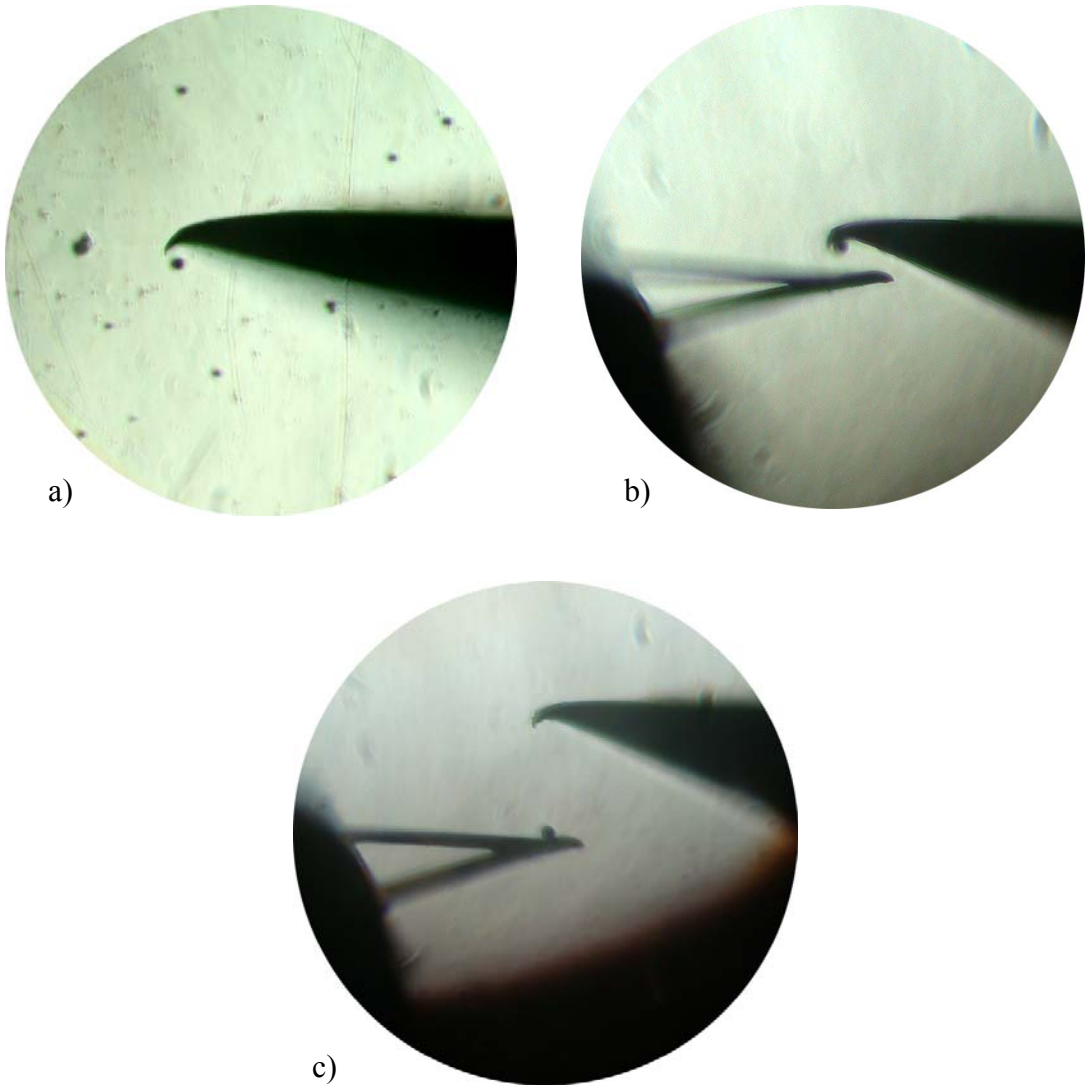

Figure 3-11: Addition of tungsten sphere. After the epoxy is added to the back of the cantilever, a) the sphere is picked up by the needle, b) the needle is moved over the cantilever, and c) then the tungsten sphere is placed on the cantilever and the needle is retracted.

Table 3-3: Measured resonance frequencies, tungsten radii, and spring constant of ten silicon nitride cantilevers using the added mass method.

Sample Number	Initial Resonance Frequency (kHz)	Resonance Frequency After Added Sphere (kHz)	Radius (μm)	k (N/m)
1	15.88	9.95	10.5	0.06
2	17.54	11.20	8.8	0.05
3	15.91	11.25	8.9	0.06
4	17.44	8.91	12.0	0.06
5	15.88	11.09	10.2	0.08
6	15.96	9.60	10.6	0.05
7	16.05	10.70	9.70	0.06
8	15.97	8.68	12.2	0.06
9	15.91	9.33	11.3	0.06
10	15.91	10.53	9.20	0.06
Average	16.25	10.12	10.34	0.06
Standard Deviation	0.66	0.96	1.22	0.01

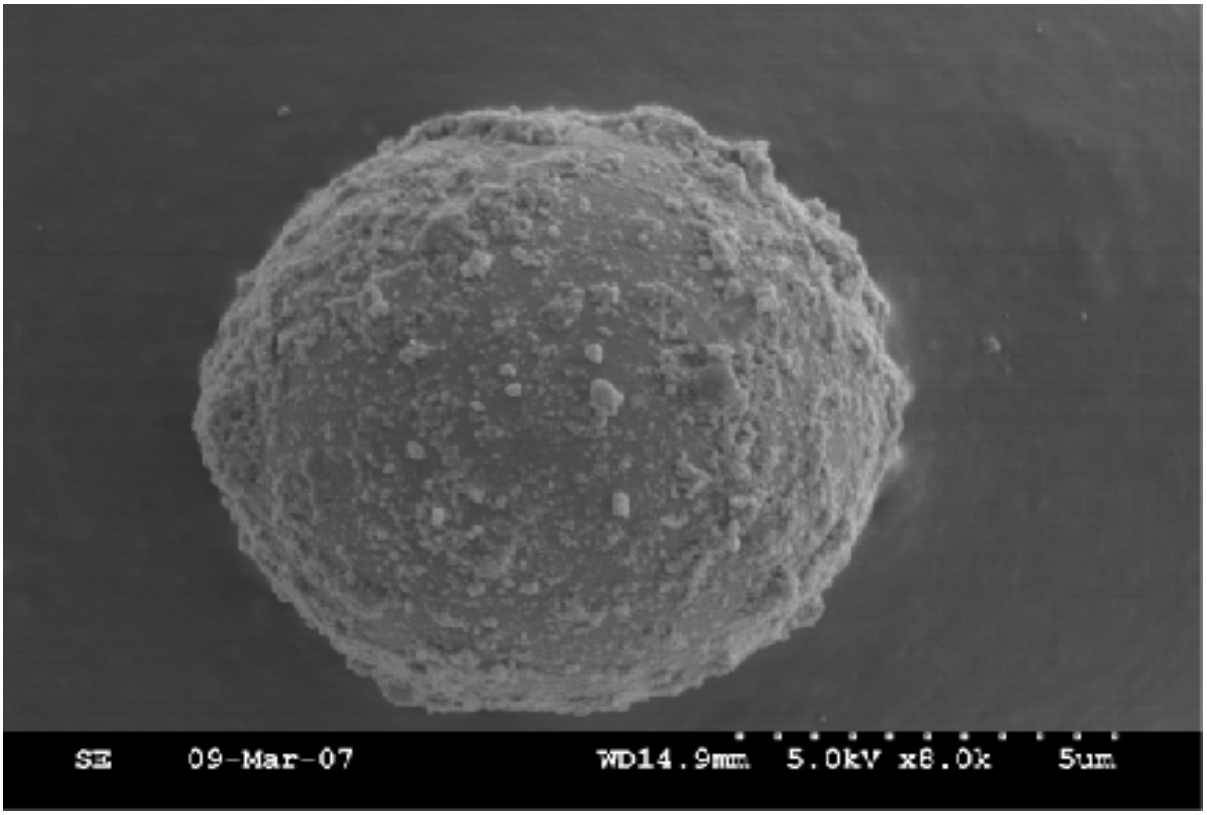

Figure 3-12: SEM image of a tungsten sphere added to an AFM cantilever.

3.6.1.2 Thermal Method

Before thermal vibration data could be collected, modifications had to be made to the AFM MultiMode circuit board and controller. A cable was attached to pin 1 at U1 of the analog to digital integrated circuit of the AFM, **Figure 3-13**. The other end of the cable was attached to the controller analog channel 1. This connection allowed the signal to go directly to the main controller and bypass electronic filters that manipulate the input signal. The raw data from U1 is the vertical deflection (A-B), which outputs thermal vertical vibrations. Once the set up was complete, instructions from Veeco were followed to collect thermal vibrations. To determine the spring constant of a cantilever in air or in a liquid:

1) Configure software for contact mode and engage microscope on a hard sample surface. Mica (Ted Pella, Inc., Redding, CA) was used as the sample surface. (NOTE: It is important that the laser position is not adjusted after this step.)
2) Once engaged, switch mode to Advanced Force Mode and set the following parameters
    a. Deflection setpoint – 0 Volts

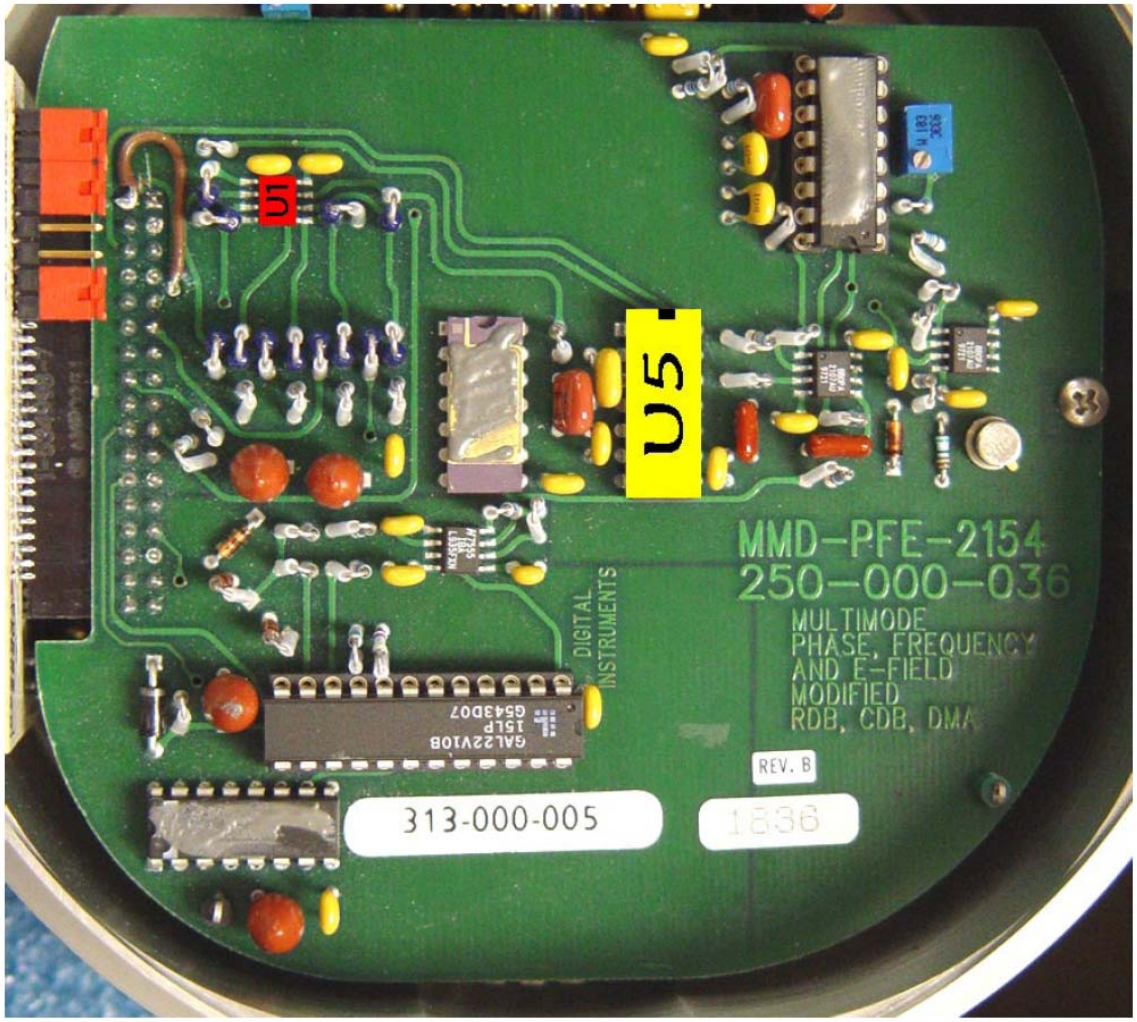

Figure 3-13: Electronics board under the AFM stage that is manipulated to bypass filters and measure raw thermal vibration to determine the cantilevers spring constant.

b. Ramp size – 500 nm

c. Trigger mode – Off

d. Input signal – Channel 1 (analog dial receiving raw data from U1)

e. Data scale – 20 Volts

f. Data center – 0 Volts

3) Adjust Z scan start until a force curve with 2-3 V of deflection relative to the non-contact deflection value is obtained, **Figure 3-14a**.

4) Capture five forces and then switch back to image mode and disengage the probe.

5) Go to the offline mode and view the force curves previously captured individually to obtain the "Sensitivity".

   a. View → Graph → Sensitivity

   b. Move the markers on the extend curve to the "contact region" of the force curve, **Figure 3-14b**, so there is 1.5 – 2 V of deflection between them.

   c. Record the average of the five force curves for **Step 7a**.

6) Go back to real time mode and set the following parameters:

   a. Scan size = 0.01 nm

   b. Scan rate = 61 Hz

   c. Samples per line = 512

   d. Lines = 512

e. Deflection setpoint = 0V

f. Channel 1 = input 1 (all other channels set to off)

g. Real time planefit = none

h. Offline planefit = none

i. Deflection setpoint = 0 V

7) Go to Microscope → Calibrate → Detector

a. Input1 Sens – Average value from **Step 5c** (including units nm/V).

8) Ensure the tip is above the surface by withdrawing the tip 4 times. Force a false engagement of the tip. The data will output quickly. Make sure the gains are set to zero for I and P and that the Z center position is in the middle. Capture three images and then withdraw the tip.

9) Switch to offline mode and double click on one of the files previously captured.

10) Go to Utility → ASCII Export and set:

a. Format = ASCII

b. Header = No

c. Image 1 units = nm

d. Number of columns = 1

e. Set filename and path desired to save

11) Each file was saved as a text file and imported into Matlab for further analysis.

a)

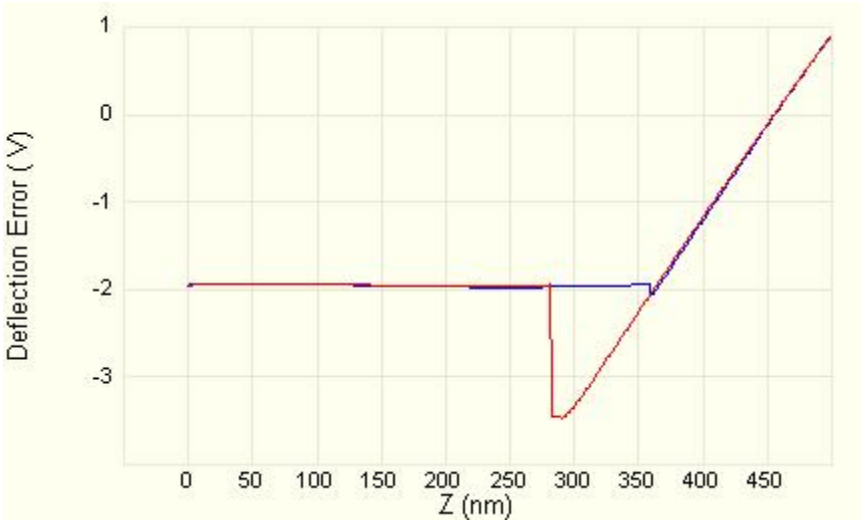

b)

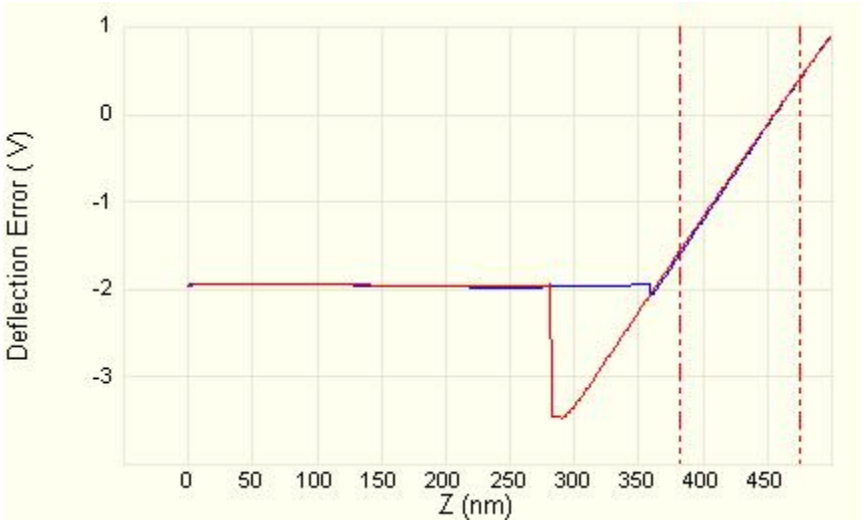

Figure 3-14: To measure the Z sensitivity for the thermal analysis, a) five force curves with a 2-3V deflection value in the non-contact region are generated, and b) the offline mode is used to determine the value.

The Matlab algorithm used to calculated the spring constant was designed to automatically generate a report each time it was run. Please refer to **Appendix 1** for an example report and **Appendix 2** for the code. The algorithm consisted of two main functions, file input and spring constant calculation. It broke down into nine sub-functions, which will each be addressed separately in the following discussion.

1) Import the tip file into a single vector (1 x 262144). The dimensions of this vector come from the number of samples per line (512) and number of lines (512). Each AFM measurement yields one thermal noise measurement.

2) To improve the precision of the Fourier Transform calculation, reshape the vector into overlapping blocks of 4096.

3) Compute the Fourier Transform from each row of the reshaped matrix.

4) Compute the complex conjugate of the new matrix to keep real numbers and eliminate imaginary numbers.

5) Compute the average of the rows to obtain a single vector (1 x 4096)

6) Smooth the output as necessary with either a moving boxcar, a cubic spline, or a 5-point Savitzky-Golay smoothing filter. The cubic spline resulted in the most appropriate and reproducible spring constant calculation.

7) Integrate the area under the smoothed resonant peak.

8) Calculate the spring constant k according to $k = k_b*T/A$, where k_b is the Boltzmann constant, T is the temperature in degrees Kelvin, and A is the peak area.

9) Output the results of the spring constant calculation and plot the resonant peak to be sure the correct area was selected.

Calibration of the spring constant was done on eight cantilevers from the same wafer as the cantilevers used in the added mass study.

With the development of a method to continually monitor the spring constant of the cantilever and the deflection acquired from the AFM measurements, the force of adhesion can be calculated using Hooke's Law. Since the primary focus of this study was to determine surface energy using the AFM measurements, the next step was to compute the work of adhesion. Surface energy was calculated after determining the force and work of adhesion.

3.6.2 Tip radius

As with measuring the spring constant, the goal for determining tip radii was to have a method for initial and repeated evaluation. Since the SEM images require a gold coating and will destroy the tip, three tips were evaluated using the blind reconstruction method. The sample used for the blind reconstruction was a tip tester (CSEM, Neuchâtel, Switzerland). The scans were made in a 1000 X 1000 nm area at a rate of 1.97 Hz. The relative trigger mode was employed, and the constant maximum loading force of 8-10 nN was maintained. The scans were then analyzed in the SPIP software (Nanoscience Instruments, Inc., Phoenix, AZ).

SEM images were taken of these tips and two unused tips with a Hitachi S-4300 FE-SEM (Hitachi, Pleasanton, CA). Two unused tips were imaged under the SEM only to make sure scanning did not affect the initial tip radius. Thus, these two tips were a baseline for viewing and measuring the tip. The samples were coated with gold prior to imaging to reduce charging and destruction of the sample. The electron beam was set to 3kV and the current supplied was maintained at 10mA. The working distance was 15mm and the

condenser lens was set to 8. Since the SPIP software works based on a deconvolution of the AFM images, comparison of the SPIP created image, **Figure 3-15b**, and the SEM image, **Figure 3-15a**, became necessary to establish consistent parameters. Images from SPIP were overlaid on the SEM images for each tip, **Figure 3-15c**, and a tip radius was obtained, **Table 3-4**.

a)

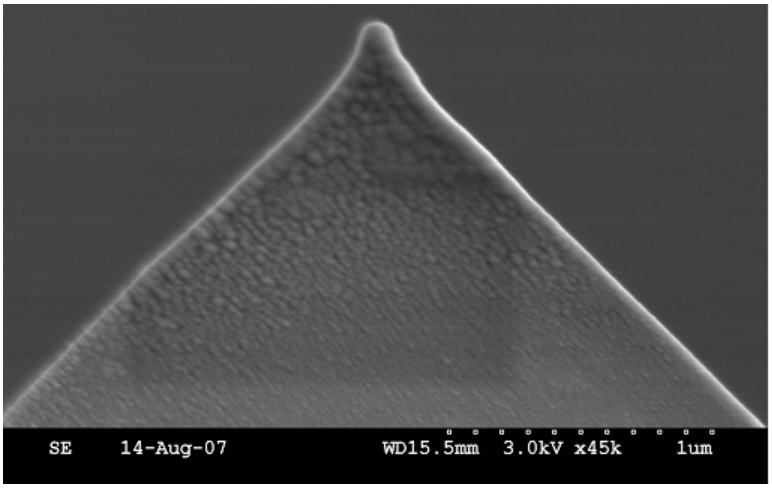

b)

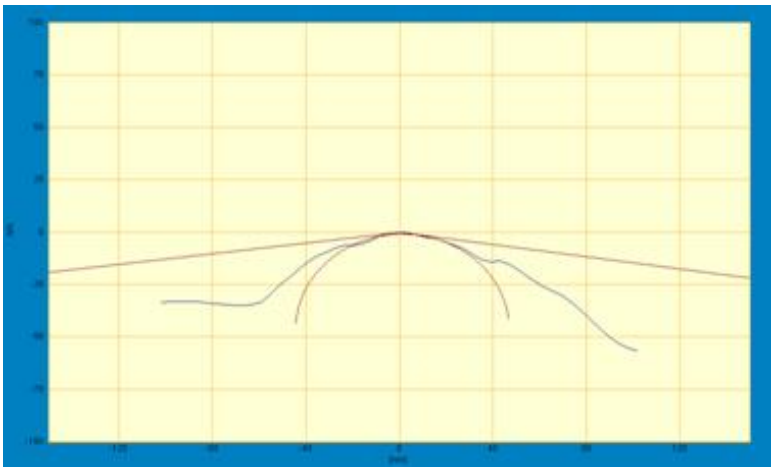

c)

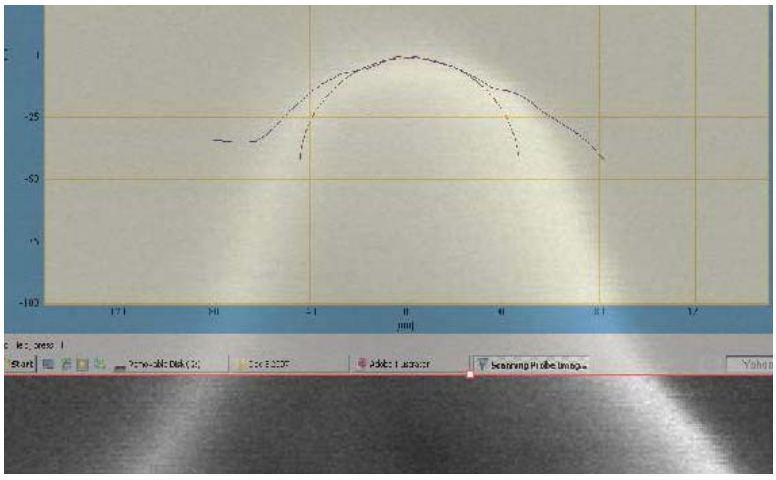

Figure 3-15: Determining tip radius with **a)** SEM image of a 200µm silicon nitride tip, **b)** SPIP image of the apex of the tip, and **c)** the image overlay, a combination of **a** and **b**.

Table 3-4: AFM tip radii measured from blind reconstruction and compared with SEM images. The first two tips were only imaged using the SEM as a baseline.

Tip	SEM Tip Radius (nm)	Blind Reconstruction Tip Radius (nm)
1	48	N/A
2	52	N/A
3	47	42
4	46	38
5	48	40

The manufacturer of the silicon nitride tip reports a maximum tip radius of 40 nm. The results from the SEM images illustrate the method does overestimate the tip radius. The results from the blind reconstruction varied depending on the settings input for the blind reconstruction in the SPIP. If there were not enough iterations, the reconstruction would be smaller than the SEM image, and with too many iterations, the reconstructed tip is larger than the SEM image. Therefore, creating the overlaid image helped provide guidance for the required input. Although it was not possible to image each tip used over all the AFM experiments, the SEM image in **Figure 3-15a** was consistently used as a reference for overlaying all blind reconstruction images produced by SPIP. The tip radius was checked after a standard set of measurements. Once the tip radius was 10 nm larger than the initial measurement, the tip was discarded and a new tip was characterized.

3.6.3 AFM scanning parameters

There were four parameters identified as critical to control during force measurements. The following was done to control scan size, scan rate, force applied, and contact area.

The scan size of each point was 0 nm. At each point 256 force curves were collected and then the tip was moved to a different spot on the sample, as described in Section 3.5. The scan rate can be set at 5 to 8 Hz when measuring forces in vapor and non-viscous liquids. In viscous liquids, like ethylene glycol, the scan rate must be reduced to 3 Hz or smaller.

The applied force can be calculated from the graph shown in Figure 5.4 The spring constant and Δz (from contact with the surface to the piezo crystal beginning retraction) shown in **Figure 3-16** need to be found. These values are used by the on-line control program to calculate the force.

$F = k * \Delta z$

Δz = number of divisions horizontally * x scale * Z piezo sensitivity.

The value can be determined more precisely with the SPIP software, but a wide range of 10-12nN allowed for flexibility in estimating the applied force in-line following these guidelines.

1. Determine the *Z piezo sensitivity*. The instructions to do so were covered in Section 3.3, under the methodology for determining spring constant with the thermal method.
2. The x scale is the *Z Position* and has (V/div) as the units of measure.
3. The number of divisions is counted by starting at the very left edge of the graph and counting over to the start of the triangle.

Once these parameters are determined, the force applied can be calculated. If the force calculated was not between 10 – 12 nN, then the *trigger threshold* in *the Z scan controls* box will have to be changed until it is. The *trigger threshold* allows for increase and decrease in force applied by shifting the force curve right and left.

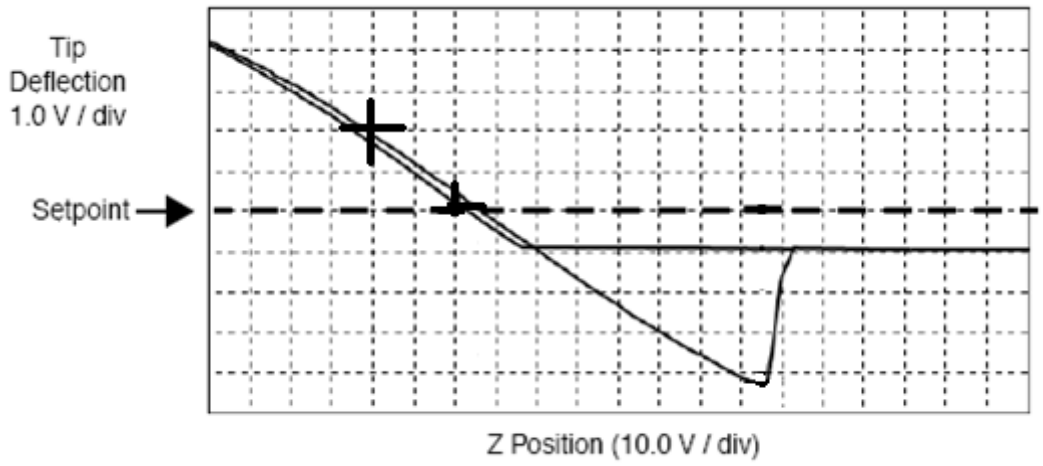

Figure 3-16: The force curve and parameters used to determine the force applied.[49] The horizontal divisions are counted until the first marked (+). It is important to estimate the number of divisions as close as possible noting the best calculation will be obtained from the SPIP software.

3.6.4 AFM measurements

In order to evaluate the AFM's potential use for studying surface energetics, the same samples used in the contact angle studies, Section 2.3, were used for the AFM studies. The conditions initially tested were in ambient environment without any control of moisture content to determine solid-vapor surface energy. Next, the vapor measurements were repeated, but in a controlled humidity environment. A near zero percent humidity was achieved by purging and environmental chamber with nitrogen gas. Last, the solid-liquid surface energy was determined using the same liquids that were used in the contact angle measurements (water, diiodomethane, ethylene glycol, and formamide). Since there were variations in the contact angles using hydrated liquids, the hygroscopic liquids were dried before measuring forces. All force curves are then analyzed using SPIP software (Nanoscience Instruments, Inc., Phoenix, AZ).

3.6.4.1 Ambient humidity measurements

The effects of humidity on the pull-off force has been previously studied.[51-53] It has been shown that stiff cantilevers can lessen the impact humidity has on the force measurements. However, if a flexible cantilever is used, which is best for sensitivity, then humidity has a major impact on the force measurements. The more humidity present the larger the spread or range in the force of adhesion. Therefore, if a flexible cantilever is used, the environmental conditions have to be controlled. In this study, it was important to compare the difference between ambient and controlled conditions. Also the contact angle measurements were made in ambient conditions, and therefore could be more comparable to AFM results in ambient environment. The ambient

environmental conditions for the three tips and two samples of mica and graphite were measured at 23-26ºC and 59-62% relative humidity (RH) measured with a hand held hygrometer. The tip holder for measurements in vapor is shown in **Figure 3-17**.

3.6.4.2 Controlled relative humidity measurements

After the forces were measured in ambient conditions, three new AFM tips and the two mica samples were then placed in a desiccator. Air was pulled out of the desiccator with a vacuum pump. The samples were held in the desiccator for 24 hours. The samples were then transferred individually to the AFM and the measurements were made in an environmental chamber with less than 10% relative humidity. To create low humidity in the environmental chamber, nitrogen gas was purged for two hours, while monitoring the relative humidity with a hygrometer. The AFM set up with the environmental chamber is shown in **Figure 3-18**.

Figure 3-17: Bottom side of a tip holder for vapor measurements. The gold piece holds the cantilever.

Figure 3-18: MultiMode AFM with an environmental chamber.

3.6.4.2 Liquid measurements

Force measurements with mica and graphite samples were made in water, diiodomethane, ethylene glycol, and formamide using a fluid cell, **Figure 3-19**. The fluid is injected through a syringe and contained in an o-ring, **Figure 3-20**. The fluid was injected, but because of interactions that can happen between the liquid and the surface, ten minutes was given to allow for a so-called "equilibrium". It was observed that measurements were less repeatable right after the liquid was injected. Thus, 10 minutes was allowed so that the "equilibrium" between the liquid and the sample surface could be attained. The measurements from formamide and ethylene glycol were made after the solvents had been dried and with the rehydrated solvents, as with contact angle measurements in Chapter 2.

In Chapter 6, additive solutions will be needed to measure forces on crystalline surfaces. The methodology will be discussed further in that chapter, but it needs to be highlighted that these types of solutions can be used with the AFM but could not be used with contact angle measurements. The set up for the additive solutions is the same. The fluid cell and syringe are used to introduce the liquid to the system. It is important to ensure the additive has completely dissolved in the solvent before use. Thus, when an aliquot is taken for injection, the concentration of the solution will be known.

Figure 3-19: Fluid cell used to measure forces with solvents and solutions.

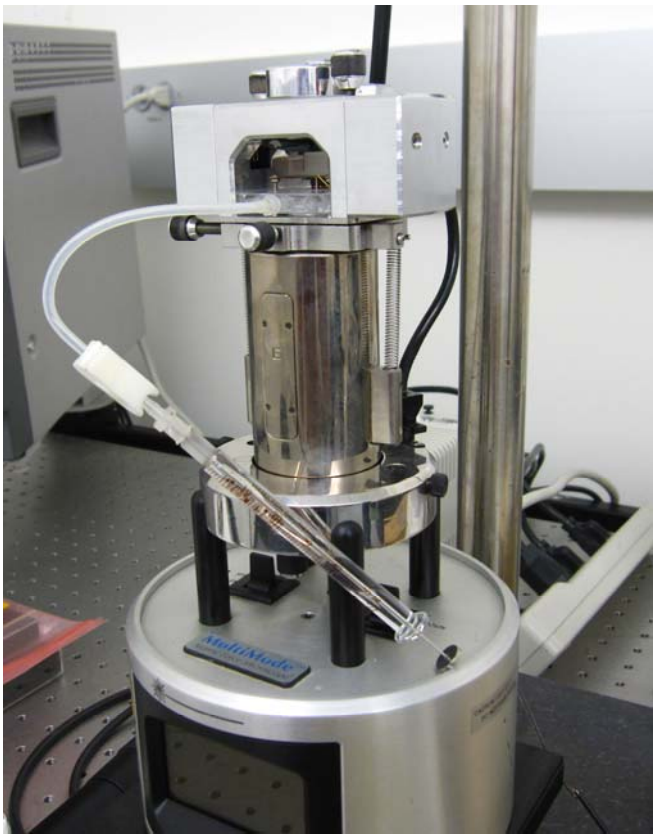

Figure 3-20: MultiMode AFM with the fluid cell and syringe to inject liquids.

3.7 Summary

The goal of this work is to use the AFM to investigate surface energy. This chapter presented the components and functions of the AFM and the methodology developed for force measurements with the AFM. The most important development in this chapter was establishing methods for measuring the cantilever spring constant and the tip radius. A scanning methodology was developed and a statistical model was chosen that will allow for comparison and error analysis.

Tip characterization is an important step for measuring forces and calculating surface energy. To calculate the force of adhesion from Hooke's Law, deflection and the spring constant are needed. The deflection is obtained from AFM data and then the forces can be determined in SPIP. To obtain an accurate force, a spring constant needs to be entered into the software. The spring constant has been determined using several methods; however, the goal was to be able to measure the spring constant of each cantilever. The value provided from the manufacturer and the destructive method was determined to be unsuitable. The literature for the thermal method was reviewed and modifications were made on the microscope to collect the data. A Matlab code was developed to analyze the AFM data. The calculated spring constant from the thermal method was successfully compared to the "gold standard" added mass method, allowing continued use of the thermal method for determining the spring constant of every tip.

Tip radius will be a required parameter in Chapter 4 to finally calculate surface energy, and therefore, a nondestructive method was needed to evaluate the radius of each tip. The blind reconstruction literature was reviewed and then successfully implemented as

compared to the manufacturer's value and SEM images. Thus, a method was developed to continually monitor the tip radius.

The scanning methodology for force measurements in vapor and in liquids was discussed and will be expanded upon in Chapters 5 and 6 to collect AFM data. The scan size, scan rate, and applied force parameters were determined for AFM measurements in vapor and in liquid. Finally, a repeated measures mixed model was implemented for statistical analysis of the AFM data. The statistical model will allow for comparison between samples and tips and show what contributions cause significant error.

The successful completion of the literature review and the AFM methodology of this chapter set the stage for taking force measurements from the AFM and calculating surface energy. To do this the next chapter will investigate various models with the goal of determining surface energy.

Chapter 4 – AFM Math Models

The previous chapter evaluated the methodology of the AFM to measure forces. However, the overall goal is to evaluate the AFM's capability to investigate surface energy. Therefore, models had to be developed to transform the force data into surface energy. Currently, there is not an experimental method to measure surface energy directly; as a result, all techniques require models. The model development for the AFM force data is presented in this chapter

4.1 Contact Mechanics

In contact angle measurements, the spreading of a liquid over a surface to reach equilibrium is dominated by the minimization of surface free energy. When two solids are in contact, reaching the equilibrium state depends on the distribution of elastic forces. Mechanical work must be expended to overcome the adhesive forces keeping two separate bodies in contact. This work is involved in the creation of a new surface. Hertz was the first to observe the contact between two smooth elastic bodies. When no surface forces act, the contact area for two spheres with radius R_1 and R_2 pressed together under load P is given by[54]

$$a_0^3 = \frac{3}{4}\pi(k_1 + k_2)\frac{R_1 R_2}{R_1 + R_2}P \qquad \textbf{4.1}$$

where k_1 and k_2 are the elastic constants of the material of the spheres and k_1 and k_2 are defined by

$$k_1 = \frac{1-\nu_1^2}{\pi E_1} \text{ and } k_2 = \frac{1-\nu_2^2}{\pi E_2} \quad \textbf{4.2}$$

where ν is the Poisson ratio and E is the Young's modulus of each material. Typically, Equation 3.7 is written in a simplified form

$$a_0^3 = \frac{RP}{K} \quad \textbf{4.3}$$

where $R=R_1R_2/(R_1+R_2)$ and $K=4/3\pi(k_1+k_2)$. To verify this theory, Hertz used an optical microscope to measure the contact between two glass spheres. Hertz showed that both the size and shape of the zone of contact followed from the elastic deformation of the two glass spheres. Later, however, there were experimental contradictions observed to the Hertzian theory. At low loads, the contact area was considerably larger than what Hertz had predicted. Strong adhesion was observed and as the load was reduced toward zero, a constant finite value of contact area was observed. This suggested that attractive surface forces became important as the load was reduced towards zero, but at high loads Hertz theory still held.[54]

Two contact mechanics models, Johnson-Kendall-Roberts (JKR)[54] and Deryaguin-Muller-Toporov (DMT),[55] were developed to evaluate this relationship. The major difference between the two models is the area each takes into account the energy of molecular attraction. The JKR model takes into account what happens inside the area of contact and DMT considers outside of the contact area. Therefore, the differences observed in the applied force, contact radius, and deformation are due to the role adhesion plays in the system. **Table** 4-1 summarizes the relationships for each model

of the contact radius, deformation of the sample, and force of adhesion. Using the tip radius, R, (determined by blind reconstruction in Section 3.6.2) the work can be calculated with the adhesion forces determined from AFM measurements.[32, 54, 55] Then, contact radius can be calculated as a function of the reduced Young's modulus, K, which is

$$\frac{1}{K} = \frac{3}{4}\left(\frac{1-v_s^2}{E_s} + \frac{1-v_t^2}{E_t}\right) \qquad \textbf{4.4}$$

where v_t, E_t, v_s, and E_s are the Poisson's ratio and Young's modulus of the tip and the sample respectively. Lastly the deformation of the sample can be determined.

Figure 4-1a, shows the interaction between completely rigid particles and **Figure 4-1b,** shows particles that deform when they come into contact. JKR showed that the attractive surface forces pull the two surfaces together giving rise to a finite contact area, even under zero external load. When surface forces are not observed (W=0), the JKR and DMT contact area equations revert back to the simple Hertz equation (**4.3**). For the JKR model when the applied load is made negative, the contact radius decreases. Thus, for a solution to be obtained

$$6W\pi RP \le \left(3\pi RW\right)^2,$$

$$P \ge -\frac{3}{2}\pi RW \qquad \textbf{4.5}$$

and separation of the sphere will occur when

$$P = -\frac{3}{2}\pi RW \qquad \textbf{4.6}$$

Thus, equation **4.6** illustrates that the applied force does not affect force of adhesion. It only affects the contact area that the AFM tip will observe, as discussed in Chapter 3. However, because of the sensitivity of the AFM and its capability to resolve sub-angstrom, force applied should be monitored. This will help control contact area so the load does not push the tip into several different chemical moieties.

Similarly for the DMT model, a solution can be obtained as long as

$$P \geq -2\pi RW \qquad \textbf{4.7}$$

Table 4-1: Contact mechanics equations for Hertzian, JKR, and DMT models.[32]

	Hertz	JKR	DMT
a (contact radius)	$\sqrt[3]{\frac{RP}{K}}$	$\sqrt[3]{\frac{R}{K}\left(P+3\pi RW+\sqrt{6\pi RWP+(3\pi RW)^2}\right)}$	$\sqrt[3]{\frac{R}{K}\left(P+2\pi RW\right)}$
δ (deformation)	$\frac{a^2}{R}=\left(\frac{P^2}{RK^2}\right)^{1/3}$	$\frac{a^2}{R}-\frac{2}{3}\sqrt{\frac{6\pi Wa}{K}}$	$\frac{a^2}{R}=\frac{\left(P+2\pi RW\right)^{2/3}}{\sqrt[3]{RK^2}}$
F (adhesion force)	0	$\frac{3}{2}\pi RW$	$2\pi RW$

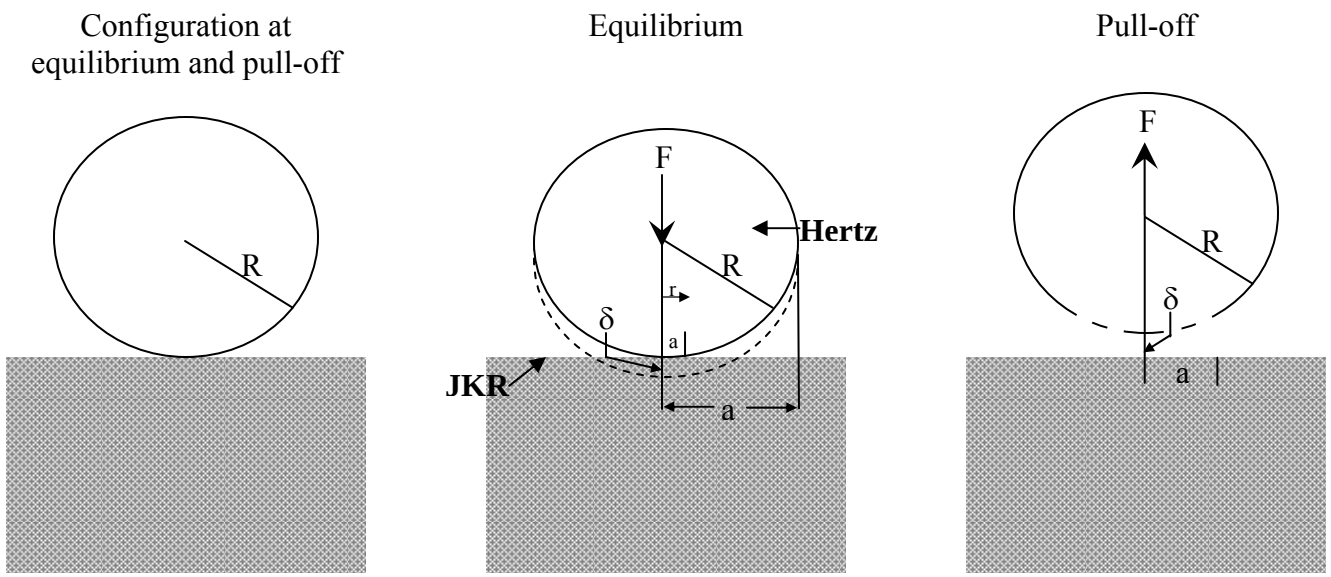

Figure 4-1: a) An illustration of a rigid sphere on a rigid surface. b) On the left is an illustration of a deformable sphere on a rigid surface in the absence of adhesion (Hertz) and in the presence of adhesion (JKR). On the right is an elastic adhering sphere about to separate from adhesive contact. [56]

Since two models were developed that established the relationship between force and work, Tabor developed a parameter to aid in the decision of which model should be used based on AFM tip properties and the sample's surface properties:[57]

$$\phi = \frac{\left(\gamma^2 R\right)^{1/3}}{\left(K^2 z_0^3\right)} \qquad \textbf{4.8}$$

where R is the radius of the sphere (or AFM tip radius), γ is determined from contact angle measurements, K is the reduced Young's modulus that occurs at contact, and z_0 is the equilibrium size of atoms at contact. The value the average atomic diameter of carbon (0.154 nm) was used for z_0, by assuming the tip and the surface were in atomic contact. When ϕ is greater than 0.3 the JKR model is used, when it is less than 0.3 the DMT theory is used. This equation requires prior knowledge of the sample's surface energy. In this study, the surface energy will come from contact angle, but other studies have used surface energy information from inverse gas chromatography.[52] To obtain tip radius, blind reconstruction (Section 3.6.3) is used.

Now that the methodology for measuring forces has been defined and the adhesion models have been identified to take force and calculate work, the next step will be to take the work of adhesion and determine surface energy. The illustration below is the overarching goal to take AFM forces and determine surface energy

$$F \rightarrow W \rightarrow \gamma \qquad \textbf{4.9}$$

4.2 Surface Energy Models

In Section 2.2, the concepts and equations for the free energy of cohesion and adhesion were introduced. These same principles are still applicable with the AFM, and just like with contact angle measurements, mathematical models must be developed to interpret the AFM data. There are no experimental methods that can be used to determine surface energy directly and stopping at work of adhesion is not the goal. The work of adhesion results makes it difficult to compare to contact angle and literature surface energy. Continuing to surface energy will give more information about the individual surfaces and it can be applied to understanding interactions with other solids and liquids.

Therefore, to determine the surface energy of a material in vapor or in a liquid using the AFM:

- First, forces are measured,
- Second, the work of adhesion is calculated, and
- Finally, the surface energy is calculated through development of a robust model.

The next few sections will present possible models to use when investigating surface energy with the AFM.

4.2.1 Surface energy model 1

In Section 2.2 and **Figure 2-2**, the change in surface free energy to separate two different media, 1 and 2, in a third medium is given by:[56]

$$W_{123} = \gamma_{13} + \gamma_{23} + \gamma_{12} \qquad \textbf{4.10}$$

where in air γ_{13}, γ_{23}, and γ_{12} represent the tip-vapor, sample-vapor, and tip-sample respectively, and in a liquid represent tip-liquid, sample-liquid, and tip-sample, respectively. Therefore, by measuring the adhesion force with the AFM it is possible to determine the surface energy of sample-vapor or sample-liquid. However there are three unknowns in Equation **4.10**,

1. γ_{13} – tip-vapor or tip-liquid
2. γ_{23} – sample-vapor or sample-liquid
3. γ_{12} – sample-tip

In order to determine γ_{23} (γ_{sv} or γ_{sl}) in Equation **4.10**, the surface energy of the γ_{12} and γ_{13} must first be calculated. Therefore, more experiments were set up in order to achieve this goal.

The tip-vapor and tip-liquid (γ_{13}) surface energies will be obtained by measuring the adhesion force between a pair of identical tips in air or in liquid (**Figure 4-2)**. An AFM tip scans the surface of the cantilever behind the AFM probe and the pull off force is measured and work is calculated. It is worthwhile to point out that it is not necessary to measure the force curve at the apex of the scanned tip because the entire cantilever and tip are composed of the same silicon nitride. Thus, when similar materials are brought together, the work of cohesion to pull them apart is equal to[56]

$$W = 2 \cdot \gamma_{tv};\ W = 2 \cdot \gamma_{tl} \qquad \textbf{4.11}$$

where γ_{tv} and γ_{tl} are tip-vapor and tip-liquid surface energies respectively.

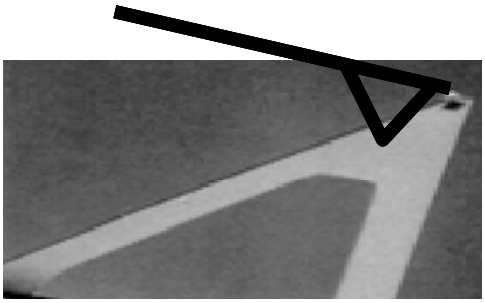

Figure 4-2: Tip-tip AFM scans are performed in both vapor and liquid environments to determine the tip-vapor and tip-liquid surface energies.

The third term, sample-tip (γ_{12}), could not be determined from separate AFM experiments. Therefore, going back to Equation **4.10**, there are still two unknowns;

1. γ_{12} – sample-tip
2. γ_{23} – sample-vapor or sample-liquid

Consequently, this model could not be used to determine either γ_{sv} and γ_{sl} without knowing γ_{st} first. To circumvent the limitation, the following is implemented:

1. Using contact angle measurements as described in Chapter 2, γ_{sv} can be determined,
2. Then tip-tip measurements provide the surface energy of the tip in air, and
3. The work is calculated from force of adhesion measurements of the sample in air.

These steps lead to determining the γ_{st} based on Equation **4.10** when the medium is vapor. The γ_{st} will then be used in:

$$W_{stl} = \gamma_{sl} + \gamma_{tl} + \gamma_{st} \qquad \textbf{4.12}$$

For γ_{sl} (solid-liquid surface energy) to be calculated the following measurements/parameters must be defined:

1. AFM force of adhesion measurements on the sample surface in a solvent,
2. Calculation of work of adhesion from the forces obtained in the first item, and
3. Tip-tip AFM measurements in the same liquid to determine γ_{tl}, Equation **4.11**.

Since there are several experiments and equations that are necessary to achieve the final goal, a flow chart in **Figure 4-3** has been developed.

In order to use this model for determining solid-liquid surface energy, a few assumptions were made. First, since contact angle measurements were used it was assumed that the liquids used for contact angle measurements did not influence the determination of solid-vapor surface energy, and it would be constant over any combination of liquids. This assumption is difficult to make because most of the indirect models used to determine solid-vapor surface energy warn against this.[2, 9] All of these models rely on fitting results from various liquids. If a different combination of liquids is chosen, the calculated solid-vapor surface energy could be different. Thus, it is difficult to use unreliable data from a second method. Also, the goal is to investigate the performance of just the AFM for determining surface energy. The use of the AFM would be extremely limited if the mathematical model needed to rely on another experimental method to obtain the parameter of interest.

The second assumption is that the sample surface from the contact angle measurements is comparable to the surface used for AFM measurements and remains unchanged in liquid environments. Hence, the surface-tip surface energy will be the same in vapor as it is in liquids. This assumption is difficult to make unless the material is inert in the liquid being used. If the liquid interacts with the sample, possibly rearranging the surface molecules, the sample-tip surface energy will vary. This was also a problem with contact angle measurements. If the liquid deforms the surface, the measured contact angle is not as accurate as an angle measured on a non-deformable surface.

Further investigation presented in Chapter 5 will also show the differences in solid-vapor surface energy when measured in ambient and controlled relative humidity. These data are more evidence that 1) using contact angle data for an AFM model is inadequate, and 2) the surface forces are different when water vapor is not present. However, since the sample-tip surface energy is currently not measurable, the assumption that it is constant must be made to use this model. The limitations discussed for this model are what led to the development of another model.

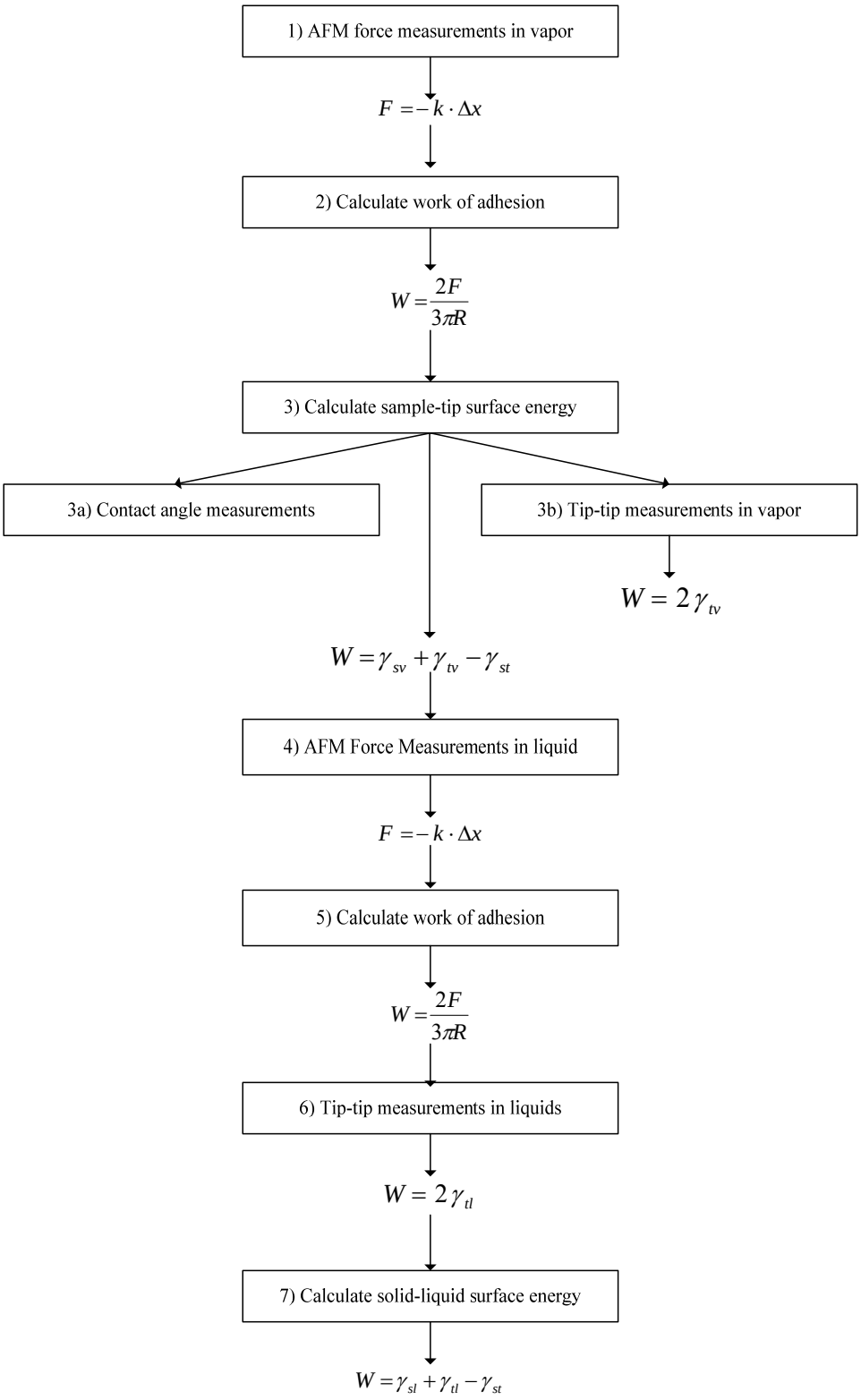

Figure 4-3: Experimental flow chart in order to study solid-liquid surface energy using the AFM and mathematical model 1.

4.2.2 Surface energy model 2

The second model eliminates relying on contact angle for determining the solid-vapor surface energy. This model, the geometric mean, is based on an existing theory continually used in the literature.[58]

$$W = 2\sqrt{\gamma_{sv}\gamma_{tv}} \qquad \textbf{4.13}$$

In section 2.2, the geometric mean and the mathematical assumptions that are made to evaluate the free energy of two dissimilar surfaces were reviewed. The geometric mean makes it possible to predict properties of the 12 interface from the separate properties of the 1 and 2 phases. Hence, the surface-tip-vapor interactions are based on the solid-vapor and tip-vapor phases. The elimination of γ_{st} from the equation leaves only one unknown, γ_{sv}. Therefore to calculate solid-vapor surface energy (γ_{sv}) the following studies are done

1. Measure the forces of adhesion on the sample surface in vapor,
2. Calculate the work of adhesion from the forces obtained in the first item, and
3. Make tip-tip AFM measurements in vapor to determine γ_{tv}, Equation **4.11**

These same steps can be followed to obtain solid-liquid surface energy, and Equation **4.13** becomes

$$W = 2\sqrt{\gamma_{sl}\gamma_{tl}} \qquad \textbf{4.14}$$

The only difference is the force measurements for the sample and tip are done in a liquid environment. The work flow to use this model and obtain solid-vapor and solid-liquid surface energies is illustrated in

Figure 4-4**.** Compared to the first model, fewer experiments are required for the second model, no assumptions have to be carried from the solid-vapor experiments to the solid-liquid experiments, and contact angle data is not required to eliminate an unknown value. This allows each set of measurements to be independent of the other, which the first model could not do.

The assumption for this model is that the geometric mean can 1) be used with the AFM and 2) the surface energy of the two separate phases (solid-vapor, tip-vapor) can be used to represent the interaction of the sample-tip (the dissimilar phases). The geometric mean, as mention in Section 2.2, only takes into consideration the van der Waals interactions and does not include polar/hydrogen bonding forces. However, it has been pointed out that the AFM measures the sum of all the forces occurring between the tip and the sample. These forces can consist of capillary, electrostatic, and Liftshitz-van der Waals forces.[58] The assumption that has to be made is the biggest limitation of this model. It was shown that using the geometric mean model overestimates the surface energy for contact angle measurements.[2, 9, 26, 59] Since the geometric mean model was developed based on van der Waals interactions, it might be difficult to employ this model with polar surfaces (mica). The best use of this model would be with surfaces that mainly consist of London dispersion forces (graphite).

Because of the limitations with the geometric mean, Neumann's lab added a modification to correct for the overestimation of the geometric mean.[19, 20] It was thought this same modification could be applied to the AFM, and therefore, another model should be tested.

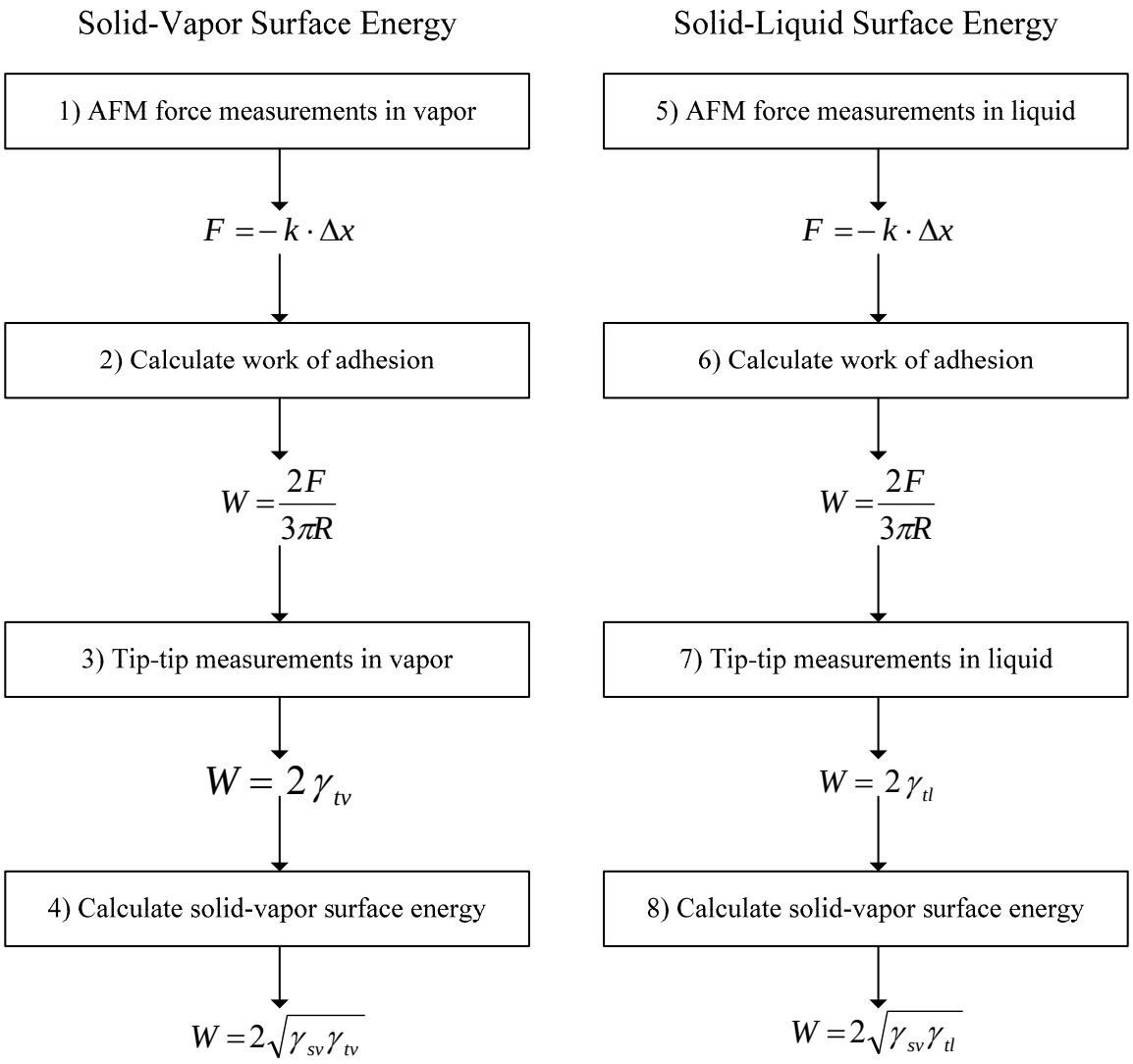

Figure 4-4: Experimental flow chart in order to study solid-liquid surface energy using the AFM and mathematical model 2.

(Note: Model 3 follows the same flow diagram; the only difference is the solid-liquid surface energy.)

4.2.3 Surface energy model 3

The third surface energy applies the modified geometric mean equation from contact angle measurements to the AFM measurements.[59]

$$W = 2\sqrt{\gamma_{sv}\gamma_{tv}}\, e^{-\beta(\gamma_{sv}-\gamma_{tv})^2} \qquad \textbf{4.15}$$

and in liquid environments the solid-liquid surface energy can be determined by:

$$W = 2\sqrt{\gamma_{sl}\gamma_{tl}}\, e^{-\beta(\gamma_{sl}-\gamma_{tl})^2} \qquad \textbf{4.16}$$

The experimental flow of this model is similar to the one shown in

Figure 4-4. The only difference is the corresponding equations that will be used. One difficulty with using this model is that the unknown variable which is being solved for, solid-vapor or solid-liquid surface energy, is in both the exponential and under the square root of the equations. For this reason, solving for these unknowns requires software that can run iterations until the surface energy is solved.

Another limitation of this model is the assumption that β, a universal constant from Neumann's lab, can be translated to use with the AFM. In order to consider deviations from the geometric mean, researchers have tried to introduce an empirical parameter that is used as a correction factor.[25] The proposed correction factor by Neumann included the universal constant β where β = 0.0001247 m^4 mJ^{-2}. This value was obtained by fitting large sets of experimental contact angle data. The data encompassed apolar, polar, aprotic, and protic liquids on low energy polymeric surfaces. The scope of this development was not to repeat such experiments to see if a universal parameter could be

established with the AFM. Thus, the assumption was made that this constant could be applied the AFM studies. However, in Chapter 5 when the models are tested, the influence of β will be explored to determine its effect on the fitting and iterations. The values between models 2 and 3 will also be compared to determine if the addition of a correction factor has any implications in calculating surface energy.

4.2.4 Surface energy model 4

In models 2 and 3 both solid-vapor and solid-liquid surface energies could be measured using the AFM. Model 1 was not able to evaluate both. Since there were no direct ways to measure γ_{st}, contact angle solid-vapor data had to be used. More evaluation was given to model 1, and it was thought that if model 2 or 3 could be used to determine solid-vapor surface energy, a mixed model could be developed (**Figure 4-5**). Then, γ_{st} would be determined by

1. Measuring the forces of adhesion on the sample surface in vapor,
2. Calculating the work of adhesion from the forces obtained in the first item,
3. Making tip-tip AFM measurements in vapor to determine γ_{tl}, Equation **4.11**, and
4. Using model 2 or 3 to calculate γ_{sv}.

Once these experiments were completed, the value for γ_{st} could be obtained. The surface-tip surface energy can then be used in Equation **4.12** to investigate the solid-liquid surface energy.

The mixed model would eliminate the need to use another technique for solid-vapor surface. Thus negating the assumption that the surface measured in contact angle

measurements was the same as the surface used for AFM measurements. However, the mixed model still requires that γ_{st} be evaluated. If any changes happen at the molecular level on the surface in a liquid environment, the sample-tip surface energy will be affected. Any changes to this surface energy cannot be captured until there is a direct way to measure the sample-tip surface energy. These effects will be seen on surfaces that are not inert. Therefore, this model may prove to be useful with surfaces like mica and graphite, but might fall apart in crystalline systems when dissolution and crystallization are occurring.

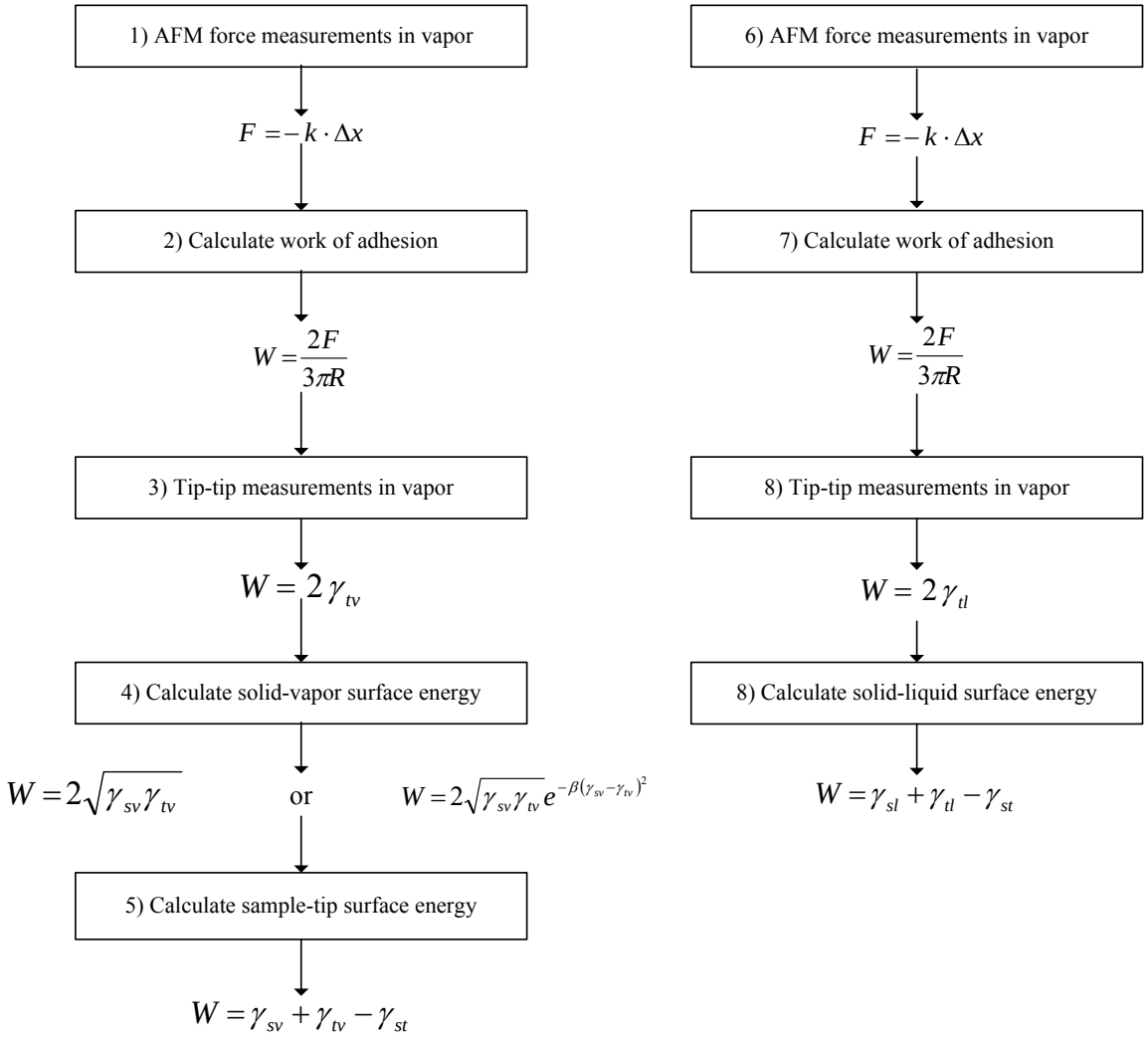

Figure 4-5: Experimental flow chart in order to study solid-liquid surface energy using the AFM and mathematical model 4.

4.3 Summary

Surface energy models complete the mathematics necessary to take AFM force measurements and determine surface energy. Currently, it is not possible to measure surface energy directly, and while computational work can be done, it is difficult to consider all environmental factors that can affect surface energy. Therefore, experimental methods and mathematical models are required. This is what has been done with contact angles, inverse gas chromatography, and the AFM. **Table** 4-2 evaluates the advantages, limitations, and assumptions of the models presented in this chapter that will be used to incorporate AFM force measurements to calculate surface energy.

Chapters 5 will utilize these models to determine the surface energy of graphite and mica. The goal of the inert surfaces is to see if any of these models can give surface energy results comparable to the results from the contact angle measurements. Based on the results from Chapter 5, the models will subsequently be applied to a crystalline material in Chapter 6. Chapter 6 will evaluate whether the models that predict well on inert surfaces can also predict well in a dynamic crystalline system.

Table 4-2: Comparison of the four mathematical used to determine surface energy with AFM force measurements.

Model	Advantages	Limitations	Assumptions
1	• Theoretical equation of all interfacial interactions is considered.	• Needs another technique to determine γ_{st}. • Cannot determine γ_{sv}.	• Contact angle results are not dependent on the fitting from the liquids used. • The surface-tip interfaces measured in liquid environments is not changed from the interface in vapor
2	• Another technique is not needed to measure γ_{sv}.	• Developed for Van der Waals interactions.	• The model can be applied to all surfaces, even polar surfaces, because the ionization potentials and molecular size are similar.
3	• Another technique is not needed to measure γ_{sv}. • Correction factor to prevent overestimation from geometric mean.	• Dependent upon an empirical universal constant from contact angle measurements.	• A universal constant from contact angle measurements is applicable to the AFM. • Iterations are able to fit the data accurately to solve for surface energy.
4	• Contact angle results are not needed to measure γ_{sv}. • Theoretical equation of all interfacial interactions is considered.	• Cannot determine γ_{sv}.	• The surface-tip interfaces measured in liquid environments is not changed from the interface in vapor

Chapter 5 – AFM Results

5.1 Introduction

Thus far, the discussion has covered the operations and methodology of the AFM force measurements and the equations needed for the calculation of surface energy. The goal of this chapter is to apply the methodology in Chapter 3 and mathematical models in Chapter 4 to determine surface energy of mica and graphite. The solid-vapor and solid-liquid surface energy will be calculated from AFM force of adhesion and compared to the results from contact angle data in Chapter 2. All four surface energy models will be evaluated to determine which model gave comparable results.

5.1 AFM Measurements

In order to evaluate the AFM's potential use for studying surface energetics, the same samples used in the contact angle studies (**Section 2.3**) were used for the AFM studies. Solid-vapor surface energy was measured first in ambient and controlled humidity environments, and solid-liquid surface energy was determined with the same liquids used in contact angle measurements (water, diiodomethane, ethylene glycol, and formamide). The variability in the ambient measurements was large despite maximizing the scan parameters discussed in Chapter 3. The capillary effect has been extensively researched and results have shown that it has less of an impact when the humidity is less than or equal to 22%.[52] Therefore, the vapor environment was controlled using an environmental chamber purged with nitrogen gas. After observing contact angle differences with rehydrated hygroscopic liquids, the hygroscopic liquids were dried prior to use. The following sections will present results for tip characterization, statistical

analysis of forces, AFM surface energy model analyses, and finally comparison to contact angle data.

5.1.1 Solid-vapor surface energy

5.1.1.1 Graphite Ambient and Controlled RH Solid-Vapor Surface Energy

The flow diagram in **Figure 4-4** (surface energy model 2 and 3) was followed for calculating solid-vapor surface energy of graphite in ambient and controlled conditions. For each cantilever used, spring constant, tip radius, and tip-vapor surface energy were measured in ambient and controlled environmental conditions. The spring constants for vapor measurements did not deviate from the manufacturers reported 0.06 N/m. The tip radius and tip-vapor surface energy for each tip used with graphite are reported in **Table 5-1**. These values were used to calculate the solid-vapor surface energy using equations from surface energy models 2 and 3.

After the forces were measured on graphite in ambient and controlled humidity, the statistical model discussed in Chapter 3 was applied. The variance within and between the analytes was quantified using a repeated measures mixed model ANOVA. **Table 5-3a and b** and **Table 5-4a and b** illustrate that the variation across locations, samples, and tips was not statistically significant in ambient and controlled environments. Thus, the null hypothesis was accepted. When the null hypothesis is accepted, an average can be obtained between all tips and all samples. The force, work, and surface energy data for ambient and controlled humidity are plotted in **Figure 5-1a** and **Figure 5-1b**, respectively. The other statistical observation of note from these measurements was the causation of variation, **Table 5-3c** and **Table 5-4c**. The AFM tips and inherent instrumental error were the largest sources of variation in ambient measurements. The

tips used were composed of silicon nitride which has a higher affinity for water than the carbon atoms of graphite. Therefore, tip variation could have been caused by the varying amount of water adsorbed to the surface graphite. In the controlled environment measurements, the largest variation was attributed to graphite*tip interaction and the instrumental error from the AFM measurements. Electrostatic forces are stronger in low humidity conditions and are known to cause variability in the force measurements.[58] Graphite is a conductive material and the individual carbon atoms in graphite have been imaged using STM.[28] The variability in force measurements caused by the electrostatic forces was picked up by the graphite*tip interaction. An increase in humidity can reduce or eliminate electrostatic variability, so increasing the relative humidity was expected to decrease the graphite*tip variability. Electrostatic forces can also be minimized by dissipating the charge with a conductive tape. Instead of using scotch tape to adhere the sample to the AFM disc, a conductive tape was used to help reduce the electrostatic charge on the surface of the sample and decrease graphite*tip variability.

The average solid-vapor surface energy for graphite in ambient and controlled environmental conditions, as determined using models 2 and 3, is reported in **Table 5-2**. There was not a large reduction in solid-vapor surface energy measured in a controlled environment as compared to the ambient surface energy. Thus, the capillary effect had a minimal impact on the graphite measurements in an ambient environment. Since graphite is a hydrophobic surface, the weak interaction with water allowed for consistent measurements in ambient and controlled humidity environments.

To evaluate the effectiveness of the AFM to determine surface energy, results needed to be compared with contact angle solid-vapor surface energy. The average contact angle solid-vapor surface energy values are shown in **Table 5-2**, which ranged from 36 to 43 mJ/m^2. The average solid-vapor surface energy from AFM force measurements ranged from 35 to 40 mJ/m^2 in ambient and controlled humidity conditions. Thus, the AFM results for graphite were comparable to contact angle results. The comparison of these data demonstrated the applicability of the geometric mean with the AFM for surfaces exhibiting London dispersion forces. It also supported the assumption and use of the geometric mean in the indirect models for contact angles.

Lastly, surface energy models were evaluated. The values in **Table 5-2** indicate similar results between the geometric mean (model 2) and the modified geometric mean (model 3). The ambient solid-vapor surface energy for model 2 was 38.0 mJ/m^2 and for model 3 was 39.4 mJ/m^2. The controlled environment solid-vapor surface energy was 34.8 mJ/m^2 and 35.2 mJ/m^2 for model 2 and model 3 respectively. As all of these results are similar to contact angle, either model can be used to calculate the solid-vapor surface energy of graphite. The modification added in model 3 did not indicate that the geometric mean overestimated the graphite solid-vapor surface energy. Solid-vapor surface energy results from model 2 are plotted in (**Figure 5-1**). For each AFM data set, histogram statistics were generated from force, work, and surface energy data. The number of bins was manually selected, using the fewest number of bins necessary to still maintain visual confirmation of a normal distribution as the selection criteria. The center point and number of elements for each bin were retained and used for construction of a test vector with 1000 linearly spaced points ranging from (min(x) - mean(x)) to (max(x) + mean(x)),

where x represents bin centers. A Gaussian distribution function was calculated from each point in the test vector. The Gaussian normal distributions were plotted over each histogram and manually assessed for goodness of fit for each AFM data file.

For model 3, one assumption that had to be made was that the empirical β determined from contact angle measurements could be translated to a surface energy model used with the AFM. While running the iterations in Matlab, it was determined that this assumption was invalid. Thus, the Matlab program was used to determine β and the solid-vapor surface energy for each sample. The left panel of **Figure 5-2** illustrates work values as calculated from a typical set of AFM force measurements. Using the known tip-vapor surface energy term and an initial estimate for β, it was possible to calculate a unique surface-vapor surface energy solution for each work value. However, the mathematical relationship between β and the surface-vapor term dictated the range of theoretically allowable work values. As shown in the right panel of **Figure 5-2**, when β was set too high, the parabolic point of inflection on the mathematically allowable work values did not bracket the range of empirically determined work values. **Figure 5-3** illustrates the constraints imposed by this equation. For example, notice that the work value highlighted in **Figure 5-3** can only be calculated from the lowest value of β (shown in black). To effectively use this equation and keep consistent with the modified Berthelot model, it was necessary to first calculate the minimum value of β, the result of which allowed for calculation of all empirically determined work values. In effect, this model essentially used a mathematically derived minimum allowable value for β, but not necessarily its true value. Once this appropriate minimum β was calculated, the surface energy surface-vapor term was calculated. Recall that the equation for this model was

quadratic, indicating that there were two solutions to the same equation. In all cases, the first solution was determined to be the correct solution as it correlated most highly with model 2 AFM results.

As described in Chapter 2, researchers caution about the indirect models' dependency on liquids to determine solid-vapor surface energy. For example, the angle of three liquids with different dispersive and polar components are measured and then fit to a model to determine the solid-vapor surface energy. However, AFM can measure the forces between tip-tip in vapor and tip-graphite in vapor to determine solid-vapor surface energy. Thus, the surface energy value calculated is free from the interferences of liquids. For contact angles with water, a saturated environment is needed to establish a contact angle. Without the water saturated environment, a true "equilibrium" is not established and an angle cannot be measured. The AFM can control the humidity and focus entirely on the solid-vapor interaction, free from water vapor. This makes the AFM a more desirable tool for graphite surface energy measurements.

Table 5-1: Tip radius and average tip-vapor surface energy (standard deviation) for the AFM tips used to measure the solid-vapor surface energy of graphite in ambient and controlled humidity environments.

Tip	Environmental Conditions	Radius (nm)	Force (nN)	Work (mN/m)	Surface Energy (mJ/m^2)
1	Ambient	44	18.9 (1.4)	91.2 (6.6)	45.6 (3.3)
2	Ambient	41	15.8 (1.6)	82.0 (8.2)	41.0 (4.1)
3	Ambient	43	17.2 (0.6)	84.9 (3.2)	42.5 (1.6)
4	Controlled Humidity	44	14.1 (0.2)	68.1 (1.2)	34.0 (0.6)
5	Controlled Humidity	42	12.3 (0.3)	62.0 (1.7)	31.0 (0.9)
6	Controlled Humidity	40	10.9 (0.6)	58.0 (3.0)	29.0 (1.5)

Table 5-2: Average solid-vapor surface energy of graphite determined using the AFM and contact angle methods. The standard deviations are shown in parenthesis.

	Solid-Vapor Surface Energy (mJ/m^2)		
Method	Indirect Model	Ambient Force Measurements	Controlled RH Force Measurements
AFM	Model 1	-	-
	Model 2	38.0 (5.9)	34.8 (4.8)
	Model 3	39.4 (5.7)	35.2 (5.8)
	Model 4	-	-
CA	Van Oss et al	42.7 (2.7)	NA
	OWRK	40.3 (0.7)	NA
	Neumann	36.8 (1.1)	NA

Table 5-3: Mixed model statistics for graphite AFM measurements in ambient environmental conditions. a) Repeated measures ANOVA for within subject effects, b) repeated measures ANOVA for between subjects, and c) the variable that demonstrates the largest percentage of variance for graphite – ambient AFM measurements.

a)

	Degrees of Freedom	Sum of Square	Mean Square	F Value	p
Location	9	142.3	15.8	1.71	0.16
Location*Graphite	9	83.5	9.3	1.00	0.42
Location*Tip	18	243.1	13.5	1.46	0.30
Error	18	166.3	9.2	-	-

b)

	Degrees of Freedom	Sum of Square	Mean Square	F Value	p
Graphite	1	15.1	15.1	0.68	0.50
Tip	2	334.3	167.1	7.54	0.12
Error	2	44.4	22.2	-	-

c)

Variable	% of the Total	% Truncated
Graphite	-1.3	0
Tip	38.0	37.5
Graphite*Tip	5.9	5.8
Graphite*Tip*Location (Error)	57.4	56.7
Total	100.0	100.0

Table 5-4: Mixed model statistics for graphite AFM measurements with controlled humidity environment. a) Repeated measures ANOVA for within subject effects, b) repeated measures ANOVA for between subjects, and c) the variable that demonstrates the largest percentage of variance for graphite – controlled humidity AFM measurements.

a)

	Degrees of Freedom	Sum of Square	Mean Square	F Value	p
Location	9	63.4	7.1	0.98	0.49
Location*Graphite	9	68.6	7.6	1.1	0.44
Location*Tip	18	132.5	7.4	1.0	0.48
Error	18	129.8	7.2	-	-

b)

	Degrees of Freedom	Sum of Square	Mean Square	F Value	p
Graphite	1	1.9	1.9	0.03	0.88
Tip	2	264.1	132.1	1.89	0.35
Error	2	140.1	70.1	-	-

c)

Variable	% of the Total	% Truncated
Graphite	-15.7	0.0
Tip	21.4	18.5
Graphite*Tip	43.4	37.5
Graphite*Tip*Location (Error)	50.9	44.0
Total	100.0	100.0

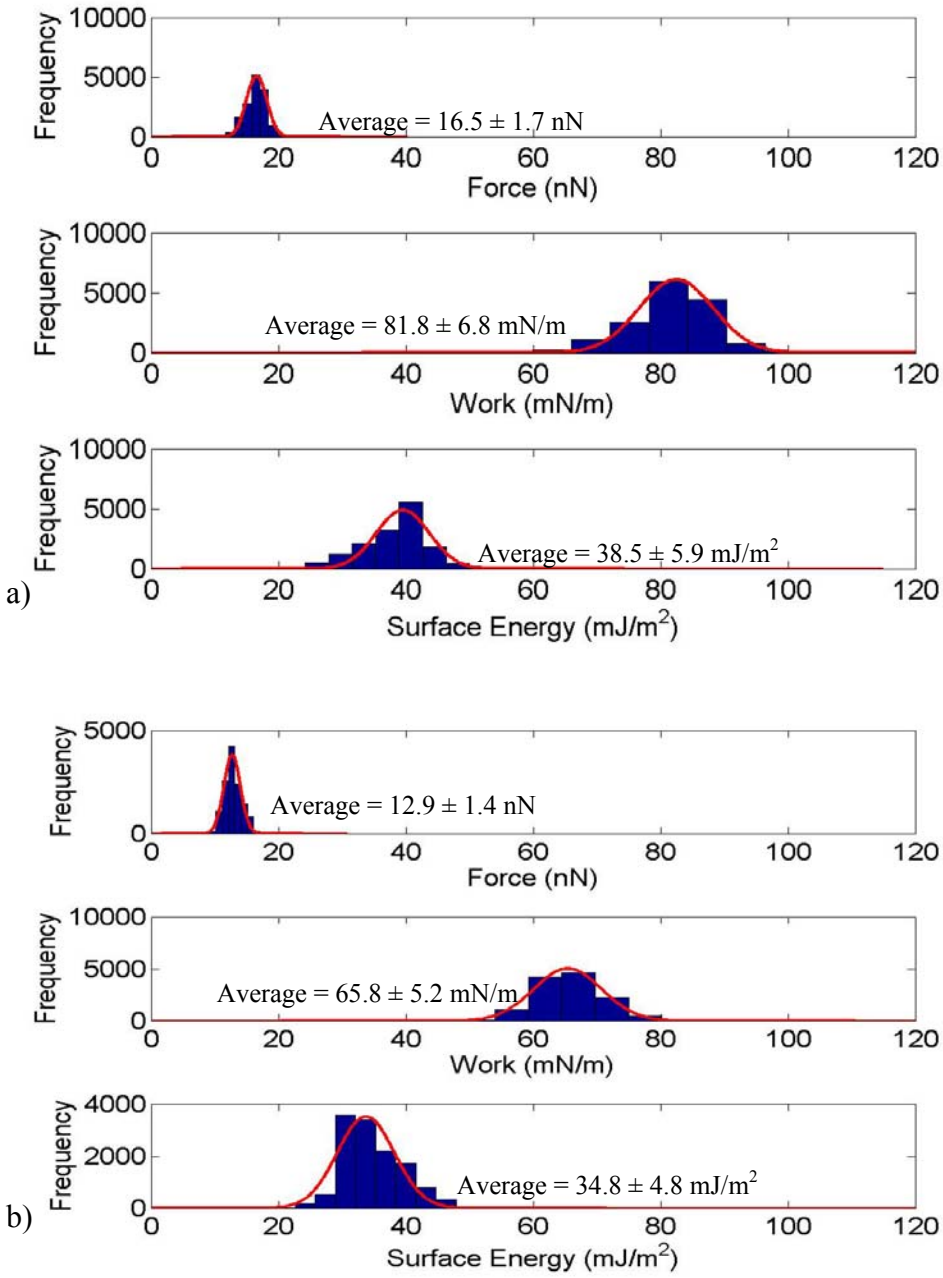

Figure 5-1: The force, work, and surface energy of a) graphite measured in ambient conditions and b) graphite measured in controlled humidity conditions. The averages and standard deviations are listed next to each histogram.

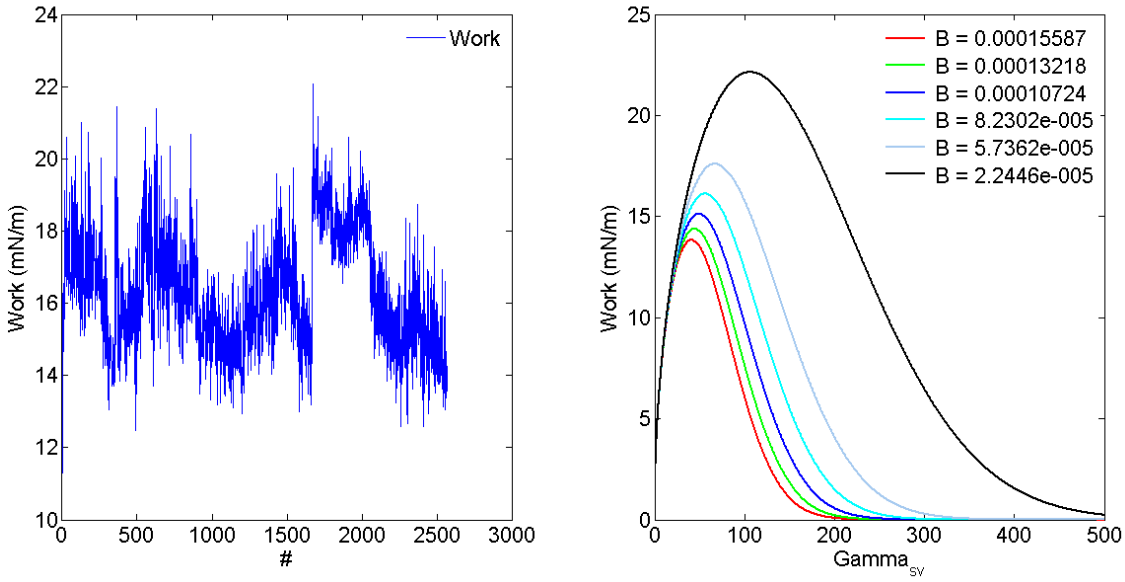

Figure 5-2: Iterative calculation to determine the value of β and the surface-vapor term.

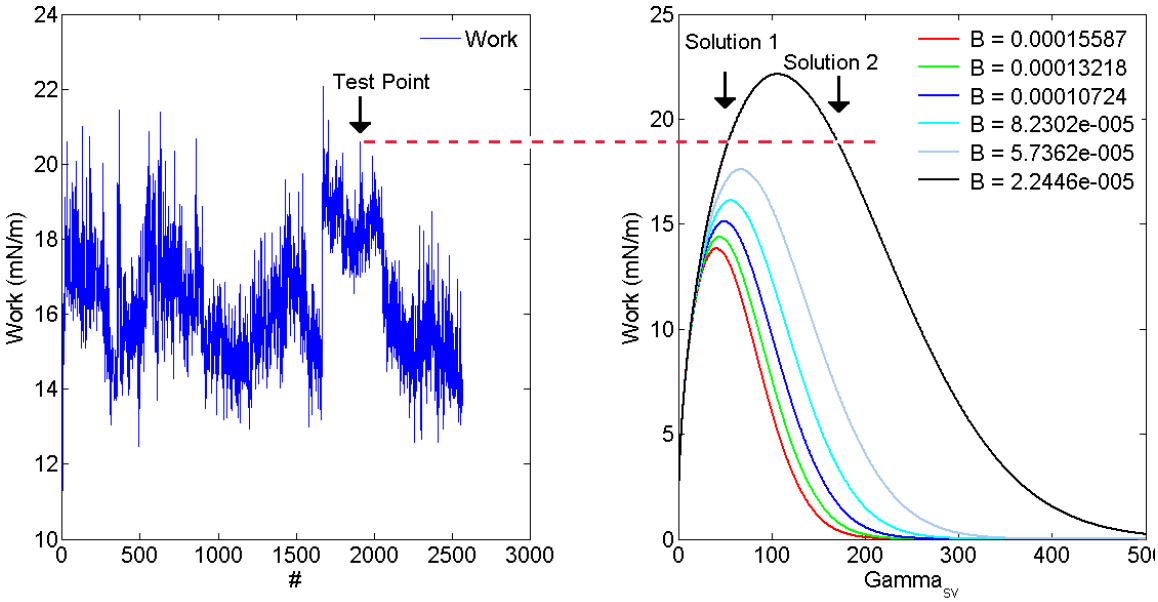

Figure 5-3: Iterative calculation to illustrate how the value of β and the surface-vapor term are determined.

5.1.1.2 Mica Ambient and Controlled RH Solid-Vapor Surface Energy

The same flow diagram (**Figure 4-4,** surface energy model 2 and 3) was followed for calculating solid-vapor surface energy of mica in ambient and controlled conditions. The tip radius and tip-vapor surface energy for each tip used with the mica measurements are reported in **Table 5-5**. These values were used to calculate the solid-vapor surface energy using equations for surface energy models 2 and 3.

In order to calculate an average surface energy using the data from different tips and samples, the repeated measures mixed model is applied to the force data of mica. The variance within the subjects and between the subjects for the ambient measurements is reported in **Table 5-6a and b, and** in **Table 5-7a and b** for controlled environment measurements**.** The results for both ambient and controlled humidity illustrated that the variation between the locations, the samples, and the tips was similar, because the p values were greater than 0.05. Thus, the null hypothesis was accepted, and an average force, work, and surface energy for the ambient and controlled environments could be calculated. The results for ambient and controlled humidity are shown in **Figure 5-4a** and **Figure 5-4b**. The variable that caused the largest error in ambient and controlled humidity is shown in **Table 5-6c** and **Table 5-7c**. In ambient measurements, the largest variation was due to the mica-tip interaction and the overall error within the measurements. In controlled environment measurements, the largest variation was from the mica*tip interaction and the overall error within the measurements. Controlled humidity can sometimes cause tribocharging or electrostatic forces.[58] The biggest concern with electrostatic forces would be on the surface of graphite, since mica is not conductive. Attempts to produce an STM image failed because mica does not carry a

charge. Thus, tribocharging was likely not contributing to the variability. The best way to eliminate electrostatic forces was to increase the humidity. However, the average forces on mica in ambient and controlled humidity were different. This indicated a strong capillary effect with mica, and increasing the humidity could introduce too many force variations. Since the p values were well above 0.05, the variability was not causing major problems for measurements between the tip and mica.

The average solid-vapor surface energy for mica in ambient and controlled environmental conditions, as determined using models 2 and 3, is reported in **Table 5-8**. The pull-off forces decreased when the relative humidity was low and the sample was allowed to sit in the desiccator for 24 hours. Since both the tip and mica are hydrophilic, the large difference between ambient and controlled environment forces was expected. In the controlled humidity measurements, water adsorption to the surface of the mica sample was significantly reduced, if not eliminated entirely. The removal of water eliminated the capillary forces present when the relative humidity was high. The water on the surface strongly interacted with mica and the tip making it difficult to pull the tip from the surface. These results illustrate the importance of measuring forces with the AFM in a controlled environment, especially with hydrophilic surfaces.

To evaluate the effectiveness of the AFM in determining surface energy, results were compared to contact angle solid-vapor surface energy. The contact angle and AFM results are listed in **Table 5-8**. The solid-vapor surface energy of mica in ambient conditions was comparable with the van Oss model obtained using contact angle measurements. The solid-vapor surface energy measured in a controlled environment was less then the contact angle solid-vapor surface energy. Due to the disparity in the

contact angle models, it was difficult to compare the results from the AFM. The contact angle method relied on measuring angles of liquids with various surface tensions and fitting them to models based on the geometric mean. Each of these models used different ways to incorporate the polar or acid/base term, and the results in Chapter 2 showed how significantly this term varied. The ambient AFM and contact angle determined solid-vapor surface energies were measured in uncontrolled conditions. Therefore, water vapor that settled on samples during contact angle measurements affected the spread of the liquids during contact angle measurements. Water vapor adsorbed on the surface of mica in ambient conditions also contributed to large pull-off forces with the AFM. For hydrophilic surfaces, the water adsorbed to the surface limited the ability for direct comparison between the AFM surface energy and the contact angle determined surface energy. For mica, controlled environment conditions most likely report the "true" solid-vapor surface energy.

Lastly, the surface energy models were evaluated. The results in **Table 5-8** indicate the calculated surface energy from the geometric mean (model 2) and the modified geometric mean (model 3) were similar. The ambient solid-vapor surface energy was 45.0 mJ/m^2 and 44.9 mJ/m^2 for model 2 and model 3, respectively. The controlled environment solid-vapor surface energy was 30.6 mJ/m^2 and 30.8 mJ/m^2 for model 2 and model 3. The modification added in model 3 indicated that the geometric mean did not overestimate the mica solid-vapor surface energy. Therefore, the solid-vapor surface energy results shown in **Figure 5-4** were calculated based on model 2. In model 3, the assumption was made that the contact angle determined empirical β value could be used with the AFM. As part of the analysis in Matlab, iterations were performed using the β

determined by Neumann's lab to determine solid-vapor surface energy. During these iterations, the Matlab program also determined an optimized the β value as previously discussed. The optimized β value was five times smaller than the empirical value determined in the Neumann lab.[59]

Table 5-5: Tip radius and average tip-vapor surface energy (standard deviation) for the tips used to calculate the solid-vapor surface energy of mica in ambient and controlled humidity environments.

Tip	Environmental Conditions	Radius (nm)	Force (nN)	Work (mN/m)	Surface Energy (mJ/m^2)
1	Ambient	43	19.0 (8.9)	93.7 (8.9)	46.9 (8.9)
2	Ambient	41	17.4 (6.2)	89.9 (6.2)	45 (6.2)
3	Ambient	44	18.8 (2.6)	90.5 (2.6)	45.2 (2.6)
4	Controlled Humidity	44	12.5 (0.8)	60.4 (3.7)	30.2 (1.8)
5	Controlled Humidity	43	12.9 (0.6)	63.6 (2.9)	31.8 (1.5)
6	Controlled Humidity	40	10.9 (0.5)	57.9 (2.6)	29.0 (1.3)

Table 5-6: Mixed model statistics for mica AFM measurements in ambient environmental conditions. a) Repeated measures ANOVA for within subject effects, b) repeated measures ANOVA for between subjects, and c) the variable that demonstrates the largest percentage of variance for mica – ambient AFM measurements.

a)

	Degrees of Freedom	Sum of Square	Mean Square	F Value	p
Location	9	18.6	2.1	0.42	0.91
Location*Mica	9	70.1	7.8	1.57	0.20
Location*Tip	18	167.7	9.31	1.87	0.10
Error	18	89.5	5.0	-	-

b)

	Degrees of Freedom	Sum of Square	Mean Square	F Value	p
Mica	1	71.3	71.3	1.07	0.41
Tip	2	58.3	29.1	0.44	0.70
Error	2	133.5	66.7	-	-

c)

Variable	% of the Total	% Truncated
Mica	1.3	1.1
Tip	-16.4	0.0
Mica*Tip	51.7	44.5
Mica*Tip*Location (Error)	63.3	54.4
Total	100.0	100.0

Table 5-7: Mixed model statistics for mica AFM measurements in controlled humidity environmental conditions. a) Repeated measures ANOVA for within subject effects, b) repeated measures ANOVA for between subjects, and c) the variable that demonstrates the largest percentage of variance for mica – controlled AFM measurements.

a)

	Degrees of Freedom	Sum of Square	Mean Square	F Value	p
Location	9	12.1	1.4	1.26	0.38
Location*Mica	9	4.1	0.5	0.43	0.90
Location*Tip	18	20.2	1.1	1.05	0.46
Error	18	19.3	1.1	-	-

b)

	Degrees of Freedom	Sum of Square	Mean Square	F Value	p
Mica	1	6.7	6.7	0.17	0.72
Tip	2	3.6	1.8	0.05	0.96
Error	2	76.7	38.3	-	-

c)

Variable	% of the Total	% Truncated
Mica	-57.9	0.0
Tip	-100.1	0.0
Mica*Tip	204.8	79.4
Mica*Tip*Location (Error)	53.2	20.6
Total	100.0	100.0

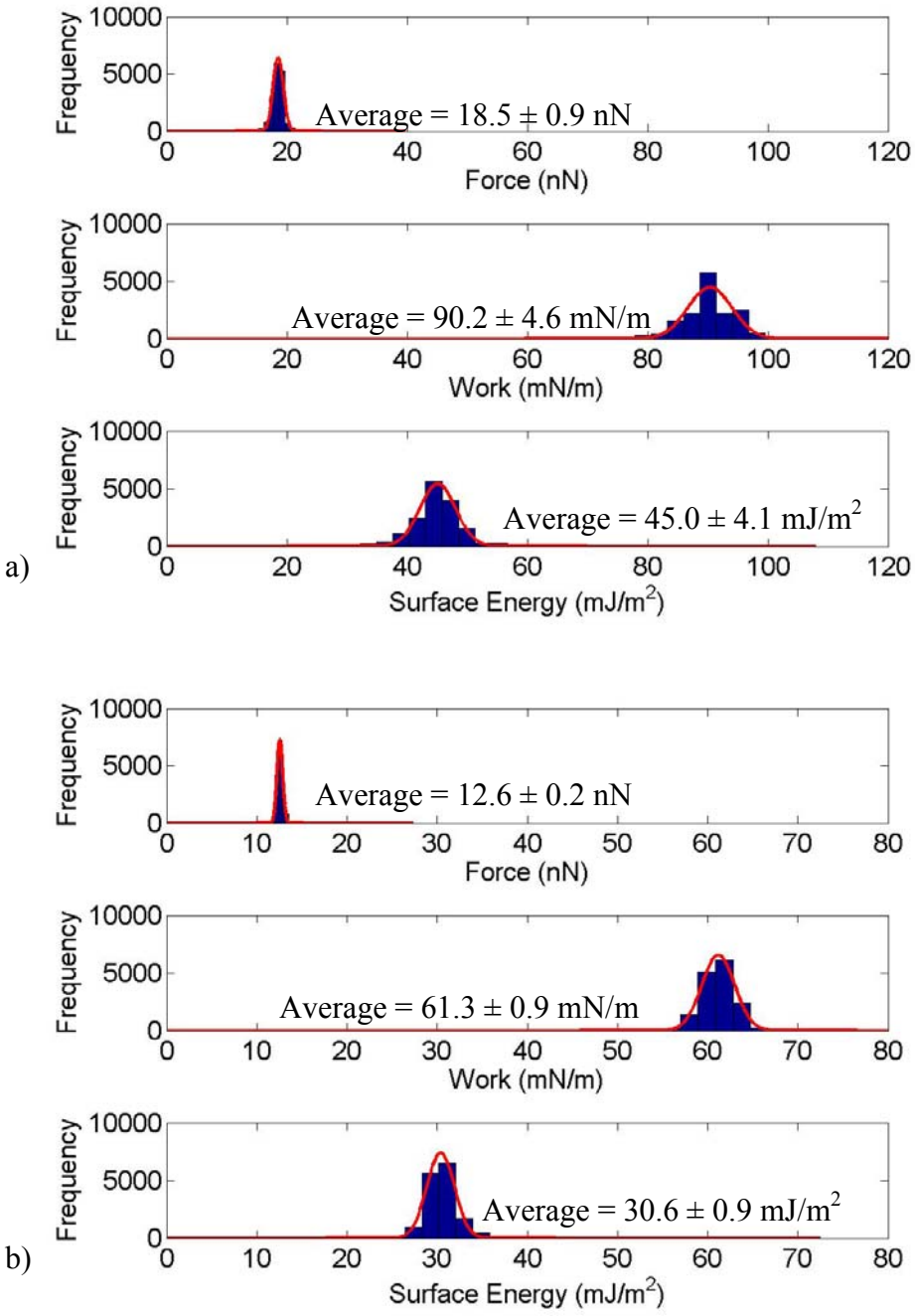

Figure 5-4: The force, work, and surface energy of a) mica measured in ambient conditions and b) mica measured in controlled humidity conditions. The averages and standard deviations are listed next to each histogram.

Table 5-8: Average solid-vapor surface energy of mica determined using the AFM and contact angle methods.

	Solid-Vapor Surface Energy (mJ/m^2)		
Method	Indirect Model	Ambient Force Measurements	Controlled RH Force Measurements
AFM	Model 1	-	-
	Model 2	45.0 (4.1)	30.6 (0.9)
	Model 3	44.9 (4.1)	30.8 (1.9)
	Model 4	-	-
CA	Van Oss et al	41.3 (2.7)	NA
	OWRK	65.2 (0.3)	NA
	Neumann	57.0 (0.4)	NA

The graphite solid-vapor surface energy from the AFM measurements was comparable to the solid-vapor surface energy from contact angle measurements. The mica solid vapor surface energy was difficult to compare because of the limitation with the indirect contact angle models, though this was not the only reason for the disparity. Since liquids were needed, uncertainties invariably exist because the thermodynamically equilibrated condition can never be satisfied. However, the AFM did not rely on several extraneous parameters to determine surface energy, and forces were measured in a controlled humidity environment. The two models proved to be effective for use with the AFM. With these results, the next objective was to evaluate solid-liquid surface energies.

5.1.2 Solid-liquid surface energy

The second part in evaluating the AFM's potential for measuring surface energy involved taking force measurements in liquid environments. With certain hygroscopic liquids more variability existed in the force measurements than with water and diiodomethane. Therefore, ethylene glycol and formamide were purified before use and rehydrated to evaluate the effect water had on the AFM measurements in those liquids. In this section, a similar presentation of data will be given. Since the solid-liquid surface energy could be calculated using all four models, refer to the the flow diagrams previously presented in Chapter 4.

5.1.2.1 Water Solid-Liquid Surface Energy

To determine the solid-liquid surface energy of mica and graphite in water, the spring constant, tip radii, and tip-liquid$_{water}$ surface energies had to first be determined. The spring constant was measured in water because the oscillations of the cantilever were different in air and in liquid. The same thermal method was used as described in Section

3.3. **Table 5-9** shows the spring constant, radii, and other values used to calculate mica and graphite solid-liquid$_{water}$ surface energy.

Statistical analysis was performed on the AFM force data from graphite-water. **Table 5-10a and b** show the results from the SAS analysis. The p values indicate that the null hypothesis was accepted. The analysis within subjects (**Table 5-10a**) for graphite*locations had a low p value, slightly larger than the requisite 0.05 necessary to indicate that the differences in the locations within the graphite samples are close to being statistically significant. Since graphite is hydrophobic, more variability between locations could have been due to the material's aversion to water. The graphite quality could have also contributed to the variability. Of the three possible grades of HOPG, the lowest grade was used in these studies, resulting in more steps during cleavage. Thus, the combination of surface roughness and hydrophobicity of graphite can cause variations in the locations. The analysis between subjects (**Table 5-10b**) for tips had a low p value that was just above 0.05, and therefore, the differences between tips are almost statistically significant. Again, the hydrophobicity of graphite was a major contributor to variation. Even though the statistics can uncover these differences, the scientific understanding of the weak interaction between water and graphite helps draw the appropriate conclusions. In this study, the JMP output in **Table 5-10c** can be used to verify the decision to accept the null hypothesis. Even though some variability was caused by the tips, the largest error was attributed to the residual error, which is just the experimental error of the measurements.

The graphite-water averages for force, work, and surface energy are plotted in **Figure 5-5**. The force of adhesion between graphite-water was large because the two are not

attracted to each other. Similarly for the contact angle measurements, the measured angle of water on graphite was 80.6 ± 3.6, indicating a weak interaction between the two. Therefore, the solid-liquid surface energy values were expected to be high. Listed in **Table 5-11** are the values for solid-liquid surface energy calculated from all four surface energy models and the contact angles. Model 1 used contact angle $\gamma_{solid\text{-}vapor}$ and AFM vapor work of adhesions (ambient and controlled humidity) to calculate $\gamma_{surface\text{-}tip}$. Model 2 and 3 were independent AFM measurements and model 4 was similar to model 1, but the AFM $\gamma_{solid\text{-}vapor}$ data are used from Section 5.1.1. Comparing the calculated graphite-water solid-liquid surface energy to contact angle data, models 2 and 3 were the most similar. However, model 1 solid-liquid surface energy using the controlled humidity work of adhesion was close to Neumann calculated solid-liquid surface energy. While model 1 indicated some success, the goal was to have one method for measuring surface energy. Models 2, 3, and 4 utilize only AFM data. AFM models 2 and 3 were similar to contact angle measurements. These results support the use of the geometric mean with the AFM and with molecules on the surfaces of samples whose interactions are dominated by London dispersion forces.

The difference in solid-liquid surface energy between models 2 and 3 was small; therefore, there was no indication that the Neumann modification improved the calculation of solid-liquid surface energy. In fact, the average solid-liquid surface energy from the modification was larger than the average of the contact angle value. Both models utilized the geometric mean, and it was shown in Section 5.1.1.1 that the geometric mean was successful for the prediction of surfaces that have mostly van der

Waals interactions. Thus, a modification to the geometric mean might not be necessary when evaluating samples with strong van der Waals forces.

Table 5-9: Spring constant, tip radius, and average tip-liquid surface energy (standard deviation) are listed for the AFM tips used to measure the solid-liquid surface energy of graphite and mica in water.

Tip	Material	Spring constant (N/m)	Radius (nm)	Force (nN)	Work (mN/m)	Tip-Liquid Surface Energy (mJ/m^2)
1	Mica	.04	43	1.2 (0.2)	6.0 (1.2)	3.0 (0.6)
2			41	1.1 (0.3)	5.7 (1.6)	2.8 (0.8)
3			42	1.0 (0.6)	5.3 (3.0)	2.6 (1.5)
1	Graphite		41	0.9 (0.2)	4.5 (1.3)	2.3 (0.7)
2			43	1.0 (0.2)	4.9 (1.0)	2.5 (0.5)
3			42	0.8 (0.5)	4.0 (2.3)	2.0 (1.2)

Table 5-10: Mixed model statistics for graphite AFM measurements with water. a) Repeated measures ANOVA for within subject effects, b) repeated measures ANOVA for between subjects, and c) the variable that demonstrates the largest percentage of variance for graphite – water AFM measurements.

a)

	Degrees of Freedom	Sum of Square	Mean Square	F Value	p
Location	9	12.7	1.4	0.19	0.99
Location*Graphite	9	155.0	17.2	2.31	0.07
Location*Tip	18	85.5	4.8	0.64	0.82
Error	18	134.4	7.5	-	-

b)

	Degrees of Freedom	Sum of Square	Mean Square	F Value	p
Graphite	1	9.4	9.4	2.18	0.28
Tip	2	118.8	59.4	13.8	0.07
Error	2	8.7	4.3	-	-

c)

Variable	% of the Total	% Truncated
Graphite	1.6	1.5
Tip	25.4	24.5
Graphite*Tip	-3.7	0.0
Graphite*Tip*Location (Error)	76.7	74.0
Total	100.0	100.0

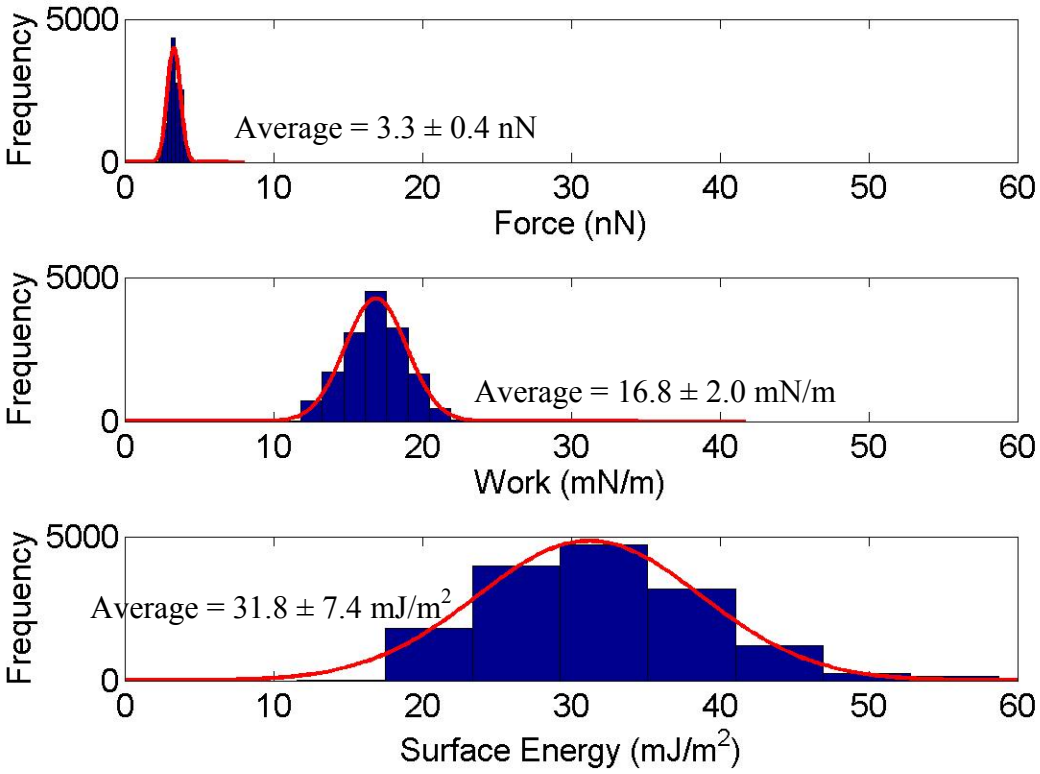

Figure 5-5: The force, work, and surface energy of graphite measured in water. The averages and standard deviations are listed next to each histogram.

Table 5-11: Average solid-liquid surface energy of graphite with water determined using the AFM and contact angle methods.

(Note: Models 2 and 3 do not rely on γ_{sv} input to calculate γ_{sl}. Therefore the data was input into the ambient column for simplicity.)

Method	Model		Ambient Force Measurements	Controlled RH Force Measurements
			Surface Energy (mJ/m^2)	
AFM	Model 1	Van Oss et al	18.5 (1.9)	22.8 (1.9)
		OWRK	16.1 (1.9)	20.4 (1.9)
		Neumann	12.6 (1.9)	16.9 (1.9)
	Model 2		31.8 (7.4)	-
	Model 3		34.5 (9.6)	-
	Model 4	Model 2 γ_{sv}	14.3 (1.9)	15.0 (1.9)
		Model 3 γ_{sv}	15.3 (1.9)	15.4 (1.9)
Contact Angle	Van Oss et al		30.0 (3.9)	NA
	OWRK		29.0 (4.2)	NA
	Neumann		25.0 (3.5)	NA

The second statistical analysis was done with the mica-water measurements. **Table 5-12a** and **Table 5-12b** give the SAS output for the analysis within subjects and between subjects. The statistical analysis for mica does not calculate any p values less than 0.05 and the null hypothesis was accepted. **Table 5-12c** captures the JMP output for the factors that contributed to variation while studying the interactions between mica and water. These results showed the majority of the variation was residual error, with a small portion attributed to tip variability. However, the SAS data did not indicate that any variability would invalidate the null hypothesis. Therefore, an average force, work, and surface energy data could be calculated (see **Figure 5-6**).

The average force of adhesion for mica, illustrated in **Figure 5-6**, was smaller compared to that of graphite. The smaller force value indicated mica's affinity for water. Similarly, the measured contact angle on mica was 10.0 ± 2.4, therefore, the water completely spread over the surface of mica. A strong interaction of water with mica meant the solid-liquid surface energy would also be small. The calculated solid-liquid surface energies from all four AFM models and contact angle are given in **Table 5-13**. Unfortunately, a direct comparison could not be made between AFM solid-liquid surface energy and contact angle solid-liquid surface energy because of the limitations with the indirect models used with contact angle measurements. Contact angles use Young's equation to balances the forces to determine solid-liquid surface energy. In some instances, negative solid-liquid surface energy values were obtained. These values did not have a physical meaning and make it challenging to evaluate the capabilities of the AFM. Scientifically, from contact angle measurements, one could suggest that the solid-liquid surface energy of water would be smaller than the solid-liquid surface energy of ethylene glycol and

diiodomethane. While this might be true according to the measured contact angles and the forces (reported in future sections), the variability of the contact angle solid-vapor surface energies of mica (41.3 – 65.2 mJ/m^2) has made it relatively impossible to unequivocally determine an average AFM solid-liquid surface energy and select the appropriate AFM model. This is illustrated further in the values shown in **Table 5-13**.

While the AFM solid-liquid surface energy could not be compared to the contact angle results, the applicability of the AFM models will still be addressed. For model 1, the solid-liquid surface energy values ranged from -0.9 to 23.0 mJ/m^2. This range was a direct reflection of the large contact angle solid-vapor surface energy range. Therefore, model 1 was not considered due to the increased level of complexity resulting from discrepancies in contact angle indirect models.

Models 2 and 3 were independent of contact measurements. The results from these two models were identical and resulted in the smallest calculated surface energy, which was consistent with expectation. The similarity of the two models also confirmed that the modification did not significantly alter the results, illustrating the small difference between $\gamma_{solid\text{-}liquid}$ and $\gamma_{tip\text{-}liquid}$. The small difference between the dissimilar components is necessary for the geometric mean to be valid. The geometric mean overestimates surface energy; therefore modifications have been made and surface energy components have been evaluated. Neumann found an empirical modification to correct for the overestimation. The geometric mean was developed for van der Waals interactions and the contact angle results indicated mica had a stronger AB or polar interaction than LW or dispersive. Therefore, to use the geometric mean with highly polar or electron donating/accepting capability, the assumption was made that the pure components'

differences in electronic properties and molecular size were small. [21] Any large differences and the geometric mean would overestimate surface energy, hence, the need for the modification. The studies done with mica-water indicate the assumption was valid.

Model 4 utilized only AFM data for the calculation of $\gamma_{surface\text{-}tip}$. There were differences in the AFM ambient and controlled $\gamma_{solid\text{-}vapor}$ surface energy (**Table 5-8**), but the solid-liquid surface energy variations were minimized by the compensating effects of two simultaneously changing variables. Without other reliable mica-water solid-liquid surface energy values, it was undetermined which of models 2, 3, or 4 is better. Since models 2 and 3 were equivalent, there was no need to go through a rigorous fitting, especially since software was not available. Also, there was no indication which model was better between model 2 and model 4. As mentioned, the overriding assumption for model 2 was that the geometric mean can be used to describe the interaction of two dissimilar materials as long as the component's differences in electronic properties and molecular size were small. Since mica also has electron donating/accepting capabilities, it was not certain that the geometric mean captured these interactions, despite model 2 and model 3 reporting the same result. The empirical correction factor in model 3 has not been used outside of contact angle measurements and might not be applicable in fitting the AFM data. Model 4 assumed that the surface was unchanged between vapor and liquid measurements. Since the surface of mica was relatively inert, this assumption might be valid. However, the assumption might not apply when using a crystalline material. Therefore, models 2, 3, and 4 were all considered viable options for evaluating hydrophilic surfaces.

Table 5-12: Mixed model statistics for mica AFM measurements with water. a) Repeated measures ANOVA for within subject effects, b) repeated measures ANOVA for between subjects, and c) the variable that demonstrates the largest percentage of variance for mica – water AFM measurements.

a)

	Degrees of Freedom	Sum of Square	Mean Square	F Value	p
Location	9	0.09	0.009	1.53	0.21
Location*Mica	9	0.03	0.003	0.54	0.83
Location*Tip	18	0.15	0.008	1.38	0.25
Error	18	0.11	0.006	-	-

b)

	Degrees of Freedom	Sum of Square	Mean Square	F Value	p
Mica	1	0.0007	0.0007	0.10	0.78
Tip	2	0.0600	0.0300	4.12	0.19
Error	2	0.0145	0.007	-	-

c)

Variable	% of the Total	% Truncated
Mica	-2.9	0.0
Tip	15.1	14.7
Mica*Tip	1.0	1.0
Mica*Tip*Location (Error)	86.7	84.3
Total	100.0	100.0

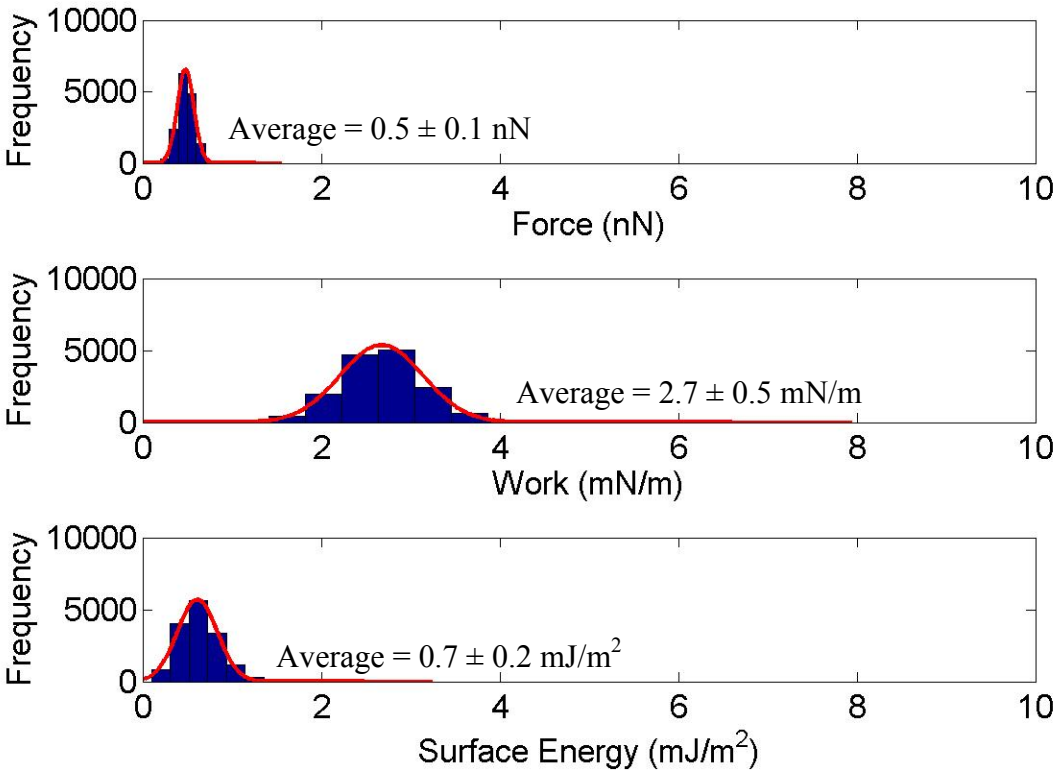

Figure 5-6: The force, work, and surface energy of mica measured in water. The averages and standard deviations are listed next to each histogram.

Table 5-13: Average solid-liquid surface energy of mica with water determined using the AFM and contact angle methods.

(Note: Models 2 and 3 do not rely on γ_{sv} input to calculate γ_{sl}. Therefore the data was input into the ambient column for simplicity.)

Method	Model		Ambient Force Measurements	Controlled RH Force Measurements
			Surface Energy (mJ/m^2)	
AFM	Model 1	Van Oss et al	-0.9 (1.1)	12.6 (1.1)
		OWRK	23.0 (1.1)	36.5 (1.1)
		Neumann	14.8 (1.1)	28.3 (1.1)
	Model 2		0.7 (0.2)	-
	Model 3		0.7 (0.2)	-
	Model 4	Model 2 γ_{sv}	2.8 (1.1)	1.9 (1.1)
		Model 3 γ_{sv}	2.6 (1.1)	2.4 (1.1)
Contact Angle	Van Oss et al		-31.1 (2.3)	NA
	OWRK		-6.4 (0.5)	NA
	Neumann		-14.7 (0.6)	NA

5.1.2.2 Diiodomethane Solid-Liquid Surface Energy

The spring constant, tip radii, and tip-liquid$_{diiodomethane}$ surface energies were determined for calculation of the solid-liquid surface energy of mica and graphite in diiodomethane. **Table 5-14** shows the spring constant, radii, and other values used for the calculation of mica and graphite solid-liquid$_{diiodomethane}$ surface energy.

Once the force measurements were collected for graphite-diiodomethane, statistical analysis was performed. **Table 5-15a and b** show the results from the SAS analysis. The p values indicated that the null hypothesis could be accepted. Diiodomethane and graphite had a strong interaction because the dominant forces were van der Waals. Therefore, the variability over the locations was expected to be smaller than that of graphite-water. However, because of the steps due to cleavage of the sample, variability between subjects still existed (i.e. graphite samples or tips). In **Table 5-15b**, the p value of tips was small, but still greater than 0.05. Thus, JMP data still indicated (**Table 5-15c**) that tips and residual instrumental errors were the largest contributors to the overall variability.

Since the null hypothesis was accepted, the average force, work, and surface energy was calculated and plotted in **Figure 5-7**. The force of adhesion between graphite-diiodomethane was small because there was a strong attractive force. The same was true for the contact angle measurements; the measured angle of diiodomethane on graphite was 37.8 ± 1.4, indicating that diiodomethane spread over graphite much more than water. Therefore, the solid-liquid surface energy values were expected to be low. The values for solid-liquid surface energy of graphite-diiodomethane, calculated from all four surface energy models, are listed in **Table 5-16** along with contact angle values. It was

challenging to compare the results of the contact angle measurements to the AFM data because of the indirect models and Young's equation. One negative number was observed from the diiodomethane measurements; therefore, the range of solid-liquid surface energies was (-3.5 to 0.7 mJ/m^2). However, the AFM results could be compared to the OWRK and van Oss contact angle models. The solid-liquid surface energy for AFM model 1 using γ_{st} determined from van Oss and OWRK contact angle model was relatively low. Thus, there were two reasons for avoiding the use of model 1. First, the solid-liquid surface energy determined by the other AFM models was smaller, and as a result, comparable to contact angle results. Second, requiring a combination of two surface energy methods suggested the AFM was not an adequate instrument for evaluating surface energy. Therefore, model 1 was still not the optimal choice for the AFM. Model 2 and 3 were similar in solid-liquid surface energy and also comparable to the contact angle OWRK solid-liquid surface energy. These two models continued to show applicability with the AFM and surfaces with van der Waals forces. Also, since the γ_{sl} and γ_{tl} were similar, the modification did not show differences when the solid-liquid surface energy was calculated. Model 4 was also successfully compared to contact angle data. Ambient and controlled humidity solid-liquid surface energies were not significantly different because the $\gamma_{solid\text{-}vapor}$ for graphite in ambient and controlled environment were also not significantly different (**Table 5-2**). Therefore, model 4 could be used. In the previous section, discussion of mica-water solid-liquid surface energy compared the advantages and disadvantages of using models 2, 3, and 4. In studies with inert surfaces, the $\gamma_{surface\text{-}tip}$ may be unchanged between vapor and liquid measurements;

however, it is cautioned that this may not be the case for crystalline material. However, consideration will be given to these models when calculating solid-liquid surface energy.

Table 5-14: Spring constant, tip radius, and average tip-liquid surface energy (standard deviation) are listed for the AFM tips used to measure the solid-liquid surface energy of graphite and mica in diiodomethane.

Tip	Material	Spring constant (N/m)	Radius (nm)	Force (nN)	Work (mN/m)	Surface Energy (mJ/m^2)
1	Mica	.04	45	0.8 (0.1)	3.8 (0.5)	1.9 (0.2)
2			43	0.9 (0.3)	4.7 (1.3)	2.3 (0.7)
3			42	0.8 (0.1)	4.1 (0.5)	2.1 (0.3)
1	Graphite		42	0.8 (0.3)	4.1 (1.3)	2.1 (0.6)
2			43	0.8 (0.2)	3.7 (1.1)	1.9 (0.6)
3			43	0.9 (0.3)	4.6 (1.4)	2.3 (0.7)

Table 5-15: Mixed model statistics for graphite AFM measurements with diiodomethane. a) Repeated measures ANOVA for within subject effects, b) repeated measures ANOVA for between subjects, and c) the variable that demonstrates the largest percentage of variance for graphite – diiodomethane AFM measurements.

a)

	Degrees of Freedom	Sum of Square	Mean Square	F Value	p
Location	9	0.29	0.03	1.45	0.24
Location*Graphite	9	0.24	0.03	1.19	0.36
Location*Tip	18	0.60	0.03	1.50	0.20
Error	18	0.40	0.02	-	-

b)

	Degrees of Freedom	Sum of Square	Mean Square	F Value	p
Graphite	1	0.02	0.024	3.00	0.23
Tip	2	0.26	0.129	16.08	0.06
Error	2	0.02	0.008	-	-

c)

Variable	% of the Total	% Truncated
Graphite	1.7	1.6
Tip	18.8	17.7
Graphite*Tip	-6.1	0.0
Graphite*Tip*Location (Error)	85.7	80.7
Total	100.0	100.0

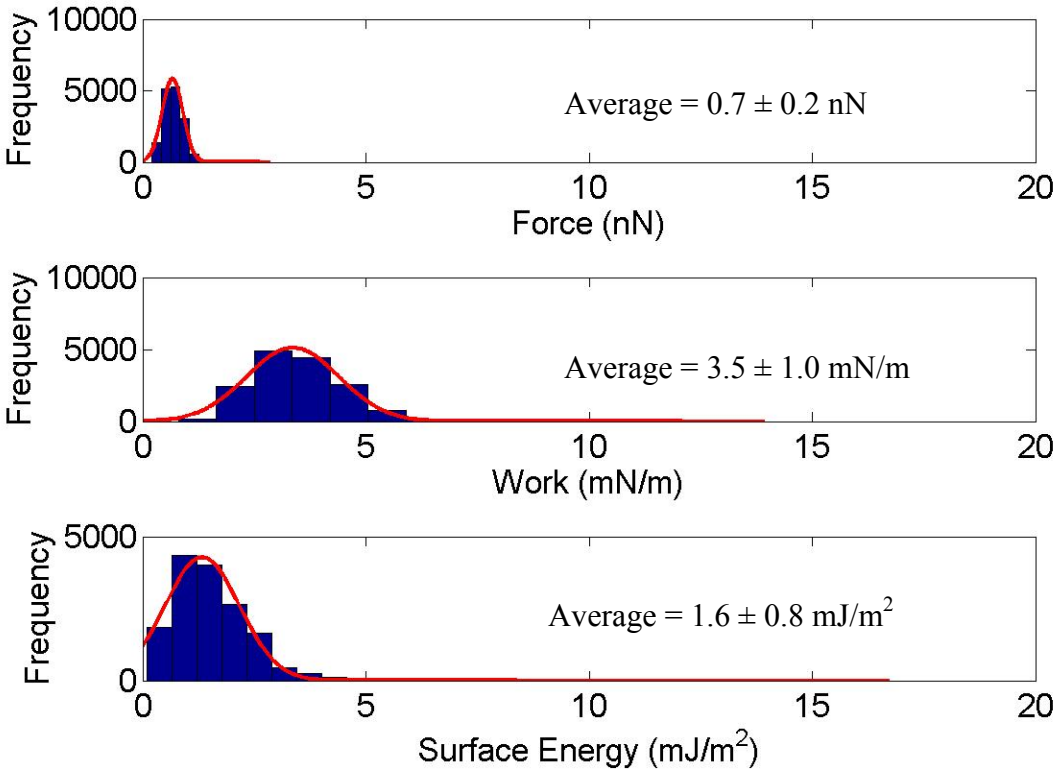

Figure 5-7: The force, work, and surface energy of graphite-diiodomethane. The averages and standard deviations are listed next to each histogram.

b)

Table 5-16: Average solid-liquid surface energy of graphite with diiodomethane determined using the AFM and contact angle methods.

(Note: Models 2 and 3 do not rely on γ_{sv} input to calculate γ_{sl}. Therefore the data was input into the ambient column for simplicity.)

Method	Model		Ambient Force Measurements	Controlled RH Force Measurements
			Surface Energy (mJ/m^2)	
AFM	Model 1	Van Oss et al	5.3 (0.9)	9.7 (0.9)
		OWRK	2.9 (0.9)	7.3 (0.9)
		Neumann	-0.6 (0.9)	3.8 (0.9)
	Model 2		1.6 (0.8)	-
	Model 3		1.6 (0.8)	-
	Model 4	Model 2 γ_{sv}	1.1 (0.9)	1.8 (0.9)
		Model 3 γ_{sv}	1.1 (0.9)	1.8 (0.9)
Contact Angle	Van Oss et al		0.6 (0.1)	NA
	OWRK		0.7 (0.9)	NA
	Neumann		-3.3 (1.6)	NA

Next, statistical analysis was done with the mica-diiodomethane measurements. The SAS output in **Table 5-17a** and **Table 5-17b** for the analysis within subjects and between subjects indicates that all p values were greater than 0.05; therefore, the null hypothesis was accepted. **Table 5-17c** gives the JMP output for the contributing factors of variation in the study of mica-diiodomethane interaction. These results showed the majority of the variation was residual error, while a small portion of error was attributed to the tips and the mica samples. The variability between mica samples and tips could have been caused by a less favorable interaction with diiodomethane. Mica did not have the same cleavage difficulties associated with graphite; therefore, few to no steps form during the removal of a layer of mica. Like the mica-water statistical analysis, the SAS data did not indicate that any variability would invalidate the null hypothesis. Therefore, an average force, work, and surface energy data could be calculated (**Figure 5-8**).

The average force of adhesion for mica, illustrated in **Figure 5-8**, was larger compared to that of graphite-diiodomethane. The large force value indicated that mica's interaction with diiodomethane was less than that of graphite-diiodomethane. Similarly, the measured contact angle on mica was 41.0 ± 2.9; therefore, the spread of diiodomethane was less than the spread of water on mica. A weak interaction of diiodomethane with mica meant the solid-liquid surface energy would be large. The calculated solid-liquid surface energies from all four AFM models and contact angle are given in **Table 5-18**. As discussed in the mica-water surface energy section, because of contact angle limitations, a direct comparison cannot be made with the AFM and contact angle data. In this study, contact angle solid-liquid surface energy values ranged from 0.8 to 26.9 mJ/m^2. Scientifically, solid-liquid surface energy of diiodomethane should be larger than

the solid-liquid surface energy of ethylene glycol and water, which was verified by the measured contact angles and the forces presented in this chapter. However, the variability of the contact angle solid-vapor surface energies of mica (41.3 – 65.2 mJ/m^2) made it relatively impossible to unequivocally determine an average AFM solid-liquid surface energy and the best AFM model. This is illustrated further in the values shown in **Table 5-18**.

Although the AFM data for one model cannot be compared to the contact angle results, the applicability of the AFM models will be evaluated. For model 1, the solid-liquid surface energy values ranged from 5.1 to 42.5 mJ/m^2. The range was a reflection of the large contact angle solid-vapor surface energy range mentioned above. Therefore, model 1 was not considered because of the level of complexity added from discrepancies in contact angle indirect models. The indirect models and Young's equation limited comparison of the AFM results for a hydrophilic surface.

Models 2 and 3 were independent of contact measurements. The results from these two models were similar and fell between the contact angle surface energy ranges. Since the true value of mica-diiodomethane γ_{sl} was unclear from contact angle measurements, the assumptions may have been invalid. So far the geometric mean and modified geometric mean have proven useful for graphite-water and graphite-diiodomethane surface energy. However, graphite had mostly van der Waals forces contributing to the overall surface energy. Therefore, using a geometric mean model to calculate surface energy was acceptable. The geometric mean, when applied to mica-ambient measurements, did show agreement with one of the contact angle results. Since the variability was so large with contact angle solid-vapor surface energy, it could not serve as the only justification

against the geometric mean. Thus, more information was needed to select between either of these models and model 4.

Model 4 used the AFM solid-vapor surface energy to determine $\gamma_{surface\text{-}tip}$ and then solid-liquid surface energy. The limitation of this model came from the assumption that $\gamma_{surface\text{-}tip}$ was constant. The results were slightly lower than the results obtained from model 2 and 3, but still larger than water and ethylene glycol solid-liquid surface energy on mica. Therefore it was difficult to completely disregard the validity of results calculated from this model.

Table 5-17: Mixed model statistics for mica AFM measurements with diiodomethane. a) Repeated measures ANOVA for within subject effects, b) repeated measures ANOVA for between subjects, and c) the variable that demonstrates the largest percentage of variance for mica – diiodomethane AFM measurements.

a)

	Degrees of Freedom	Sum of Square	Mean Square	F Value	p
Location	9	16.1	1.8	1.48	0.23
Location*Mica	9	12.7	1.4	1.17	0.37
Location*Tip	18	34.7	1.9	1.60	0.16
Error	18	21.7	1.2	-	-

b)

	Degrees of Freedom	Sum of Square	Mean Square	F Value	p
Mica	1	12.3	12.3	3.27	0.21
Tip	2	0.4	0.2	0.06	0.95
Error	2	7.5	3.8	-	-

c)

Variable	% of the Total	% Truncated
Mica	15.3	14.0
Tip	-9.5	0.0
Mica*Tip	12.0	10.9
Mica*Tip*Location (Error)	82.3	75.1
Total	15.3	14.0

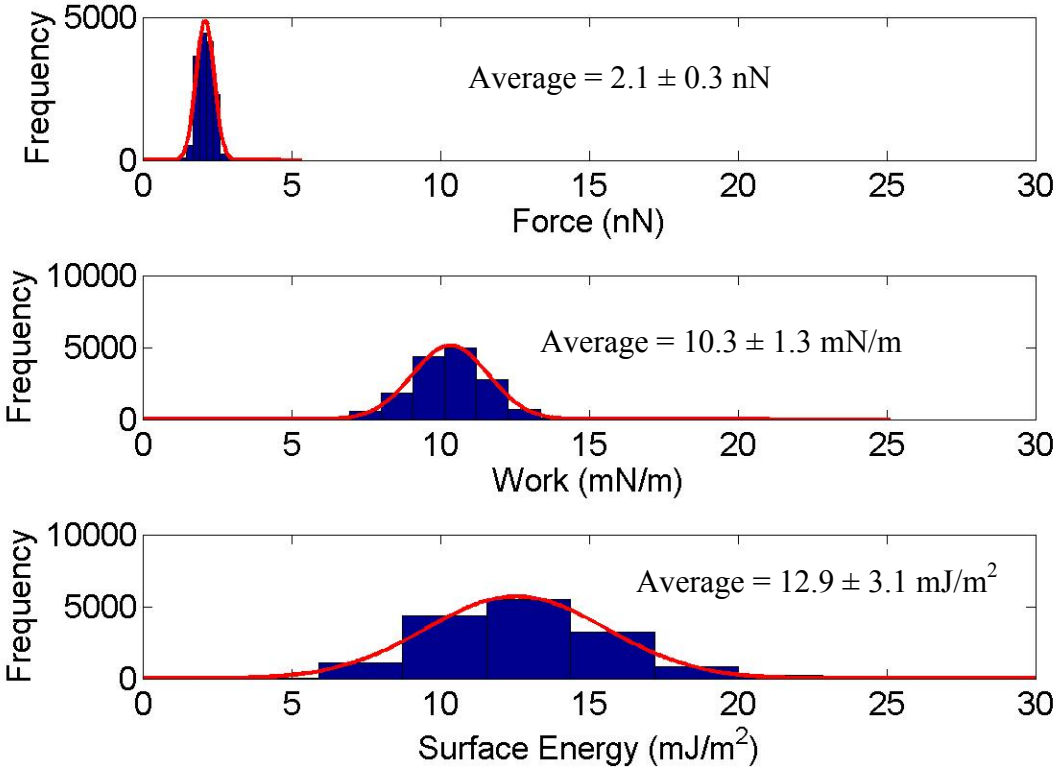

Figure 5-8: The force, work, and surface energy of mica-diiodomethane. The averages and standard deviations are listed next to each histogram.

Table 5-18: Average solid-liquid surface energy of mica with diiodomethane determined using the AFM and contact angle methods.

(Note: Models 2 and 3 do not rely on γ_{sv} input to calculate γ_{sl}. Therefore the data was input into the ambient column for simplicity.)

Method	Model		Ambient Force Measurements	Controlled RH Force Measurements
			Surface Energy (mJ/m^2)	
AFM	Model 1	Van Oss et al	5.1 (1.5)	18.6 (1.5)
		OWRK	29.0 (1.5)	42.5 (1.5)
		Neumann	20.8 (1.5)	34.3 (1.5)
	Model 2		12.9 (3.1)	-
	Model 3		13.6 (4.3)	-
	Model 4	Model 2 γ_{sv}	8.8 (1.5)	7.9 (1.5)
		Model 3 γ_{sv}	8.6 (1.5)	8.4 (1.5)
Contact Angle	Van Oss et al		0.8 (0.2)	NA
	OWRK		26.9 (0.4)	NA
	Neumann		18.7 (1.7)	NA

5.1.2.3 Formamide Solid-Liquid Surface Energy

The spring constant, tip radii, and tip-liquid$_{formamidel}$ surface energies were measured to determine the solid-liquid surface energy of graphite in formamide. **Table 5-19** shows the values used to calculate graphite solid-liquid$_{formamide}$ surface energy.

Since formamide is a hygroscopic liquid, it was dried using distillation prior to use for AFM and contact angle measurements. The dried liquid was then rehydrated to 0.5%, 1%, and 5% w/w water/formamide. The water amount was confirmed using Coulometric Karl Fisher titration. Each liquid was used the day it was prepared.

Force measurements were made on graphite in formamide using the tips in **Table 5-19**. Data analysis was performed in SAS and JMP. The statistics for dried, 0.5%, 1%, and 5% w/w water/formamide are listed in **Table 5-20**, **Table 5-21**, **Table 5-22**, and **Table 5-23**. From the statistics for graphite with dry, 0.5% w/w, and 1% w/w, and .5% w/w water/formamide the null hypothesis was accepted and an average force, work, and surface energy could be calculated. The plots of the these averages for graphite with dry formamide, 0.5%, 1%, and 5% are shown in **Figure 5-9**, **Figure 5-10**, **Figure 5-11**, and **Figure 5-12**.

Table 5-19: Tip radius and average tip-liquid surface energy (standard deviation) are listed for the AFM tips used to measure the solid-liquid surface energy of graphite in formamide. There are four conditions listed for formamide, dried, 0.5%, 1%, and 5% w/w water in formamide.

Tip	Condition	Spring constant (N/m)	Radius (nm)	Force (nN)	Work (mN/m)	Surface Energy (mJ/m^2)
1	Dry	.05	41	0.6 (0.2)	3.0 (0.8)	1.5 (0.4)
2			40	0.6 (0.4)	2.9 (1.9)	1.4 (0.9)
3			41	0.5 (0.3)	2.6 (1.8)	1.3 (0.9)
1	0.5% w/w water		41	0.6 (0.2)	3.3 (1.2)	1.7 (0.6)
2			40	0.8 (0.2)	4.1 (1.1)	2.1 (0.6)
3			41	0.6 (0.2)	3.3 (0.8)	1.7 (0.4)
1	1% w/w water		41	0.8 (0.2)	4.1 (1.1)	2.0 (0.6)
2			40	0.9 (0.3)	4.6 (1.6)	2.3 (0.8)
3			41	0.9 (0.2)	4.5 (1.2)	2.2 (0.6)
1	5% w/w water		41	0.7 (0.2)	3.8 (0.8)	1.9 (0.4)
2			40	0.8 (0.2)	4.3 (1.0)	2.2 (0.5)
3			41	0.9 (0.2)	4.8 (1.1)	2.4 (0.6)

The average force of adhesion from the AFM measurements increased with the increase in water content in the formamide, demonstrating that moisture in the formamide had a clear effect of the AFM measurements.

$$F_{dry} > F_{0.5\%\ w/w} > F_{1\%\ w/w} > F_{5\%w/w}$$

The solid-liquid surface energy of graphite-water was about 30 mJ/m^2 and with 5% w/w water added to formamide, the AFM calculated solid-liquid surface energy trended towards the graphite-water solid-liquid surface energy. Thus, the AFM was extremely sensitive to changes in liquid compositions. It is important to note that this is a limitation of contact angles. In chapter 2, the problem of non-homogenous distribution of additives at the three phases of contact angle measurements was discussed. These data from the AFM demonstrated the instrument's ability to detect changes to a solvent and more importantly, how the changes affect the interaction between the solvent and surface. The data also showed the effect that water had on the variations in measurements. There was an increase in the range of forces, which was exacerbated in the surface energy calculations as the water in formamide increased from about 0% to 5% w/w water/formamide. The variability was also evident in the JMP data, as shown in **Table 5-20c**, **Table 5-21c** ,**Table 5-22c**, and **Table 5-23c**. As the water increased, the cause of variability started to shift from purely residual error of the measurements to large error in graphite samples, tips, and the interaction between the sample and tip (**Table 5-23c**). Therefore, it was important to ensure hygroscopic liquids were dried before use in AFM measurements for a "true" surface energy value.

The force of adhesion measurements for dried formamide were expected to fall somewhere between the measurements from diiodomethane and water since formamide

has polar and nonpolar components. Therefore, the surface energy would also project in the middle. This was also observed in the contact angle measurements. The contact angle measurement of dried formamide on graphite was 60.9 ± 2.4. The force of adhesion from AFM measurements reflected the same. In **Table 5-24**, the graphite-dried formamide solid-liquid surface energy is shown for AFM and contact angle measurements. This was the first time that the choice of models was not straightforward. The contact angle data gave a solid-liquid surface energy range of 8.7 to 13.7 mJ/m^2 and the range from the four AFM models is 5 to 15.2 mJ/m^2.

Model 1 used the γ_{sv} from contact angle measurements to determine γ_{st}. Since the graphite-ambient solid-vapor surface energy was only 4 mJ/m^2 higher than the controlled humidity solid-vapor surface energy, the difference between the solid-liquid surface energies for model 1 was also small. Although the values were similar, the controlled RH force calculated solid-liquid surface energy was closest to the corresponding contact angle method. This was the first data set to have comparable results with contact angle results. However, for the AFM to be a standalone instrument, it was still not recommended to include other surface energy measurements into an AFM model. Models 2 and 3, which use the geometric mean, calculated an average surface energy equivalent to the van Oss contact angle solid-liquid surface energy. These models consistently showed the best comparability between the AFM and contact angle results. Since, graphite has mostly van der Waals forces; it satisfied the necessary assumptions for a model developed for non-bonding interactions. Model 4 used the AFM γ_{sv} to determine γ_{st}. Since γ_{sv} from the AFM measurements was smaller than the γ_{sv} of the contact angle measurements, the γ_{sl} was also expected to be smaller. These results were

relatively comparable to the lower end of the contact angle results (Neumann model). Compared to water and diiodomethane, formamide has both dispersive and polar intramolecular forces. Water has more polar forces and diiodomethane has more dispersive forces. From these results, it seemed that the liquid with both forces gave the best and most consistent results from the all four models. The extremes, water and diiodomethane, each seemed to have a few differences whether it's from the limitations of contact angle measurements or the inherent variability in the AFM measurements. Formamide created more of an optimal condition for determining surface energy from indirect models.

The average force of adhesion measurements made in rehydrated formamide increased immediately even with only a 0.5% w/w increase in water content, causing the surface energy to increase accordingly. The AFM and contact angle solid-liquid surface energy are shown in **Table 5-25**. The contact angle for the 0.5% w/w water changed as well, with the corresponding increase in solid-liquid surface energy. The contact angle solid-liquid surface energy with 0.5% w/w water in formamide ranged from 11.7 to 18.2 mJ/m^2 and from 7.6 to 19.8 mJ/m^2 with AFM measurement The evaluation of the AFM models for this liquid is the same as the results for dried formamide. Model 1solid-liquid surface energy from the controlled RH γ_{st}, was comparable to the corresponding contact angle models. Models 2 and 3 were comparable to the van Oss contact angle solid-liquid surface energy, and model 4 was on the lower end of the range closer to the Neumann contact angle solid-liquid surface energy. The change in force of adhesion and contact angles with added water in formamide illustrates the importance of drying hygroscopic

liquids. The true solid-liquid surface energy between the solvent and sample's surface cannot be found if the water is not removed.

The average force of adhesion measurements made in 1% w/w and 5% w/w water/formamide continued to increase; subsequently causing the surface energy to increase. The AFM and contact angle solid-liquid surface energy are shown for 1% and 5% w/w added water in **Table 5-26** and **Table 5-27**. The contact angle with 1% w/w water decreased (62.4 ± 3.8) as compared to the angle measured with 0.5% w/w water, and then increased at 5% w/w water (64.3 ± 4.1). This lack of a clear trend illustrates why additive solutions are not used with contact angle measurements. Since the contact angles did not increase in the same manner as the AFM measurements, comparing the solid-liquid surface energies became more challenging. For 1% w/w water in formamide, model 1 (ambient measurements) and model 4 were most comparable. Model 1 (controlled RH), model 2, and model 3 were less comparable to the contact angle values because the solid-liquid surface energy increased. It is hard to determine the validity of the comparison because of the lack of confidence in the contact angle values with mixtures. Similarly, for the 5% w/w water, model 1 (ambient measurements) and model 4 were more comparable to the contact angle solid-liquid surface energy, and model 1 (controlled RH), model 2, and model 3 were less comparable. The JMP statistics in **Table 5-22c** and **Table 5-23c** for 1% and 5% w/w water/formamide also indicate that the variability increased in the AFM measurements. The propagation of error through other variables showed possible challenges with the AFM. These limitations might also have been attributed to the use of a water mixture on a hydrophobic surface. The AFM is a more sensitive instrument than the macroscopic sessile drop contact angles. Thus, the

spread and variability in the AFM measurements could be due to both formamide-graphite and water-graphite interactions. To evaluate the AFM's ability to measure the force of adhesion in a mixture solution, the next study was the investigation of the hydrophilic surface of mica with dried and rehydrated ethylene glycol.

Table 5-20: Mixed model statistics for graphite AFM measurements with dry formamide. a) Repeated measures ANOVA for within subject effects, b) repeated measures ANOVA for between subjects, and c) the variable that demonstrates the largest percentage of variance for graphite – dry formamide AFM measurements.

a)

	Degrees of Freedom	Sum of Square	Mean Square	F Value	p
Location	9	16.4	1.8	0.87	0.56
Location*Graphite	9	14.4	1.6	0.77	0.65
Location*Tip	18	40.3	2.2	1.07	0.45
Error	18	37.7	2.1	-	-

b)

	Degrees of Freedom	Sum of Square	Mean Square	F Value	p
Graphite	1	4.8	4.8	2.33	0.27
Tip	2	0.6	0.3	0.16	0.86
Error	2	4.1	2.1	-	-

c)

Variable	% of the Total	% Truncated
Graphite	4.5	4.3
Tip	-4.2	0.0
Graphite*Tip	0.1	0.0
Graphite*Tip*Location (Error)	99.7	95.7
Total	100.0	100.0

Table 5-21: Mixed model statistics for graphite AFM measurements with 0.5% w/w water/formamide. a) Repeated measures ANOVA for within subject effects, b) repeated measures ANOVA for between subjects, and c) the variable that demonstrates the largest percentage of variance for graphite – 0.5% w/w water/formamide AFM measurements.

a)

	Degrees of Freedom	Sum of Square	Mean Square	F Value	p
Location	9	4.3	0.5	0.94	0.52
Location*Graphite	9	3.6	0.4	0.80	0.62
Location*Tip	18	9.4	0.5	1.04	0.47
Error	18	9.1	0.5	-	-

b)

	Degrees of Freedom	Sum of Square	Mean Square	F Value	p
Graphite	1	1.3	1.3	1.63	0.33
Tip	2	1.5	0.7	0.91	0.52
Error	2	1.6	0.8	-	-

c)

Variable	% of the Total	% Truncated
Graphite	-2.5	0.0
Tip	-4.7	0.0
Graphite*Tip	5.9	5.5
Graphite*Tip*Location (Error)	101.3	94.5
Total	100	100

Table 5-22: Mixed model statistics for graphite AFM measurements with 1% w/w water/formamide. a) Repeated measures ANOVA for within subject effects, b) repeated measures ANOVA for between subjects, and c) the variable that demonstrates the largest percentage of variance for graphite – 1% w/w water/formamide AFM measurements.

a)

	Degrees of Freedom	Sum of Square	Mean Square	F Value	p
Location	9	127.9	14.2	0.72	0.69
Location*Graphite	9	134.9	15.0	0.76	0.66
Location*Tip	18	497.3	27.6	1.39	0.24
Error	18	356.6	19.8	-	-

b)

	Degrees of Freedom	Sum of Square	Mean Square	F Value	p
Graphite	1	26.9	26.9	1.60	0.33
Tip	2	289.8	144.9	8.61	.10
Error	2	33.7	16.8	-	-

c)

Variable	% of the Total	% Truncated
Graphite	1.2	1.2
Tip	22.7	22.3
Graphite*Tip	-1.8	0.0
Graphite*Tip*Location (Error)	77.9	76.5
Total	100.0	100.0

Table 5-23: Mixed model statistics for graphite AFM measurements with 5% w/w water/formamide. a) Repeated measures ANOVA for within subject effects, b) repeated measures ANOVA for between subjects, and c) the variable that demonstrates the largest percentage of variance for graphite – 5% w/w water/formamide AFM measurements.

a)

	Degrees of Freedom	Sum of Square	Mean Square	F Value	p
Location	9	106.6	11.8	0.85	0.59
Location*Graphite	9	203.9	22.7	1.62	0.18
Location*Tip	18	335.4	18.6	1.33	0.28
Error	18	252.0	14.0	-	-

b)

	Degrees of Freedom	Sum of Square	Mean Square	F Value	p
Graphite	1	138.9	138.9	3.11	0.22
Tip	2	202.3	101.2	2.27	0.31
Error	2	89.2	44.6	-	-

c)

Variable	% of the Total	% Truncated
Graphite	12.0	12.0
Tip	10.8	10.8
Graphite*Tip	10.2	10.3
Graphite*Tip*Location (Error)	67.0	67.0
Total	100.0	100.0

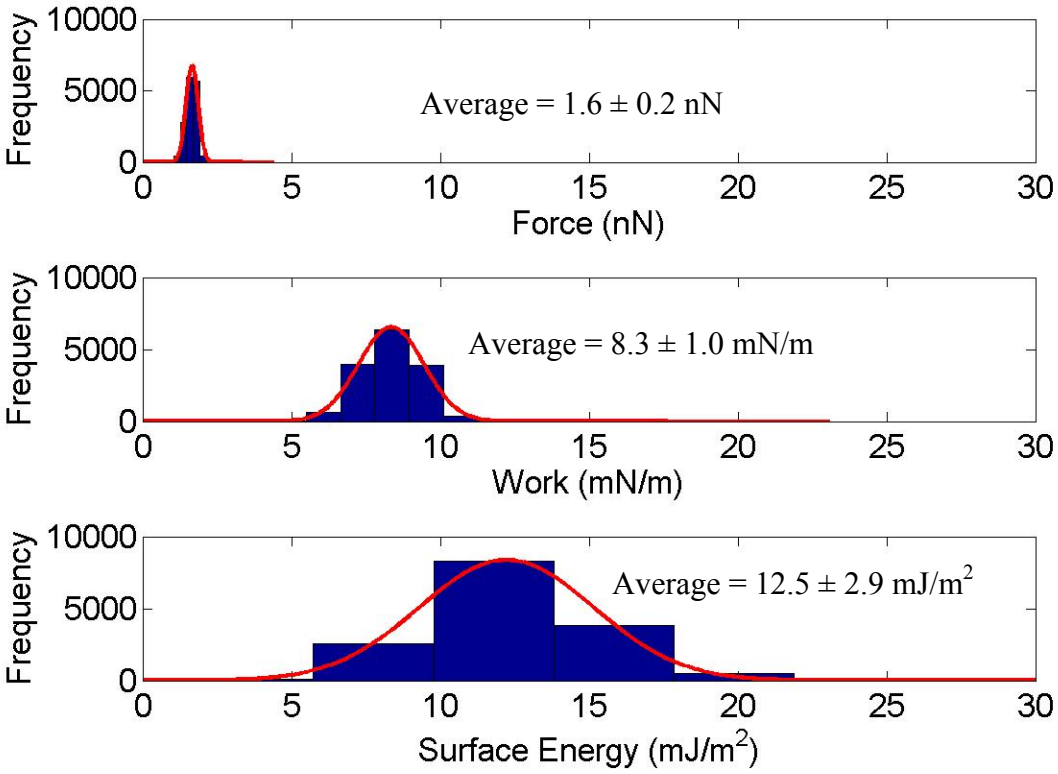

Figure 5-9: The force, work, and surface energy of graphite-dried formamide. The averages and standard deviations are listed next to each histogram.

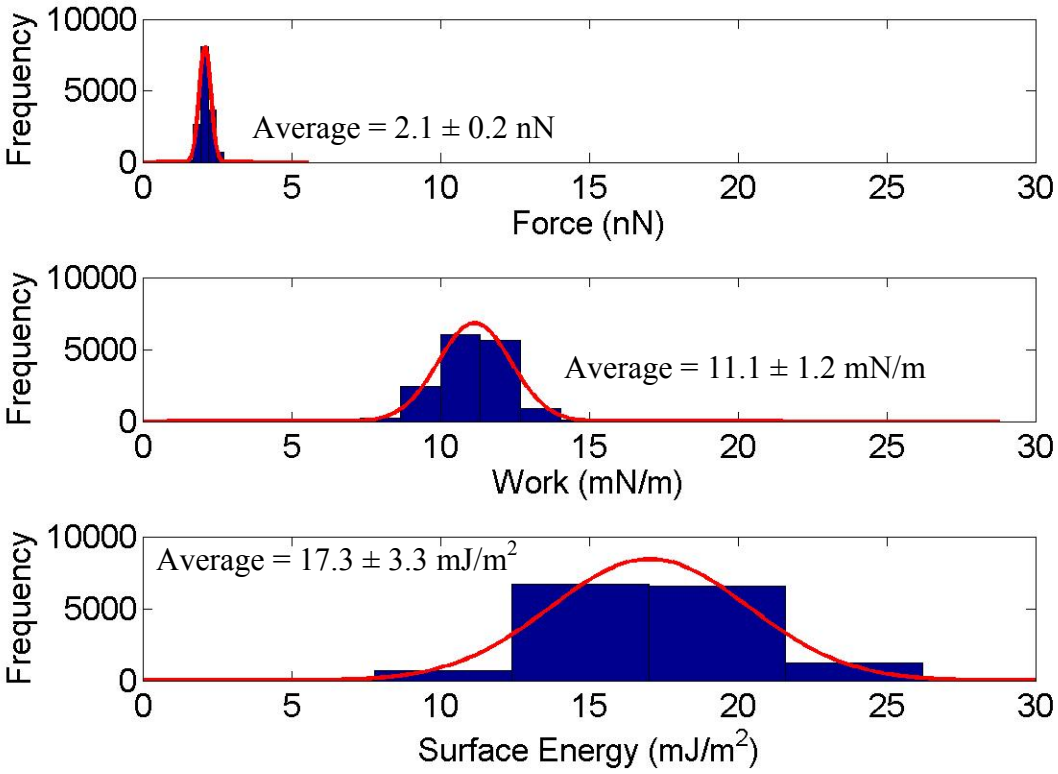

Figure 5-10: The force, work, and surface energy of graphite-0.5% w/w formamide. The averages and standard deviations are listed next to each histogram.

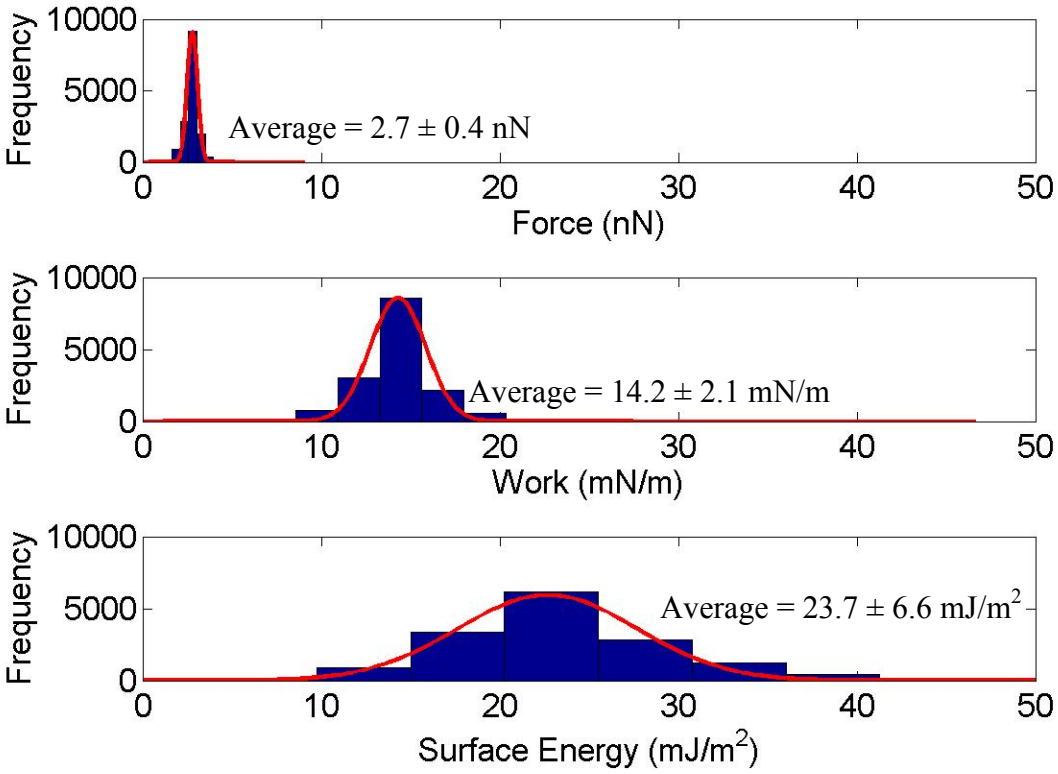

Figure 5-11: The force, work, and surface energy of graphite-1% w/w formamide. The averages and standard deviations are listed next to each histogram.

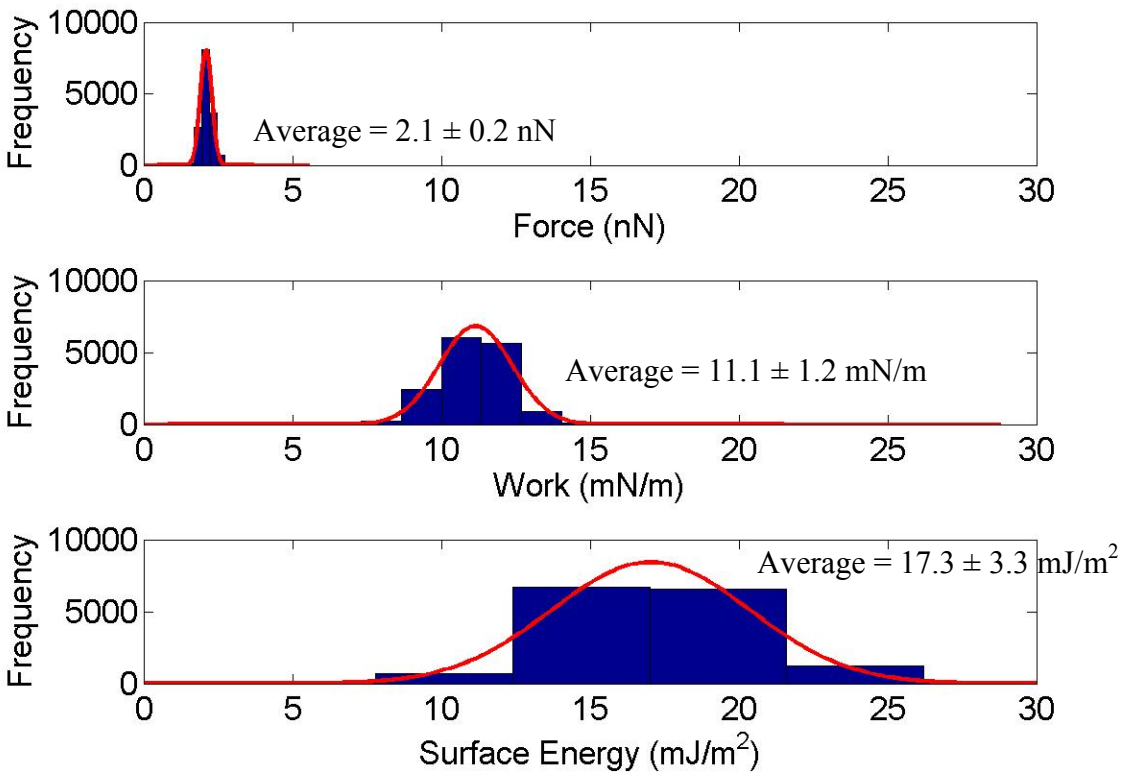

Figure 5-12: The force, work, and surface energy of graphite-5% w/w formamide. The averages and standard deviations are listed next to each histogram.

Table 5-24: Average solid-liquid surface energy of graphite with dry formamide determined using the AFM and contact angle methods.

(Note: Models 2 and 3 do not rely on γ_{sv} input to calculate γ_{sl}. Therefore the data was input into the ambient column for simplicity.)

Method	Model		Ambient Force Measurements	Controlled RH Force Measurements
			Surface Energy (mJ/m^2)	
AFM	Model 1	Van Oss et al	10.9 (1.0)	15.2 (1.0)
		OWRK	8.5 (1.0)	12.8 (1.0)
		Neumann	5.0 (1.0)	9.3 (1.0)
	Model 2		12.5 (2.9)	-
	Model 3		13.0 (3.3)	-
	Model 4	Model 2 γ_{sv}	6.7 (1.0)	7.3 (1.0)
		Model 3 γ_{sv}	7.6 (1.0)	7.7 (1.0)
Contact Angle	Van Oss et al		13.7 (2.8)	NA
	OWRK		12.6 (2.2)	NA
	Neumann		8.7 (1.9)	NA

Table 5-25: Average solid-liquid surface energy of graphite with 0.5% w/w water/formamide determined using the AFM and contact angle methods.

(Note: Models 2 and 3 do not rely on γ_{sv} input to calculate γ_{sl}. Therefore the data was input into the ambient column for simplicity.)

Method	Model		Ambient Force Measurements	Controlled RH Force Measurements
			Surface Energy (mJ/m^2)	
AFM	Model 1	Van Oss et al	13.5 (1.4)	17.8 (1.4)
		OWRK	11.1 (1.4)	15.4 (1.4)
		Neumann	7.6 (1.4)	11.9 (1.4)
	Model 2		17.3 (3.3)	-
	Model 3		19.8 (4.9)	-
	Model 4	Model 2 γ_{sv}	9.3 (1.4)	10.0 (1.4)
		Model 3 γ_{sv}	10.3 (1.4)	10.4 (1.4)
Contact Angle	Van Oss et al		18.2	NA
	OWRK		14.8	NA
	Neumann		11.7	NA

Table 5-26: Average solid-liquid surface energy of graphite with 1% w/w water/formamide determined using the AFM and contact angle methods.

(Note: Models 2 and 3 do not rely on γ_{sv} input to calculate γ_{sl}. Therefore the data was input into the ambient column for simplicity.)

Method	Model		Ambient Force Measurements	Controlled RH Force Measurements
			Surface Energy (mJ/m^2)	
AFM	Model 1	Van Oss et al	16.0 (2.0)	20.3 (2.0)
		OWRK	13.6 (2.0)	17.9 (2.0)
		Neumann	10.1 (2.0)	14.4 (2.0)
	Model 2		23.7 (6.6)	-
	Model 3		25.1 (8.0)	-
	Model 4	Model 2 γ_{sv}	11.8 (2.0)	12.5 (2.0)
		Model 3 γ_{sv}	12.8 (2.0)	12.9 (2.0)
Contact Angle	Van Oss et al		13.6	NA
	OWRK		12.9	NA
	Neumann		8.8	NA

Table 5-27: Average solid-liquid surface energy of graphite with 5% w/w water/formamide determined using the AFM and contact angle methods.

(Note: Models 2 and 3 do not rely on γ_{sv} input to calculate γ_{sl}. Therefore the data was input into the ambient column for simplicity.)

Method	Model		Ambient Force Measurements	Controlled RH Force Measurements
			Surface Energy (mJ/m^2)	
AFM	Model 1	Van Oss et al	17.6 (1.9)	21.9 (1.9)
		OWRK	15.2 (1.9)	19.5 (1.9)
		Neumann	11.7 (1.9)	16.0 (1.9)
	Model 2			-
	Model 3		31.4 (8.5)	-
	Model 4	Model 2 γ_{sv}	13.4 (1.9)	14.1 (1.9)
		Model 3 γ_{sv}	14.4 (1.9)	14.5 (1.9)
Contact Angle	Van Oss et al		16.3	NA
	OWRK		14.0	NA
	Neumann		10.6	NA

5.1.2.4 Ethylene Glycol Solid-Liquid Surface Energy

The spring constant, tip radii, and tip-liquid$_{\text{ethylene glycol}}$ surface energies were measured to determine the solid-liquid surface energy of mica in ethylene glycol. **Table 5-28** shows the values used to calculate mica solid-liquid$_{\text{ethylene glycol}}$ surface energy.

Ethylene glycol was dried using molecular sieves, then rehydrated to 0.5%, 1%, and 5% w/w water/ethylene glycol prior to use in AFM and contact angle measurements. Water content was measured using Coulometric Karl Fisher titration. Each liquid was used the day it was prepared.

Force measurements were made on mica in ethylene glycol using the tips in **Table 5-28**. The data analysis was performed in SAS and JMP. The statistics for mica-dried, -0.5%, -1%, and -5% w/w water/ethylene glycol are listed in **Table 5-29**, **Table 5-30**, **Table 5-31**, and **Table 5-32**. The p values were all greater than 0.05, meaning the null hypotheses was accepted. The average values and data for the force, work, and surface energy of graphite with dry formamide, 0.5%, 1%, and 5% are shown in **Figure 5-13**, **Figure 5-14**, **Figure 5-15**, and **Figure 5-16**.

Table 5-28: Tip radius and average tip-liquid surface energy (standard deviation) are listed for the AFM tips used to measure the solid-liquid surface energy of mica in ethylene glycol. There are four conditions listed for ethylene glycol, dried, 0.5%, 1%, and 5% w/w water in ethylene glycol.

Tip	Condition	Spring constant (N/m)	Radius (nm)	Force (nN)	Work (mN/m)	Surface Energy (mJ/m^2)
1	Dry	.04	40	0.4 (0.1)	2.1 (0.6)	1.0 (0.3)
2			42	0.4 (0.2)	1.9 (1.0)	1.0 (0.5)
3			40	0.3 (0.1)	1.8 (0.5)	0.9 (0.3)
1	0.5% w/w water		40	0.4 (0.1)	2.1 (0.5)	1.0 (0.2)
2			42	0.4 (0.2)	2.2 (1.0)	1.1 (0.5)
3			40	0.8 (0.2)	3.9 (0.8)	1.9 (0.4)
1	1% w/w water		40	0.5 (0.1)	2.4 (0.3)	1.2 (0.1)
2			42	0.5 (0.1)	2.4 (0.6)	1.2 (0.3)
3			40	0.5 (0.1)	2.7 (0.4)	1.3 (0.2)
1	5% w/w water		40	0.5 (0.1)	2.4 (0.3)	1.2 (0.1)
2			42	0.5 (0.1)	2.4 (0.6)	1.2 (0.3)
3			40	0.5 (0.1)	2.7 (0.3)	1.3 (0.1)

The average force of adhesion did not vary on mica with the rehydrated ethylene glycol. This meant that the calculated solid-liquid surface energy should remain constant barring any variations in the tip-liquid. **Table 5-28** indicates there are no changes in the tip-liquid surface energy. Thus, the water in the ethylene glycol had no effect on the AFM measurements on mica. However, the contact angle measurements with rehydrated ethylene glycol did show a difference. The measured contact angle with dried ethylene glycol was 23.1 ± 1.2. The angle increased with the addition of 0.5% w/w water from 23.1 to 30.9 ± 1.3. It increased again 2 more degrees with 1% w/w water, and then fell back down to 30.5 ± 1.3 with 5% w/w water (**Table 2-9**). The increase in the angles also increased the contact angle solid-liquid surface energy of mica-ethylene glycol. However, the same trend was not observed with the AFM. The increase in the contact angle measurements due to the addition of water was unexpected. Since water has a strong interaction with mica, it was thought that the presence of water would reduce the contact angle measurements. This verified Good and Zografi's conclusion that solutions cannot be used to measure contact angles.[17, 22] As for the AFM, the forces stayed relatively constant and subsequently so did the solid-liquid surface energies. There were changes observed in the surface energy measurements between graphite and hydrated formamide. However, the AFM did not detect a change in the interaction when ethylene glycol was hydrated. A decrease in surface energy was predicted in the presence of more water. However, the miscibility of the water in ethylene glycol was high and allowed for all water molecules present to interact with the surface of mica. Therefore, the prediction was incorrect.

The force of adhesion measurements were expected to fall somewhere between the force measurements from diiodomethane and water because ethylene glycol has similar polar and nonpolar components. Therefore, the surface energy was also projected to be in the middle. Once again, the results from mica contact angle measurements and AFM measurements were difficult to compare because of contact angle model limitations. With mica, it was determined that model 1 does not work. The variability in the contact angle measurements was too great to have any use with AFM measurements. Model 2 and 3 give results that could be plausible considering that scientifically, the surface energy trend should be:

$$\gamma_{sldiiodomethane} > \gamma_{sletheylene\ glycol} > \gamma_{slwater}$$

where solid-liquid surface energy of diiodomethane is the largest and solid-liquid surface energy of water is the smallest. Overall, model 4 upholds this trend as well. The only difference in models 2, 3, and 4 was the distribution of the solid-liquid surface energies. For model 2 and 3 the range of the three solid-liquids surface energy was from 1 to 14 mJ/m^2, where the range in model 4 was from 3 to 9 mJ/m^2. Unfortunately, it is still not apparent which model is best for polar surfaces. The geometric mean was developed for van der Waals forces, and model 4 assumes the surface molecules will not rearrange from a vapor environment to a liquid environment. While this assumption may hold on inert surfaces, it will be challenged in chapter 6 with a crystalline compound.

The statistics from the ethylene glycol studies did not require rejection of the null hypothesis under any solvent variation. The variability between the mica samples and the mica-ethylene glycol interaction did not increase significantly with the increase in water. Most of the variability was attributed to the overall residual error of the measurements.

These studies differed from graphite in regards to the fact that the water interaction was strong with mica. The AFM did not detect differences in the solutions as it did with graphite and rehydrated formamide. Therefore, it could be similar to the phenomenon discussed with contact angle measurements. The adsorption of the water might not be homogeneous and therefore, the changes in the liquids' properties might not be reflected in contact angle measurements or AFM measurements. Therefore, in addition to the formamide results, these results justify the use of pure solvents with the AFM and contact angle methods.

Table 5-29: Mixed model statistics for mica AFM measurements with dry ethylene glycol. a) Repeated measures ANOVA for within subject effects, b) repeated measures ANOVA for between subjects, and c) the variable that demonstrates the largest percentage of variance for mica – dry ethylene glycol AFM measurements.

a)

	Degrees of Freedom	Sum of Square	Mean Square	F Value	p
Location	9	10.8	1.2	2.06	0.09
Location*Mica	9	6.9	0.8	1.32	0.29
Location*Tip	18	18.9	1.1	1.81	0.11
Error	18	10.4	0.6	-	-

b)

	Degrees of Freedom	Sum of Square	Mean Square	F Value	p
Mica	1	0.2	0.2	0.56	0.53
Tip	2	0.8	0.4	1.07	0.48
Error	2	0.7	0.4	-	-

c)

Variable	% of the Total	% Truncated
Mica	-0.7	0.0
Tip	0.2	0.2
Mica*Tip	10.2	8.7
Mica*Tip*Location (Error)	106.3	91.1
Total	100.0	100.0

Table 5-30: Mixed model statistics for mica AFM measurements with 0.5% w/w ethylene glycol. a) Repeated measures ANOVA for within subject effects, b) repeated measures ANOVA for between subjects, and c) the variable that demonstrates the largest percentage of variance for mica – 0.5% w/w ethylene glycol AFM measurements.

a)

	Degrees of Freedom	Sum of Square	Mean Square	F Value	p
Location	9	6.6	0.7	0.70	0.70
Location*Mica	9	8.3	0.9	0.8	0.56
Location*Tip	18	5.7	0.3	0.3	0.99
Error	18	18.9	1.1	-	-

b)

	Degrees of Freedom	Sum of Square	Mean Square	F Value	p
Mica	1	4.6	4.6	3.88	0.19
Tip	2	4.6	2.3	1.95	0.34
Error	2	2.36	1.18	-	-

c)

Variable	% of the Total	% Truncated
Mica	12.0	12.0
Tip	5.9	5.9
Mica*Tip	4.8	4.8
Mica*Tip*Location (Error)	77.2	77.2
Total	100.0	100.0

Table 5-31: Mixed model statistics for mica AFM measurements with 1% w/w ethylene glycol. a) Repeated measures ANOVA for within subject effects, b) repeated measures ANOVA for between subjects, and c) the variable that demonstrates the largest percentage of variance for mica – 1% w/w ethylene glycol AFM measurements

a)

	Degrees of Freedom	Sum of Square	Mean Square	F Value	p
Location	9	6.3	0.7	1.21	0.35
Location*Mica	9	6.9	0.8	1.32	0.29
Location*Tip	18	7.5	0.4	0.72	0.75
Error	18	10.5	0.58	-	-

b)

	Degrees of Freedom	Sum of Square	Mean Square	F Value	p
Mica	1	0.9	0.9	4.63	0.16
Tip	2	0.8	0.4	2.07	0.33
Error	2	0.4	0.2	-	-

c)

Variable	% of the Total	% Truncated
Mica	4.3	4.1
Tip	1.9	1.8
Mica*Tip	-6.4	0.0
Mica*Tip*Location (Error)	100.2	94.1
Total	100.0	100.0

.

Table 5-32: Mixed model statistics for mica AFM measurements with 5% w/w ethylene glycol. a) Repeated measures ANOVA for within subject effects, b) repeated measures ANOVA for between subjects, and c) the variable that demonstrates the largest percentage of variance for mica – 5% w/w ethylene glycol AFM measurements.

a)

	Degrees of Freedom	Sum of Square	Mean Square	F Value	p
Location	9	9.5	1.1	0.53	0.84
Location*Mica	9	9.3	1.0	0.52	0.84
Location*Tip	18	21.5	1.2	0.60	0.86
Error	18	36.1	2.0	-	-

b)

	Degrees of Freedom	Sum of Square	Mean Square	F Value	p
Mica	1	0.02	0.02	0.04	0.86
Tip	2	16.8	8.4	14.65	0.06
Error	2	1.1	0.6	-	-

c)

Variable	% of the Total	% Truncated
Mica	-1.0	0.0
Tip	22.1	20.8
Mica*Tip	-5.2	0.0
Mica*Tip*Location (Error)	84.1	79.2
Total	100.0	100.0

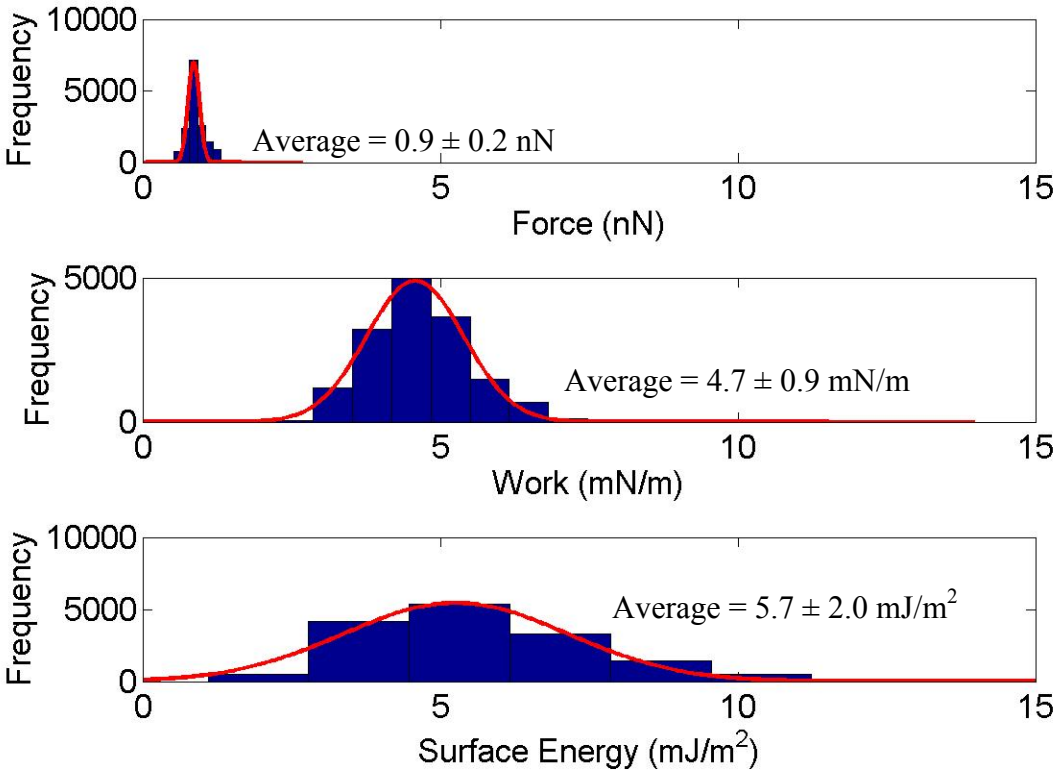

Figure 5-13: The force, work, and surface energy of mica-dried ethylene glycol. The averages and standard deviations are listed next to each histogram.

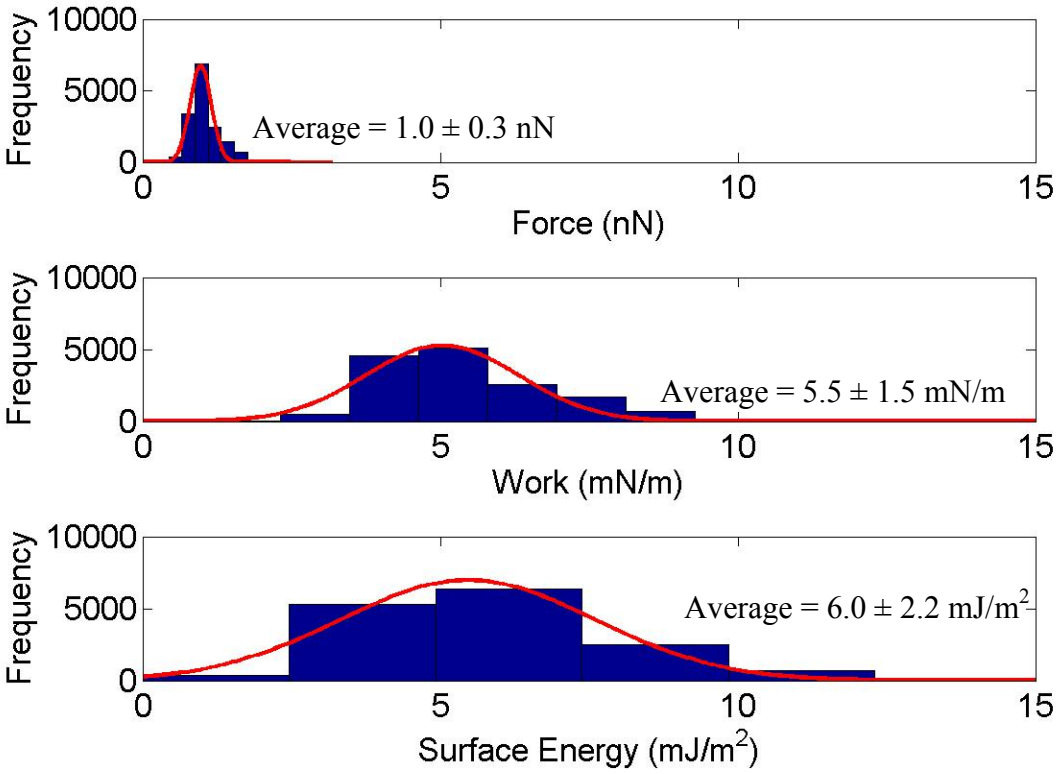

Figure 5-14: The force, work, and surface energy of mica-0.5% w/w ethylene glycol. The averages and standard deviations are listed next to each histogram.

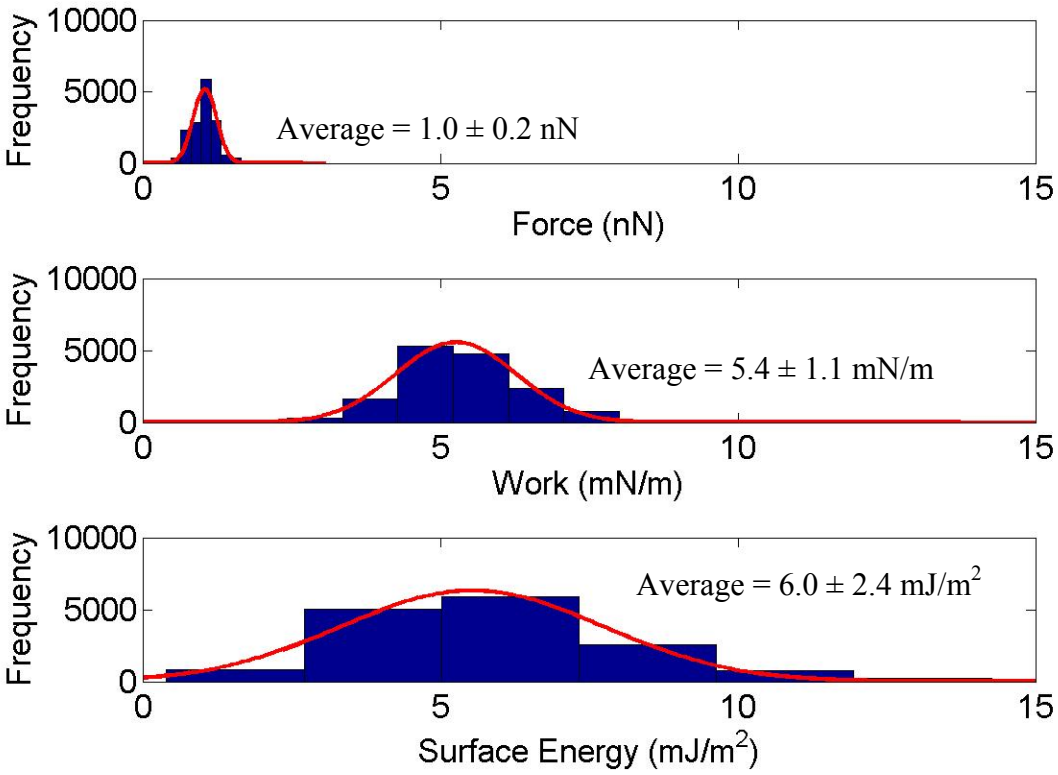

Figure 5-15: The force, work, and surface energy of mica-1% w/w ethylene glycol. The averages and standard deviations are listed next to each histogram.

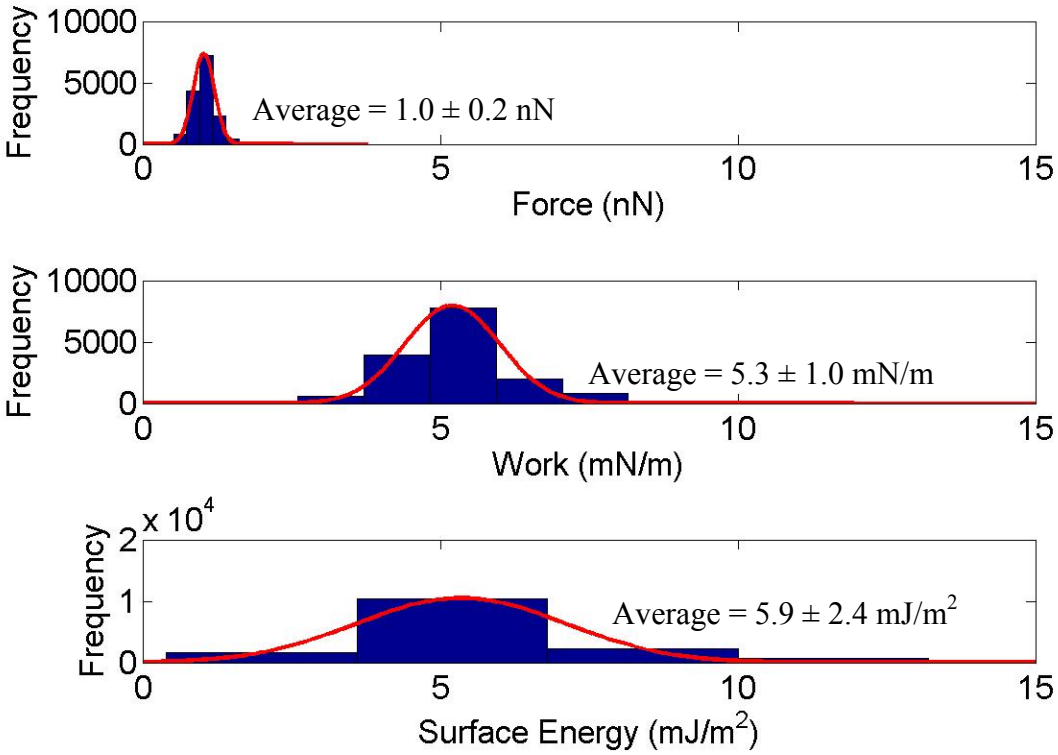

Figure 5-16: The force, work, and surface energy of mica-5% w/w ethylene glycol. The averages and standard deviations are listed next to each histogram.

Table 5-33: Average solid-liquid surface energy of mica and dry ethylene glycol determined using the AFM and contact angle methods.

(Note: Models 2 and 3 do not rely on γ_{sv} input to calculate γ_{sl}. Therefore the data was input into the ambient column for simplicity.)

Method	Model		Ambient Force Measurements	Controlled RH Force Measurements
			Surface Energy (mJ/m^2)	
AFM	Model 1	Van Oss et al	0.5 (0.8)	14.0 (0.8)
		OWRK	24.4 (0.8)	37.9 (0.8)
		Neumann	16.2 (0.8)	29.7 (0.8)
	Model 2		5.7 (2.0)	-
	Model 3		5.7 (2.1)	-
	Model 4	Model 2 γ_{sv}	4.2 (0.8)	3.3 (0.8)
		Model 3 γ_{sv}	4.0 (0.8)	3.8 (0.8)
Contact Angle	Van Oss et al		-3.6	NA
	OWRK		21.1	NA
	Neumann		13.5	NA

Table 5-34: Average solid-liquid surface energy of mica with 0.5% w/w water/ethylene glycol determined using the AFM and contact angle methods.

(Note: Models 2 and 3 do not rely on γ_{sv} input to calculate γ_{sl}. Therefore the data was input into the ambient column for simplicity.)

Method	Model		Ambient Force Measurements	Controlled RH Force Measurements
			Surface Energy (mJ/m^2)	
AFM	Model 1	Van Oss et al	1.0 (1.2)	14.5 (1.2)
		OWRK	24.9 (1.2)	38.4 (1.2)
		Neumann	16.7 (1.2)	30.2 (1.2)
	Model 2		6.0 (2.2)	-
	Model 3		6.0 (2.3)	-
	Model 4	Model 2 γ_{sv}	4.7 (1.2)	3.8 (1.2)
		Model 3 γ_{sv}	4.5 (1.2)	4.3 (1.2)
Contact Angle	Van Oss et al		-0.4	NA
	OWRK		22.8	NA
	Neumann		15.7	NA

Table 5-35: Average solid-liquid surface energy of mica with 1% w/w water/ethylene glycol determined using the AFM and contact angle methods.

(Note: Models 2 and 3 do not rely on γ_{sv} input to calculate γ_{sl}. Therefore the data was input into the ambient column for simplicity.)

Method	Model		Ambient Force Measurements	Controlled RH Force Measurements
			Surface Energy (mJ/m^2)	
AFM	Model 1	Van Oss et al	0.9 (1.1)	14.4 (1.1)
		OWRK	24.8 (1.1)	38.3 (1.1)
		Neumann	16.6 (1.1)	30.1 (1.1)
	Model 2		6.0 (2.4)	-
	Model 3		6.1 (2.5)	-
	Model 4	Model 2 γ_{sv}	4.6 (1.1)	3.7 (1.1)
		Model 3 γ_{sv}	4.4 (1.1)	4.2 (1.1)
Contact Angle	Van Oss et al		1.2	NA
	OWRK		23.7	NA
	Neumann		16.2	NA

Table 5-36: Average solid-liquid surface energy of mica with 5% w/w water/ethylene glycol determined using the AFM and contact angle methods.

(Note: Models 2 and 3 do not rely on γ_{sv} input to calculate γ_{sl}. Therefore the data was input into the ambient column for simplicity.)

Method	Model		Ambient Force Measurements	Controlled RH Force Measurements
			Surface Energy (mJ/m^2)	
AFM	Model 1	Van Oss et al	0.9 (1.0)	14.4 (1.0)
		OWRK	24.8 (1.0)	38.3 (1.0)
		Neumann	16.6 (1.0)	30.1 (1.0)
	Model 2		5.9 (2.4)	-
	Model 3		6.0 (2.6)	-
	Model 4	Model 2 γ_{sv}	4.6 (1.0)	3.7 (1.0)
		Model 3 γ_{sv}	4.4 (1.0)	4.2 (1.0)
Contact Angle	Van Oss et al		-0.3	NA
	OWRK		22.6	NA
	Neumann		15.2	NA

5.2 Summary

The overall goal of this project was AFM method development for the measurement of surface energy. In Chapter 4, the equations for converting the AFM force of adhesion measurements to surface energy were introduced. In this chapter the goals were:

1. To measure the forces of adhesion on graphite and mica in vapor and liquid conditions.
2. To evaluate the statistical model discussed in Chapter 3.
3. To evaluate the four AFM surface energy models developed in Chapter 4.
4. To compare the results obtained from the AFM surface models to contact angle results.

The collection of data began with the ambient and controlled environmental conditions, measuring the solid-vapor surface energy of mica and graphite. The controlled environment was tested because of the capillary effect present in ambient conditions. The capillary effect was shown to increase the measured force of adhesion, and that relative humidity needed to be regulated to find the "true" surface-energy. This phenomenon was observed between the mica ambient and controlled RH measurements. The surface energy significantly decreased when the humidity was lowered. The difference between the graphite ambient and controlled RH was very small if not absent entirely. Therefore, it was concluded that non-polar, hydrophobic surfaces have less interaction with water and subsequently less capillary effects as compared to a polar, hydrophilic surface like mica. The mica results had a substantial change in solid-vapor surface energy when the humidity was controlled.

To evaluate the overall hypothesis and demonstrate the AFM's capability for determining surface energy, results were compared to contact angle measurements. For graphite, both models 2 and 3 were useful for calculating solid-vapor surface energy when compared to the contact angle surface energy. For ambient mica, surface energy was comparable with the van Oss contact angle method. Controlled solid-vapor surface energy was not comparable to any contact angle results. Thus, it was also concluded that the environmental conditions can affect the solid-vapor surface energy. As a result, it may be necessary to investigate surface energy in a lower humidity environment. This puts contact angles at a disadvantage since some liquids require that an environmental chamber be saturated with the liquid to measure an equilibrium contact angle. However, the AFM is ideally suited for this type of measurement, and may be better adapted for surface energy studies.

As for the four AFM surface energy models, there was not a substantial difference between models 2 and 3. Since there were comparable results between the AFM and contact angle, the models were effective for the calculation of surface energy even with the necessary assumptions. It was shown that the universal β from contact angle measurements was not applicable to the AFM. A smaller β than the universal β was necessary to return the experimental work values. However, since model 3 did not result in values different from model 2, the modification was not an improvement from the geometric mean. Since, the geometric mean was developed for van der Waals forces, it was not clear if the use of the equation with polar surfaces would overestimate or underestimate the surface energy. Unfortunately, the mica AFM measurements could not be compared to the contact angle results because of the limitations observed with the

indirect models. Only the van Oss model was comparable to the mica-ambient AFM solid-vapor surface energy.

For solid-liquid surface energy investigation with graphite, AFM results were comparable to contact angle results illustrating the ability of the AFM to be used for hydrophobic surfaces. Models 2 and 3 were effective in determining surface energy for all three conditions: water, formamide, and diiodomethane. However, all four models were useful when using formamide. Formamide had similar surface tension components as compared to the extremes of water and diiodomethane surface tension components. The contact angle method showed limitations at the extremes. The difficulty for contact angle measurements is mostly from the limited number of equations. Young's equation balances the forces, often yielding a negative solid-liquid surface. This was observed with graphite-diiodomethane. These negative numbers make it difficult to determine the applicability of the AFM. Thus, dried formamide showed the effectiveness of the AFM surface energy models. However, because of extremes it was easier to decide that model 2 was the most useful surface energy model. Models 1 and 4 break down when applied to extreme interactions. Models 1 and 4 also break down later in Chapter 6 when investigating inert surfaces. Model 2 is limited because the geometric mean is based only on van der Waals interactions. However, this model has been used for other interactions. In order to use the geometric mean with the polar and AB interactions, the assumption made is that the pure components' differences in electronic properties and molecular size are small. [21] The advantage of using the geometric mean is that the solid-liquid surface energy is not dependent on the interaction of the surface in vapor. Depending on solid-vapor surface energy measurements to determine the surface-tip interaction, is similar to

the dependence contact angle has the measurements of three liquids. It seems the fewer dependent variables there are, the easier it is to determine surface energy.

The solid-liquid surface energy for mica was difficult to compare directly to results from the contact angle method because of the equation limitation of the contact angle method. However, the trend was still there. The contact angle results showed:

$$\theta_{\text{diiodomethane}} > \theta_{\text{ethylene glycol}} > \theta_{\text{water}}$$

This same observation was seen with the forces:

$$F_{\text{diiodomethane}} > F_{\text{ethylene glycol}} > F_{\text{water}}$$

Therefore, if the solid-liquid surface energy (γ_{sl}) for contact angle measurements could be used, it would follow the same trend that was seen from the AFM measurements:

$$\gamma_{\text{sl-diiodomethane}} > \gamma_{\text{sl-ethylene glycol}} > \gamma_{\text{sl-water}}$$

Although the final results were difficult to compare, model 1 was ruled out because of the contact angle variability on hydrophilic surfaces. This variability caused a much larger range in the solid-liquid surface energy for mica with water, diiodomethane, and ethylene glycol. Model 2 and 3 showed distinct ranges between the three solvents on mica. Model 4 was also useful, but had a smaller distribution of surface energy. Also, it was not clear until Chapter 6 that model 4 would become invalid. However, for inert hydrophilic surfaces, model 4 could be used. Model 3 did not offer a benefit over model 2. It was thought the modification would be needed on hydrophilic surface. These results showed that if the difference between the binary components' electronic properties and molecular size are small, the geometric mean could be applied to van der Waals interactions and polar interactions. Yet still, it was the limitations of the contact angle method that made

it difficult to evaluate the AFM's capabilities and the functionality of the AFM surface energy models on a hydrophilic surface.

The hygroscopic liquid measurements also made it clear that care should be taken to dry solvents prior to use so that the "true" solid-liquid surface energy can be observed. It was also necessary so AFM results were not confounded by the presence of water. The results from hydrated ethylene glycol and formamide showed that the increase in water started to affect the spread and repeatability of the AFM measurements.

Finally, to make a concise recommendation on a surface energy model, investigation on a surface that has both polar and nonpolar interactions is required. The promising results from graphite-formamide indicate an intermediate interaction is needed to evaluate the AFM's capability. This intermediate would circumvent the limitations of the contact angle and allow for a full comparison with AFM results.

Since this was not included in the scope of this work, all of the models were carried through to Chapter 6 where the AFM was applied to measurements on crystalline surfaces. The crystalline system was chosen so that the strengths learned in this chapter could be leveraged. Since the best results were obtained from graphite, it was decided to try and identify a crystalline system with more hydrophobicity.

Chapter 6 – Applying the AFM Methodology to Aspirin

The goal of this chapter is to apply the methodology in Chapter 3, the surface energy models in Chapter 4 and the knowledge obtained in Chapter 5 to determine the solid-vapor and solid-liquid surface energy of a crystalline material. In order to explain the surface energy results, there has to be a fundamental understanding of the surface chemistry. Therefore a review of the structure and chemical moieties of the model crystalline material is also given.

6.1 Aspirin Crystal Growth and Indexing Review

6.1.1 Introduction

The majority of pharmaceutical materials are in the solid crystalline form. This includes the active pharmaceutical ingredient and excipients used in formulating the solid dosage form. The arrangement or packing of the molecules in a crystal determines it physical, chemical, and mechanical properties. These properties also vary when crystal packing is fixed and the shape or crystal habit is modified. Thus control of crystal packing and habit is crucial in the pharmaceutical industry.[63] Ritonavir is a well known example of the importance of controlling crystal packing. This product was pulled from the market after multiple batches failed dissolution testing. X-Ray crystallography studies were performed on the failed batches and a new polymorph was discovered that was more thermodynamically stable than the marketed form.[64] Conversely, acetaminophen has two different polymorphs with Form I being the most thermodynamically stable and is thus the marketed form. However, the orthorhombic Form II has better compression

behavior for tableting. So to improve tableting of Form I, studies have been done to modify the crystal habit.[65]

Crystal habit is governed by the relative rates of particle deposition on the various faces, with the general rule being, faces that grow the slowest will develop as major faces. These rates are primarily determined from the binding strength of the solute molecules at the various crystal surfaces.[66, 67] However, several factors can cause modifications in the rate of deposition at specific surfaces, thus varying the crystal's habit. Such factors include temperature, degree of supersaturation, solvents, and additives/impurities.[63]

The ability of solvents to enhance or inhibit crystal growth is not completely resolved, but has been approached with two different theories. The first theory states that favorable interactions between solute and solvent on specific faces leads to reduced interfacial tension, causing a transition from a smooth to a rough interface and a concomitant faster surface growth.[68] The second theory proposed states that it is preferential adsorption at specific faces that will inhibit crystal faces growth. The removal of bound solvent adsorbed poses an additional energy barrier for continued growth, thus slowing down the growth on the crystal face.[69]

Studies have also been done on the influence of "tailor-made" additives on crystal habit. It is believed these so called "tailor-made" additives inhibit growth through preferential adsorption at specific faces. These "tailor-made" additives have a similar base molecule with one altered functional moiety. Lahav and coworkers have proposed that structurally similar additives will adsorb stereospecifically because of the similar shape with the host molecule. The adsorbed additive essentially replaces the host molecules and hinders or slows adsorption of more solute molecules to this face. This growth change occurs

because the additive molecule emerges from the crystal surface in a different orientation than the host molecule, disrupting the previous repeating pattern.[67, 69, 70]

6.1.2 Background on aspirin

The model crystalline compound chosen was acetylsalicylic acid (ASA). ASA is still used today as an analgesic and antiplatelet medication. For many years it was thought that there were at least two polymorphs of ASA.[71] There has been a very recent discovery that eluded to a second form,[72] but the stability and elucidation of this polymorph has been questioned.[73] Before this second polymorph was found only different crystal habits had been observed.[71]

Depending on the conditions of preparation, pharmaceutical crystals may exhibit variations in habit with the consequence that interfacial properties can be modulated by the various morphologically important faces. This is what made aspirin an interesting molecule to study, because of the reported literature differences in morphology.[71] To study crystal habit and understand the physical and chemical properties it is crucial to have molecular level knowledge of the crystal structure at the surface.[74] In order to determine and characterize the surface structure of particular crystal faces, the molecular packing and the face indices must be assigned properly.

Despite the persistent investigations since its discovery in late 1800s,[75] it was discovered early in the aspirin studies that there is still confusion over classification of the crystal morphology. In the 1930s, the lattice parameters of aspirins were defined by X-ray diffraction (XRD) using oscillation and Weissenberg photographs. The conclusion was aspirin belonged to the P21/*a* (a nonstandard setting of space group number 14) space group.[76, 77] If this space group is used, the predominant face is identified as

(001).[78, 79] However, the first full structure determination by single crystal XRD in 1964,[80] assigned a different setting of the same space group, that is, P21/*c*.[81-83] In this setting, the largest face is (100).[84, 85] A likely cause of the confusion over face indexing was then the use of alternative space group settings, which was exacerbated by the almost identical metrics of the *a* and *c* axes.[86] Consequently the two possible space groups caused the functional groups to be assigned improperly to the indexed face. If P21/*a* is used for indexing instead of P21/*c*, any conclusions drawn with regard to surface properties of a particular face will be in error, particularly from the viewpoint of structure-property relationships.[86] Several studies, included contact angle work from the Li lab, have probed the chemical nature of functional groups exposed on the two major faces of aspirin crystals an incorrectly concluded that the (100) face was more hydrophilic than the (001) face due to the presence of the carboxyl group on the (100).[87] The conclusion that the smaller contact angle observed with water was on the supposed (100) face, was justified by the presence of the carboxyl group. Upon closer inspection of the face indexing of aspirin single crystals with XRD, it was shown that the common assignment of the (100) face as more hydrophilic (due to the exposure of carboxyl group) is not correct.[86] The confusion seemed to stem from the original assignment of the space group and indices of the crystal faces.[77-79, 88] Therefore before the surface energy can be evaluated with contact angle and AFM measurements, the crystal indexing must be clear. This lab published a communication that presented experimental evidence to clarify the difference between the two major faces of aspirin crystal. This published communication included contact angle data for further interpretation of surface wettability.[86] However, in this chapter we will further the

contact angle data and add the AFM data to present solid-vapor and solid-liquid surface energy. These results will be added to the initial investigation from the communication. This will also allow for testing the four AFM surface energy models and the method developed in the previous chapters on pharmaceutical crystalline material.

6.1.3 Crystal growth

Aspirin single crystals were grown by slow evaporation from ethanol and acetone. Aspirin and the solvent were dissolved in a beaker to its solubility (0.2 gm/mL in ethanol and 0.18 gm/mL in acetone), by stirring. The beakers were covered with Parafilm®. Small holes were punched through the seal using a needle, and stored in ambient conditions. Aspirin crystals were grown in water with a supersaturation ratio of 225% based on its water solubility of 3.3 mg/mL. The beakers were sealed with Parafilm® and stored in ambient conditions. The morphology of aspirin was also manually generated by the Cerius^2 program (Accelrys, Inc., San Diego, CA) using the single crystal X-ray data and the observed habits of the crystals grown from the different solvents.[86]

Aspirin crystallized in ethanol, water, and acetone results in plate morphology with two major faces and a few different minor faces, shown in **Figure 6-1**. The effects of solvent on crystallization of aspirin demonstrate some morphological differences but no polymorphism. This was validated in both the XRD and PXRD studies.[86]

6.1.4 Aspirin crystal structure

The aspirin crystals grown in the Li lab were evaluated by single X-ray diffraction. The results indicated the crystals were of the monoclinic space group P21/c with a = 11.242(7), b = 6.539(4), c = 11.245(9) Å, and β = 95.9(3)°. These values were in

agreement with the literature.[80-83] The some controversy exists the elusive second form (form II) of aspirin has been identified and characterized by single crystal X-ray diffraction.[72, 73] The unit cell parameters are superficially quite different from those of form I, although they are likely related. Nonetheless, both forms exhibit the same space group, P21/*c*.[89] In our crystallization studies only form I was produced,[86] though the presence of a very small amount of form II cannot be discounted.[72, 73]

Our results demonstrate that for crystals indexed as P21/*c*, the largest growth face is (100) and the second largest is (001), as shown in **Figure 6-2**. Based on these assignments and an intimate view of the crystal packing, it is apparent that there are two possible truncations for the (100) face. One truncation goes through the carboxyl group and another passes through the acetyloxy groups. It is important to make this distinction on the (100) face, especially when probing surface properties in relation to functional groups on that surface. As shown in **Figure 6-2**, if a surface property, such as wettability, is measured on the (100) face but explained using the functional groups present on the (001) face, conclusions will be misleading.[86]

The crucial point is to recognize which functional groups are exposed on the major faces whether the space group is assigned as P21/*a* or P21/*c*. The axes could be assigned according to any number of conventions, but the functional groups assigned to the physical faces are invariant. The dominant face will *always* have the acetyloxy group (not the carboxyl group as discussed below) and the other major face will *always* have the methyl and phenyl groups. This is illustrated in **Figure 6-2**.[86]

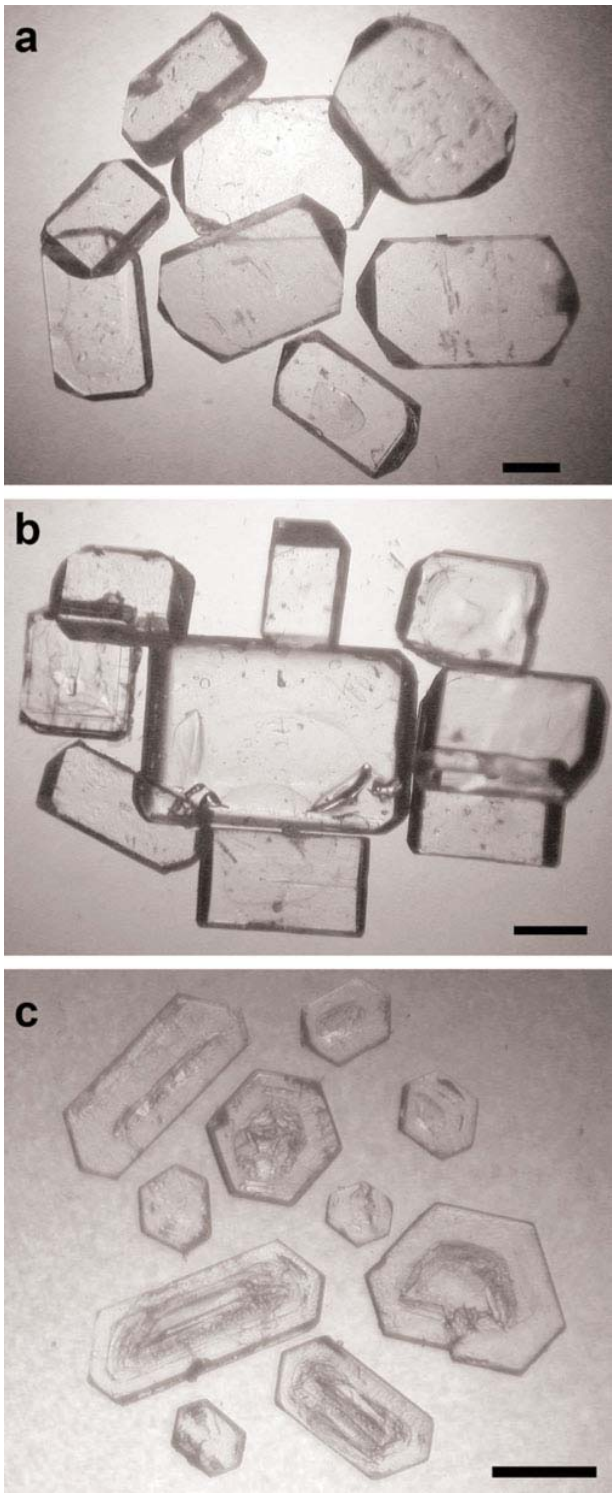

Figure 6-1: Aspirin crystals grown from a) ethanol, b) acetone, and c) water. Scale bars denote 1 mm.

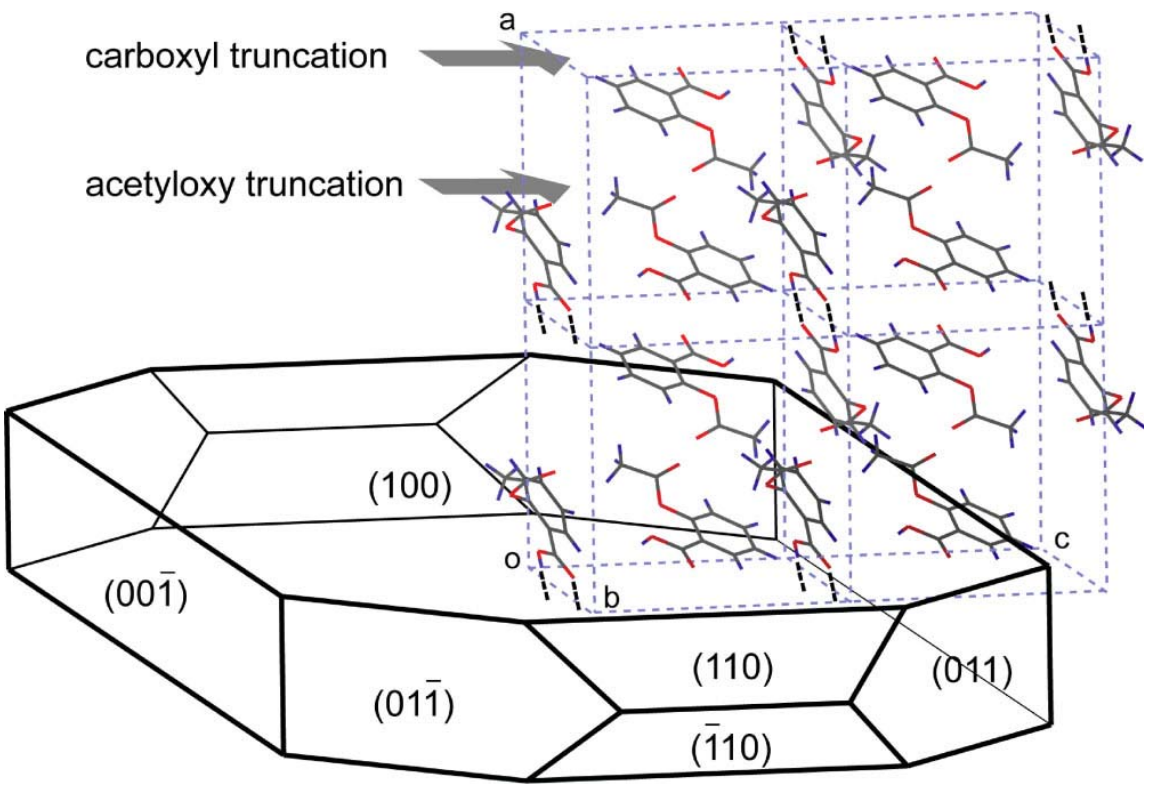

Figure 6-2: Growth morphology and crystal structure of aspirin. As indicated, there are two possible truncations of the (100) face, one with carboxyl groups and another with acetyloxy groups.

6.2 Contact Angle Method

6.2.1 Contact angles

Contact angles were measured with various solvents on the two major faces of aspirin, and the results are summarized in **Table 6-1**. All of the contact angles measured on the (100) face are larger than those on the (001) face. Due to the polar nature of the solvents used, the measurements indicate the (100) face is less hydrophilic than the (001), emphasizing the importance of knowing the surface crystal structure. Although the (100) face may expose the carboxyl acid group, the contact angle measurements indicate otherwise. It appears to be the acetyloxy truncation that is exposed, which leads to the (100) face being less hydrophilic than the (001) face. The hydrogen bonding between carboxyl groups in the crystal is strong; cleavage through this bonding to expose the carboxyl group is unlikely. Once again, the relationship between the interfacial properties and surface structure could be misconstrued when using the improper labeling and thereby identifying the wrong surface functional groups. If the more hydrophilic face is mistaken as the (100), carboxyl groups would be thought as the dominant surface group and that it would be involved in solvent interactions. These results show that the carboxyl group is not exposed and therefore a lower contact angle by a polar liquid is not expected.[86]

Table 6-1: Contact angles on the (100) and (001) faces of aspirin measure in selected solvents.

	Water	Diiodomethane	Glycerol
(100)	66.9 ± 2.9	41.2 ± 1.7	65.1 ± 1.1
(001)	56.4 ± 2.4	36.2 ± 1.9	56.5 ± 0.9

6.2.2 Surface energy calculations from contact angle indirect models

6.2.2.1 Solid-Vapor Surface Energy

Once the contact angles were measured, the three indirect contact angle models discussed in Chapter 2 were used to calculate solid-vapor surface energy. From the contact angle data, the (100) and (001) faces of aspirin were more similar to graphite. These faces showed more of a hydrophobic nature. Therefore, it was hypothesized that the solid-vapor surface energy calculated using the three models would be more similar than the results on a hydrophilic surface. The solid vapor surface energies from contact angle data are shown in **Table 6-2**. The overall solid-vapor surface energy between each model was fairly similar, ranging from 40.2 to 42.8 mJ/m^2 on the (100) face and 44.6 to 49.2 mJ/m^2 on the (001) face. Therefore, as hypothesized, there was not a huge disparity in the models. While there was roughly a 10 degree difference in water and glycerol contact angles, the solid-vapor surface energies did not show large differences in the two faces. Since these two faces are the major faces of aspirin, this was expected given that the morphology of a crystal is the result of relative growth rates of its various faces, and that the slowest growing faces are expressed in the crystal habit. The growth rates of the crystalline faces are determined by intermolecular interaction between the molecules in the crystal as well as external parameters such as solvent, supersaturation, temperature, and impurities.[90] As these two faces are major faces, it was expected that their surface energies would be similar, while minor faces would have distinctly different surface energies. The minor faces are the faces growing faster and thus "disappearing" or becoming much smaller in the resultant crystal morphology.

Table 6-2: Average solid-vapor surface energy calculated from the three indirect contact angle models used in Chapter 2.

Van Oss- Chaudhury – Good Model					
	γ_{sv}	γ_{sv}^{LW}	γ_{sv}^{AB}	γ_{sv}^{-}	γ_{sv}^{+}
(mJ/m^2)					
(001) Face	**44.6 ± 2.1**	42.6 ± 1.2	2.0 ± 1.4	24.8 ± 2.7	0.1 ± 0.1
(100) Face	**40.2 ± 1.6**	39.3 ± 1.0	0.8 ± 0.8	17.8 ± 3.0	0.2 ± 0.4
Owens-Wendt-Rabel-Kaelble Model					
	γ_{sv}	γ_{sv}^{p}	γ_{sv}^{d}		
(001) Face	**49.2 ± 1.2**	13.3 ± 1.1	35.9 ± 1.1		
(100) Face	**42.8 ± 0.5**	8.8 ± 1.0	34.0 ± 1.1		
Neumann Model					
	γ_{sv}				
(001) Face	**45.3 ± 0.9**				
(100) Face	**41.6 ± 0.7**				

6.2.2.1 Solid-Liquid Surface Energy

Lastly, the solid-vapor surface energy and measured contact angles were plugged back into Young's Equation (Equation 2.1), to determine the solid-liquid surface energies on the (001) and (100) faces. The solid-liquid surface energy values are listed in **Table 6-3**. The measured contact angles indicate that on both faces, the solid-liquid surface energies ordered from smallest to largest would be diiodomethane, water and glycerol. A smaller solid-liquid surface energy means a stronger interaction, as illustrated in **Figure 2-1**. Therefore, the larger contact angles have larger solid-liquid surface energies because the solvents have a reduced interaction with that surface. Evaluating the results on the (001) face, the solid-liquid surface energy trend is

$$\gamma_{sl\text{-}glycerol} > \gamma_{sl\text{-}water} > \gamma_{sl\text{-}diiodomethane}$$

The trend on the (001) face is best illustrated in **Figure 6-3**. Also, the trend is best viewed if compared within each model. While there were small differences in the solid-vapor surface energy, the range of contact angles and the use of the Young's equation caused the large distribution of surface energies. Therefore, even small changes in the angles are causing a large distribution when balancing the forces. Also, while the contact angles from water and glycerol are the same, there is a difference in the solid-liquid surface energies because of the difference between the solvents' surface tensions. The surface tension of water and glycerol is 72.8 and 63.4 mJ/m^2, respectively. Therefore, a smaller solid-liquid surface energy is obtained from 1) multiplying the cosine (θ) by the water surface tension, and 2) subtracting that value from the solid-vapor surface energy. So, even though the angles point towards the same interaction, the output from Young's equation gives a different result.

Evaluating the results on the (100) face, the solid-liquid surface energy trend was the same as observed on the (001) face. The trend is illustrated in **Figure 6-4** and can be observed better within each model. On the (100) face, there was also a more distinct difference observed between diiodomethane solid-liquid surface energy and the solid-liquid surface energies of water and glycerol for all three contact angle models. The small differences between the water and glycerol solid-liquid surface energy was again expected because the contact angles were the same. Therefore, the observed surface energy differences were the result of the different properties between the two liquids.

Unfortunately, crystals could not be grown from glycerol. The calculated solid-liquid surface energy, however, did indicate potential morphology differences than those observed in **Figure 6-1** as a result of the different interactions on the two major faces. However, without being able to measure the contact angles on the minor faces, it was difficult to predict whether other major faces would result from glycerol crystallization. The data does indicate that there are differences in the solid-liquid surface energies between water and glycerol on both faces.

The next comparison that can be made is the solid-liquid surface energy differences between the two faces. This is illustrated in **Figure 6-5** for diiodomethane, **Figure 6-6** for water, and **Figure 6-7** for glycerol. The contact angle data pointed to the (100) face being more hydrophobic because the carboxylic group was not exposed. The comparisons of the solid-liquid surface energies made in Figures 6.5, 6.6, and 6.7 confirm this statement. For each model in **Figure 6-5**, the diiodomethane solid-liquid surface energy of the (100) face was lower than the (001) face. These results were unexpected from the contact angle data. Smaller surface energy equates to a stronger interaction.

The diiodomethane contact angle was smallest on the (001) face, which indicated a stronger interaction. However, the solid-vapor surface energy was larger on the (001) face, so the five degree contact angle difference did not make up for the solid-vapor surface energy difference in Young's equation. The water and glycerol angles indicated a weaker interaction on the (100) face (**Figure 6-6** and **Figure 6-7)**. The solid-liquid surface energies between the models were larger on the (100) face and smaller on the (001) face. These results confirm that the carboxylic group was not exposed or cannot be exposed during cleavage. These data taken together, and with the water contact angle measurements, illustrate the increased hydrophobicity of the (100) face as compared to the (001) face.

It is extremely important to note the differences seen between the three models. The solid-liquid surface energy is smallest as calculated by the van Oss model, which is a direct result of the smaller solid-vapor surface energy for the (100) and (001) faces. Conversely, the largest solid-liquid surface energy is from the OWRK model because the higher solid-vapor surface energy. It was important to find a method that could either corroborate contact angle results or allow for a more robust evaluation, since an agreement has yet to be reached on which model is more applicable based on a sample's surface chemistry. These were the driving factors for selecting AFM for measuring surface energy.

Table 6-3: Average solid-liquid surface energy on the (001) and (100) faces determined from contact angle measurements.

	(001) Face			(100) Face		
	OWRK	Van Oss-Chaudhury-Good	Neumann	OWRK	Van Oss-Chaudhury-Good	Neumann
	γ_{sl} (mJ/m^2)					
Diiodomethane	7.9 ± 0.9	2.5 ± 1.4	4.3 ± 0.6	4.7 ± 0.9	1.6 ± 0.7	3.3 ± 0.9
Water	8.6 ± 1.6	3.2 ± 2.4	5.1 ± 1.1	14.4 ± 2.4	11.3 ± 3.2	13.0 ± 2.6
Glycerol	13.9 ± 1.6	8.2 ± 1.2	10.3 ± 1.8	16.4 ± 0.8	13.0 ± 1.4	15.0 ± 1.1

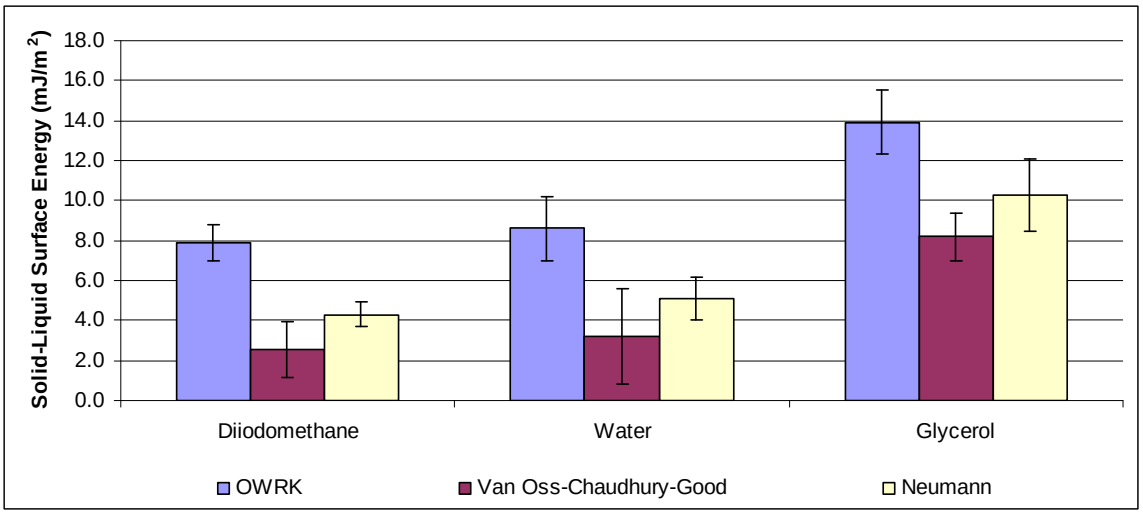

Figure 6-3: The solid-liquid surface energies on the (001) face determined from three contact angles models.

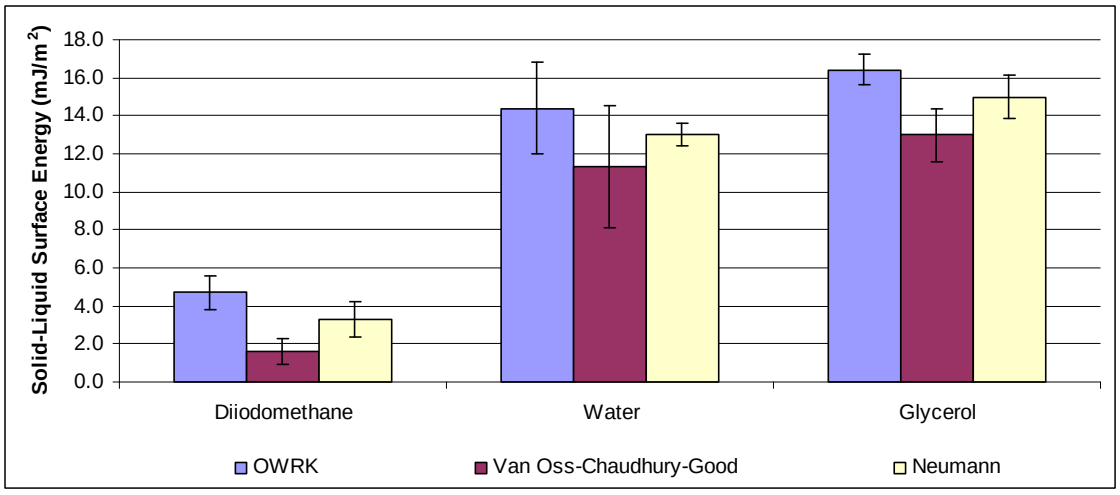

Figure 6-4: The solid-liquid surface energies on the (100) face determined from three contact angles models.

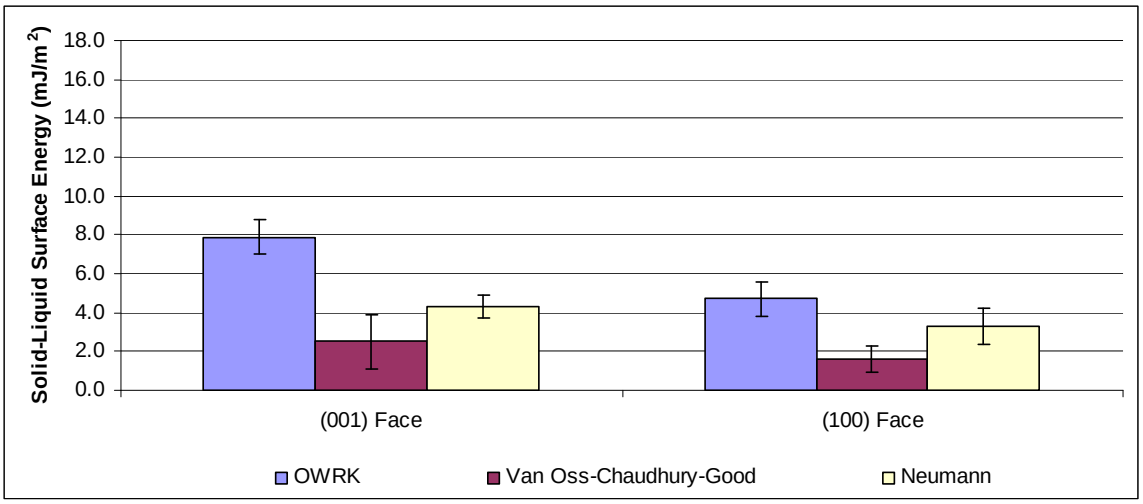

Figure 6-5: The diiodomethane solid-liquid surface energy from three contact angle models calculated on the (001) and (100) faces of aspirin crystals.

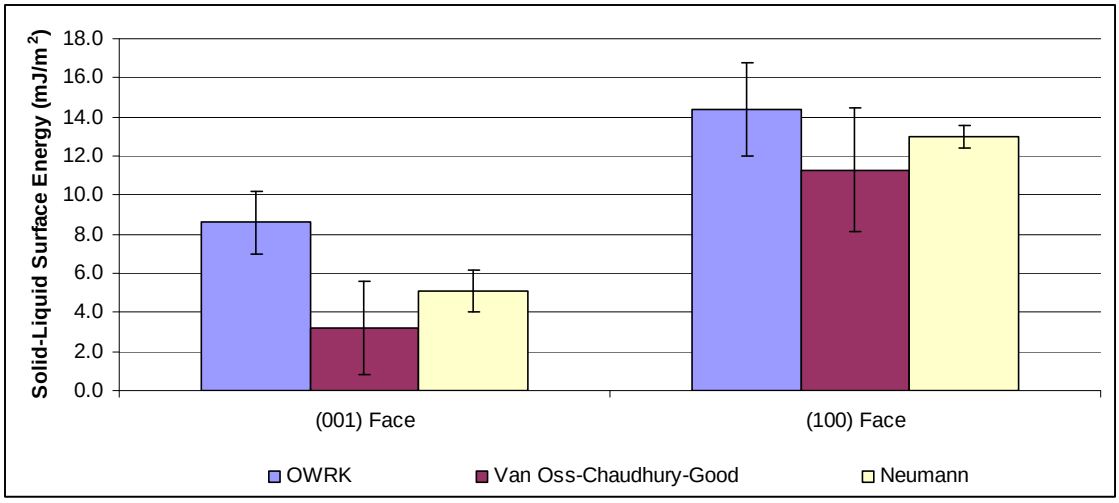

Figure 6-6: The water solid-liquid surface energy from three contact angle models calculated on the (001) and (100) faces of aspirin crystals.

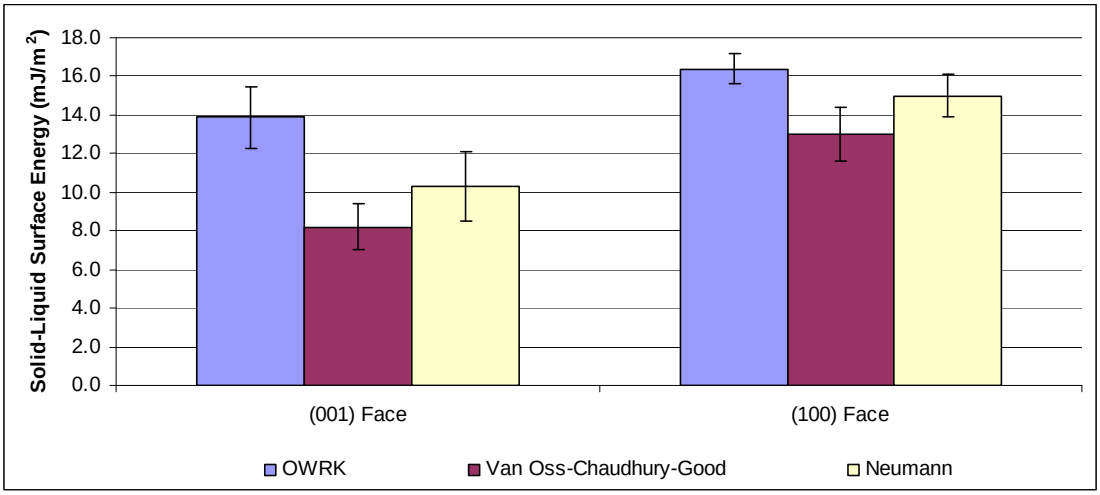

Figure 6-7: The glycerol solid-liquid surface energy from three contact angle models calculated on the (001) and (100) faces of aspirin crystals.

6.3 AFM Application

The next phase of this research was to investigate how methods developed with inert surfaces could be extended to crystalline systems. The first part of Chapter 6 used contact angles to determine solid-vapor and solid-liquid surface energy. In this section the work done in Chapters 3, 4, and 5 was applied to determine the solid-vapor and solid-liquid surface energy from AFM force of adhesion measurements on aspirin.

6.3.1 Solid-vapor surface energy

In Chapter 5, AFM measurements for solid-vapor surface energy were performed in ambient conditions and controlled humidity. The goal was to duplicate these measurements with aspirin to demonstrate the effects of environmental conditions. Recall that under ambient conditions, results obtained from AFM and contact angle measurements matched better than those obtained in a controlled environment. This is likely due the fact that contact angles were also measured in an ambient environment. The solvent trapped in the crystals caused a capillary effect on the two major faces of aspirin that made it impossible to engage the microscope. Like mica and graphite, the crystals were cleaved to take measurements on an unexposed face. During crystallization, solvent can get trapped in the crystal, where it remains even after cleavage. The crystals were placed in a desiccator for 24 hours prior to measuring the forces of adhesion. Initially, in the absence of the capillary effect, forces match those collected in a controlled environment. However, after only a few minutes the forces started to increase as water adsorbs to the surface. At that point, engaging the microscope was again, problematic. The capillary effect was not the only reason for variability; the adsorbed water also caused a local dissolution or a solvated state, making

it hard to move the tip towards the surface. The high solubility of aspirin in water (3.3 mg/mL), coupled with the AFM's sensitivity, and the capillary forces were all contributing factors for the difficultly in engaging the microscope. Since the data appeared to be unreliable in the ambient environment, subsequent measurements were limited to a controlled humidity environment.

To determine the solid-vapor surface energy of the (100) and (001) face in a controlled RH environment, the spring constants, tip radii, and tip-vapor surface energies were determined first. **Table 6-4** shows the values that were used to finally calculate the (100) and (001) solid-vapor surface energy.

Force measurements were made on the (100) and (001) surfaces in a controlled humidity environment using the tip values in **Table 6-4**. The data was then analyzed in SAS and JMP. The statistics for the (100) and (001) faces are listed in **Table 6-5** and **Table 6-7**, respectively. The p values were all greater than 0.05, meaning the null hypotheses was accepted. The plots of the force, work, and surface energy of the (001) and (100) faces are shown in **Figure 6-8** and **Figure 6-9**, respectively.

The JMP statistics indicated on the (100) face that the variability was mainly from experimental error. However, the JMP statistics showed there were more contributing factors to the variability on the (001) face. Variability existed between the samples and the tip-sample interaction. Typically, the cause for the tip-sample variability is assigned to tribocharging of the surface, and the most effective way to eliminate this charging is to increase the humidity. However, the increased humidity presents other challenges previously discussed, and the variability caused by electrostatic charge was not significant enough to reject the null hypothesis. High humidity conditions are often

necessary to effectively measure the forces on samples with the potential to become electrically charged. . Roberts' lab concluded that the humidity effect starts to become negligible at less than or equal to 22% RH..[54] The variability attributed to the samples might be due to the fact that cleavage of the (001) face was not as clean as the (100) face. Surface roughness of the cleaved (001) face was plainly evident under light microscopy; therefore, more variability was expected between samples for the (001) face. The variability between the AFM tips was largely attributed to the sensitivity of the AFM measurements and the interactions with different chemical moieties on the crystalline surfaces. Depending on the roughness of each sample, measurements can vary between samples.

As expected, the surface energy as calculated by the AFM was significantly less for the two major faces of aspirin as compared with the contact angle surface energy. Though a direct number-to-number comparison was not possible, this was consistent with the trend observed on the inert surfaces. The solid-vapor surface energy was larger on the (001) face in both contact angle and AFM measurements. The inability to measure the solid-vapor surface energy in ambient conditions and the inability to engage the microscope confirmed that solid-vapor surface energy measurements needed to be conducted in a controlled environment, as there was an obvious bias due to water adsorption on the surface. For contact angle measurements, the adsorption of water has always been regarded as not having a low impact on surfaces with high surface energies (Equation **2.2**). The AFM measurements indicate the opposite. The reduced solid-vapor surface energy and elimination of water vapor allowed for forces to be measured without environmental impacts.

The two surface energy models from Chapter 4 used to calculate solid-vapor surface energy were models 2 and 3. The results were similar for both models. Model 2 uses the geometric mean, which was developed based on the van der Waals force of the two separate phases. The contact angle measurements indicated that the (100) and (001) faces were both hydrophobic and that the carboxylic group was not exposed on the (100) face. Thus, the use of the geometric mean for surface energy calculations of hydrophobic surfaces is supported. Model 3 (modification to the geometric mean) produced similar results to model 2. Because the interactions between the sample-vapor and tip-vapor (the separate phases) are similar, these results also support those from model 2. When the interactions were similar, the exponential was equal to 1, and model 3 could be reduced to model 2. The results for model 2 are illustrated in **Figure 6-8** and **Figure 6-9**.

Table 6-4: Tip radius and average tip-vapor surface energy (standard deviation) for the tips used to calculate the solid-vapor surface energy of the (001) and (100) faces of aspirin.

Tip	Environmental Conditions	Radius (nm)	Force (nN)	Work (mN/m)	Surface Energy (mJ/m^2)
1	Controlled Environment	40	9.3 (0.7)	49.6 (3.5)	24.8 (1.8)
2	Controlled Environment	42	9.7 (2.1)	48.8 (10.7)	24.4 (5.3)
3	Controlled Environment	42	10.4 (0.7)	52.8 (3.7)	26.4 (1.8)

Table 6-5: Mixed model statistics for AFM Measurements on the (100) face of aspirin in a controlled humidity environment. a) Repeated measures ANOVA for within subject effects, b) repeated measures ANOVA for between subjects, and c) the variable that demonstrates the largest percentage of variance (100) ASA-controlled RH AFM measurements.

a)

	Degrees of Freedom	Sum of Square	Mean Square	F Value	p
Location	9	7.9	0.9	0.32	0.95
Location*(100)	9	7.3	0.8	0.30	0.97
Location*Tip	18	40.0	2.2	0.81	0.68
Error	18	49.3	2.7	-	-

b)

	Degrees of Freedom	Sum of Square	Mean Square	F Value	p
(100) Face	1	0.03	0.03	0.01	0.94
Tip	2	2.85	1.43	0.42	0.71
Error	2	6.82	3.41	-	-

c)

Variable	% of the Total	% Truncated
(100) Face	-4.8	0.0
Tip	-5.5	0.0
(100) Face*Tip	6.1	5.6
(100) Face*Tip*Location (Error)	104.2	94.4
Total	100.0	100.0

Table 6-6: Average solid-vapor surface energy of the (100) face of aspirin determined using the AFM and contact angle methods. The standard deviations are shown in parenthesis.

Method	Indirect Model	Solid-Vapor Surface Energy (mJ/m^2)
AFM	Model 1	-
	Model 2	25.7 (2.5)
	Model 3	25.8 (2.4)
	Model 4	-
CA	Van Oss et al	40.2 (1.6)
	OWRK	42.8 (0.5)
	Neumann	41.6 (0.7)

Table 6-7: Mixed model statistics for AFM Measurements on the (001) face of aspirin in a controlled humidity environment. a) Repeated measures ANOVA for within subject effects, b) repeated measures ANOVA for between subjects, and c) the variable that demonstrates the largest percentage of variance (001) ASA-controlled RH AFM measurements.

a)

	Degrees of Freedom	Sum of Square	Mean Square	F Value	p
Location	9	0.60	0.07	1.26	0.32
Location*(001)	9	0.28	0.03	0.59	0.79
Location*Tip	18	1.47	0.08	1.53	0.19
Error	18	0.96	0.05	-	-

b)

	Degrees of Freedom	Sum of Square	Mean Square	F Value	p
(001) Face	1	0.70	0.70	0.90	0.44
Tip	2	4.57	2.29	2.92	0.26
Error	2	1.57	0.78	-	-

c)

Variable	% of the Total	% Truncated
(001) Face	36.7	36.2
Tip	-1.3	0.0
(001) Face*Tip	35.3	34.8
(001) Face*Tip*Location (Error)	29.4	29.0
Total	100.0	100.0

Table 6-8: Average solid-vapor surface energy of the (001) face of aspirin determined using the AFM and contact angle methods. The standard deviations are shown in parenthesis.

Method	Indirect Model	Solid-Vapor Surface Energy (mJ/m^2)
AFM	Model 1	-
	Model 2	33.7 (2.5)
	Model 3	34.8 (3.2)
	Model 4	-
CA	Van Oss et al	44.6 (2.1)
	OWRK	49.2 (1.2)
	Neumann	45.3 (0.9)

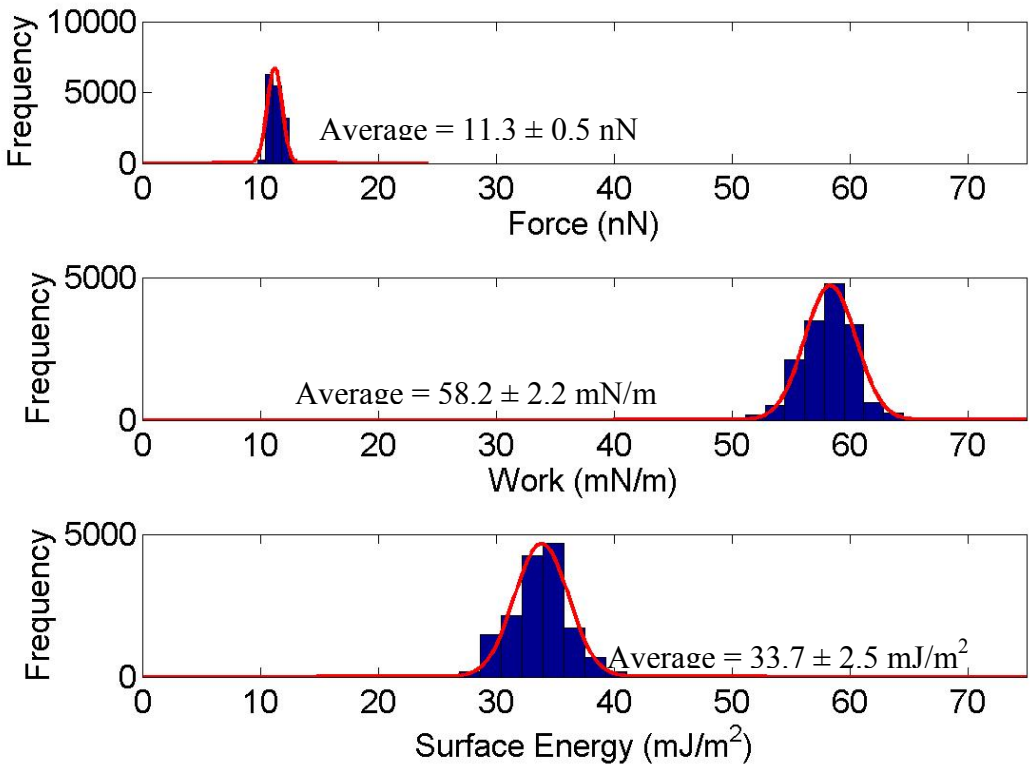

Figure 6-8: The solid-vapor surface energy from AFM force measurements in controlled humidity environment on the (001) face of aspirin crystals.

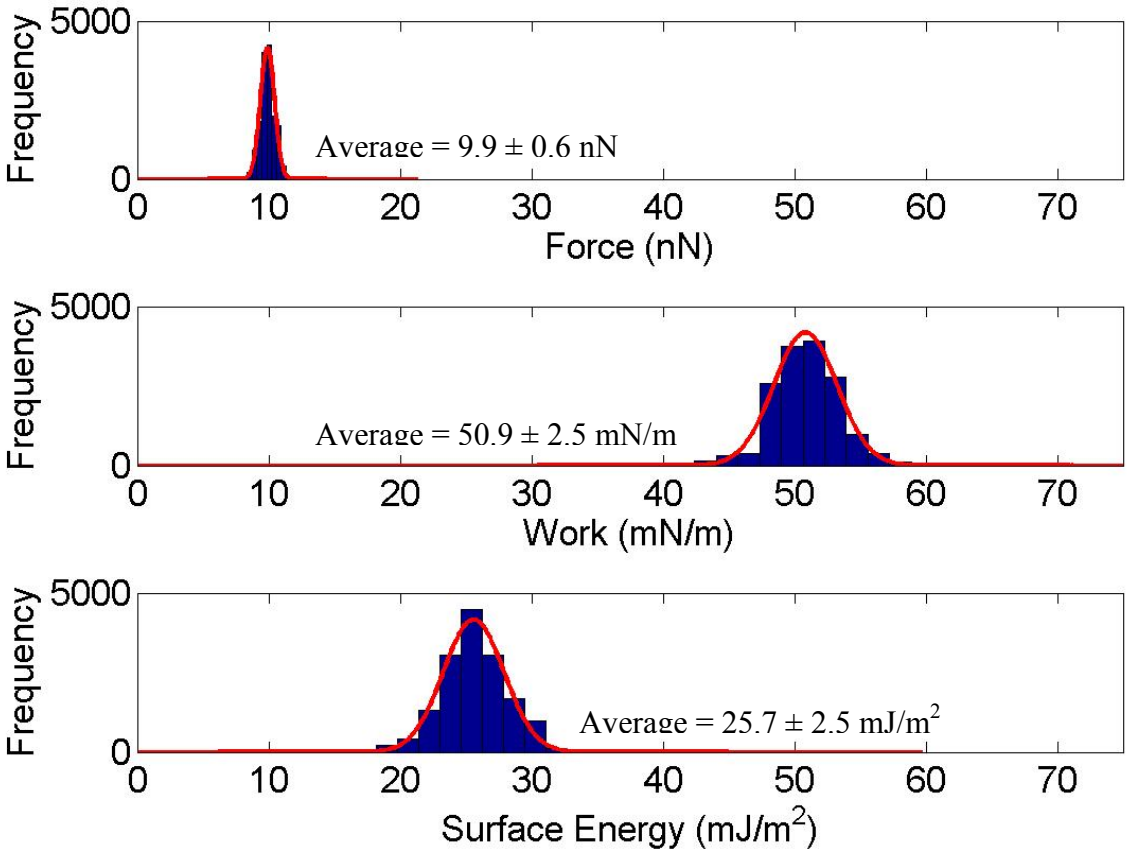

Figure 6-9: The solid-vapor surface energy from AFM force measurements in controlled humidity environment on the (100) face of aspirin crystals.

6.3.2 Solid-liquid surface energy

6.3.2.1 Diiodomethane Solid-Liquid Surface Energy

To determine the solid-liquid surface energy of the (100) and (001) face with diiodomethane, the spring constants, tip radii, and tip-vapor surface energies were determined first. **Table 6-9** shows the values used to calculate the (100) and (001) solid-liquid$_{diiodomethane}$ surface energy.

Force measurements were made on the (100) and (001) surfaces in diiodomethane using the tip values in **Table 6-9**. The data was then analyzed in SAS and JMP. The statistics for the (100) and (001) faces are listed in **Table 6-10** and **Table 6-12**, respectively. The p values were all greater than 0.05, meaning the null hypotheses was accepted. The p value for the tips from the force measurements on the (100) face was low (0.08) and thus, close to being statistically significant. The force range on the (100) face was 0.6 to 0.7 nN. The distribution for each tip was also small with a 0.1 nN standard deviation (n=5120 per tip). These results indicated the tip variation was negligible. The other variable with a p value that was close to statistical significance was the locations on the (001) face. This face was observed to be more rough than the (100) face. Therefore, it was not surprising that the locations being measured on each crystalline sample would causing variability. With a standard deviation of 0.3 nN (n=5120), the force distribution confirmed that location variability was insignificant. The plots of the force, work, and surface energy of the (100) and (001) faces are shown in **Figure 6-10** and **Figure 6-11**, respectively.

The forces between the two major faces of aspirin and diiodomethane were expected to be small. Small forces were indicative of strong adhesion between the sample and the

liquid. The same was observed from the contact angle measurements. The angle between the two major faces of aspirin and diiodomethane was smaller than the angles from water and glycerol. Thus the solid-liquid surface energy was also smaller on these two faces. The interesting observation between the two methods was the difference observed from the forces compared to the contact angles. The smallest angle was measured on the (001) face, **Table 6-1**, but the smallest force was measured on the (100) face. However, comparison of the surface energy from contact angle method to the AFM method indicates that the (100) face has a stronger interaction with diiodomethane. According to water contact angle measurements, the (100) face was more hydrophobic. The contact angles created a bit of confusion because the largest angles for water and glycerol are observed on the (100) face. The large angle from liquids with polar components means the (100) face is more hydrophobic. If the (100) face was more hydrophobic, a smaller angle from diiodomethane would have been expected. For contact angle results, the solid-liquid surface energy had to be calculated and the interaction between the three liquids had to be considered before the stronger diiodomethane interaction with the (100) face was seen. The AFM does not need multiple liquids to determine the solid-liquid surface energy. The measurements in the liquid of interest and surface energy models 2 and 3 are sufficient to calculate solid-liquid surface energy values directly, making AFM an attractive alternative to contact angle for surface energy measurements.

To compare the solid-liquid surface energy values of the AFM with contact angle measurements, the AFM surface-energy models are discussed first. The results from the (100) and (001) faces of aspirin are listed in **Table 6-11** and **Table 6-13**, respectively.

Model 1 used the contact angle solid-vapor surface energy results to calculate the solid-liquid surface energy. The contact angle solid-vapor surface energy was extremely high, and thus the surface-tip surface energy was large. Therefore, model 1 was not useful for AFM measurements. It was not ideal to integrate two methods to determine the solid-liquid surface energy.

The AFM results from models 2, 3, and 4, however, can be compared to certain contact angle models. The solid-liquid surface energy distribution from contact angle measurements was wide. The AFM results for the (100) face did not have an extremely wide distribution but they did fall within the lower end of the contact angle results (van Oss model). For the (001) face, AFM measurements had a much wider distribution and fell within all the contact angle results. The average solid-liquid surface energy value for the (001) face was closer in comparison with the average solid-liquid surface energy of the OWRK contact angle model. It was interesting that model 4 had comparable values with contact angle measurements. Model 4 used the solid-vapor surface energy obtained from AFM measurements to determine the surface-tip surface energy. The concern with using model 4 was that the surface would be different in vapor and liquid measurements. However, the solubility of aspirin in diiodomethane is negligible; therefore, there is no dissolution and no surface reconstruction. Also, as described previously, the solid-vapor surface energy determination could only be done in controlled humidity. Since there were no differences between models 2, 3, and 4, each of them could be used in this scenario. However, the next section will describe that when the conditions are not ideal, model 4 starts to break down.

Table 6-9: Tip radius and average tip-vapor surface energy (standard deviation) for the tips used to calculate the solid-liquid surface energy of the (001) and (100) faces of aspirin with diiodomethane.

Tip	Spring constant (N/m)	Radius (nm)	Force (nN)	Work (mN/m)	Tip-Liquid Surface Energy (mJ/m^2)
1	0.04	40	0.9 (0.2)	4.6 (1.3)	2.3 (0.6)
2		43	0.9 (0.1)	4.5 (0.6)	2.3 (0.3)
3		42	0.8 (0.2)	4.3 (1.2)	2.2 (0.6)

Table 6-10: Mixed model statistics for AFM Measurements on the (100) face of aspirin in diiodomethane. a) Repeated measures ANOVA for within subject effects, b) repeated measures ANOVA for between subjects, and c) the variable that demonstrates the largest percentage of variance (100) ASA-diiodomethane AFM measurements.

a)

	Degrees of Freedom	Sum of Square	Mean Square	F Value	p
Location	9	0.007	0.0008	0.30	0.97
Location*(100)	9	0.009	0.001	0.38	0.93
Location*Tip	18	0.056	0.003	1.12	0.41
Error	18	0.050	0.003	-	-

b)

	Degrees of Freedom	Sum of Square	Mean Square	F Value	p
(100) Face	1	0.0001	.0001	0.13	0.75
Tip	2	0.1243	0.622	12.03	0.08
Error	2	0.0103	0.005	-	-

c)

Variable	% of the Total	% Truncated
Tip	51.7	50.4
(100) Face	-2.7	0.0
(100) Face*Tip	4.8	4.6
(100) Face*Tip*Location (Error)	46.2	45.0
Total	100.0	100.0

Table 6-11: Average solid-liquid surface energy of the (100) face of aspirin with diiodomethane determined using the AFM and contact angle methods.

(Note: Contact angle measurements are made in ambient conditions and AFM vapor measurements are done in controlled humidity environment.)

Method	Model		Solid-Liquid Surface Energy (mJ/m^2)
AFM	Model 1	Van Oss et al	15.6 (0.6)
		OWRK	18.2 (0.6)
		Neumann	17.0 (0.6)
	Model 2		1.2 (0.4)
	Model 3		1.2 (0.4)
	Model 4	Model 2 γ_{sv}	1.1 (0.6)
		Model 3 γ_{sv}	1.1 (0.6)
Contact Angle	Van Oss et al		1.6 (0.7)
	OWRK		4.7 (0.9)
	Neumann		3.3 (0.9)

Table 6-12: Mixed model statistics for AFM Measurements on the (001) face of aspirin in diiodomethane. a) Repeated measures ANOVA for within subject effects, b) repeated measures ANOVA for between subjects, and c) the variable that demonstrates the largest percentage of variance (001) ASA-diiodomethane AFM measurements.

a)

	Degrees of Freedom	Sum of Square	Mean Square	F Value	p
Location	9	0.09	0.011	2.18	0.08
Location*(001)	9	0.08	0.009	1.87	0.12
Location*Tip	18	0.16	0.008	1.81	0.11
Error	18	0.09	0.005	-	-

b)

	Degrees of Freedom	Sum of Square	Mean Square	F Value	p
(001) Face	1	0.01	0.01	0.6	0.51
Tip	2	0.19	0.10	4.4	0.18
Error	2	0.04	0.02	-	-

c)

Variable	% of the Total	% Truncated
Tip	30.8	30.1
(001) Face	-2.2	0.0
(001) Face*Tip	11.8	11.5
(001) Face*Tip*Location (Error)	59.7	58.4
Total	100.0	100.0

Table 6-13: Average solid-liquid surface energy of the (001) face of aspirin with diiodomethane determined using the AFM and contact angle methods.

(Note: Contact angle measurements are made in ambient conditions and AFM vapor measurements are done in controlled humidity environment.)

Method	Model		Solid-Liquid Surface Energy (mJ/m^2)
AFM	Model 1	Van Oss et al	16.8 (1.4)
		OWRK	21.4 (1.4)
		Neumann	17.5(1.4)
	Model 2		6.4 (2.3)
	Model 3		6.6 (2.4)
	Model 4	Model 2 γ_{sv}	5.9 (1.4)
		Model 3 γ_{sv}	7.0 (1.4)
Contact Angle	Van Oss et al		2.5 (1.4)
	OWRK		7.9 (0.9)
	Neumann		4.3 (0.6)

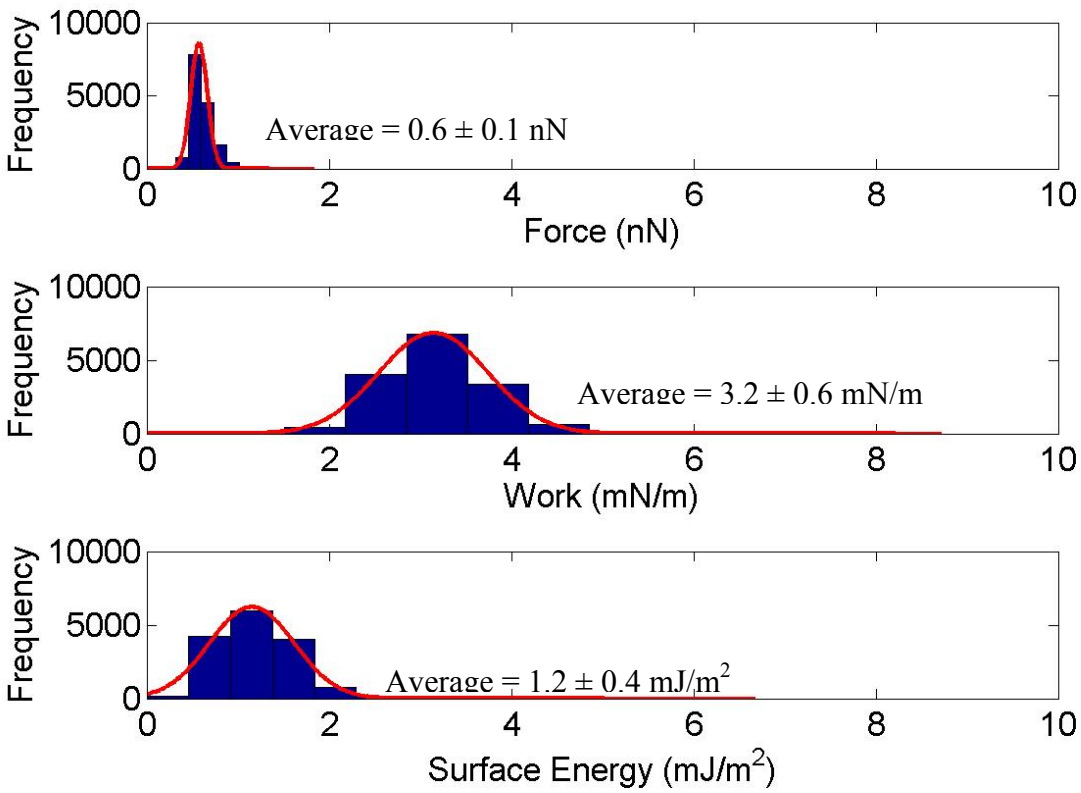

Figure 6-10: The solid-liquid surface energy from AFM force measurements with diiodomethane on the (100) face of aspirin crystals.

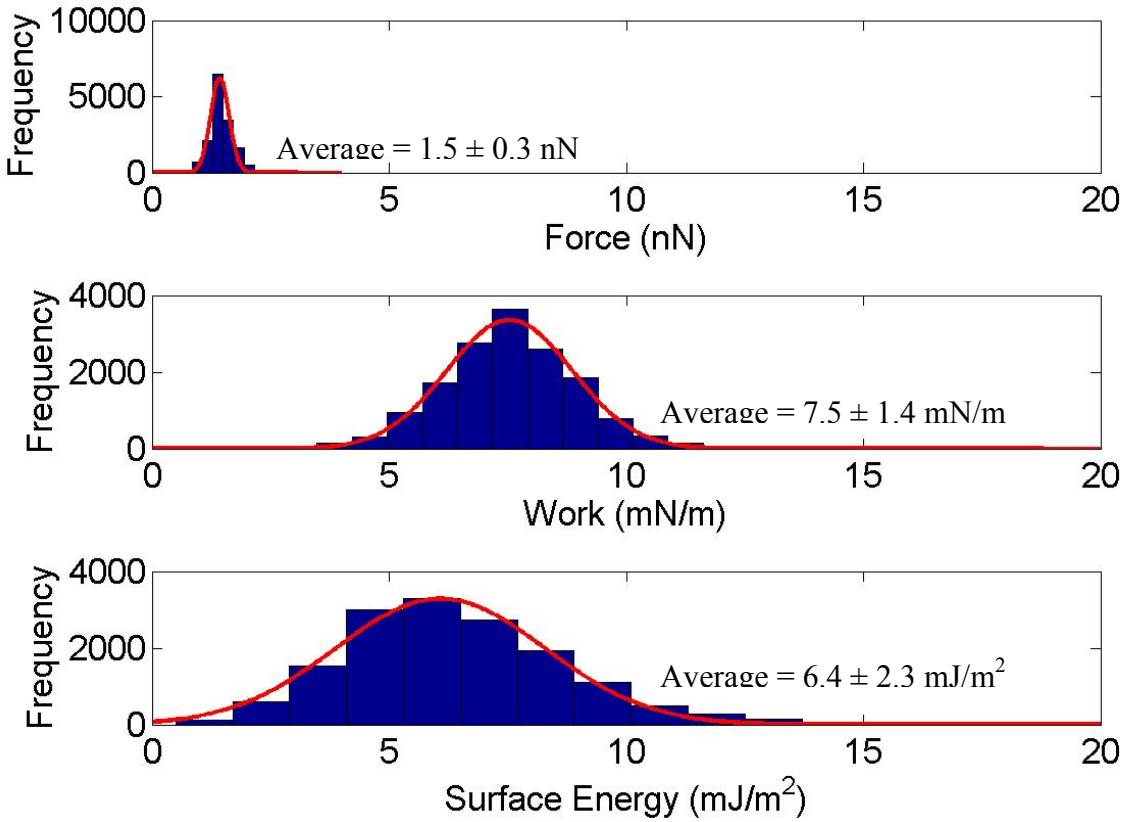

Figure 6-11: The solid-liquid surface energy from AFM force measurements with diiodomethane on the (001) face of aspirin crystals.

6.3.2.1 Water Solid-Liquid Surface Energy

Unlike the inert surface, ASA's solubility in water caused dissolution on the major surfaces. Therefore, it was hard to control the consistency of the measurements, and it was difficult to know the specific interaction that was being measured. As a result, surface energy measurements were captured from ASA crystals immersed in ASA solutions at various concentrations. The ASA solutions were prepared at concentrations surrounding 18 mM, the saturation solubility of ASA in water. The presence of the additive eliminated the possibility for direct comparison with contact angle measurements with pure water. Additives are known to affect crystal growth; therefore, differences were expected between the force of adhesion in a pure solvent and a solvent with an additive. The contact angles cannot be measured in additive solutions because of the risk of preferential absorption at one of the three interfaces.[16] Therefore, the solid-liquid surface energy measurements with the AFM were focused towards evaluating the differences between ASA solutions prepared at different concentrations. The same principles from Chapter 5 still applied to these experiments.

To determine the solid-liquid surface energy of the (100) and (001) face with varying concentration of ASA, the spring constants, tip radii, and tip-vapor surface energies were determined first. **Table 6-14** lists the tip properties for each tip used in the 12, 14, 16, 18, and 20 mM solutions. These values were later used for calculation the solid-liquid surface energy on the (100) and (001) faces of ASA.

Force measurements were made first on the (100) and (001) surfaces in all five solutions using the tips in **Table 6-14**. The data were then analyzed in SAS and JMP. The statistics for the (001) and (100) faces in a 12mM ASA solution are listed in **Table 6-15**

and **Table 6-16**, respectively. The data could not be combined to calculate an average force, work, and surface energy because of the p values in **Table 6-15a** and **Table 6-16a** show the results for within subjects, the time intervals. The p values for time were significantly below 0.05, which meant the values were changing over the time interval studied. These early results prompted another change in the methodology of measuring the forces on ASA. Instead of taking measurements quickly in 10 different spots, the measurements were taken 10 minutes apart until it was confirmed that a steady state had been reached. When the p values are small and there was no steady state for force measurements, it was not possible to calculate an average using the entire data set. In this scenario, an overall average would be misleading. For the measurements in 12mM ASA, no experimental adjustments could be made to induce a steady-state. Since the 12mM condition was well below saturation solubility, dissolution of the crystal continued until equilibrium was reached.

Even though all an overall average for force, work, and surface energy could not be determined, plots were developed that incorporated the data at each ten minute time interval. **Figure 6-12**, **Figure 6-13,** and **Figure 6-14** show the solid-liquid surface energy from model 1, models 2 and 3, and model 4, respectively. Models 2 and 3 are the only surface energy equations that apply under conditions where the surface is changing since they do not rely on solid-vapor surface energy data and do not operate under the assumption that the surface is unchanged from vapor to liquid measurements. **Figure 6-12** showed extremely high solid-liquid surface energy because of the large solid-vapor surface energy from contact angle. **Figure 6-14**, showed the lowest solid-liquid surface

energy, but still relied on a calculated surface-tip surface energy from an unchanged surface in vapor. Therefore, use of models 2 or 3 was required for these experiments.

Table 6-14: Tip radius and average tip-vapor surface energy (standard deviation) for the tips used to calculate the solid-liquid surface energy of the (001) and (100) faces of aspirin with 12, 14, 16, 18, and 20mM ASA solutions.

Tip	ASA Solution Concentration (mM)	Spring constant (N/m)	Radius (nm)	Force (nN)	Work (mN/m)	Tip-Liquid Surface Energy (mJ/m^2)
1	12	0.04	41	0.5 (0.2)	2.8 (1.1)	1.4 (0.5)
2			40	0.5 (0.1)	2.6 (0.6)	1.3 (0.3)
1	14		41	0.7 (0.2)	3.4 (1.0)	1.7 (0.5)
2			42	0.7 (0.2)	3.7 (1.1)	1.8 (0.6)
1	16		40	0.7 (0.3)	4.0 (1.6)	2.0 (0.8)
2			38	0.8 (0.2)	4.5 (1.0)	2.2 (0.5)
3			45	0.9 (0.2)	4.3 (0.8)	2.1 (0.4)
1	18		40	0.7 (0.2)	3.9 (1.1)	2.0 (0.6)
2			41	0.7 (0.1)	3.8 (0.6)	1.9 (0.3)
3			39	0.7 (0.1)	3.7 (0.4)	1.9 (0.2)
1	20		41	0.9 (0.3)	4.4 (1.7)	2.2 (0.9)
2			43	0.8 (0.2)	3.7 (0.8)	1.9 (0.4)
3			40	0.7 (0.2)	4.0 (1.0)	2.0 (0.5)

Table 6-15: Mixed model statistics for AFM Measurements on the (001) face of aspirin in 12mM ASA Solution. a) Repeated measures ANOVA for within subject effects, b) repeated measures ANOVA for between subjects, and c) the variable that demonstrates the largest percentage of variance (001) ASA-diiodomethane AFM measurements.

a)

	Degrees of Freedom	Sum of Square	Mean Square	F Value	p
Time	5	1.20	0.24	492.69	<0.0001
Time*(001)	5	0.09	0.02	36.64	0.0006
Time*Tip	5	0.16	0.03	66.68	0.0001
Error	5	0.002	0.0005	-	-

b)

	Degrees of Freedom	Sum of Square	Mean Square	F Value	p
(001) Face	1	0.005	0.005	12.96	0.17
Tip	1	0.252	0.252	605.16	0.03
Error	1	0.0004	0.0004	-	-

c)

Variable	% of the Total	% Truncated
(001) Face	1.2	1.1
Tip	58.9	54.7
(001) Face*Tip	-7.7	0.0
(001) Face*Tip*Time (Error)	47.6	44.2
Total	100.0	100.0

Table 6-16: Mixed model statistics for AFM Measurements on the (100) face of aspirin in 12mM ASA solution. a) Repeated measures ANOVA for within subject effects, b) repeated measures ANOVA for between subjects, and c) the variable that demonstrates the largest percentage of variance (001) ASA-diiodomethane AFM measurements.

a)

	Degrees of Freedom	Sum of Square	Mean Square	F Value	p
Time	5	0.31	0.06	79.17	<0.0001
Time*(100)	5	0.02	0.004	6.24	0.0329
Time*Tip	5	0.06	0.01	15.85	0.0044
Error	5	0.004	0.0008	-	-

b)

	Degrees of Freedom	Sum of Square	Mean Square	F Value	p
(100) Face	1	0.03	0.03	68.44	0.08
Tip	1	0.07	0.07	133.30	0.06
Error	1	0.0005	0.0005	-	-

c)

Variable	% of the Total	% Truncated
(100) Face	10.2	9.6
Tip	40.6	38.2
(100) Face*Tip	-6.3	0.0
(100) Face*Tip*Time (Error)	55.5	52.2
Total	100.0	100.0

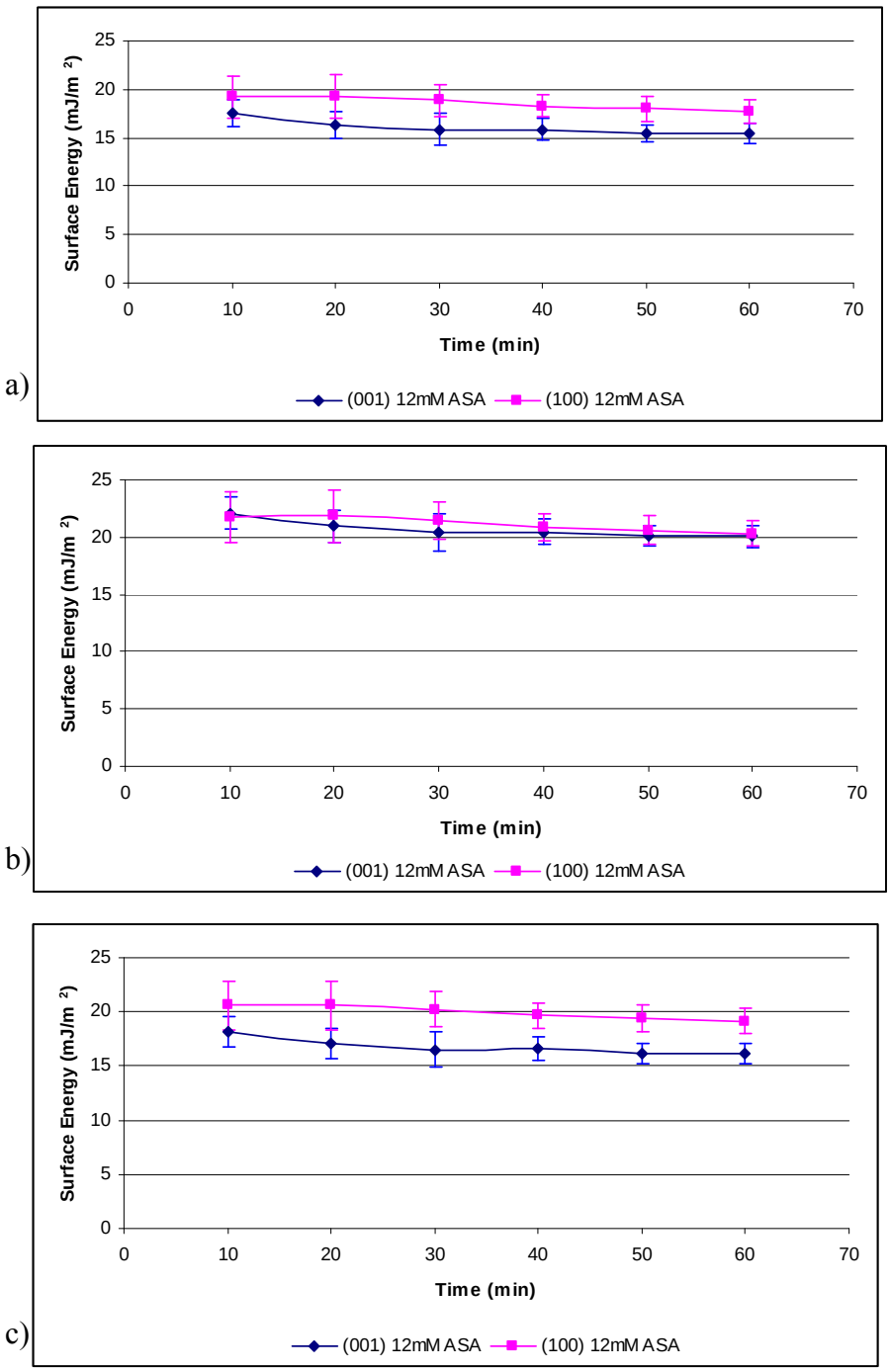

Figure 6-12: Model 1 solid-liquid surface energy from AFM force measurements using a 12mM ASA solution on the (001) and (100) faces of aspirin crystals. Model 1 uses solid-vapor contact angle results from a) the van Oss, b) OWRK, and c) Neumann indirect models.

a)

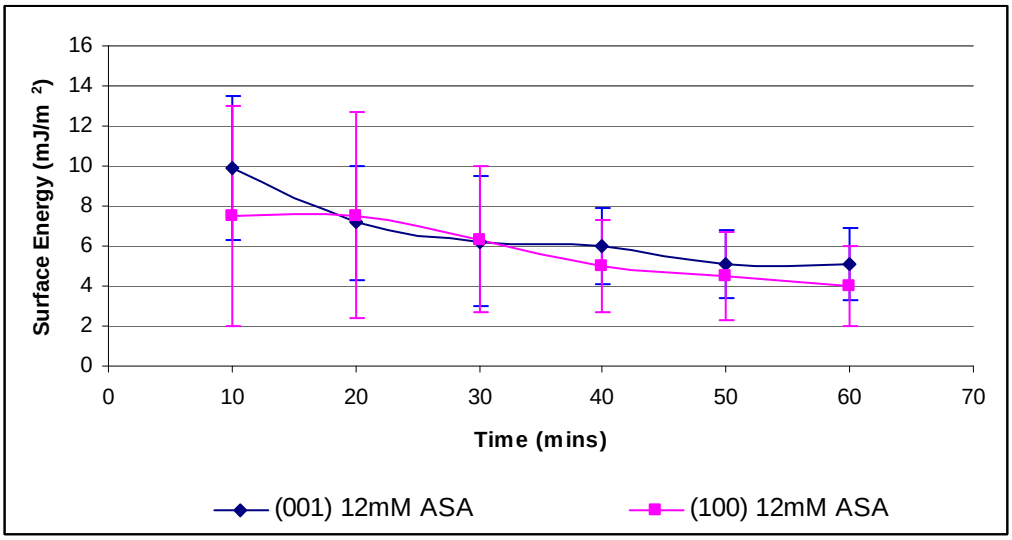

b)

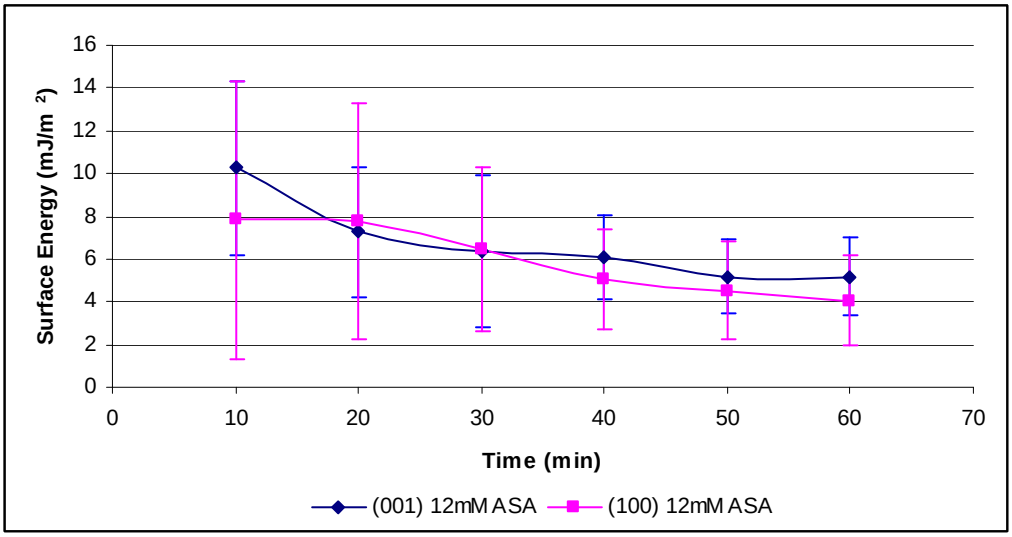

Figure 6-13: Model 2 and model 3 solid-liquid surface energy from AFM force measurements using a 12mM ASA solution on the (001) and (100) faces of aspirin crystals. Model 2 uses the geometric mean, a), and model 3 uses the modified geometric mean, b).

a)

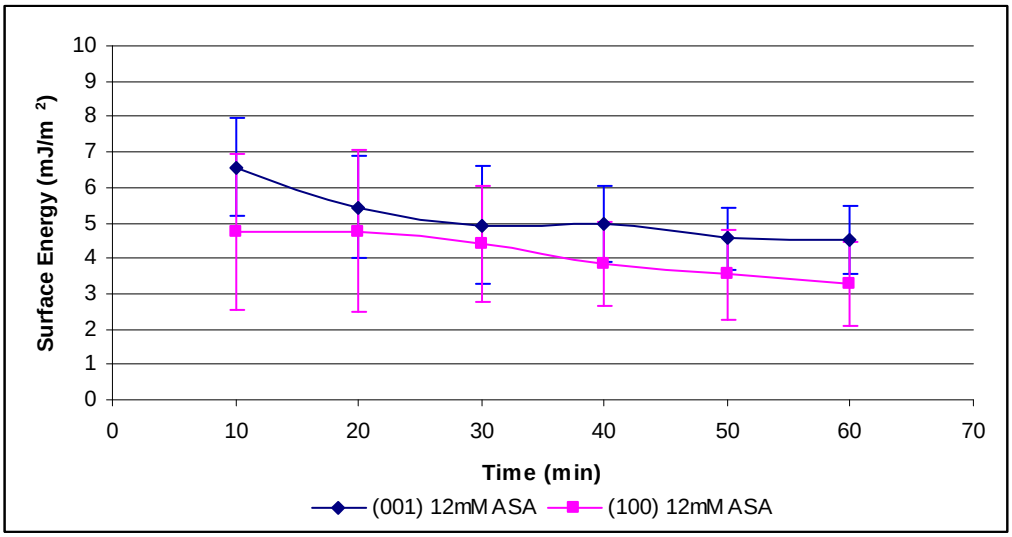

b)

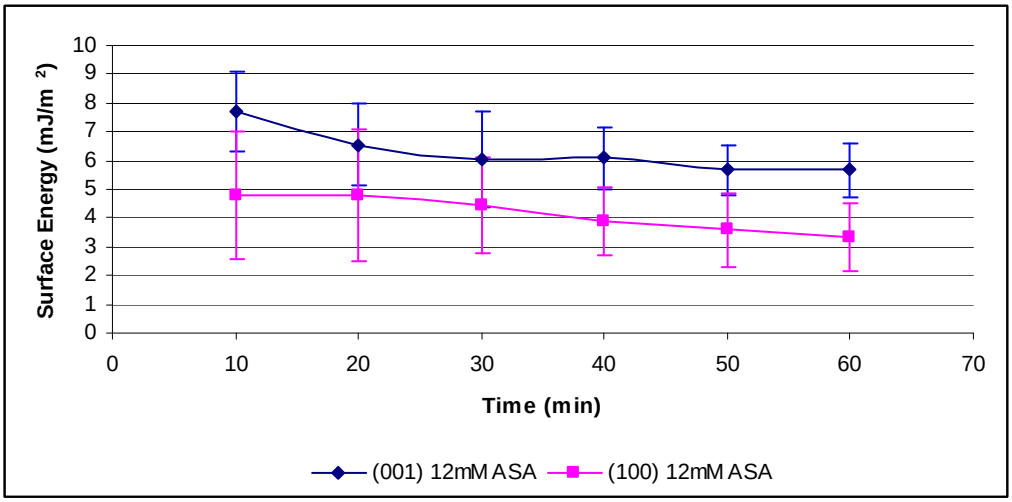

Figure 6-14: Model 4 solid-liquid surface energy from AFM force measurements using a 12mM ASA solution on the (001) and (100) faces of aspirin crystals.

The data from the 14mM ASA solutions was similar to the 12 mM. The statistics in **Table 6-17** and **Table 6-18** show the p values of the times within subjects are significantly smaller than 0.05. Hence, the null hypothesis must be rejected and an average force, work, and surface energy with the entire data set was not calculated. However, the times' p values have gone up and are closer to the required 0.05, the significance level set for accepting or rejecting the null hypothesis. Therefore, the environmental conditions were improved as compared to the 12mM solution. In 14mM solutions, the data could not be combined and instead was plotted to show the changes over time in **Figure 6-15, Figure 6-16**, and **Figure 6-17**.

Figure 6-15 shows the results from model 1, which used contact angle based solid-vapor surface energy values. These values were higher than the contact angle results and mostly reflected the large values of the calculated surface-tip surface energy. The results from surface energy model 4 are shown in **Figure 6-17**. Since the forces were still changing over time, this model was also not ideal for determining surface energy because the assumption cannot be made that the surface in vapor was the same as it was in liquid. Therefore, model 2 and 3 are best suited for determining solid-liquid surface energy. The modification in model 3 was not necessary when the interaction of the two separate phases were similar. Therefore, model 2 can be used to calculate the surface energy.

There are three important observations that need to be pointed out from the 12mM and 14mM ASA solution results. First, at the 10 minute time point, the solid-liquid surface energy was high, similar to the results obtained from contact angle measurements. Over time, the surface energy decreased, indicating a more favorable interaction between the solution and the surface of the aspirin crystal. This could be due to the exchange of

molecules at the surface until an equilibrium state was reached. The second observation was the smaller solid-liquid surface energy on the (100) face than the (001) face in models 2, 3, and 4. Model 1 was the only surface energy model that required knowledge of the solid-vapor surface energy *a priori*. The trend was the reversed from contact angle measurements where the (001) face had a smaller solid-liquid surface energy. During AFM measurements, it was possible that dissolution on the (100) face revealed the carboxylic acid. If this chemical moiety was revealed, the surface was more hydrophilic, resulting in a stronger interaction with water and a smaller surface energy. The high sensitivity of the AFM probes made it possible to distinguish between chemical moieties. This was not possible with contact angle measurements since they are conducted at the macroscopic scale. In all cases, the angles measured on the (100) face with water were larger than those on the (001) face. The AFM measurements have helped gain critical knowledge about the effects of environment and additive concentration on surface energy. These results may be more beneficial than just looking at pure solvents because the actual crystallization environment is under direct investigation.

Since a true average surface energy value was not calculated from the data because a steady state was not reached under these conditions, the JMP data was not relevant. The JMP data helped to understand the variation between subjects, the sample, the tips, the interaction of the tip with the sample in a certain environmental conditions, and the overall residual error. However, the JMP data did not consider time variability because the entire use of repeated measures mixed model broke down when there is time variability. When the statistical variance between times was not equal, the null hypothesis was rejected. In this instance, the experimental methodology needed to be

reconsidered and modified to find a condition where times within the subjects did not change. To do this, the aspirin concentration was increased to 16mM.

During these measurements, the degradation of aspirin was not monitored or evaluated. Aspirin is known to degrade to salicylic acid and the pH of the solution was not controlled to stop or slow the degradation. Therefore, it is also possible, in the solutions below saturation, that the liquid injected for measurements had a mixture of salicylic acid and aspirin. The purpose of these measurements was to find a point when dissolution on the surface was minimized and a constant surface energy could be measured. Hence, this study will not report the degradation of aspirin to salicylic acid.

Table 6-17: Mixed model statistics for AFM Measurements on the (001) face of aspirin in 14mM ASA Solution. a) Repeated measures ANOVA for within subject effects, b) repeated measures ANOVA for between subjects, and c) the variable that demonstrates the largest percentage of variance (001) ASA-diiodomethane AFM measurements.

a)

	Degrees of Freedom	Sum of Square	Mean Square	F Value	p
Time	5	1.10	0.22	13.26	0.007
Time*(001)	5	0.24	0.05	2.94	0.13
Time*Tip	5	0.11	0.022	1.38	0.37
Error	5	0.08	0.02	-	-

b)

	Degrees of Freedom	Sum of Square	Mean Square	F Value	p
(001) Face	1	0.12	0.12	2.80	0.34
Tip	1	0.09	0.09	2.12	0.38
Error	1	0.04	0.04	-	-

c)

Variable	% of the Total	% Truncated
(001) Face	16.6	16.6
Tip	6.8	6.8
(001) Face*Tip	4.2	4.2
(001) Face*Tip*Time (Error)	72.4	72.4
Total	100.0	100.0

Table 6-18: Mixed model statistics for AFM Measurements on the (100) face of aspirin in 14mM ASA solution. a) Repeated measures ANOVA for within subject effects, b) repeated measures ANOVA for between subjects, and c) the variable that demonstrates the largest percentage of variance (001) ASA-diiodomethane AFM measurements.

a)

	Degrees of Freedom	Sum of Square	Mean Square	F Value	p
Time	5	1.33	0.27	54.94	0.0002
Time*(100)	5	0.04	0.009	1.87	0.25
Time*Tip	5	0.05	0.01	2.06	0.22
Error	5	0.24	0.005	-	-

b)

	Degrees of Freedom	Sum of Square	Mean Square	F Value	p
(100) Face	1	0.0007	0.0007	0.02	0.91
Tip	1	0.005	0.005	0.16	0.76
Error	1	0.03	0.03	-	-

c)

Variable	% of the Total	% Truncated
(100) Face	-28.8	0.0
Tip	-22.6	0.0
(100) Face*Tip	39.2	25.9
(100) Face*Tip*Time (Error)	112.3	74.1
Total	100.0	100.0

a)

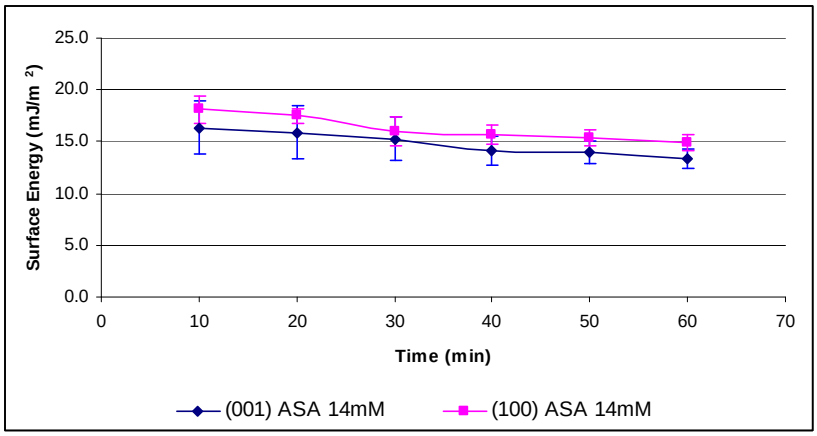

b)

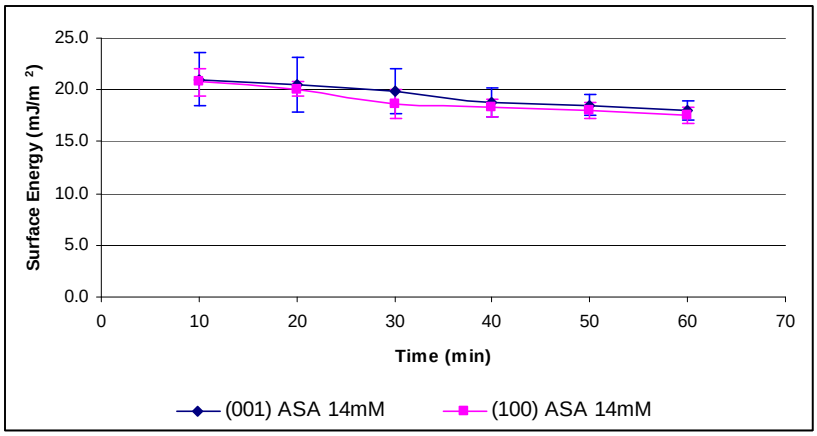

c)

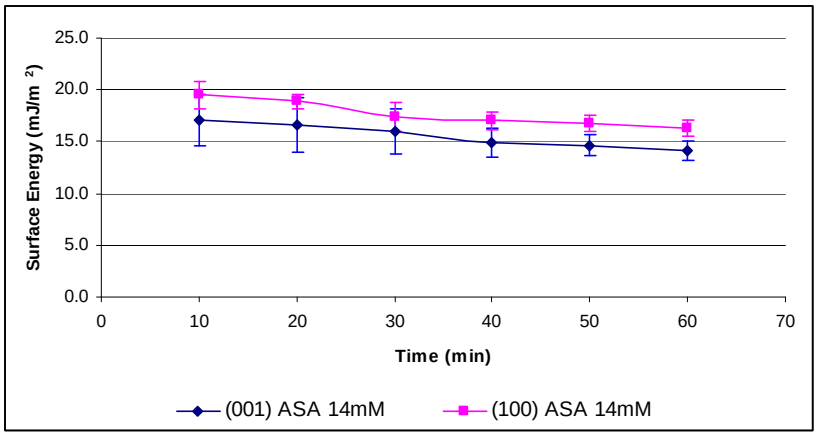

Figure 6-15: Model 1 solid-liquid surface energy from AFM force measurements using a 14mM ASA solution on the (001) and (100) faces of aspirin crystals. Model 1 uses solid-vapor contact angle results from a) the van Oss, b) OWRK, and c) Neumann indirect models.

a)

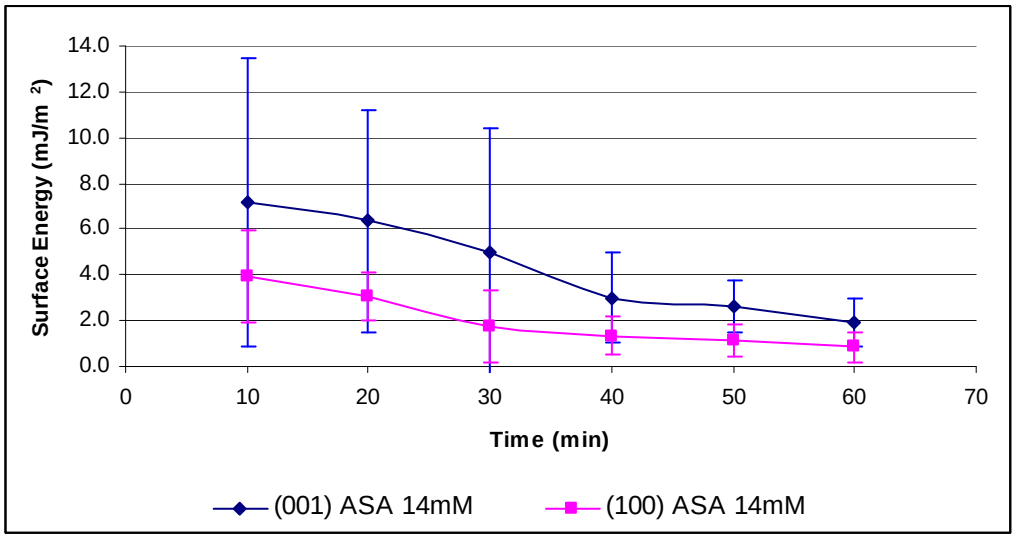

b)

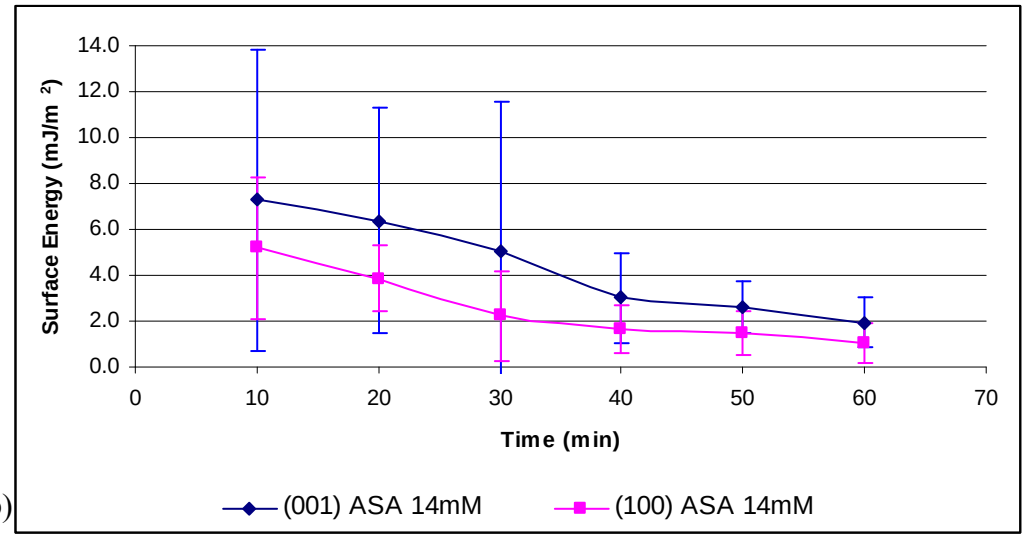

Figure 6-16: Model 2 and model 3 solid-liquid surface energy from AFM force measurements using a 14mM ASA solution on the (001) and (100) faces of aspirin crystals. Model 2 uses the geometric mean, a), and model 3 uses the modified geometric mean, b).

a)

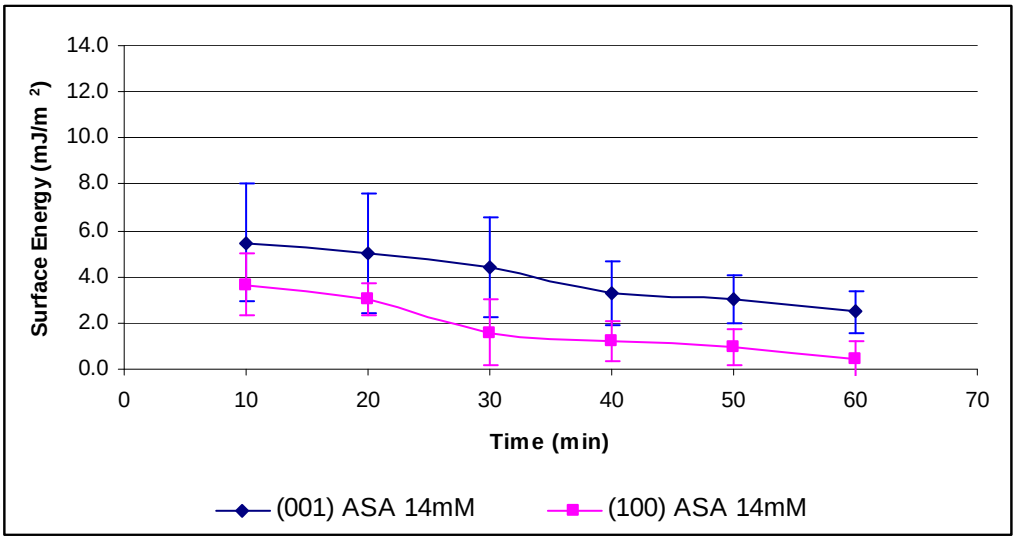

b)

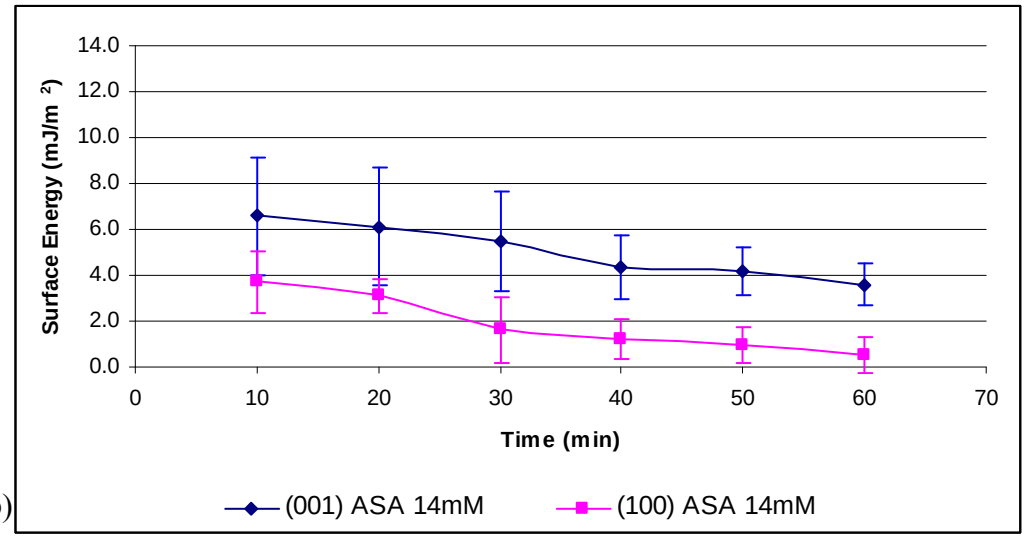

Figure 6-17: Model 4 solid-liquid surface energy from AFM force measurements using a 14mM ASA solution on the (001) and (100) faces of aspirin crystals.

The force measurements were made in a 16mM ASA solution and then analyzed with the statistical repeated measures mixed model. The SAS and JMP statistics are shown in **Table 6-19** and **Table 6-20**. The p values within subjects and between subjects are all above 0.05; therefore, the null hypothesis was accepted and the data was combined to calculate an average force, work, and surface energy. This was the first aqueous additive condition that did not show changes over time. The 16mM solution was about 2mM under the ASA saturation solubility in water. The first force measurements were not made until 10 minutes after the solution has been injected. It was observed when measuring the forces in liquids on inert surfaces that an "equilibrium" period was necessary to eliminate some of the variation. The "equilibrium" period began from the moment the liquid was injected onto the surface until little to no variability was observed between the force measurements at one spot or at different locations. Since the "equilibrium" period was required for the inert surfaces, it was applied to the crystalline material as well. In the 12mM and 14mM solutions, each 10 minute interval brought about a measurable change in solid-liquid surface energy. Thus, it can be assumed that between 0 and 10 minutes, there was also a reduction in surface energy. Dissolution on the crystalline surface could have occurred on this time scale at the 16mM condition to bring the solution's concentration up to 18 mM, which would explain the apparent steady state.

The average force, work, and surface energy for the (001) and (100) faces are shown in **Figure 6-18**. From the previous measurements in a 14mM solution, the final surface energy on the (001) face was about 2 mJ/m^2. The average solid-vapor surface energy in 16mM was about 2.6 mJ/m^2. For the (100) face, the average for the final solid-liquid

surface energy measurement in 14mM was 0.9 mJ/m^2 and the average solid-liquid surface energy for the 16mM solution was 1.0 mJ/m^2. Therefore, it seems the decrease in surface energy is starting to level off and the dissolution has slowed down or stopped on both of the faces.

In **Table 6-21**, the average solid-liquid surface energy values for the (100) and (001) faces of aspirin are listed for the four AFM surface energy models side by side with the contact angle measurements. The results calculated with model 1 were still higher than those determined by contact angle measurements. The use of contact angles to determine surface-tip surface energy was unreliable when an additive solution was used. The ASA and water molecules interacted with the surface molecules, causing reorientation, dissolution, and crystallization. With all of these changes, the assumption that the surface and the surface-tip surface energy remained identical is likely invalid. The assumption is applied to both models 1 and 4, and even though model 4 used only AFM data, the changes occurring on the surface caused concern for the applicability of these models. Therefore, it is thought that the results from models 2 and 3 were more reliable. These two models only required AFM data, and the similarities of the geometric mean and the modified geometric mean results confirmed the use of the geometric mean. The modification did not change the surface energy, which showed the geometric mean could be used. The geometric mean was developed for van der Waals interactions, and therefore, can be used due to the chemical moieties present on the surface of the (100) and (001) faces. The reduction in the surface energy from the 12mM to 16mM solution showed that the AFM was sensitive enough to detect differences in the environmental conditions which could be quantified by model 2. However, if the carboxylic acid was

revealed on the (100) face the geometric mean may be over or under estimate the surface energy. The similarities between models 2 and 3 help to justify the use of the geometric mean for any interactions other than van der Waals. To restate, the difference in the forces of the individual phases is similar enough to reduce the exponential to one, leaving only the geometric mean.

Table 6-19: Mixed model statistics for AFM Measurements on the (001) face of aspirin in 16mM ASA Solution. a) Repeated measures ANOVA for within subject effects, b) repeated measures ANOVA for between subjects, and c) the variable that demonstrates the largest percentage of variance (001) ASA-diiodomethane AFM measurements.

a)

	Degrees of Freedom	Sum of Square	Mean Square	F Value	p
Time	5	0.007	0.001	0.16	0.97
Time*(001)	5	0.09	0.018	2.12	0.15
Time*Tip	10	0.10	0.010	1.14	0.42
Error	10	0.08	0.008	-	-

b)

	Degrees of Freedom	Sum of Square	Mean Square	F Value	p
(001) Face	1	0.01	0.011	2.00	0.29
Tip	2	0.006	0.003	0.53	0.65
Error	2	0.01	0.006	-	-

c)

Variable	% of the Total	% Truncated
(001) Face	1.4	1.3
Tip	-2.1	0.0
(001) Face*Tip	-6.3	0.0
(001) Face*Tip*Time (Error)	107.0	107.0
Total	100.0	100.0

Table 6-20: Mixed model statistics for AFM Measurements on the (100) face of aspirin in 16mM ASA solution. a) Repeated measures ANOVA for within subject effects, b) repeated measures ANOVA for between subjects, and c) the variable that demonstrates the largest percentage of variance (001) ASA-diiodomethane AFM measurements.

a)

	Degrees of Freedom	Sum of Square	Mean Square	F Value	p
Time	5	0.01	0.002	0.85	0.54
Time*(100)	5	0.003	0.0006	0.21	0.95
Time*Tip	10	0.02	0.002	0.72	0.69
Error	10	0.03	0.003	-	-

b)

	Degrees of Freedom	Sum of Square	Mean Square	F Value	p
(100) Face	1	0.001	0.001	1.71	0.32
Tip	2	0.010	0.005	8.19	0.11
Error	2	0.001	0.0006	-	-

c)

Variable	% of the Total	% Truncated
(100) Face	1.9	1.7
Tip	22.9	20.2
(100) Face*Tip	-13.6	0.0
(100) Face*Tip*Time (Error)	88.8	78.1
Total	100.0	100.0

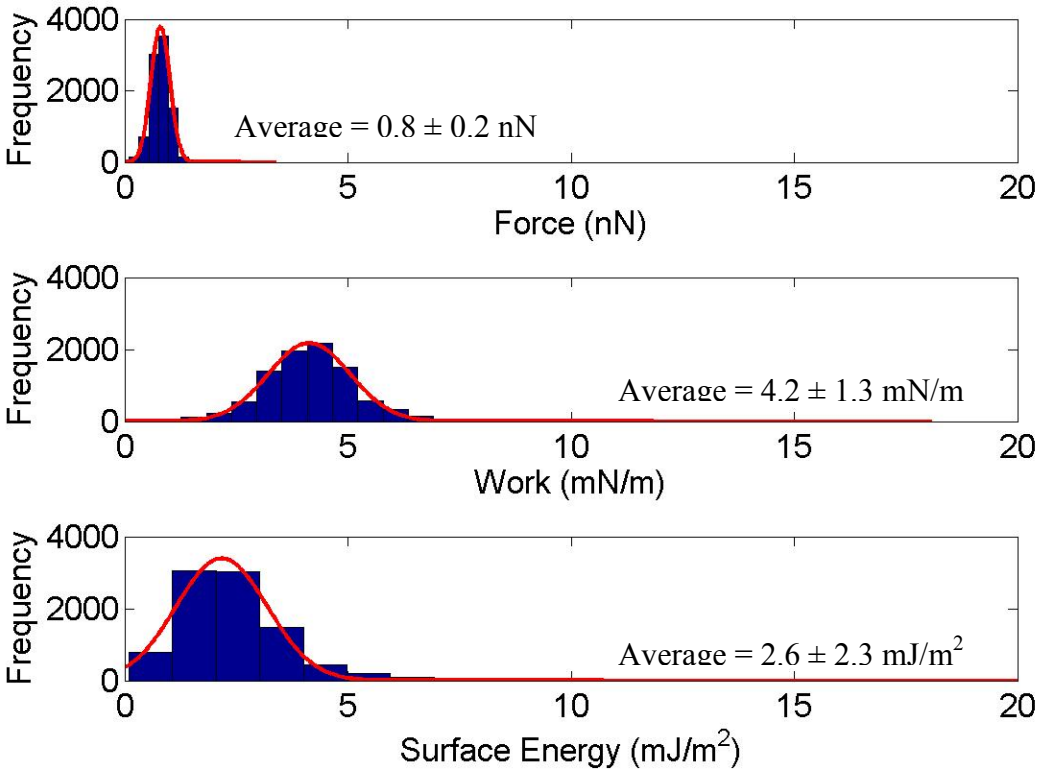

Figure 6-18: The solid-liquid surface energy from AFM force measurements with 16mM ASA solution on the (001) face of aspirin crystals.

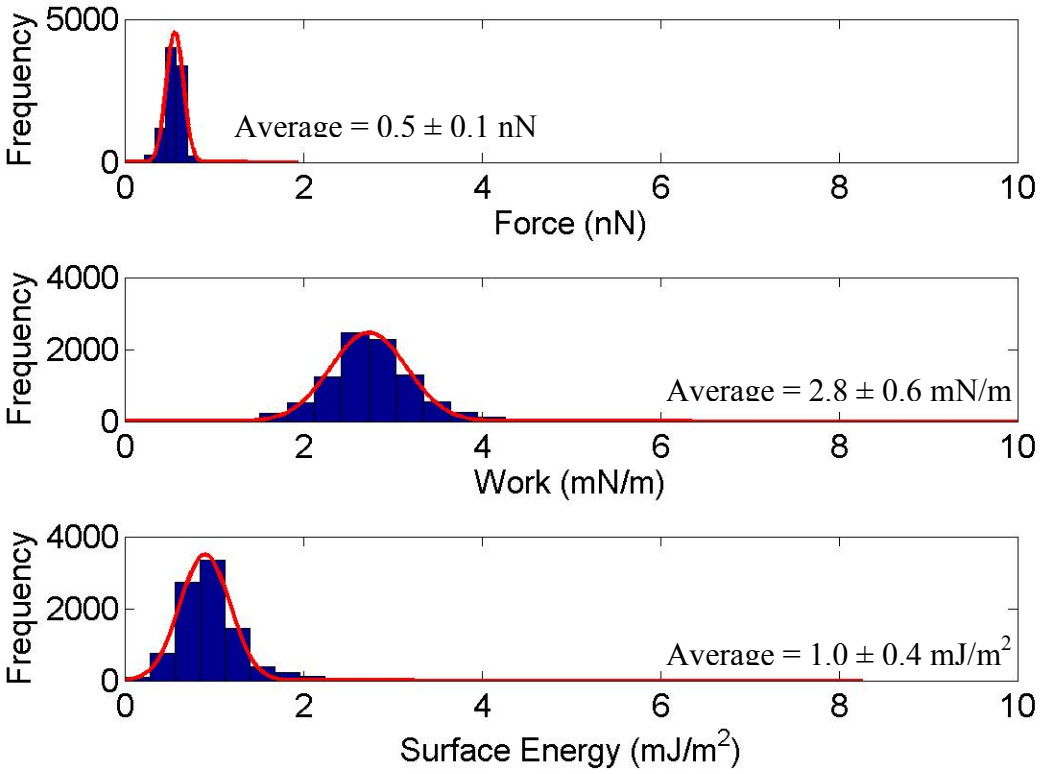

Figure 6-19: The solid-liquid surface energy from AFM force measurements with 16mM ASA solution on the (100) face of aspirin crystals.

Table 6-21: Average solid-liquid surface energy of the (001) and (100) faces of aspirin with 16mM ASA solution determined using the AFM and contact angle methods.

(Note: Contact angle measurements are made in ambient conditions and AFM measurements are done in controlled humidity environment.)

Method	Model		(001) Solid-Liquid Surface Energy mJ/m^2	(100) Solid-Liquid Surface Energy mJ/m^2
AFM	Model 1	Van Oss et al	13.9 (1.3)	15.3 (0.6)
		OWRK	18.5 (1.3)	17.9 (0.6)
		Neumann	14.6 (1.3)	16.7 (0.6)
	Model 2		2.6 (2.3)	1.0 (0.4)
	Model 3		2.6 (2.6)	1.0 (0.4)
	Model 4	Model 2 γ_{sv}	3.0 (1.3)	0.8 (0.6)
		Model 3 γ_{sv}	4.1 (1.3)	0.9 (0.6)
Contact Angle	Van Oss et al		3.2 (2.4)	11.3 (3.2)
	OWRK		8.6 (1.6)	14.4 (2.4)
	Neumann		5.1 (1.1)	13.0 (2.6)

No changes were observed in forces over time using the 16mM solutions. Thus, when using an 18mM and 20mM solution, it was hypothesized that the forces would not vary over time. It was thought that the 18mM solution would show similar results to the 16mM solution and the 20mM solution would lower the surface energy even more because it would create a supersaturated condition. In this supersaturated condition, the solid-liquid surface energy should be strong on the (100) and (001) faces since these are the two major faces of ASA. By definition, a major face must grow the slowest. Therefore, more work was required to separate either the additive or water molecule that blocks the solute molecules from binding to that face and increasing the crystal growth rate of that face.

As always, the forces were measured first in the 18mM and 20mM solutions. The statistics for the 18mM solution measurements on the (001) and (100) are listed in **Table 6-22** and **Table 6-23**, respectively. The statistics for the 20mM solution measurements on the (001) and (100) faces are listed in **Table 6-25** and **Table 6-26**, respectively. The p values for within and between subjects on both faces and in both conditions were greater than 0.05. The null hypothesis was accepted and the data was collated so that an average force, work, and surface energy could be calculated and plotted together. The force, work, and surface energy results for the (001) and (100) faces with 18mM ASA solution are shown in **Figure 6-20** and **Figure 6-21**, respectively. **Figure 6-22** and **Figure 6-23** illustrate the force, work, and surface energy results for the (001) and (100) faces in a 20mM ASA solution.

As for the surface energy models used to determine solid-liquid surface energy, models 2 and 3 were still the best choice. Model 1, which requires the use of contact angle

measurements, still output higher values than the contact angle results for both 18mM and 20mM ASA solutions. There were still changes in the solid-liquid surface energy values as compared with other ASA solutions because it was still a dynamic environment. Since the surface was succeptible to environmental conditions, models 1 and 4 were invalid. Determining the surface energy in a kinetic condition does not uphold the assumption that the surface in vapor and surface in liquid remain identical. Also, when using model 4 for the 20mM solution, a negative value was obtained on the (100) surface. Once the forces and consequently the work of adhesion in the liquid become smaller than the tip-liquid surface energy, the solid-liquid surface energy becomes negative. Consequently, like Young's equation for contact angle surface energy determination, model 4 cannot be used when there is a stronger interaction between a sample and the environment. This leaves model 2 and 3. The results between the two models on both faces and from both solutions showed similarities between models 2 and 3. These similarities have been consistent throughout the entire study. There was no indication that model 3 was better than model 2. To eliminate the reliance on β from contact angle measurements, model 2 was chosen as the best model for determining solid-liquid surface energy, even if the surface had interactions other than van der Waals.

As hypothesized, the model 2 results with the 18mM solution were comparable to the results from the 16mM, but only on the (100) face. Since there was no statistical difference over time with the 16mM ASA solution, it was thought that saturation was reached. Based on ASA solubility, the 18 mM solution was at saturation once it was injected. There was a small difference between the (001) face in 16 mM and 18 mM. The results in the 18mM solution indicate equivalent surface energies between the (100)

and (001) faces, likely due to the fact that they are both major faces and the solution was saturated. The saturation of the environment has created an equilibrium between the surface and the liquid on both faces, and since both are major faces the solid-liquid surface energies are the same.

This observation changes in the 20mM solution. The 20mM solution was a supersaturated condition, which becomes a driving force for crystallization. The decrease in forces on both faces indicated the possibility that crystallization was occurring. Although it was not statistically significant, the average solid-liquid surface energy from model 2 on the (001) face was still larger than values on the (100) face. While the contact angle indicated a stronger interaction on the (001) face, it made more sense scientifically that a stronger interaction would be seen on the (100) face. This stronger interaction could be because the carboxylic group is present, but it also could be because the (100) face is larger than the (001) face. Hence, it was growing the slowest out of the two. If a face grows the slowest, it is possible that interactions between solvents or additives with the surface are blocking more solute molecules from adhering to that face. The measured force of adhesion on both faces was small indicating a stronger interaction with the solution and subsequently a small surface energy.

Table 6-22: Mixed model statistics for AFM Measurements on the (001) face of aspirin in 18mM ASA Solution. a) Repeated measures ANOVA for within subject effects, b) repeated measures ANOVA for between subjects, and c) the variable that demonstrates the largest percentage of variance (001) ASA-diiodomethane AFM measurements.

a)

	Degrees of Freedom	Sum of Square	Mean Square	F Value	p
Time	5	0.009	0.0018	0.97	0.48
Time*(001)	5	0.002	0.0003	0.16	0.97
Time*Tip	10	0.011	0.0011	0.57	0.80
Error	10	0.019	0.0019	-	-

b)

	Degrees of Freedom	Sum of Square	Mean Square	F Value	P
(001) Face	1	0.006	0.0064	10.11	0.09
Tip	2	0.010	0.0050	7.95	0.11
Error	2	0.001	0.0006	-	-

c)

Variable	% of the Total	% Truncated
(001) Face	17.3	16.4
Tip	19.9	18.8
(001) Face*Tip	-5.7	0.0
(001) Face*Tip*Time (Error)	68.5	64.8
Total	100.0	100.0

Table 6-23: Mixed model statistics for AFM Measurements on the (100) face of aspirin in 18mM ASA solution. a) Repeated measures ANOVA for within subject effects, b) repeated measures ANOVA for between subjects, and c) the variable that demonstrates the largest percentage of variance (001) ASA-diiodomethane AFM measurements.

a)

	Degrees of Freedom	Sum of Square	Mean Square	F Value	p
Time	5	0.009	0.0018	1.15	0.40
Time*(100)	5	0.004	0.0009	0.56	0.73
Time*Tip	10	0.006	0.0006	0.42	0.91
Error	10	0.150	0.0015	-	-

b)

	Degrees of Freedom	Sum of Square	Mean Square	F Value	P
(100) Face	1	0.0008	0.0008	0.16	0.72
Tip	2	0.0164	0.0082	1.68	0.37
Error	2	0.0098	0.0049	-	-

c)

Variable	% of the Total	% Truncated
(100) Face	-13.1	0.0
Tip	15.8	14.0
(100) Face*Tip	36.8	32.5
(100) Face*Tip*Time (Error)	60.5	53.5
Total	100.0	100.0

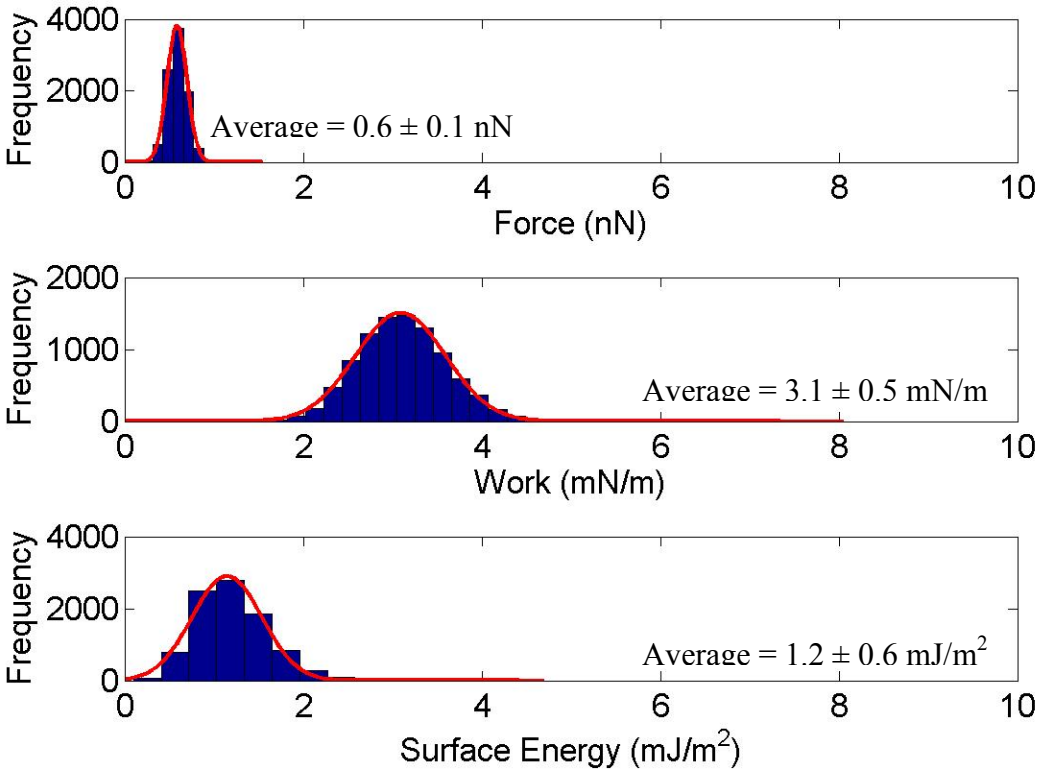

Figure 6-20: The solid-liquid surface energy from AFM force measurements with 18mM ASA solution on the (001) face of aspirin crystals.

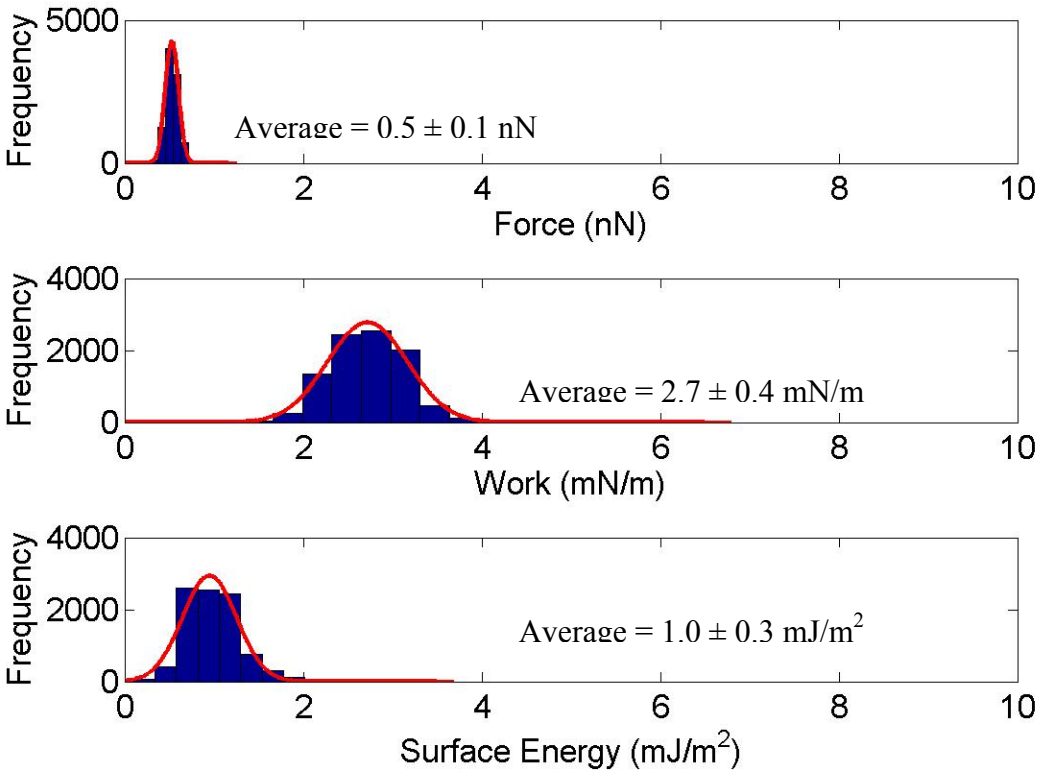

Figure 6-21: The solid-liquid surface energy from AFM force measurements with 18mM ASA solution on the (100) face of aspirin crystals.

Table 6-24: Average solid-liquid surface energy of the (001) and (100) faces of aspirin with 18mM ASA solution determined using the AFM and contact angle methods.

(Note: Contact angle measurements are made in ambient conditions and AFM measurements are done in controlled humidity environment.)

Method	Model		(001) Solid-Liquid Surface Energy mJ/m^2	(100) Solid-Liquid Surface Energy mJ/m^2
AFM	Model 1	Van Oss et al	12.6 (0.5)	15.4 (0.4)
		OWRK	17.2 (0.5)	18.0 (0.4)
		Neumann	13.3 (0.5)	16.8 (0.4)
	Model 2		1.2 (0.4)	1.0 (0.3)
	Model 3		1.2 (0.4)	1.0 (0.3)
	Model 4	Model 2 γ_{sv}	1.72 (0.5)	0.9 (0.4)
		Model 3 γ_{sv}	2.9 (0.5)	0.9 (0.4)
Contact Angle	Van Oss et al		3.2 (2.4)	11.3 (3.2)
	OWRK		8.6 (1.6)	14.4 (2.4)
	Neumann		5.1 (1.1)	13.0 (2.6)

Table 6-25: Mixed model statistics for AFM Measurements on the (001) face of aspirin in 20mM ASA Solution. a) Repeated measures ANOVA for within subject effects, b) repeated measures ANOVA for between subjects, and c) the variable that demonstrates the largest percentage of variance (001) ASA-diiodomethane AFM measurements.

a)

	Degrees of Freedom	Sum of Square	Mean Square	F Value	p
Time	5	0.0008	0.00017	0.47	0.79
Time*(001)	5	0.0008	0.00016	0.46	0.80
Time*Tip	10	0.0007	0.00007	0.20	0.99
Error	10	0.0036	0.00036	-	-

b)

	Degrees of Freedom	Sum of Square	Mean Square	F Value	p
(001) Face	1	0.0003	0.00028	4.00	0.18
Tip	2	0.0005	0.00022	3.24	0.24
Error	2	0.0001	0.00007	-	-

c)

Variable	% of the Total	% Truncated
(001) Face	5.6	5.0
Tip	6.3	5.7
(001) Face*Tip	-10.9	0.0
(001) Face*Tip*Time (Error)	99.0	89.3
Total	100.0	100.0

Table 6-26: Mixed model statistics for AFM Measurements on the (100) face of aspirin in 20mM ASA solution. a) Repeated measures ANOVA for within subject effects, b) repeated measures ANOVA for between subjects, and c) the variable that demonstrates the largest percentage of variance (001) ASA-diiodomethane AFM measurements.

a)

	Degrees of Freedom	Sum of Square	Mean Square	F Value	p
Time	5	0.0006	0.0001	0.25	0.93
Time*(100)	5	0.0042	0.0008	1.87	0.19
Time*Tip	10	0.0124	0.0012	2.73	0.06
Error	10	0.0045	0.0005	-	-

b)

	Degrees of Freedom	Sum of Square	Mean Square	F Value	P
(100) Face	1	0.003	0.003	1.09	0.41
Tip	2	0.032	0.016	6.28	0.14
Error	2	0.005	0.003	-	-

c)

Variable	% of the Total	% Truncated
(100) Face	-1.0	0.0
Tip	28.9	28.6
(100) Face*Tip	32.5	32.2
(100) Face*Tip*Time (Error)	39.6	39.2
Total	100.0	100.0

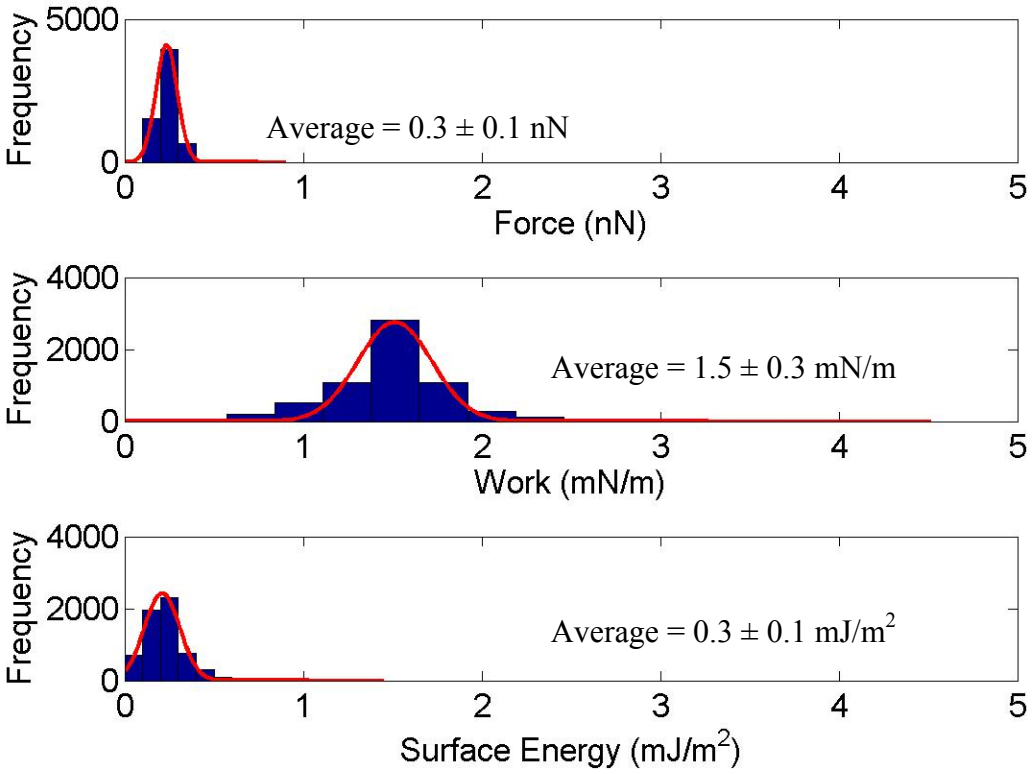

Figure 6-22: The solid-liquid surface energy from AFM force measurements with 20mM ASA solution on the (001) face of aspirin crystals.

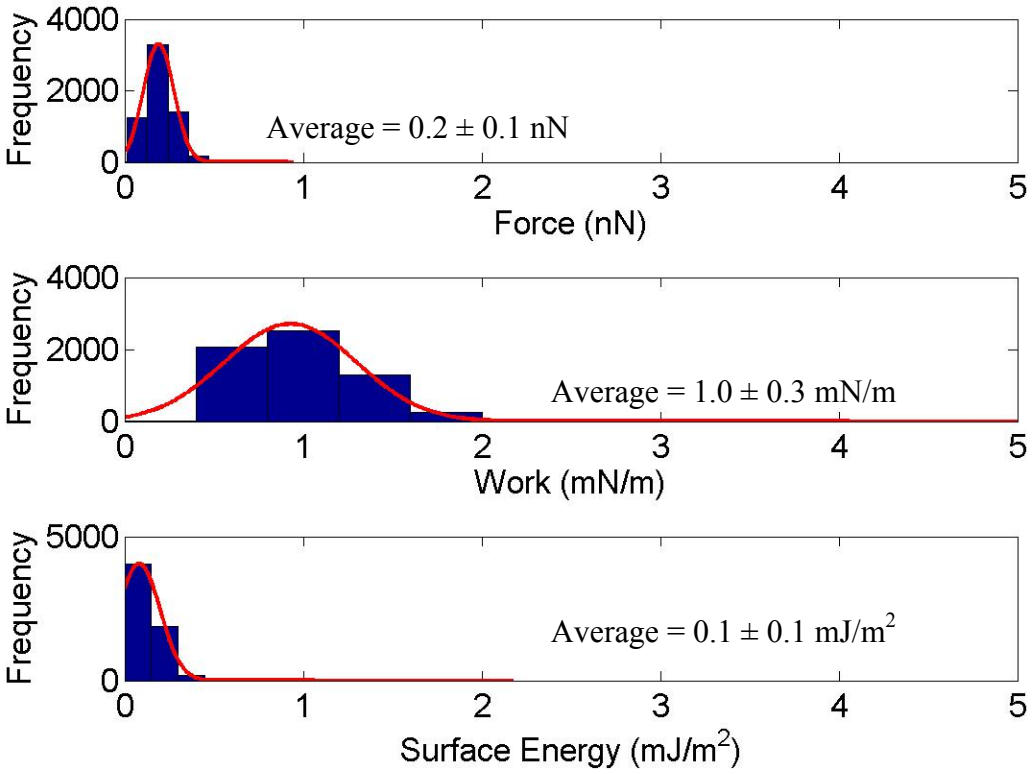

Figure 6-23: The solid-liquid surface energy from AFM force measurements with 20mM ASA solution on the (100) face of aspirin crystals.

Table 6-27: Average solid-liquid surface energy of the (001) and (100) faces of aspirin with 20mM ASA solution determined using the AFM and contact angle methods.

(Note: Contact angle measurements are made in ambient conditions and AFM measurements are done in controlled humidity environment.)

Method	Model		(001) Solid-Liquid Surface Energy mJ/m^2	(100) Solid-Liquid Surface Energy mJ/m^2
AFM	Model 1	Van Oss et al	11.0 (0.4)	13.5 (0.4)
		OWRK	15.6 (0.4)	16.1 (0.4)
		Neumann	11.7 (0.4)	14.9 (0.4)
	Model 2		0.3 (0.1)	0.2 (0.1)
	Model 3		0.3 (0.1)	0.1 (0.1)
	Model 4	Model 2 γ_{sv}	0.1 (0.4)	-1.0 (0.4)
		Model 3 γ_{sv}	1.2 (0.4)	-1.0 (0.4)
Contact Angle	Van Oss et al		3.2 (2.4)	11.3 (3.2)
	OWRK		8.6 (1.6)	14.4 (2.4)
	Neumann		5.1 (1.1)	13.0 (2.6)

6.4 Summary

Several observations were made when the AFM methodology was applied to a crystalline material. First, there were experimental challenges between contact angle and AFM measurements. There were substantial differences observed between solid-vapor surface energy measurements collected in ambient conditions for contact angles and humidity controlled conditions for the AFM. Vapor adsorption on the sample surfaces during AFM measurements did not allow for consistent measurements, and sometimes it did not allow the microscope tip to engage with the surface. The inability to measure forces in pure water indicated the surface was not inert and that the surface deformation shown in **Figure 2-3** was highly possible during the contact angle measurements. Inaccurate contact angle measurements were the direct result of this surface deformation. The solid-vapor surface energy from contact angle measurements relies solely on the measured angles, the accuracy of which is affected by vapor adsorption to the surface. Vapor adsorption causes surface deformation (as a result of dissolution) and interferes with the spreading of solvents. All of these contact angle limitations make the AFM a more attractive tool for determining solid-vapor surface energy.

Since AFM overcomes some of these experimental challenges with contact angle, surface energy models developed for the AFM are critical in determining the final solid-vapor or solid-liquid surface energy. Thus, the second observation in this chapter is the applicability of surface energy models 1 through 4. Models 1 and 4 rely heavily on the assumptions that surface-tip surface energy can be determined from vapor measurements and then used to calculate the solid liquid surface energy (**Figure 4-3** and **Figure 4-5**). If dissolution, crystallization, and/or surface reconstruction are observed, the assumption

that the surface is identical is no longer valid. During the ASA AFM measurements in 12mM and 14mM solutions, the solid-liquid surface energy decreased over time. This decrease is a result of changes occurring on the surface. Likewise, there are differences between the initial (time 10 minutes) solid-liquid surface energy from the 12 and 14mM measurements and the average solid-liquid surface energy from the 16, 18, and 20mM measurements. These various values also indicate that the surface is experiencing dissolution, reorientation, and/or crystallization. Therefore, the surface measured in vapor is not identical to the surface measured in the liquids, and the assumption that the $\gamma_{surface\text{-}tip}$ value is a constant value is not valid. Model 3 relies on β from contact angle measurements and has not shown any differences in the calculated solid-liquid or solid-vapor surface energy. Thus, the modification is not finding an overestimation in surface energy. Therefore, model 2, like with the inert studies, has been deemed acceptable for use with the AFM and these surfaces. However, there could be surfaces whose interactions are too dissimilar to the silicon nitride tip causing the geometric mean model to become invalid.

Lastly, it was stated earlier that comparisons would not be possible between water contact angle results and AFM aqueous values because a solution was used instead of a pure solvent. However, an obvious decrease in solid-liquid surface energy was observed as the ASA concentration increased. As a result, one last graphical analysis was done to see if any trend could be established between the pure solvent solid-liquid surface energy from contact angle data and the various ASA solutions from the AFM. To do this, each contact angle model was compared individually to models 2 and 3, models 4 (using solid-vapor surface energy from models 2 and 3), and model 1 of the corresponding contact

angle method. For example, to compare the (001) van Oss contact angle results, the (001) van Oss AFM results and data from models 2, 3, and 4 were in one figure (**Figure 6-24c**). The water contact angle solid-liquid surface energy was smallest on the (001) face. The AFM measured a force that in turn calculated a higher solid-liquid surface energy in a 12mM solution than what was observed from pure contact angle measurements. This is why there was a spike in the solid-liquid surface energy value at the 12mM ASA concentration. The only model without a large increase in surface energy was the OWRK. The reason there was not a large increase in solid-liquid surface energy at 12mM is because the contact angle solid-liquid surface energy was similar to the AFM solid-liquid surface energy (**Figure 6-24b**). The largest difference and the reason a difference in solid-liquid surface energy is observed on the (001) face for van Oss, OWRK, and Neumann is due to the AFM model 1 results (**Figure 6-24**). The contact angle results were always less than the AFM solid-liquid surface energy from model 1. This same trend was observed on the (100) face as well (**Figure 6-25**). These graphs show clearly the reason model 1 is not applicable to crystalline materials. For the (100) face at all concentrations, the AFM solid-liquid surface energy calculate from models 2, 3, and 4 was always less than the contact angle solid-liquid surface energy. The contact angle on the (100) face was larger than the angle on the (001) face possibly because the carboxylic group was not exposed. The carboxylic group however, could be exposed in the AFM measurements through dissolution or crystallization. The increased sensitivity of the AFM relative to the contact angle allowed for the observation of these changes in the surface. This is why a decrease in solid-liquid surface energy was in models 2-4. The negative solid-liquid surface energy values calculated with model 4 on

the (100) face also show the limitations of this model. The trend observed using the AFM to evaluate solid-liquid surface energy in different additive enhances the capabilities in measuring forces in various environments. It also calls into question the use of the indirect models and Young's equation of balancing the forces for an accurate solid-liquid surface energy determination.

Until a method exists that allows for direct measurement of surface energy, the current standard methods and the models will be limited by their dependence on assumptions. While limitations of the contact angle and AFM made it difficult for direct comparisons, there is confidence that the AFM will help researchers understand different interactions on the surfaces of crystalline materials. This knowledge could help pharmaceutical scientists make decisions for dissolution methods, stability packaging, and formulation development. Unfortunately, the time and training necessary for proper AFM investigation necessitate its use as a research tool, as it has not yet been developed to the point at which it could speed up the decision making process for practical decisions in the pharmaceutical industry.

a)

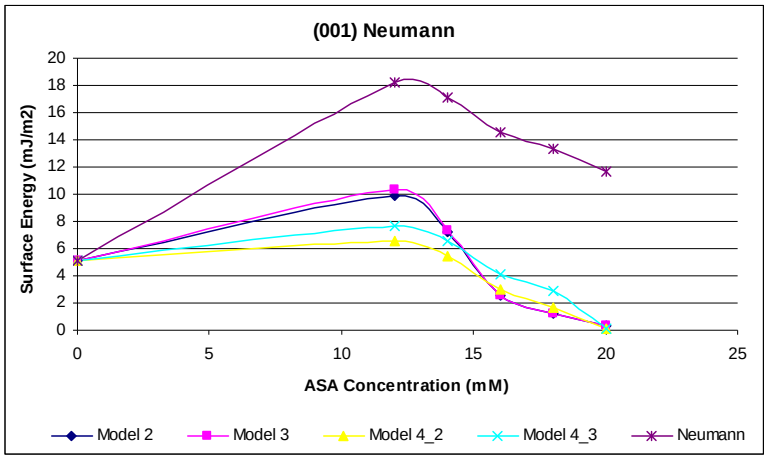

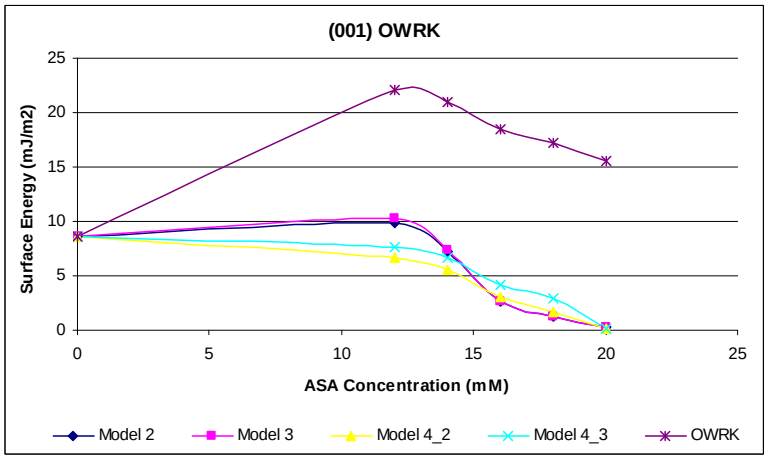

c)

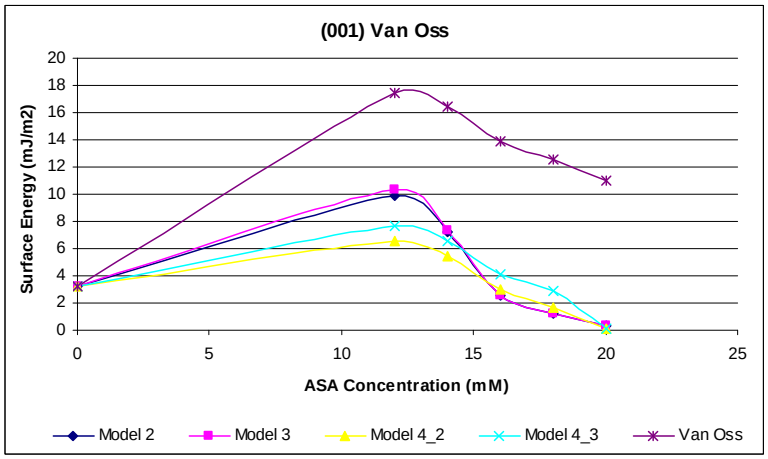

Figure 6-24: The solid-liquid surface energy from the AFM force measurements with 12mM to 20mM ASA solution on the (001) face of aspirin crystals compared with contact angle solid-liquid surface energy from a) the Neumann method, b) the OWRK method, and c) the van Oss method.

a)

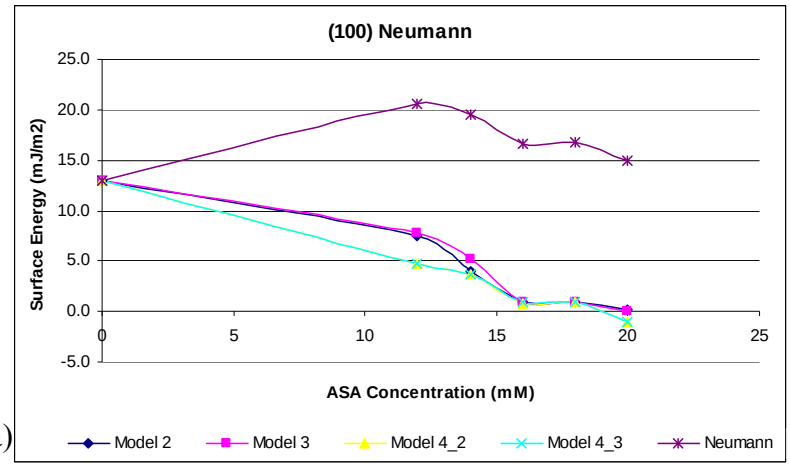

b)

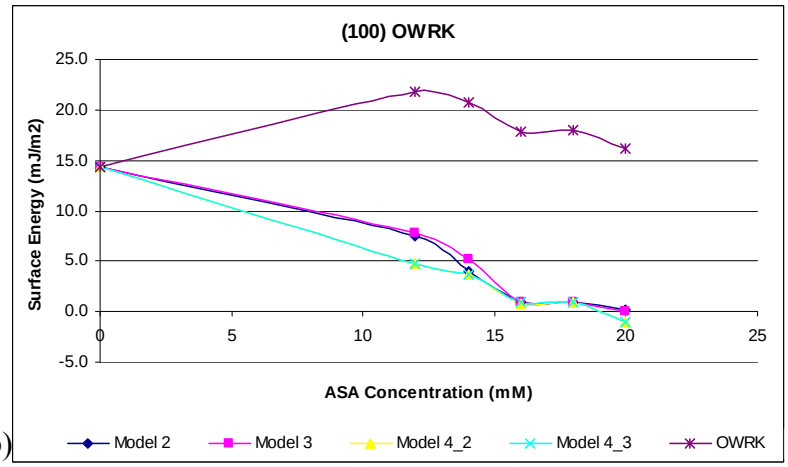

c)

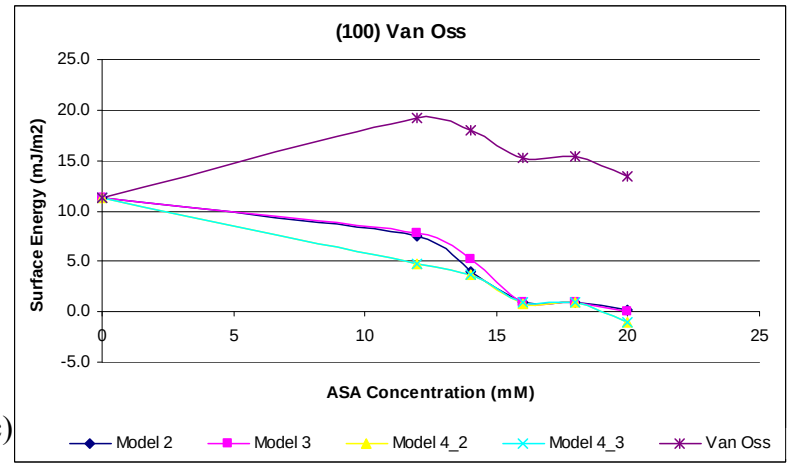

Figure 6-25: The solid-liquid surface energy from the AFM force measurements with 12mM to 20mM ASA solution on the (100) face of aspirin crystals compared with contact angle solid-liquid surface energy from a) the Neumann method, b) the OWRK method, and c) the van Oss method.

Chapter 7 – Conclusion and Future Directions

Development of a new analytical tool to substitute for the gold standard is certainly not without an extensive list of challenges. It was necessary to diligently examine each aspect surrounding the analytical technique and methodology including mathematical models and selection of the appropriate statistical analyses for post-collection processing and interpretation. The mathematical models and methodology must be fit for purpose, robust, and be applicable to a range of materials. Post-collection, the data has to be processed and evaluated for precision within the new analytical tool. Also to validate an instrument's capabilities, the data must be checked for accuracy against the industry "gold" standard as a reference for comparison.

The overall goal of this dissertation was to follow these principles and to develop the atomic force microscope as an analytical method capable of an all-encompassing solution to surface energy measurement. The two criteria selected for verifying the correct choice in mathematical models and physicochemical assumptions were trend matching between contact angle measurements and the extension of models developed on inert surfaces to crystalline materials. Additionally, the AFM methodology and components were rigorously evaluated to increase the precision of the measurements. The methodology was developed so there would be good control over environmental conditions and the AFM tips. Scanning parameters were evaluated to establish repeatability of the measurements. The repeated measures mixed model allowed for the use of multiple samples and tips in the data collection, challenging the development of the AFM. Developmental work was performed on mica and graphite, which are inert, flat,

homogeneous materials. The use of these samples served as an approximation of an ideal test case, thereby allowing for direct identification of the error inherent with the instrument. With this information in hand, it was possible to extend the AFM's use to more complicated systems, systems in which IGC and contact fall short for the measurement of surface energy, such as crystalline surfaces. The limitations of IGC and contact angle for surface energy measurements necessitated the exploration of a different analytical technique, one in which individual crystalline surfaces could be selectively resolved and investigated in their native growth environments. In conclusion, the research presented in this dissertation has helped to advance the understanding between lab-bench theory and potential industrial implementation for the AFM. This work offers a concise yet comprehensive review of surface energetics, setting the stage for pharmaceutical scientists to more effectively estimate, predict, and control the physical behaviors of their final drug products.

At the conclusion of this dissertation, consideration must be given to the studies that could be pursued to further the development and use of the atomic force microscope. The two overall goals of this project were to develop the AFM so that it could be a better method for surface energy evaluation and then to apply this methodology to investigate surface energy of crystals in various growth environments. However, the success of the AFM was limited to the effectiveness of the contact angle method. The contact angle method did not provide meaningful results in the ideal case of mica. The surface energy results also varied when AFM vapor measurements were performed in a controlled environment, illustrating another limitation with the contact angle method. Therefore, it was concluded that other studies on an intermediate surface could be performed to

evaluate the applicability of the AFM for surface energy investigation. With a stronger foundation in the methodology, more crystalline surfaces and environments can be investigated without needing a supplemental method and results to corroborate the AFM data.

The AFM should also not be limited to force measurements. In the pharmaceutical industry as well as academia, there are other applications and modules being developed to further the use of the AFM. One application is nanoindentation to determine mechanical properties on a small scale. Nanoindentation has been used to measure the hardness of tablets, the coating wear durability of tables, and the coating thickness of tablets. It has also been used to measure the elastic modulus of thin films. Knowing the hardness of a solid dispersion or a multiparticule sphere will help a formulator and an analyst understand the performance of a prototype because the hardness can affect the compactability, dissolution, and overall bioperformance of a solid dosage form.

The AFM in conjunction with Raman microscopy has been used to evaluate the physical stability of solid dispersion, specifically evaluating the interaction of an active pharmaceutical ingredient (API) with a polymer. Using a temperature stage, the solid dispersion can be heated passed the glass transition temperature and then cooled to evaluate for phase separation. Knowing the physical stability of a solid dispersion is critical for pharmaceutical formulations. Any detection of phase separation can indicate poor miscibility or interaction of the API and polymer. It is critical to show at ICH (International Conference on Harmonisation) conditions that the enabled formulation is stable. Any observation that the API has crystallized will immediately eliminate that prototype for further development.

While the AFM will become more applicable for many other scientific areas, the instrument requires that the operator receive a rigorous amount of training. The repeatability for any of its applications is its largest drawback. Furthermore, it takes a considerable amount of time and effort to obtain meaningful results. Thus, these disadvantages keep the AFM from breaking through to the forefront of research.

Appendix 1 - Report Generation for Calculation of Spring Constant

Instructions

```
% Inputs

   % freqs = [a:b], region of the spectrum containing resonance peak for integration, start
with ([1010:1250])
   % option = 1, for moving boxcar
   % option = 2 for trapezoidal integration
   % option = 3 for a cubic spline fit
   % option = 4 for savitzky-golay filtering (5-point default)
   % bxcrpts is the number of points to use when smoothing
   % liquid = 0, for air measurement
   % liquid = 1, for liquid measurement
```

% Outputs

```
   % ft = All FT results (127 x 4096 matrix)
   % ave = average FT results (1 4096 matrix)
   % k = The calculated value for spring constant (scalar)
   % fs1 = x-axis for frequency plot (1 x 4096)
   % z = peak area in m^2
   % peakarea1 = peak area in nm^2
```

% Example

```
   % To run in publisher mode:
      % Enter in the command line:
         % freqs = 1100:1230; option = 3; bxcrpts = 15; liquid= 0;
         % afmSpringConstant
   % To run in function mode:
      % Replace top line of this function with:
         % function [ft,ave,k,fs1,z,peakarea] =
afmSpringConstant(freqs,option,bxcrpts,liquid);
      % Enter in the command line:
         % [ft,ave,k,fs1,z,peakarea] = afmSpringConstant([1140:1230],3,15,0);
```

Import the file

```
clc
[filename pathname] = uigetfile('*.*', 'MultiSelect', 'on');
fid = [pathname filename];
newData1 = importdata(fid);
```

```
% Create new variables in the base workspace from those fields.
vars = fieldnames(newData1);
for i = 1:length(vars)
   assignin('base', vars(i), newData1.(vars(i)));
end
input = newData1.data;
```

Divide the file into equal spaced intervals

```
x = 1:2048:262144;
x = x(1:127);
y = 4096:2048:262144;
fs = (1:1/4.19678:62464);
```

Calculate the FFT and Complex Conjugate of the Spectra

```
for i = 1:127;
   %f = fft(input(x(i):y(i)),4096);
   inputtemp = input(x(i):y(i))-mean(input(x(i):y(i)));
   f = abs(fft(inputtemp)*2)/4096;
   ft(i,:) = f.*(f);
end
```

Average the FFTs to obtain one power spectrum

```
[nrows,ncols] = size(ft);
for i = 1:ncols;
   ave(:,i) = sum(ft(:,i));
end
ave = ave/nrows;

fs1 = fs(1:64:end);

if liquid == 0; % use if air
```

Integrate the resonant frequency

```
   if option == 1;
      ave = bxcar(ave,bxcrpts);
      z = trapz(ave(freqs));
   elseif option == 2;
      z = trapz(ave(freqs));
   elseif option == 3;
      [values,p] = csaps(fs1,ave,0.000001,fs1);
      z = trapz(values(freqs));
   elseif option == 4;
      ave = smooth(ave,25,'sgolay',2);
      z = trapz(ave(freqs));
   end
```

```
elseif liquid == 1;    % use if liquid
```

Integrate the resonant frequency

```
   if option == 1;
      ave = bxcar(ave,bxcrpts);
      z = trapz(ave(freqs));
   elseif option == 2;
      z = trapz(ave(freqs));
   elseif option == 3;
      [values,p] = csaps(fs1,ave,0.000001,fs1);
      z = trapz(values(freqs));
   elseif option == 4;
      ave = smooth(ave,25,'sgolay',2);
      [x,ind] = max(ave(freqs));
      z = trapz(ave(freqs(ind:end)));
      z = 2*z;
   end

end
```

Convert the integration to m^2 from nm^2

```
peakarea1 = z*0.000000001*0.000000001;
kb = 0.00000000000000000000000138;
T = 298;
```

Calculate spring constant, k

```
k = kb*T/peakarea1;
disp('File ID = ')
fid
disp('Spring Constant = ')
k
if liquid == 1;
   disp('Max Frequency = ')
   freqs(ind)
end
```

% Plot the resonant peak

```
% Create figure
figure1 = figure;

% Create axes
axes1 = axes('Parent',figure1,'FontSize',16);
box(axes1,'on');
hold(axes1,'all');
```

```
% Create plot
plot(fs1(1080:1280),ave(1080:1280),'Marker','.','LineStyle','none','Color',[1 0 0]);

% Create xlabel
xlabel(('Frequency (kHz)'),'FontSize',16);

% Create ylabel
ylabel(('PSD (m^2)'),'FontSize',16);

File ID =

fid =

F:\AFM_Experiments\2nd Measurements of Tip 1\tip1_13

Spring Constant =

k =

    0.06
```

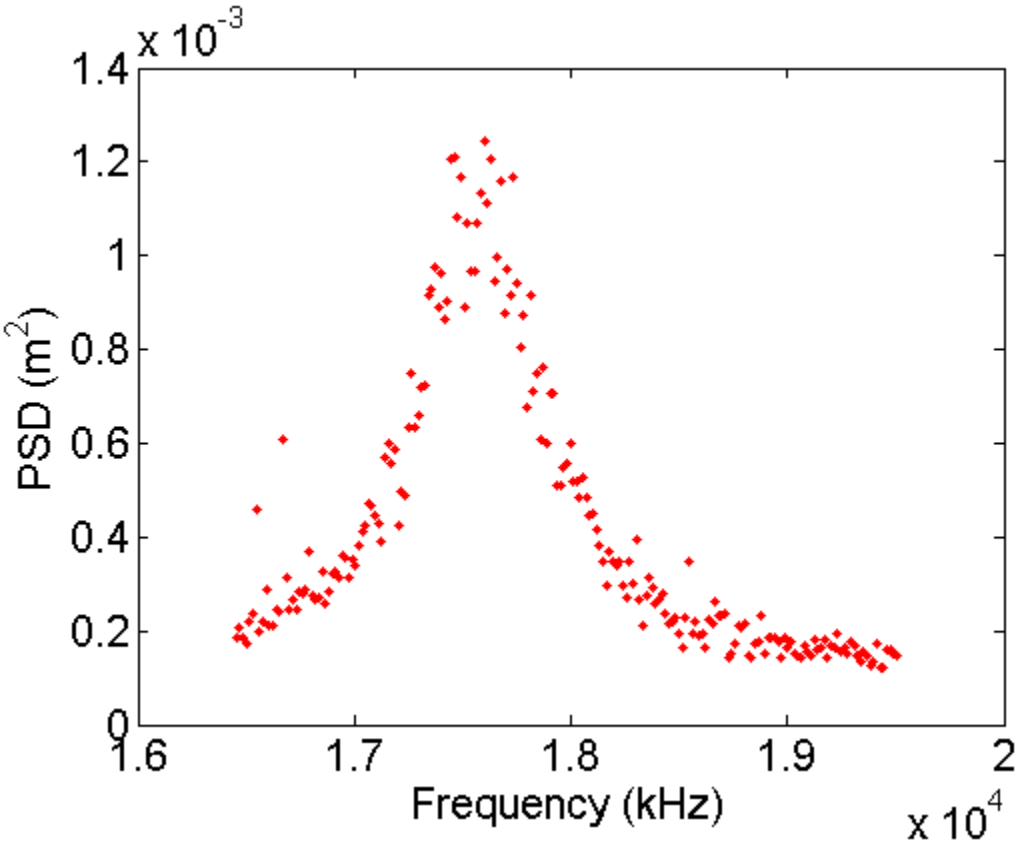

Appendix 2 - Matlab code for Calculation of Spring Constant

```
%% Instructions

% Inputs

    % freqs = [a:b], region of the spectrum containing resonance peak
for integration, start with ([1010:1250])
    % option = 1, for moving boxcar
    % option = 2 for trapezoidal integration
    % option = 3 for a cubic spline fit
    % option = 4 for savitzky-golay filtering (5-point default)
    % bxcrpts is the number of points to use when smoothing
    % liquid = 0, for air measurement
    % liquid = 1, for liquid measurement

% Outputs

    % ft = All FT results (127 x 4096 matrix)
    % ave = average FT results (1 4096 matrix)
    % k = The calculated value for spring constant (scalar)
    % fs1 = x-axis for frequency plot (1 x 4096)
    % z = peak area in m^2
    % peakarea1 = peak area in nm^2

% Example

    % To run in publisher mode:
        % Enter in the command line:
            % freqs = 1100:1230; option = 3; bxcrpts = 15; liquid= 0;
            % afmSpringConstant
    % To run in function mode:
        % Replace top line of this function with:
            % function [ft,ave,k,fs1,z,peakarea] =
afmSpringConstant(freqs,option,bxcrpts,liquid);
        % Enter in the command line:
            % [ft,ave,k,fs1,z,peakarea] =
afmSpringConstant([1140:1230],3,15,0);


%% Import the file
clc
[filename pathname] = uigetfile('*.*', 'MultiSelect', 'on');
fid = [pathname filename];
newData1 = importdata(fid);

% Create new variables in the base workspace from those fields.
vars = fieldnames(newData1);
for i = 1:length(vars)
    assignin('base', vars(i), newData1.(vars(i)));
end
input = newData1.data;
```

```
%% Divide the file into equal spaced intervals
x = 1:2048:262144;
x = x(1:127);
y = 4096:2048:262144;
fs = (1:1/4.19678:62464);

%% Calculate the FFT and Complex Conjugate of the Spectra

for i = 1:127;
    %f = fft(input(x(i):y(i)),4096);
    inputtemp = input(x(i):y(i))-mean(input(x(i):y(i)));
    f = abs(fft(inputtemp)*2)/4096;
    ft(i,:) = f.*(f);
end

%% Average the FFTs to obtain one power spectrum
[nrows,ncols] = size(ft);
for i = 1:ncols;
    ave(:,i) = sum(ft(:,i));
end
ave = ave/nrows;

fs1 = fs(1:64:end);

if liquid == 0; % use if air
    %% Integrate the resonant frequency
    if option == 1;
        ave = bxcar(ave,bxcrpts);
        z = trapz(ave(freqs));
    elseif option == 2;
        z = trapz(ave(freqs));
    elseif option == 3;
        [values,p] = csaps(fs1,ave,0.000001,fs1);
        z = trapz(values(freqs));
    elseif option == 4;
        ave = smooth(ave,25,'sgolay',2);
        z = trapz(ave(freqs));
    end

elseif liquid == 1;    % use if liquid
    %% Integrate the resonant frequency
    if option == 1;
        ave = bxcar(ave,bxcrpts);
        z = trapz(ave(freqs));
    elseif option == 2;
        z = trapz(ave(freqs));
    elseif option == 3;
        [values,p] = csaps(fs1,ave,0.000001,fs1);
        z = trapz(values(freqs));
    elseif option == 4;
        ave = smooth(ave,25,'sgolay',2);
        [x,ind] = max(ave(freqs));
        z = trapz(ave(freqs(ind:end)));
        z = 2*z;
    end
end
```

```
%% Convert the integration to m^2 from nm^2

peakarea1 = z*0.000000001*0.000000001;
kb = 0.00000000000000000000000138;
T = 298;

%% Calculate spring constant, k
k = kb*T/peakarea1;
disp('File ID = ')
fid
disp('Spring Constant = ')
k
if liquid == 1;
    disp('Max Frequency = ')
    freqs(ind)
end

% Plot the resonant peak

% Create figure
figure1 = figure;

% Create axes
axes1 = axes('Parent',figure1,'FontSize',16);
box(axes1,'on');
hold(axes1,'all');

% Create plot
plot(fs1(1080:1280),ave(1080:1280),'Marker','.','LineStyle','none','Col
or',[1 0 0]);

% Create xlabel
xlabel(('Frequency (kHz)'),'FontSize',16);

% Create ylabel
ylabel(('PSD (m^2)'),'FontSize',16);
```

References

1. Adamson, A.W., *Physical Chemistry of Surfaces*. 5th ed. 1990, New York: John Wiley & Sons.

2. Etzler, F.M., *Contact Angle, Wettability and Adhesion*. Characterization of Surface Free Energies and Surface Chemistry of Solids. Vol. 3. 2003: K.L Mittal.

3. Grimsey, I.M., Feeley, J.C., York, P., *Analytis of the Surface Energy of Pharmaceutical Powders by Inverse Gas Chromatography.* Journal of Phamaceutical Sciences, 2002. **91**: p. 571-583.

4. Planinsek, O., Buckton, G., *Inverse Gas Chromatography: Considerations about Appropriate Use for Amorphous and Crystalline Powders.* Journal of Pharmaceutical Sciences, 2003. **92**: p. 1286-1294.

5. Lester, G.R., *Contact Angles of Liquids at Deformable Solid Surfaces.* Journal of Colloid Science, 1961. **16**: p. 315-326.

6. Saiz, E., Tomsia, A.P., Cannon, R.M., *Ridging Effects on Wetting and Spreading of Liquids on Solids.* Acta Materialia 1998. **46**: p. 2349-2361.

7. Heng, J.Y.Y., Bismark, A., Lee, A.F., Wilson, K., Williams, D.R., *Anisotropic Surface Energetics and Wettability of Macroscopic Form I Paracetamol Crystals.* Langmuir, 2006. **22**: p. 2760-2769.

8. Heng, J.Y.Y., Bismarck, A., Lee, A.F., Wilson, K., Williams, D.R., *Anisotropic Surface Chemistry of Aspirin Crystals.* Journal of Pharmaceutical Sciences, 2007. **96**: p. 2134-2144.

9. Good, R.J., *Contact Angle, Wetting, and Adhesion: A Critical Review.* J. Adhesion Sci. Tech., 1992. **6**: p. 1269-1302.

10. Busscher, H.J.V.P., A. W. J.; De Boer, P.; De Jong, H. P.; Arends, J., *The Effect of Surface Roughening of Polymers on Measured Contact Angles of Liquids.* Colloids and Surfaces, 1984. **9**: p. 319-331.

11. Stroem, G., Fredriksson, M., Stenius, P., *Contact angles, Work of Adhesion, and Interfacial Tensions at a Dissolving Hydrocarbon Surface.* Journal of Colloid and Interface Sciences, 1987. **119**: p. 352-361.

12. Van Oss, C.J.J., L.; Chaudhury, M. K.; Good, R. J.. *Estimation of the Polar Parameters of the Surface Tension of Liquids by Contact Angle Measurements on Gels.* Journal of Colloid and Interface Sciences, 1989. **128**: p. 313-319.

13. Fowkes, F.M., Mostafa, M.A., *Acid-Base Interactions in Polymer Adsorption.* Industrial Engineering Chemistry Product Research and Development, 1978. **17**: p. 3-7.

14. Owens, D.K., Wendt, C.R., *Estimation of the Surface Free Energy of Polymers.* Journal of Applied Polymer Science, 1969. **13**: p. 1741-1747.

15. Chen. F., C., W.V., *Applicability Study of a New Acid-Base Interaction Model in Polypeptides and Polyamides.* Langmuir, 1991. **7**: p. 2401-2404.

16. van Oss, C.J., Good, R.J., Chaudhury, M.K., *Additive and nonadditive surface tension components and the interpretation of contact angle.* Langmuir, 1988. **4**: p. 884-891.

17. Good, R.J., *Contact angles and the Surface Free Energy of Solids.* Surface and Colloid Science, 1979. **11**: p. 1-30.

18. Chibowski, E., Perea-Carpio, R., *Problems of Contact Angle and Solid Surface Free Energy Determination.* Advances in Colloid and Interface Science, 2002. **98**: p. 245-264.

19. Kwok, D.Y.H., *Contact Angles and Surface Energetics*, in *Mechanical and Industrial Engineering*. 1998, University of Toronto: Ottawa. p. 230.

20. Li, D., Nuemann, A.W., *Contact Angles on Hydrophobic Solid Surfaces and Their interpretation.* Journal of Colloid and Interface Sciences, 1992. **148**: p. 190-200.

21. Pesult, D.R., *Binary Interaction Constants for Mixtures with a Wide Range in Component Properties.* Industrial & Engineering Chemistry Fundamentals, 1978. **17**: p. 235-242.

22. Pyter, R.A., Zografi, G., Mukerjee, P., *Wetting of Solids by Surface-Active Agents: The Effects of Unequal Adsorption to Vapor-Liquid and Solid-Liquid Interaces.* Journal of Colloid and Interface Sciences, 1982. **89**: p. 144-153.

23. McGuire, J., Lee, E., Sproull, R.D., *Temperature Influences on Surface Energetic Parameters Evaluated at Solid-Liquid Intefaces.* Surface and Interface Analysis, 1990. **15**: p. 603-608.

24. Adam, N.K., *The Chemical Structure of Solid Surfaces as Deduced from Contact Angles.* Contact Angle, Wettability, Adhesion, 52, Advanced Chemical Series, 1964. **43**: p. 52-56.

25. Correia, N.T., Ramos, J. J. M., Saramago, B. J. V., Calado, J. C. G., *Estimation of the Surface Tension of a Solid: Application to a Liquid Cyrstalline Polymer.* Journal of Colloid and Interface Sciences, 1997. **189**: p. 361-369.

26. del Rio, O.I., Neumann, A.W., *Axisymmetric Drop Shape Analysis: Computational Methods for the Measurement of Interfacial Properties from the Shape and Dimensions of Pendant and Sessile Drops.* Journal of Colloid and Interface Science, 1997. **196**: p. 136-147.

27. Van Oss, C.J., Giese, R.F., *The Hydrophilicity and Hydrophobicity of Clay Minerals.* Clays and Clay Minerals, 1995. **43**: p. 474-477.

28. Pong, W.T., Durkan, C., *A Review and Outlook for an Anomaly of Scanning Tunnelling Microscopy (STM): Superlattices on Graphite.* Journal of Physics D: Applied Physics, 2005. **38**: p. R329-R355.

29. Bonnell, D.A. and B.D. Huey, *Scanning Probe Microscopy and Spectroscopy: theory, techniques, and applications*. 2nd ed, ed. D. Bonnel. 2001, New York, NY: Wiley-VCH.

30. Binning, G., Quate, C.F., Gerber, Ch., *Atomic Force Microscope.* Physical Review Letters, 1986. **56**: p. 930-933.

31. Morris, V.J., Kirby, A.R., Gunning, A.P., *Atomic Force Microscopy for Biologist*. 1 ed. 1999, London: Imperial College Press. 332.

32. Hans-Jurgen Butt, B.C., Michael Kappl, *Force measurements with the atomic force microscope: Technique, interpretation and applications.* Surface Science Reports, 2005. **59**: p. 1-152.

33. Leite, F.L., Herrmann, P. S. P., *Application of Atomic Force Spectroscopy (AFS) to Studies of Adhesion Phenomena: A Review.* Journal of Adhesion Science & Technology, 2005. **19**: p. 365-405.

34. Tersoff, J., Hamann, D.R., *Theory of Scanning Tunneling Microscope.* American Physical Society: Physical Review B, 1985. **31**: p. 805-813.

35. Binning, G., Rohrer, H., Gerber, C., Weibel, E., *Surface Studies by Scanning Tunneling Microscopy.* American Physical Society: Physical Review Letters, 1982. **49**: p. 57-61.

36. Jenkins, C., Westwood, D.I., Elliott, M., Macdonald, J.E., Meaton, C., Bland, S., *Metrology of Seminconductor Device Structures by Cross-Sectional AFM.* Materials Science and Engineering B, 2001. **80**: p. 138-141.

37. Plomp, M., Rice, M.K., Wagner, E.K., McPherson, A., Malkin, A., *Rapid Visualization at High Resolution of Pathogens by Atomic Force Microscopy.* American Journal of Pathology, 2002. **160**: p. 1959-1966.

38. Li, T., Park, K., Morris, K.R., *Understanding the Formation of Etching Patterns Using a Refined Monte Carlo Simulation Model.* Crystal Growth & Design, 2002. **2**: p. 177-184.

39. Li, T., Morris, K.R., Park, K., *Influence of Tailor-Made Addivites on Etching Patterns of Acetaminophen Single Crystals.* Pharmaceutical Research, 2001. **18**: p. 398-402.

40. Abendan, R.S., Swift, J.A., *Dissolution on Cholesterol Monohydrate Single-Crystal Surfaces Monitored by in Situ Atomic Force Microscopy.* Crystal Growth & Design, 2005. **5**: p. 2146-2153.

41. Bonnell, D.A., Huey, B.D., *Scanning Probe Microscopy and Spectroscopy: Theory, Techniques, and Applications.* Vol. 1. 2001, New York: Wiley-VCH.

42. Butt, H.J., Cappella, B., Kappl, M. , *Force measurements with the Atomic Force Microscope: Technique, Interpretation and Applications.* Surface Science Reports, 2005. **59**: p. 1-152.

43. Albrecht, T.R., Akamine, S., Carver, T.E., Quate, C.F., *Microfabrication of Cantilever Styli for the Atomic Force Microscope.* Journal of Vacuum Science and Technology A, 1990. **8**: p. 3386-3396.

44. Khan, A., Philip, J., Hess, P., *Young's Modulus of Silicon Nitride Used in Scanning Force Microscope Cantilevers.* Journal of Applied Physics, 2004. **95**: p. 1667-1672.

45. Cleveland, J.P., Manne, S., Bocek, D., Hansma, P. K., *A Nondestructive Method for Determining the Spring Constant of Cantilevers for Scanning Force Microscopy.* Review of Scientific Instruments, 1993. **64**: p. 403-405.

46. Hutter, J.L., Bechhoefer, J., , *Calibration of Atomic-Force Microscope Tips.* Review of Scientifi Instruements, 1993. **64**: p. 1868-1873.

47. Dongmo, L.S., Villarrubia, J.S., Jones, S.N., Renegar, T.B., Postek, M.T., Song, J.F., *Experimental Test of Blind Tip Reconstruction for Scanning Probe Microscopy.* Ultramicroscopy, 2000. **85**: p. 141-153.

48. Todd, B.A., Eppell, S. J., *A Method to Improve the Quantitative Analysis of SFM Images at the Nanoscale.* Surface Science, 2001. **491**: p. 473-483.

49. Villarrubia, J.S., *Scanned Probe Microsocpe Tip Characterization Without Calibrated Tip Characterizers.* Journal of Vacuum Science & Technology B, 1996. **14**: p. 1518-1521.

50. Williams, P.M.S., K.M., Davies, M.C., Jackson, D.E., Roberts, C.J., , *Blind Reconstruction of Scanning Probe Image Data.* Journal of Vacuum Science & Technology, 1996. **14**: p. 1557-1562.

51. Veeco, *di MultiMode SPM Instruction Manual*. Vol. 5. 2004.

52. Rosner, B., *Fundamentals of Biostatistics*. 2000, Pacific Grove: Brooks/Cole.

53. Finot, E., Lesniewska, E., Mutin, J.C., Hosain, S.I., Goudonnet, J.P., *Contact Force Dependence on Relative Humidity: Investigations Using Atomic Force Microscopy.* Scanning Microscopy, 1996. **10**: p. 697-708.

54. Hooton, J.C., German, C. S., Allen, S., Davies, M. C., Roberts, C. J., Tendler, S. J. B., Williams, P. M., *Characterization of Particl-Interactions by Atomic Force Microscopy: Effect of Contact Area.* Pharmaceutical Research, 2003. **20**: p. 508-514.

55. Jang, J., Yang, M., Schatz, G., *Microscopic Origin of the Humidity Dependence of the Adhesion Force in Atomic Force Microscopy.* The Journal of Chemical Physics, 2007. **126**: p. 174705-1 - 174705-6.

56. Johnson, K.L., Kendall, K., Roberts, A.D., *Surface Energy and the Contact of Elastic Solids.* Proceedings of the Royal Society of London A, 1971. **324**: p. 301-313.

57. Derjaguin, B.V., Muller, V.M., Toporov, Y.P., *Effect of Contact Deformations on the Adhesion of Particles.* Journal of Colloid Interface Science, 1975. **53**: p. 314-326.

58. Butt, H.-J., Cappella, Brunero, Kappl, Michael *Force measurements with the atomic force microscope: Technique, interpretation and applications.* Surface Science Reports, 2005. **59**: p. 1-152.

59. Israelachvili, J., *Adhesion: In Intermolecular & Surfaces Forces*. Vol. 2nd. 1991, San Diego: Academic Press Inc.

60. Tabor, D., *Surface Forces and Surface Interactions.* Journal of Colloid and Interface Science, 1977. **58**: p. 2-13.

61. Zhang, J., Ebbens, S., Chen, X., Jin, Z., Luk, S., Madden, C., Patel, N., and Roberts, C.J., *Determination of the Surface Free Energy of Cyrstalline and Amorphous Lactose by Atomic Force Microscopy Adhesion Measurement.* Pharmaceutical Research, 2006. **23**: p. 401-407.

62. Li, D., *Thermodynamic Theory of the Equation of State for Interfacial Tensions of Solid-Liquid Systems*. 1990, University of Toronoto. p. 242.

63. Byrn, S.R., Pfeiffer, R.R., Stowell, J.G., *Solid-State Chemistry of Drugs*. Vol. 2nd. 1999, West Lafayette: SSCI, Inc.

64. Bauer, J., Spanton, Stephen., Henry, R., Quick, J., Dziki, W., Porter, W., Morris, J., *Ritonavir: An Extraordinary Example of Conformational Polymorphism.* Pharmaceutical Research, 2001. **18**: p. 859-866.

65. Rasenack, N., Muller, B.W., *Crystal Habit and Tableting Behavior.* International Journal of Pharmaceutics, 2002. **244**: p. 45-57.

66. Berkovitch-Yellin, Z., *Toward an Ab Intio Derivation of Crystal Morphology.* J Am. Chem. Soc., 1985. **107**: p. 8239-8235.

67. Weissbuch, I., Popovitz-Biro, R., LaHav, M., Leiserowitz, L., *Understanding and Control of Nucleation, Growth, Habit, Dissolution, and Structure of Two- and Three-Dimensional Crystals Using 'Tailor-Made' Auxiliaries.* Acta Cryst., 1995. **B51**: p. 115-148.

68. Bennema, P., *Theory of Growth and Morphology Applied to Organic Crystals; Possible Applications to Protein Crystals.* Journal of Crystal Growth, 1992. **122**: p. 110-119.

69. Lahav, M., Leiserowitz., *The Effect of Solvent on Crystal Growth and Morphology.* Chemical Engineering Science, 2001. **56**: p. 2245-2253.

70. Weissbuch, I., Addadi, L., LaHav, M., Leiserowitz, L., *Molecular Recognition at Crystal Interfaces.* Science, 1991. **253**: p. 637-645.

71. Hilfiker, R., *Polymorphism in the Pharmaceutical Industry*. 2006, Weinheim: Wiley-VCH.

72. Bond, A.D., Boese, R., Desiraju, G.R., *On the Polymorphism of Aspirin.* Angewandte Chemie International Edition, 2007. **46**: p. 615-617.

73. Bond, A.D., Boese, R., Desiraju, G.R., *On the Polymorphism of Aspirin: Crystalline Aspirin as Intergrowths of Two "Polymorphic" Domains.* Angewandte Chemie International Edition, 2007. **46**: p. 618-622.

74. Kiang, Y.H., Shi, H.G., Mathre, D.J., Xu, W., Zhang, D., Panmai, S., *Crystal Structure and Surface Properties of an Investigational Drug - A Case Study.* International Journal of Pharmaceutics, 2004. **280**: p. 17-26.

75. Hoffmann, F., *Acetyl Salicylic Acid*, in *United States Patent Office*. 1900: Germany.

76. Kozu, S., Takane, K., *Cell-Dimensions and Space-Group of Acetylsalicylic Acid.* Proceeding of the Imperial Academy, 1935. **11**: p. 381-382.

77. Nitta, I., Watanabe, T., *Unit Cell and Space Group of Acetylsalicylic Acid.* Scientific Papers of the Institute of Physical and Chemical Research, 1937. **31**: p. 125-128.

78. Watanabe, A., Yamaoka, Y., and Kuroda, K., *Study of Crystalline Drugs by Means of Polarizing Microscope. III. Key Refractive Indices of Some Crystalline Drugs and Their Measurement Using an Improved Immersion Method.* Chemical & Pharmaceutical Bulletin, 1980. **28**: p. 372-378.

79. Watanabe, A., Yamaoka, Y., and Takada, K., *Crystal Habits and Dissolution Behavior of Aspirin.* Chemical & Pharmaceutical Bulletin, 1982. **30**: p. 2958-2963.

80. Wheatley, P.J., *The Crystal and Molecular Structure of Aspirin.* Journal of the Chemical Society, Suppl, 1964: p. 6036-6048.

81. Harrison, A., Ibberson, R., Robb, G., Whittaker, G., Wilson, C., Youngson, D., *In Situ Neutron Diffraction Studies of Single Crystals and Powders During Microwave Irradiation.* Faraday Discussions, 2002. **122**: p. 363-379.

82. Kim, Y., Machida, K., Taga, T., Osaki, K., *Structure Redetermination and Packing Analysis of Aspirin Crystal.* Chemical & Pharmaceutical Bulletin, 1985. **33**(2641-2647).

83. Wilson, C.C., *Interesting Proton Behaviour in Molecular Structures. Variable Temperature Neutron Diffraction and Ab Initio Study of Acetylsalicylic Acid: Characterising Librational Motions and Comparing Protons in Different Hydrogen Bonding Potentials.* New Journal of Chemistry, 2002. **26**: p. 1733-1739.

84. Hammond, R.B., Pencheva, K., Roberts, K.J., *A Structural-Kinetic Approach to Model Face-Specific Solution/Crystal Surface Energy Associated with the Crystallization of Acetyl Salicylic Acid from Supersaturated Aqueous/Ethanol Solution.* Crystal Growth and Design, 2006. **6**: p. 1324-1334.

85. Meenan, P., *Crystal Morphology Predictive Techniques to Characterize Crystal Habit: Application to Aspirin ($C_9H_8O_4$).* ACS Symposium Series: Separation and Purification by Crystallization, 1997. **667**: p. 2-17.

86. Aubrey-Medendorp, C., Parkin, S., Li, T., *The Confusion of Indexing Aspirin Crystals.* Journal of Phamaceutical Sciences, 2008. **97**: p. 1361-1367.

87. Li, T., Shubin, L., Feng, S., Aubrey, C.E., *Face-Integrated Fukui Function: Understanding Wettability Anisotropy of Molecular Crystals from Density Function Theory.* Journal of American Chemical Society, 2005. **127**: p. 1364-1365.

88. Niini, R., *The Crystal Form and Optical Constants of Aspirin.* Zeitschrift fuer Kristallographie, Kristallgeometrie, Kristallphysik, Kristallchemie, 1931. **79**: p. 532-536.

89. Vishwesher, P., McMahon, J.A., Oliveira, M., Peterson, M.L., Zaworotko, M.J., *The Predictably Elusive Form II of Aspirin.* Journal of American Chemical Society, 2005. **127**: p. 16802-16803.

90. Berkovitch-Yellin, Z., van Mil, J., Addadi, L., Idelson, M., Lahav, M., Leiserowitz, L., *Crystal Morphology Engineering by "Tailor-Made" Inhibitors: A New Probe to Fine Intermolecular Interactions.* Journal of American Chemical Society, 1985. **107**: p. 3111-3122.

Vita

CLARE AUBREY-MEDENDORP
Born: July 21, 1980
Birthplace: Lexington, KY

EDUCATION

- **University of Tennessee**, Bachelor of Sciences, December 2002

PROFESSIONAL

- Senior Research Scientist, Merck & Co., Summit, NJ, 2009 - Present
- Research Assistant, University of Kentucky College of Pharmacy, 2003-2009

HONORS AND AWARDS

- PhRMA Foundation Pre Doctoral Fellowship in Pharmaceutics for 2007-2009.
- Peter G. Glavinos, Jr., Ph.D. Graduate Student Travel Award Fall 2007.
- Computational and Computer Sciences Research Fellow for 2006.
- Elected chair of the University of Kentucky's AAPS chapter for 2006.

PUBLICATIONS

1. **Aubrey-Medendorp, C.**, Parkin, S., Li, T., "The Confusion of Indexing Aspirin Crystals", Journal of Pharmaceutical Sciences, 97(4) 1361-1367.
2. **Aubrey-Medendorp, C.**, Swadley, M., Li, T., "The Polymorphism of Indomethacin: An Analysis by Density Functional Theory Calculations", Pharmaceutical Research, 25(4) 953-959.
3. Li, T., Shubin, L., Feng, S., **Aubrey, C.**, "Face-Integrated Fukui Function: Understanding Wettability Anisotropy of Molecular Crystals from Density Functional Theory", Journal of American Chemical Society 2005, 127(5), 1364-1365.

PRESENTATIONS

1. **Aubrey-Medendorp, C.,** Merrick, J., Hoerner, J., Gandhi, R., Medendorp, J., and Burlage, R. "Raman vs. Near Infrared Spectroscopy: An Investigation of Process Analytical Technology Tools in Determining Low Drug Load Content Uniformity in

Blends and Roller Compacted Granulations", Association of Pharmaceutical Sciences Annual Meeting, New Orleans, LA 2010.

2. **Aubrey-Medendorp, C.**, Li, T., "The Confusion of Indexing Aspirin Crystals", Midwest Organic Solid-State Chemistry Symposium, Manhattan, KS 2008.
3. **Aubrey-Medendorp, C.**, Li, T., "A Novel Method for Measuring Surface Energy using Atomic Force Microscopy", Association of Pharmaceutical Sciences Annual Meeting, San Diego, CA 2007.
4. **Aubrey-Medendorp, C.**, Li, T., "Developing an AFM Method for Determining Surface Energy", Midwest Organic Solid-State Chemistry Symposium, Lexington, KY 2007.
5. **Aubrey-Medendorp, C.**, Li, T., "Investigation of Surface Energy using Atomic Force Microscopy", Association of Pharmaceutical Sciences Annual Meeting, San Antonio, TX 2006
6. **Aubrey-Medendorp, C.**, Li, T., "Investigation of Surface Energy of Single Aspirin Crystals with Contact Angle and Atomic Force Microscopy", Midwest Organic Solid-State Chemistry Symposium, Iowa City, Iowa 2006.
7. **Aubrey, C.**, Li, T., "Investigation of Surface Energy of Single Aspirin Crystals with Contact Angle and Atomic Force Microscopy", American Association of Pharmaceutical Sciences Annual Meeting, Nashville, TN 2005.
8. **Aubrey, C.**, Li, T., "Investigation of Surface Energy of Aspirin Crystals using Contact Angle and Atomic Force Microscopy", Pharmaceutics Graduate Student Research Meeting, Lawrence, KS 2005.
9. **Aubrey, C.**, Li, T., "Investigation of Surface Energy of Single Aspirin Crystals with Atomic Force Microscopy", American Association of Pharmaceutical Sciences Annual Meeting, Baltimore, MD 2004.